

# **Use of multiple functionalised ligand sets in metal-organic framework formation: synthesis, characterisation and gas uptake studies**

**Oliver Rowe**

A thesis submitted in accordance with the requirements for the degree of Doctor of Philosophy by research at the University of East Anglia

**University of East Anglia**

**School of Chemistry**

March 2013

©This copy of the thesis has been supplied on condition that anyone who consults it is understood to recognise that its copyright rests with the author and that no quotation from the thesis, nor any information derived therefrom, may be published without the author's prior, written consent.

## Abstract

A variety of metal-organic frameworks have been synthesised and structurally characterised and their gas uptake behaviours investigated.

The solvothermal reaction of  $\text{Zn}(\text{NO}_3)_2 \cdot 6\text{H}_2\text{O}$  with 5-aminoisophthalic acid ( $\text{H}_2$ -5-AIP) and 4,4'-bipyridyl (4,4'-bipy) led to the self-assembly of the 3D hybrid H-bonded/covalent structure  $\{[\text{Zn}(\text{5-AIP})(4,4'\text{-bipy})_{0.5}].\text{DMF}\}_n$  (**1**), with an analogous reaction using the related molecule 4,4'-azopyridine (4,4'-azopy) in place of 4,4'-bipy giving the isostructural framework  $\{[\text{Zn}(\text{5-AIP})(4,4'\text{-azopy})_{0.5}].\text{DMF}\}_n$  (**2**). Similar solvothermal reactions of  $\text{Co}(\text{NO}_3)_2 \cdot 6\text{H}_2\text{O}$ ,  $\text{Mn}(\text{NO}_3)_2 \cdot 4\text{H}_2\text{O}$  and  $\text{Cd}(\text{NO}_3)_2 \cdot 4\text{H}_2\text{O}$  with 5-aminoisophthalate and the potential linkers 4,4'-bipy, 1,2-di(4-pyridyl)ethylene (DPE) and 4,4'-azopy afforded the porous 3D structures  $\{[\text{Co}_2(\text{NO}_3)_2(\text{5-AIP})(4,4'\text{-bipy})_2].2\text{EtOH}\}_n$  (**3**),  $\{[\text{Co}(\text{5-AIP})(\text{DPE})].3\text{DMF}\}_n$  (**4**),  $\{[\text{Co}(\text{5-AIP})(4,4'\text{-azopy})].2\text{DMA}\}_n$  (**5**),  $\{[\text{Mn}(\text{5-AIP})(4,4'\text{-bipy})].2\text{DMA}\}_n$  (**6**),  $\{[\text{Mn}(\text{5-AIP})(\text{DPE})].1.5\text{DMF}\}_n$  (**7**),  $\{[\text{Mn}(\text{5-AIP})(4,4'\text{-azopy})].1.5\text{DMF}\}_n$  (**8**),  $\{[\text{Cd}(\text{5-AIP})(4,4'\text{-bipy})].3\text{DMF}\}_n$  (**9**),  $\{[\text{Cd}(\text{5-AIP})(\text{DPE})].\text{DMF}\}_n$  (**10**) and  $\{[\text{Cd}(\text{5-AIP})(4,4'\text{-azopy})].\text{DMF}\}_n$  (**11**), with structures **4-10** bearing the same network topology. Carbon dioxide uptakes for these structures, whilst modest, reveal an interesting pattern, with enhanced uptakes observed for those structures which bear larger pore sizes and polar functionalities.

Hydrothermal reactions of the reduced Schiff base 4-carboxy-phenylene-methyleneamino-4-benzoic acid ( $\text{L}^1\text{H}_2$ ) with  $\text{Zn}(\text{OH})_2$  and DPE afforded a non-porous 2D coordination polymer of the formula  $\{[\text{Zn}_2(\text{L}^1)_2(\text{DPE})].\text{H}_2\text{O}\}_n$ , (**12**) with the analogous reaction of  $\text{L}^1\text{H}_2$  with  $\text{Zn}(\text{OH})_2$  and 4,4'-azopy giving the porous 3D structure  $\{[\text{Zn}_3(\text{L}^1)_3(4,4'\text{-azopy})].7.5\text{H}_2\text{O}\}_n$  (**13**), which exhibits interesting hysteretic behaviour on  $\text{CO}_2$  adsorption and desorption.

Lower-rim acid functionalised calix[4]arene structures (**14**, **15**) were prepared by the reaction of 25,27-bis(methoxycarboxylic acid)-26,28-dihydroxycalix[4]arene ( $\text{L}^2\text{H}_2$ ) coordination polymers with  $\text{Li}_2\text{CO}_3$  and *tert*-butyllithium respectively, with the solvothermal reaction of  $\text{L}^2\text{H}_2$  with zinc nitrate affording the 1D coordination polymer of  $\{[\text{Zn}(\text{L}^2)_2](\text{DMF})(\text{H}_2\text{O})\}_n$  (**16**). Solvothermal reactions of the related calix[4]arene molecule 25,27-bis(methoxycarboxylic acid)-26,28-dihydroxy-4-*tert*butylcalix[4]arene ( $\text{L}^3\text{H}_2$ ) with  $\text{Zn}(\text{NO}_3)_2 \cdot 6\text{H}_2\text{O}$  and 4,4'-bipy, DPE and 4,4'-

azopy gave a series of 2D structures of the formulae  $\{[\text{Zn}(4,4'\text{-bipy})(\mathbf{L}^3)].2.25\text{DEF}\}_n$  (**17**),  $\{[\text{Zn}_2(\mathbf{L}^3)(\text{DPE})].\text{DEF}\}_n$  (**18**) and  $\{[\text{Zn}(\text{OH}_2)_2(\mathbf{L}^3)(4,4'\text{-azopy})].\text{DEF}\}_n$  (**19**). The structures have been fully characterised and their porosities investigated using TGA.

## Abbreviations

1D	One dimensional
2D	Two dimensional
3D	Three dimensional
4,4'-azopy	4,4'-Azopyridine
4,4'-bipy	4,4'-Bipyridyl
BDC	Benzene-1,4-dicarboxylate
BET	Brunauer-Emmett-Teller
DEF	<i>N, N</i> -diethylformamide
DMA	<i>N, N</i> -dimethylacetimide
DMF	<i>N, N</i> -dimethylformamide
DMSO	Dimethylsulfoxide
DPE	1,2-Di(4-pyridyl)ethylene
dpNI	<i>N, N'</i> -di(4-pyridyl)-1,4,5,8-naphthalenediimide
Dptz	Di-3,6-(4-pyridyl)-1,2,4,5-tetrazine
EtOH	Ethanol
FMA	Fumarate
H <sub>4</sub> btpa	1,1'-Biphenyl-2,2',6,6'-tetracarboxylic acid
HKUST	Hong Kong University of Science and Technology
MeOH	Methanol
MOF	Metal-organic framework
OAc	Acetate
SBU	Secondary building unit
SDC	Styrene dicarboxylate
<sup>t</sup> BuLi	<i>tertiary</i> -Butyl lithium
TGA	Thermogravimetric analysis
THF	Tetrahydrofuran
wt%	Weight percent
NMR	Nuclear magnetic resonance
s	Singlet
d	Doublet
t	Triplet

J	Coupling constant
$\delta$	Chemical shift
IR	infra-red
m	medium
s	strong
w	weak
MS	Mass spectrometry
MALDI	Matrix-assisted laser desorption ionisation

## Contents

Abstract.....	i
Abbreviations.....	iii
Contents .....	v
Acknowledgements.....	viii
Chapter 1. General introduction.....	1
1.1. Introduction.....	2
1.1.1. Synthesis and structure of MOFs.....	3
1.1.2. Secondary building units and isorecticular synthesis .....	10
1.1.3. The pillar/layer technique .....	19
1.1.4. Post-synthetic modification .....	26
1.1.5. Interpenetration and dynamic MOFs .....	30
1.1.6. Classification of porous structures.....	35
1.2. Hydrogen storage in MOFs .....	37
1.2.1. Pore optimisation for hydrogen uptake.....	41
1.3. Carbon dioxide sequestration in MOFs .....	50
1.3.1. CO <sub>2</sub> loading capacity in MOFs.....	51
1.3.2. Target gas selectivity .....	57
1.4. Aims of the study.....	59
1.5. Thesis overview .....	61
1.6. References.....	62
Chapter 2. Pillared metal-organic frameworks based on 5-aminoisophthalic acid....	68
2.1. Introduction.....	69
2.2. Results and Discussion .....	83
2.2.1. Zinc structures.....	83
2.2.2. Cobalt structures .....	89
2.2.3. Manganese structures.....	96
2.2.4. Cadmium structures .....	101
2.2.5. Thermogravimetric analysis .....	107
2.2.6. Gas adsorption behaviour .....	111
2.3. Conclusion .....	115
2.4. References.....	117
Chapter 3. Pillared metal-organic frameworks based on a reduced Schiff base dicarboxylic acid .....	119
3.1. Introduction.....	120

3.2. Results and Discussion .....	129
3.2.1. Thermogravimetric analysis .....	135
3.2.2. Gas adsorption behaviour .....	137
3.3. Conclusion .....	138
3.4. References.....	139
Chapter 4. 1D structures based on a lower-rim acid appended calix[4]arene.....	140
4.1. Introduction.....	141
4.1.1. Metal-organic frameworks based on lower-rim acid functionalised calix[4]arenes.....	151
4.2. Results and Discussion .....	152
4.2.1. Lithium structures .....	152
4.2.2. Zinc structure .....	158
4.2.3. Thermogravimetric analysis .....	160
4.2.4. Gas adsorption behaviour .....	161
4.3. Conclusion .....	161
4.4. References.....	163
Chapter 5. Pillared metal-organic frameworks based on a lower-rim acid appended calix[4]arene.....	165
5.1. Introduction.....	166
5.2. Results and discussion .....	168
5.2.1. Thermogravimetric analysis .....	177
5.3. Conclusion .....	179
5.4. References.....	180
Chapter 6. Experimental section .....	181
6.1. General considerations.....	182
6.2. Synthesis of known compounds .....	183
6.3. Pillared MOFs based on 5-aminoisophthalic acid .....	183
6.3.1. Synthesis of $\{[\text{Zn}(5\text{-AIP})(4,4'\text{-bipy})_{0.5}]\cdot 2\text{DMF}\}_n$ (1) .....	183
6.3.2. Synthesis of $\{[\text{Zn}(5\text{-AIP})(4,4'\text{-azopy})_{0.5}]\cdot 1.5\text{DMF}\}_n$ (2).....	184
6.3.3. Synthesis of $\{[\text{Co}_2(\text{NO}_3)_2(5\text{-AIP})(4,4'\text{-bipy})_2]\cdot 2\text{EtOH}\}_n$ (3) .....	186
6.3.4. Synthesis of $\{[\text{Co}(5\text{-AIP})(\text{DPE})]\cdot 3\text{DMF}\}_n$ (4) .....	187
6.3.5. Synthesis of $\{[\text{Co}(5\text{-AIP})(4,4'\text{-azopy})]\cdot 2\text{DMA}\}_n$ (5) .....	189
6.3.6. Synthesis of $\{[\text{Mn}(5\text{-AIP})(4,4'\text{-bipy})]\cdot 2\text{DMA}\}_n$ (6) .....	190
6.3.7. Synthesis of $\{[\text{Mn}(5\text{-AIP})(\text{DPE})]\cdot 1.5\text{DMF}\}_n$ (7) .....	192
6.3.8. Synthesis of $\{[\text{Mn}(5\text{-AIP})(\text{Azopy})]\cdot \text{DMF}\}_n$ (8).....	193
6.3.9. Synthesis of $\{[\text{Cd}(5\text{-AIP})(4,4'\text{-bipy})]\cdot 3\text{DMF}\}_n$ (9) .....	195
6.3.10. Synthesis of $\{[\text{Cd}(5\text{-AIP})(\text{DPE})]\cdot 1.7\text{DMF}\}_n$ (10).....	196
6.3.11. Synthesis of $\{[\text{Cd}(5\text{-AIP})(4,4'\text{-azopy})]\cdot \text{DMF}\}_n$ (11).....	198

6.4. Pillared MOFs based on a reduced Schiff base dicarboxylic acid.....	199
6.4.1. <i>Synthesis of</i> $\{[\text{Zn}_2(\text{L})_2(\text{DPE})]\cdot\text{H}_2\text{O}\}_n$ (12) .....	199
6.4.2. <i>Synthesis of</i> $\{[\text{Zn}_3(\text{L})_3(4,4'\text{-azopy})]\cdot 7.5\text{H}_2\text{O}\}_n$ (13) . .....	201
6.5. 1D structures based on a lower-rim acid appended calix[4]arene.....	202
6.5.1. <i>Synthesis of</i> $\text{Li}_2(\text{L}^2)$ (14) .....	202
6.5.2. <i>Synthesis of</i> $\text{Li}_2(\text{L}^2)(\text{C}_2\text{H}_6\text{O})_2$ (15) .....	204
6.5.3. <i>Synthesis of</i> $[\text{Zn}(\text{L}^2)(\text{DMF})(\text{H}_2\text{O})]_n$ (16).....	205
6.6. Pillared metal-organic frameworks based on a lower-rim acid appended calix[4]arene .....	207
6.6.1. <i>Synthesis of</i> $\{[\text{Zn}(\text{L}^3)(4,4'\text{-bipy})]\cdot 2.25\text{DEF}\}_n$ (17).....	207
6.6.2. <i>Synthesis of</i> $\{[\text{Zn}_2(\text{L}^3)(\text{DPE})]\cdot\text{DEF}\}_n$ (18).....	208
6.6.3. <i>Synthesis of</i> $\{[\text{Zn}(\text{OH}_2)_2(\text{L}^2)(4,4'\text{-azopy})]\cdot\text{DEF}\}_n$ (19).....	210
6.7. References.....	212
Chapter 7. Appendix .....	213
Table 2. Crystallographic data for structures 1, 3, 5 and 6.....	214
Table 3. Crystallographic data for structures 7, 9, 11 and 12.....	215
Table 4. Crystallographic data for structures 13, 14, 15 and 16.....	216
Table 5. Crystallographic data for structures 17, 18, and 19.....	217

## **Acknowledgements**

Firstly, I would like to thank Prof. Carl Redshaw for giving me the opportunity to continue my studies to Ph.D level and for the support and guidance he has given me over the last four years. I would also like to thank all members of the Redshaw research group with whom I have had the privilege to work, and in particular Abdessamad Arbaoui, Lucy Clowes and Mark Walton whose friendship has been invaluable.

I am very grateful to Mark Elsegood at the University of Loughborough, for his time and expertise in solving my crystal structures, and also to David Hughes and Anna-Marie Fuller for their contributions to X-ray data analysis. Thanks also go to Simon Teat at the ALS at Lawrence Berkeley National Laboratory, California and to the EPSRC National X-ray Crystallography service at the University of Southampton for data collections. For conducting gas uptake testing I would like to express my gratitude to Simon M. Humphrey and Maxwell Chang from the University of Texas at Austin, Qiaowei Li and Qingqing Pang from Fudan University, Shanghai and Yuna Song of the Beijing Institute of Technology. Thank you to the EPSRC, to all technical staff at the School of Chemistry and Pharmacy, UEA and to Stephen Boyer at London Metropolitan University for elemental analyses.

Finally, a special thank you to my partner Rachael and our daughter Heidi, without whom I would be lost.

# **Chapter 1**

## **General introduction**

## 1.1. Introduction

Porous materials research over the last fifty years has led to a multitude of solids with applications ranging from size/shape selective catalysis,<sup>1</sup> gas phase separation and storage,<sup>2</sup> and drug delivery.<sup>3</sup> Until two decades ago, however, research in this field was limited to three distinct areas, microporous inorganic materials known as zeolites, porous silicon and organic carbon-based materials. Zeolites are naturally occurring materials, which form by the reaction of basic ground-water with volcanic rock and ash deposits, giving aluminosilicate framework structures composed of corner sharing  $\text{SiO}_4$  and  $\text{AlO}_4$  tetrahedra. Removal of guest water molecules from these materials yields microporous materials with channels whose dimensions are defined by the number of aluminosilicate polyhedra surrounding the pores. Synthetic zeolites are also prepared *via* the crystallisation of alumina-silica gels over organic templates. Post-synthetic removal of the organic templates gives rise to an open framework structure with uniformed pores whilst giving pore size tunability over the range of 1-10 Å diameter.<sup>4</sup> The applications of zeolites, whilst incredibly diverse, are limited to the ability to control the pore size of the bulk material, excluding molecules by size or shape, and allowing target molecules to selectively diffuse into the material. These limitations result from the narrow range of elements from which they are composed, usually aluminium, silicon and the calcogens. Porous silicon is prepared by the anodisation of silicon wafers in ethanolic HF solution, with the size and distribution of pores in the resulting material being dictated by current, allowing pore size to be tuned in the range of a few Angstroms to tens of microns. These materials exhibit interesting non-linear optical and electrical properties and have applications ranging from drug delivery<sup>5</sup> to sensing,<sup>6</sup> however they are similarly limited in elemental composition to zeolites. In comparison to the close control of pore size and uniformity offered by zeolite and porous silicon chemistry, porous carbons are disordered structures, offering no control over pore size uniformity. These materials possess high surface areas, and due to the ability to include small functional groups and heteroatoms on the surfaces of the carbon structures, a degree of selectivity towards particular target molecules can be achieved.<sup>7</sup>

In order to diversify the field, further functionality must be built in and it is in this respect that metal-organic frameworks (MOFs) offer such opportunities to the

synthetic chemist. These hybrid organic-inorganic materials are a recently reported class of coordination polymer and are as such, formed by the reaction of bridging multidentate organic ligands with metal ions in the presence of templating molecules. Though it has been almost fifty years since the phrase ‘coordination polymer’ first appeared in the literature, it is only in the last twenty years that the synthesis of multidimensional coordination polymers which are crystalline and stable to the removal of templating molecules, has been achieved. Not only do the resulting microporous materials offer the control of pore size which has made zeolites and porous silicon such valuable materials, but due to the ability to select organic components with tunable characteristics, the affinity of the resultant materials to target molecules based on size, shape, magnetic properties or polarity can be intrinsically designed, offering greater control and variability of pore environment than can porous carbons.

#### **1.1.1. Synthesis and structure of MOFs**

The synthesis of MOFs is achieved through the self-assembly of polytopic organic ligands bearing divergent binding sites with metal ions, usually under acidic, solvothermal conditions, though syntheses based on classical coordination chemistry are also reported, as is the use of microwave radiation.<sup>8</sup> The synthetic method chosen to prepare these structures must take into account the stability of the organic linker, with conditions which are mild enough to maintain the integrity of the linker whilst being reactive enough to facilitate the formation of coordinate bonds to the metal. Due to the importance of forming the crystalline thermodynamic product and achieving the growth of crystals of suitable size and quality to determine the structure of the resultant framework by X-ray diffraction, the solubility of the growing polymeric species and the lability of the metal-organic bond to undergo coordinative rearrangements are key factors. In traditional organic polymer synthesis, the formation of irreversible covalent bonds between monomer units gives an amorphous polymeric species which quickly becomes insoluble. The synthesis of MOFs requires control over the solubility of the growing polymer, and the choice of metal centres which demonstrate lability towards coordinative rearrangement, so that kinetically formed crystal defects can be ‘rewritten’ giving the crystalline thermodynamic product. Early attempts to synthesise these structures are dominated by the use of classical coordination chemistry techniques, using very soluble organic

linkers in conjunction with the late transition metals, which demonstrate a high degree of reversibility in coordinate bond formation.<sup>9</sup> The use of solvothermal methods allows for greater variation of organic linkers and metal centres due to the increased solubility of reactants, though a balance must still be struck between the reversibility of metal-organic bond formation and the strength of the bond, which ultimately dictates the stability of the MOF. The structure of the resultant MOF is dictated by Werner-type coordination chemistry about the metal centre and by the characteristics of the organic ligand. Variation of ligand topology, length, steric bulk and bond angle have a major influence on the topology of the resulting material.

The modular nature of MOF synthesis, based on the selection of appropriate metal ‘nodes’ with tetrahedral or octahedral coordination geometries with rod-like organic ‘linkers’ as a means to synthesise crystalline materials with framework structures was first postulated in 1990 by Hoskins and Robson.<sup>10</sup> The structural elucidation of crystalline  $\text{Zn}(\text{CN})_2$  and  $\text{Cd}(\text{CN})_2$  prepared by the reaction of zinc acetate with acetone cyanohydrin in an aqueous medium in the first example and by the reaction of cadmium nitrate with sodium cyanide in an aqueous medium in the second, revealed the self-assembly of two isomorphous diamondoid networks, resulting from the reaction of a metal centre with a strong propensity to adopt tetrahedral geometry, with rod-like organic linkers, figure 1.

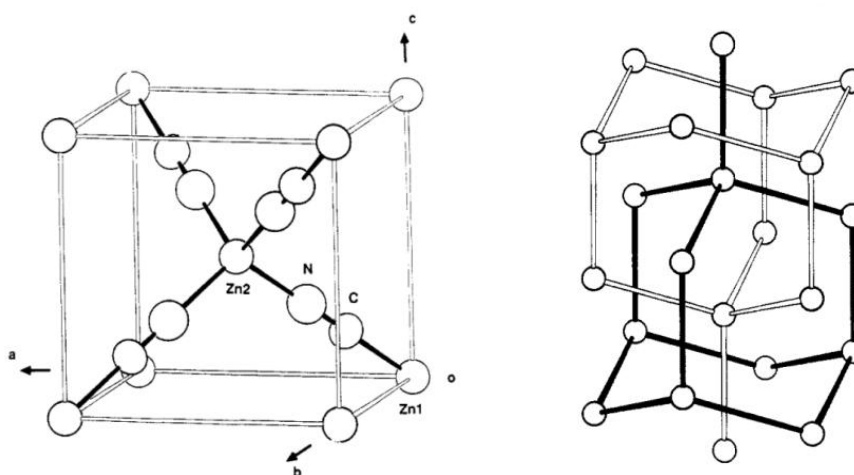


**Figure 1.** Diagram of the diamondoid network  $\text{Zn}(\text{CN})_2$  showing the coordination environment around the metal centres, and the interpenetrated adamantane units. Reproduced from ref. 10.

Crystallographic analysis of these structures revealed a system of highly interpenetrated diamondoid networks, with each adamantane unit having at its centre a metal ‘node’ from the neighbouring network. Additionally, two types of metal centres were clearly distinguishable, those which were coordinated to four nitrogen atoms and those which bound to four carbon atoms, demonstrating that some mechanism for coordinative rearrangement must be present, allowing kinetically formed mistakes in the crystal structure to be rearranged to give this highly ordered material.

Attempts to synthesise analogous structures using the reaction of the tetrahedral potential linker 4,4',4'',4'''-tetracyanotetraphenylmethane with  $[\text{Cu}(\text{CH}_3\text{CN})][\text{BF}_4]$  in acetonitrile and nitrobenzene lead to the synthesis of the distorted diamondoid network  $[\text{Cu}(4,4',4'',4'''\text{-tetracyanotetraphenylmethane})][\text{BF}_4] \cdot x\text{C}_6\text{N}_5\text{NO}_2$  ( $x \geq 7.7$ ), figure 2. It is of particular note that this structure did not display the same interpenetration of networks previously described, giving large cavities of approximately two thirds of the total volume of the structure which contained vast amounts of disordered nitrobenzene.

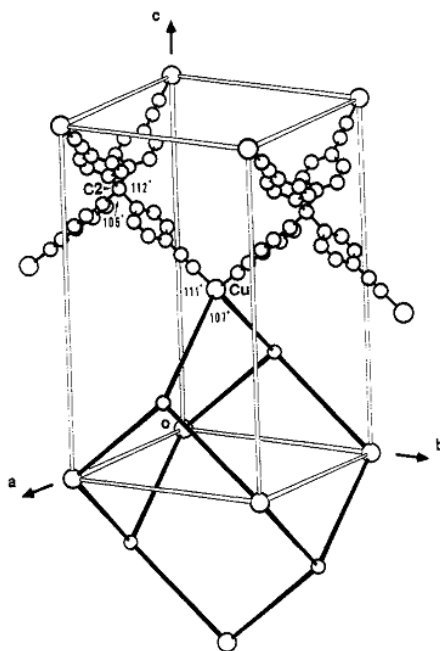


**Figure 2.** Diagram showing the coordination environment around the copper centres in  $[\text{Cu}(4,4',4'',4'''\text{-tetracyanotetraphenylmethane})][\text{BF}_4] \cdot x\text{C}_6\text{N}_5\text{NO}_2$ . Reproduced from ref. 10.

The successful synthesis of the structure described above, using a tetrahedral linker with a source of  $\text{Cu}^{\text{I}}$  which preferentially adopts tetrahedral coordination geometry can be considered the first example of a metal-organic framework being deliberately designed using the principles of coordination chemistry. Using these structures as examples, Hoskins and Robson postulated that the selection of 'rods' with sufficient rigidity may allow for the synthesis of open framework structures 'despite nature's abhorrence of a vacuum' and that these materials, possessing large cavities, would allow the diffusion of guest species throughout the structure of the material, giving molecular sieve-like properties. It was also predicted that the unimpeded diffusion of other chemical species through these cavities may allow for post-synthetic modification of the frameworks, though this will be discussed in greater detail in later parts of this chapter.

In the same year, Fujita reported the synthesis of the palladium structure  $[(\text{en})\text{Pd}(4,4'\text{-bipy})]_4(\text{NO}_3)_8$ , (where en = ethylenediamine), using these same principles of deliberate design.<sup>11</sup> Noting that while they demonstrated high specificity for the recognition of particular guest molecules, the design and modification organic/inorganic frameworks was extremely difficult; a programme to explore the use of macromolecules for molecular recognition was embarked upon. The reaction of  $[(\text{en})\text{Pd}](\text{NO}_3)_2$ <sup>5</sup> with 4,4'-bipy in an aqueous alcoholic solution lead to the formation of a square planar macrocyclic polynuclear complex, figure 3, demonstrating that the use of a metal with a preference for square planar coordination geometry with a rod-like organic linker will predictably give a square planar macromolecule.

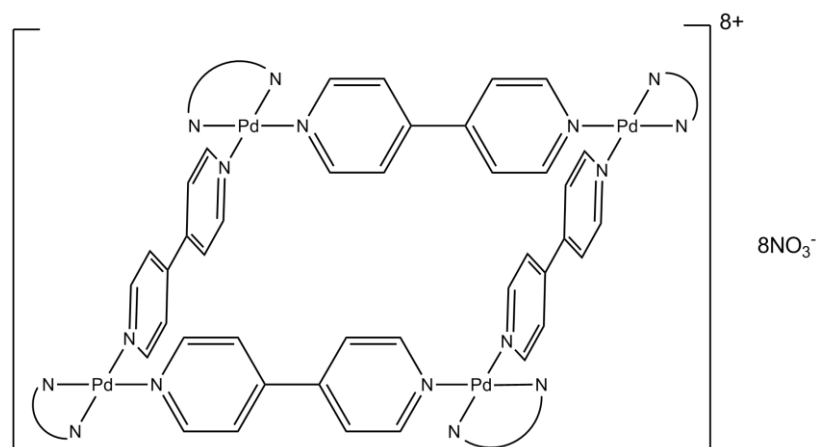


**Figure 3.** Diagram of the square planar complex  $[(\text{en})\text{Pd}(4,4'\text{-bipy})]_4(\text{NO}_3)_8$ .<sup>11</sup>

NMR spectroscopic studies on the formation of this complex show that the self-assembly is performed under thermodynamic control, with increasing concentrations of 4,4'-bipy giving the monomer, the dimer and the macrocyclic tetramer without the formation of intermediate linear oligomers, precluding the necessity for coordinative rearrangement.

The ability to predict the resultant network geometry of the MOF from these basic principles of coordination chemistry is central to the deliberate design of open framework structures. Due to nature's abhorrence of vacuums, it is not possible to synthesise open frameworks in a single concerted step as postulated by Robson and Hoskins, as the pore volume will always contain guest or templating molecules. The choice of solvent molecules which bear the correct dimensions to act as templates, whilst being volatile enough to be removed from the pores, either under reduced pressure or by solvent exchange, is vital to the success of the chosen synthetic method. Figure 4 illustrates the modular nature of MOF design, and displays some of the possible outcomes from the reaction of the primary building units (PBUs) commonly observed in MOF synthesis.

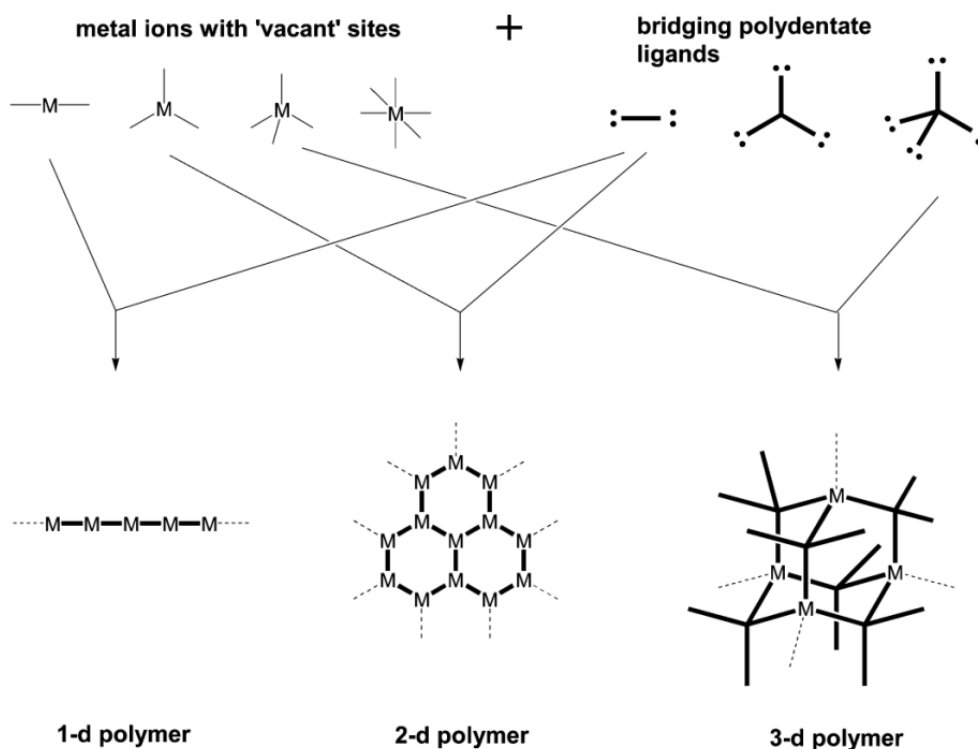


**Figure 4.** Schematic representation of the modular nature of MOF synthesis. Reproduced from ref. 9.

Prediction of the resulting network geometry when using rigid organic linkers in conjunction with metal nodes which have a strong preference for particular coordination geometry can therefore be achieved to some degree. The reaction of  $\text{Cu}(\text{NO}_3)_2 \cdot 3\text{H}_2\text{O}$  with 4,4'-bipyridine in the presence of camphoric acid, as reported by Zhang *et al.* gives a good example of this network geometry prediction.<sup>12</sup> The  $\text{Cu}^{\text{I}}$  centre in this example, formed by the *in-situ* oxidation of  $\text{Cu}^{\text{II}}$  by water under hydrothermal conditions, is tetrahedrally coordinated to four 4,4'-bipyridine molecules *via* N donor bonding. These 4,4'-bipyridine units bridge two copper centres giving a positively charged diamondoid network which is charge balanced by the presence of partially deprotonated camphoric acid units (D-Hcam), figure 5.

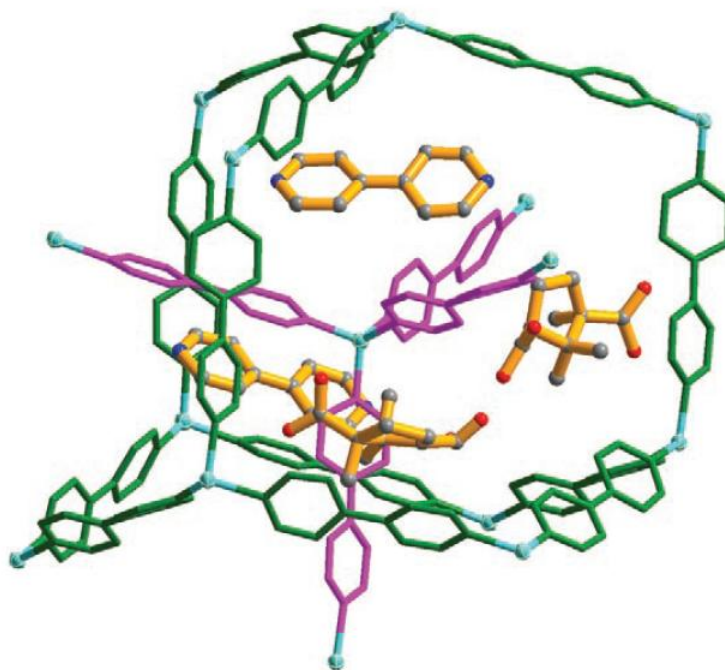


**Figure 5.** Diagram of  $\{[\text{Cu}_2(4,4'\text{-bipy})_4] \cdot (\text{D-Hcam})_2 \cdot (4,4'\text{-bipy})_2 \cdot 12\text{H}_2\text{O}\}_n$  showing the catenation of the diamondoid networks, with organic linkers coloured green and pink indicating the independent nets. Guest molecules are included and are coloured yellow and copper atoms are coloured blue. Hydrogen atoms are omitted for clarity. Reproduced from ref. 12.

As with the  $\text{Zn}(\text{CN})_2$  and  $\text{Cd}(\text{CN})_2$  frameworks described previously, the structure demonstrates interpenetration of the diamondoid networks, with each adamantane unit having at its centre the  $\text{Cu}^{\text{I}}$  node from a neighbouring net, however unlike the previous examples, the use of the much longer organic linker 4,4'-bipy gives a

framework with far larger cavities, able to accommodate two 4,4'-bipy molecules, two D-Hcam anions and 12 water molecules per formula unit as guests, despite the catenation of the networks, giving the structural formula  $\{[\text{Cu}_2(4,4'\text{-bipy})_4](\text{D-Hcam})_2(4,4'\text{-bipy})_2 \cdot 12\text{H}_2\text{O}\}_n$ . The use of a metal centre with octahedral coordination geometry in conjunction with a trigonal planar organic linker as reported by Hasegawa *et al.* offers another example of this structural prediction.<sup>13</sup> The reaction of  $\text{Cd}(\text{NO}_3)_2 \cdot 4\text{H}_2\text{O}$  in MeCN with 1, 3, 5-benzene tricarboxylic acid tris[N-(4-pyridyl)amide] (4-btapa) in DMF by slow diffusion of the reactants affords the 3D coordination network  $\{[\text{Cd}(4\text{-btapa})_2(\text{NO}_3)_2] \cdot 6\text{H}_2\text{O} \cdot 2\text{DMF}\}_n$ , in which each  $\text{Cd}^{\text{II}}$  centre is octahedrally coordinated to the pyridyl nitrogens of six 4-btapa units, figure 6.

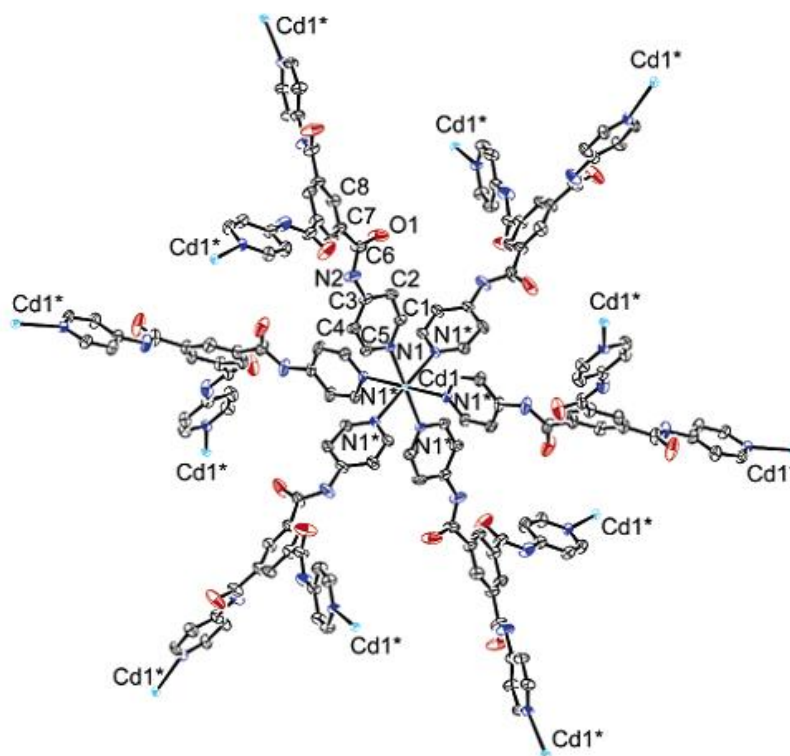


**Figure 6.** Diagram of  $\{[\text{Cd}(4\text{-btapa})_2(\text{NO}_3)_2] \cdot 6\text{H}_2\text{O} \cdot 2\text{DMF}\}_n$  showing the coordination environment around the metal centres. Carbon, nitrogen, oxygen and cadmium atoms are coloured black, blue, red and light blue respectively. Hydrogen atoms are excluded for clarity. Reproduced from ref. 13.

The 4-btapa units act as bridging ligands, linking three symmetrically equivalent  $\text{Cd}^{\text{II}}$  centres to give an extended 3D structure composed of distorted 6 membered  $(\text{Cd}^{\text{II}})_3(4\text{-btapa})_3$  rings. Again, this structure displays two-fold interpenetration of

networks, giving a material with 3D channels of 4.7 x 7.4 Å visible along the crystallographic *b* axis. These channels accommodate two nitrate anions per formula unit, charge balancing the cationic network, as well as six water and two DMF molecules as unbound guests. Removal of the guest molecules, by heating to 140 °C under vacuum for 7.5 h leads to the structural collapse of the framework with powder X-ray analysis confirming the creation of the amorphous [Cd(4-btapa)<sub>2</sub>(NO<sub>3</sub>)<sub>2</sub>]<sub>2</sub> species. Gas uptake studies performed on this desolvated species using N<sub>2</sub> showed no uptake, giving evidence that this crystalline to amorphous transformation is also accompanied by the lost of porosity. It is of particular interest however that immersion of this amorphous species in methanol leads to the formation of the crystalline compound {[Cd(4-btapa)<sub>2</sub>(NO<sub>3</sub>)<sub>2</sub>].6MeOH.yH<sub>2</sub>O}<sub>n</sub>, whose structure is analogous to that of {[Cd(4-btapa)<sub>2</sub>(NO<sub>3</sub>)<sub>2</sub>].6H<sub>2</sub>O.2DMF}<sub>n</sub>. The dynamic nature of this structure can be attributed to the rotational freedom of amide groups of the organic linker and the Cd-N coordinate bonds, allowing the framework to compress in the absence of guest molecules without breaking the coordinate bonds.

### 1.1.2. Secondary building units and isorecticular synthesis

The structural themes for MOFs are not limited to this combination of organic bridging linkers and single metal ion PBUs. Introduced by Li *et al.* in 1999,<sup>14</sup> and further defined by Eddouadi *et al.* in 2001,<sup>15</sup> the concept of the secondary building unit (SBU) gives greater scope for variability of these structures. Borrowing nomenclature from zeolite chemistry, the SBU refers to a recurring metal/metal oxide coordination motif around which MOFs bearing the same basic topology, but due to variation of the organic linker, vastly different pore size/shapes, can be synthesised. Identifying the inherent instability of MOFs bearing only N donor bonding to solvent removal, the group embarked on a programme to research the use of metal-carboxylate bonding in the formation of frameworks. These multidentate linkers allow the aggregation of metal and metal/oxide clusters, which are intrinsically more stable than single metal-N donor bonds. Typically, a Cu<sup>I</sup>-N bond has a bond energy of around 55 kJ mol<sup>-1</sup>, and Cu<sup>II</sup>-N around 90 kJ mol<sup>-1</sup> (based on the heats of formation of CuCl.3NH<sub>3</sub> and CuCl<sub>2</sub>.2NH<sub>3</sub>), in comparison to 180 kJ mol<sup>-1</sup> for a single Zn-O bond (based on the heat of formation of ZnO).<sup>16</sup> The resulting structures also bear zero charge enabling the construction of neutral

frameworks which require no counter ions, therefore increasing the likelihood of the frameworks retaining structural integrity following the removal of guest molecules.

The first of these structures, bearing the  $M_2(O_2CR)_4$  or ‘paddlewheel’ SBU was reported by Li *et al.*<sup>17</sup> The reaction of  $Zn(NO_2)_3 \cdot 6H_2O$  with benzene-1,4-dicarboxylic acid by slow vapour diffusion of triethylamine into a DMF solution of the reactants leads to the formation of the 3D framework  $[Zn(BDC) \cdot (DMF)(H_2O)]_n$  (where BDC= benzene-1,4-dicarboxylate) figure 7.

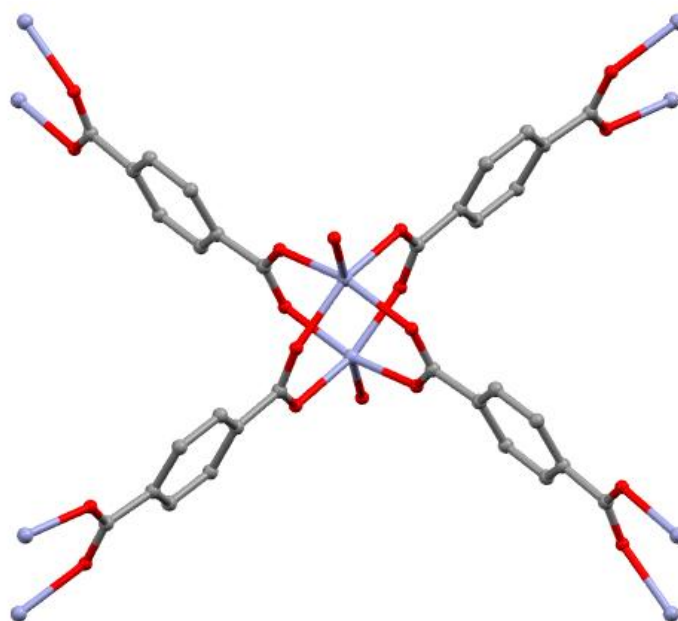


**Figure 7.** Diagram showing the coordination environment around the metal centres in  $[Zn(BDC) \cdot (DMF)(H_2O)]_n$  as viewed along the  $a$  axis. Carbon, nitrogen oxygen and zinc atoms are coloured grey, blue, red and purple respectively. Hydrogen atoms are excluded for clarity.<sup>17</sup>

In this example, the four individual but symmetry equivalent BDC units bind in a dimonodentate fashion through their carboxylate groups to two zinc atoms, giving rigid square planar vertices. This metal-carboxylate binding motif is observed at either end of the BDC unit giving a 2D square net. Water molecules bound to the zinc atoms above and below the plane of the metal-carboxylate paddlewheel hydrogen bond to the carboxylate groups of neighbouring sheets along the crystallographic  $a$  axis, giving a 3D structure with channels inhabited by templating DMF molecules, figure 8.

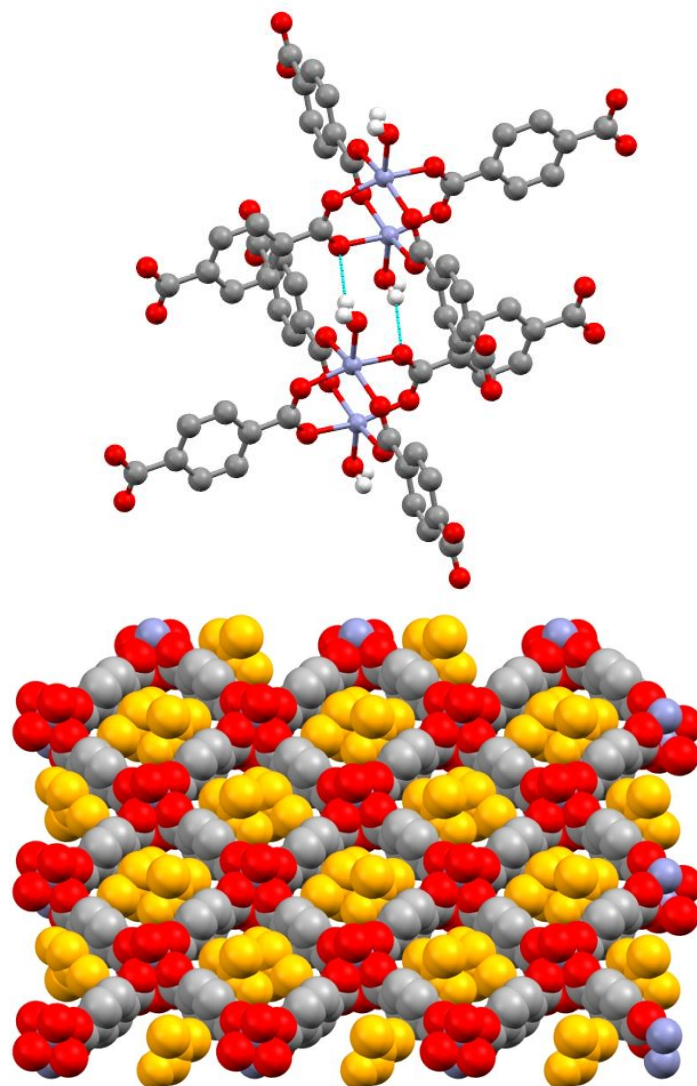


**Figure 8.** Diagrams of  $[\text{Zn}(\text{BDC})\cdot(\text{DMF})(\text{H}_2\text{O})]_n$  showing the hydrogen bonding interactions, indicated by light blue lines, between the apically bound water molecules and the carboxylate functions of neighbouring 2D sheets (top), and a space-filling representation of the framework as viewed along the  $a$  axis, with guest DMF molecules coloured orange (bottom). Carbon, oxygen and zinc atoms are coloured grey, red and purple respectively. Hydrogen atoms, except those involved in H-bonding have been excluded.<sup>17</sup>

Thermogravimetric analysis (TGA) of the framework reveals a two stage weight loss. The initial weight loss of 5.5 %, observed at 65 °C, is attributed to the removal of a single water molecule per formula unit. The second weight loss of 22.5 % observed at 160 °C is attributed to the loss of DMF molecules from the pores. It is of particular interest that the removal of the terminally bound water molecule at 65 °C

is not accompanied by the collapse of the framework, as may be expected. Instead, the structure undergoes crystal to crystal transformation to Zn(BDC), a structure bearing Zn-O coordinate bonds between the 2D sheets, with the crystallinity of the evacuated species being confirmed by powder X-ray diffraction. The permanent microporosity of the evacuated species is confirmed by gas adsorption studies, with CO<sub>2</sub> and N<sub>2</sub> uptakes following the type I isotherm, which is typical of such materials. Due to the rigidity and thermal stability of the SBU, it can be considered a permanently square planar node around which a huge variety of ligands bearing divergent carboxylate groups can be linked. The reaction of the trigonal planar linker benzene-1,3,5,-tricarboxylic acid (trimesic acid, TMA-H<sub>3</sub>) with cupric nitrate trihydrate in a 50:50 mixture of ethanol and water under solvothermal conditions (180 °C, 12 h) as reported by Chui and co-workers is a good example of this.<sup>18</sup> Bearing the same paddlewheel SBU, this structure demonstrates a very different topology due to the increased dimensionality of the organic linker, figure 9.

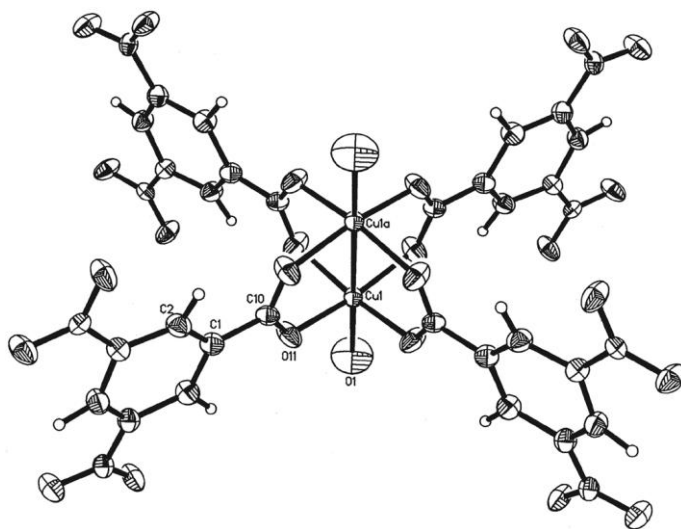


**Figure 9.** ORTEP diagram showing the coordination environment around the metal centres in  $[\text{Cu}_3(\text{TMA})_2(\text{H}_2\text{O})_3]_n$ . Reproduced from ref. 18.

Crystallographic analysis of the resulting MOF  $[\text{Cu}_3(\text{TMA})_2(\text{H}_2\text{O})_3]_n$  (referred to as HKUST-1), reveals a large pseudo-octahedral unit comprised of six Cu 'paddlewheels' linked by four TMA units in an alternate 'up/down' arrangement, figure 10. Bridging Cu dimers at the vertices of this pseudo-octahedron link this unit to others giving an extended 3D structure bearing intersecting square channels of 9 x

9 Å. Unusually, in this example the porosity is due not to the voids created by the binding of the organic linker to the copper dimer units, but by the linking of these octahedral units to form the bulk material.

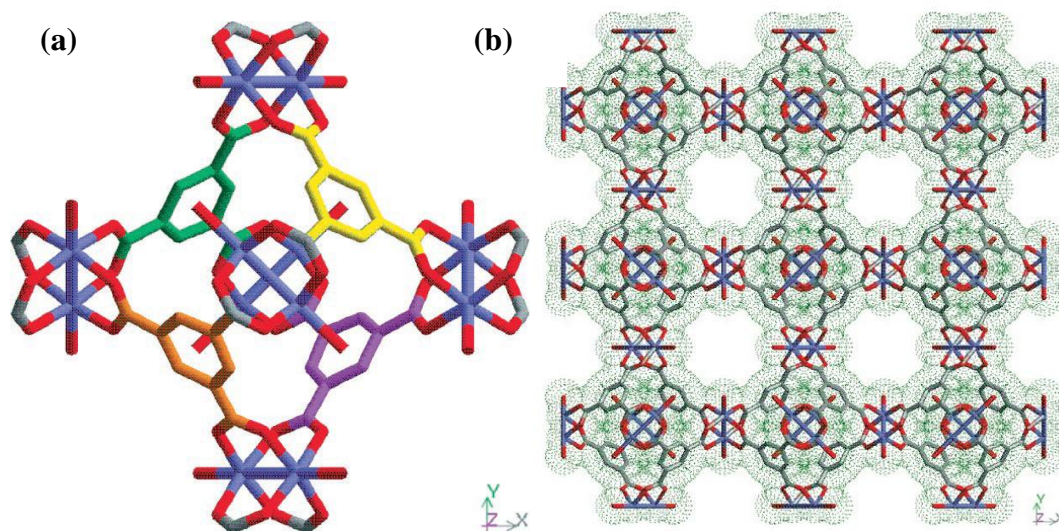


**Figure 10.** Diagrams of HKUST-1 showing (a) the pseudo-octahedral  $\text{Cu}_{12}(\text{TMA})_4$  unit. Alternate TMA molecules are coloured yellow, green, orange and purple for clarity. Oxygen and copper atoms are coloured red and blue respectively. (b) The extended structure of HKUST-1 formed by linked octahedra. Carbon, oxygen and copper atoms are coloured grey, red and blue respectively. The Van der Waals surface is highlighted in green. Hydrogen atoms are excluded. Reproduced from ref. 18.

The importance of reaction conditions to the morphology of the resulting framework is also identified by this research. Previous attempts to synthesise multidimensional networks by the reaction of  $\text{Cu}^{\text{II}}$  with benzene-1,2,3-tricarboxylic acid in alcoholic solutions at room temperature yield the 1D coordination polymers  $[\text{Cu}(\text{TMA}-\text{H})(\text{H}_2\text{O})_3]_n$  or  $[\text{NaCu}(\text{TMA})(\text{H}_2\text{O})_5]_n$  with the dimensionality of the resulting compounds limited by the presence of multiple ancillary water molecules.<sup>19</sup> The use of high temperature solvothermal conditions in the synthesis of HKUST-1 facilitates the formation of the paddlewheel unit, which bears only one terminal aqua ligand per metal centre. The stability of the MOF to guest removal is confirmed by TGA, with the framework maintaining crystallinity after the removal of ten guest water molecules per formula unit (28.3 wt%). The complete dehydration of the framework

is also possible without structural collapse by heating to 100 °C in air giving the anhydrate  $[\text{Cu}_3(\text{TMA})_2]_n$ , on which nitrogen adsorption studies were conducted. These studies reveal a bulk material with a Brunauer-Emmett-Teller (BET) surface area of  $692.2 \text{ m}^2 \text{ g}^{-1}$  and Langmuir surface area of  $917.6 \text{ m}^2 \text{ g}^{-1}$  with accessible pore volume of 40.7 % of the total volume of the material. The treatment of the anhydrate with pyridine in dichloromethane leads to the formation of  $[\text{Cu}_3(\text{TMA})_2(\text{py})_3]_n$  with pyridine units replacing the ancillary water molecules, demonstrating both the incredible stability of the paddlewheel unit and the lability of the terminally coordinated water molecules.

The addition of hydrogen peroxide to the same reaction mixture used in the preparation of  $[\text{Zn}(\text{BDC})\cdot(\text{DMF})(\text{H}_2\text{O})]_n$  as discussed above, leads to the synthesis of  $[\text{Zn}_4\text{O}(\text{BDC})_3\cdot(\text{DMF})_8(\text{C}_6\text{H}_5\text{Cl})]_n$  (referred to as MOF-5).<sup>12</sup> In this example, the inclusion of hydrogen peroxide provides a source of  $\text{O}^{2-}$  facilitating the assembly of a different SBU. The  $\text{Zn}_4\text{O}(\text{O}_2\text{CR})_6$  SBU displays an oxo centred zinc tetrahedron coordinated to six carboxylate groups in a di-monodentate fashion, with each of the four zinc centres being bound to three oxygens from three different carboxylate groups. The resulting structure, analogous to that of crystalline basic zinc acetate with the carboxylate groups of the organic linker taking the place of the acetate groups, can be considered a rigid octahedral node, figure 11.

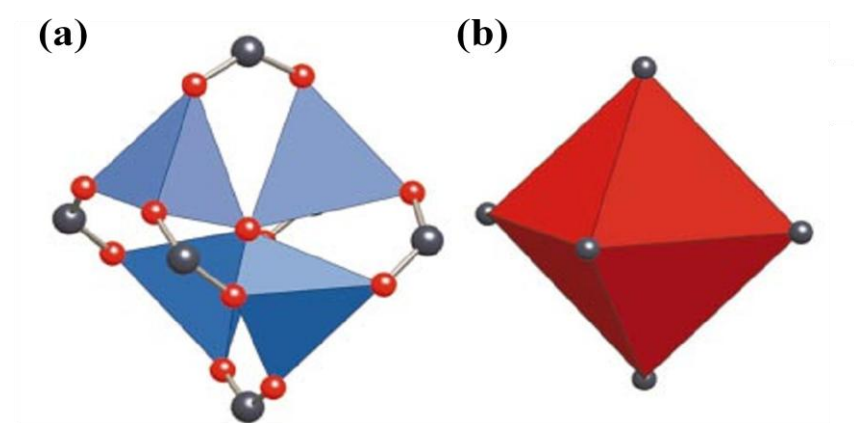


**Figure 11.** Diagram of (a) the basic zinc acetate or  $\text{Zn}_4\text{O}(\text{O}_2\text{CR})_6$  SBU, carbon and oxygen atoms are coloured black and red respectively, with zinc atoms represented by blue tetrahedra, and (b) the equivalent rigid octahedral node. Reproduced from ref. 14.

These nodes are linked through BDC units into a cubic network displaying intersecting channels of 8 Å diameter oriented along each of the crystallographic axes, figure 12. The channels contain eight DMF and one nitrobenzene molecule per formula unit as unbound guests, which can be removed either *via* solvent exchange by immersion of the material in chloroform, or by heating to 350 °C at standard pressure, without the collapse of the network. Such is the stability of this structure that it is possible to conduct single crystal X-ray diffraction studies on the desolvated species, with cell parameters matching those of the solvated  $\{[\text{Zn}_4\text{O}(\text{BDC})_3] \cdot (\text{DMF})_8(\text{C}_6\text{H}_5\text{Cl})\}_n$  framework. The volume of the removed guests, calculated using the Van der Waals radii of the respective atoms, is 9.5 Å<sup>3</sup>, suggesting that 55 % of the total volume of the unit cell is accessible void space and giving the material a density of only 0.59 g cm<sup>-3</sup>.

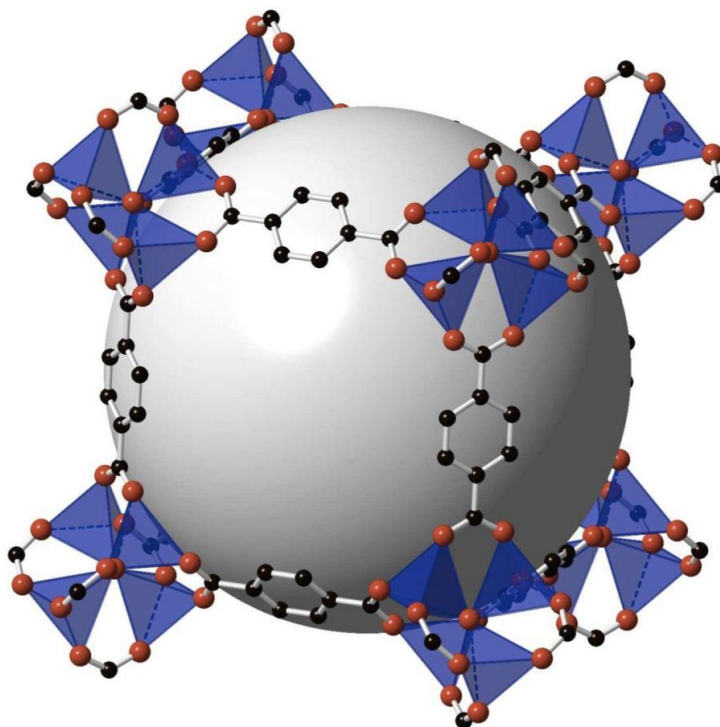


**Figure 12.** Diagram of the cubic lattice forming MOF-5. Carbon, oxygen and zinc atoms are represented by black and orange spheres, and blue tetrahedra respectively. The large grey sphere represents the void space encapsulated by the lattice. Reproduced from ref. 14.

Gas uptake studies on the desolvated species using a variety of analyte gases allow the pore volumes to be calculated using the Dubinin-Radushkevich equation, which confirms a pore size of between 0.54 -0.61 cm<sup>3</sup> cm<sup>-3</sup>, and allows the calculation of

the Langmuir surface area, giving an estimated  $2900 \text{ m}^2 \text{ g}^{-1}$ , far in excess of those commonly seen in zeolites. These studies also reveal a type I isotherm for the analyte gases, with no hysteresis occurring during desorption, offering more evidence of a permanently microporous material.

In later studies, it was discovered that the self-assembly of the MOF-5 structure could also be achieved using solvothermal methods, by heating zinc nitrate and benzene-1,4-dicarboxylic acid ( $\text{H}_2\text{BDC}$ ) in DEF to  $85 \text{ }^\circ\text{C}$  in a closed vessel, giving high yields of pure IRMOF-1.<sup>20</sup> The relative ease with which this compound can be prepared prompted the substitution of  $\text{H}_2\text{BDC}$  with the potential linkers 2-bromo-1,4-benzene dicarboxylic acid ( $\text{H}_2\text{-}o\text{-BrBDC}$ ), and 2-amino-1,4-benzene dicarboxylic acid ( $\text{H}_2\text{-BDCNH}_2$ ) with solvothermal reactions with zinc nitrate in DEF giving the structures  $\{[\text{Zn}_4\text{O}(o\text{-BrBDC})_3]\cdot 7\text{DEF}\}_n$  and  $\{[\text{Zn}_4\text{O}(\text{BDCNH}_2)_3]\cdot 7\text{DEF}\}_n$  (referred to as IRMOF-2 and IRMOF-3 respectively), see figure 13. These structures display the same network topology as IRMOF-1, whilst bearing increased functionality at the organic linker, demonstrating the potential for MOFs of this type to be tuned to particular target molecules based on adsorbant/adsorbate interactions. The pattern of reticular synthesis also extends to organic linkers bearing the much larger *n*-propoxy, *n*-pentoxy and cyclobutyl groups as well as naphthalene-1,4-dicarboxylic acid, predictably yielding the cubic networks derived from the reaction of the octahedral  $\text{Zn}_4\text{O}$  SBU with rigid linear organic linkers.

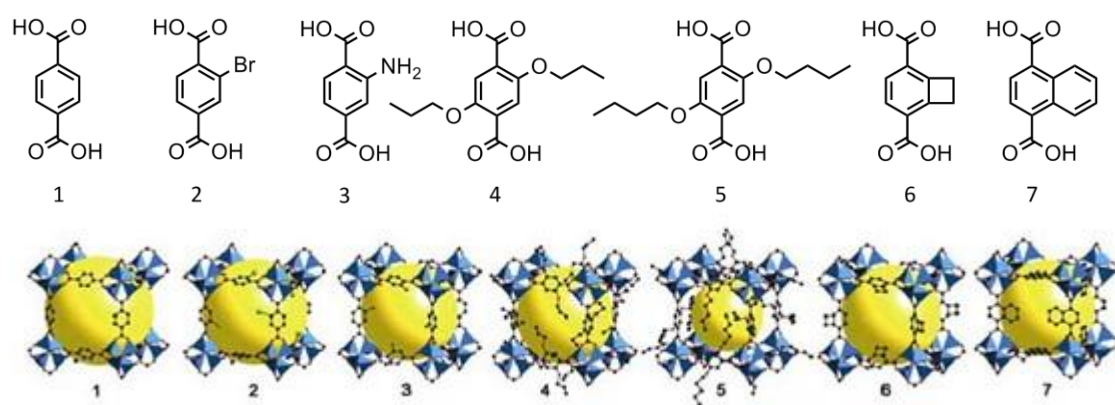


**Figure 13.** Diagram of the benzenedicarboxylic acids used in the synthesis of the isorecticular MOFs bearing the same number. The yellow spheres represent the void spaces contained in the primitive cubic lattices. Reproduced from ref. 20.

The isorecticular (bearing the same network topology) series extends even further with cubic networks being prepared from the longer linkers as detailed in figure 13. In total, sixteen isorecticular MOFs are prepared with only minor adjustments required in the synthetic method, figure 14. The free pore volume of these MOFs varies from 55.8 % for IRMOF-5, which bears large sterically-hindering *n*-propoxy groups which extend into the pore space, to 91.1 % for IRMOF-16. The free diameter of these pores, defined as the diameter of the largest sphere which could pass through the framework unhindered varies from 3.8 to 19.1 Å, demonstrating the ease with which materials can be prepared which separate molecules on a size exclusion basis.

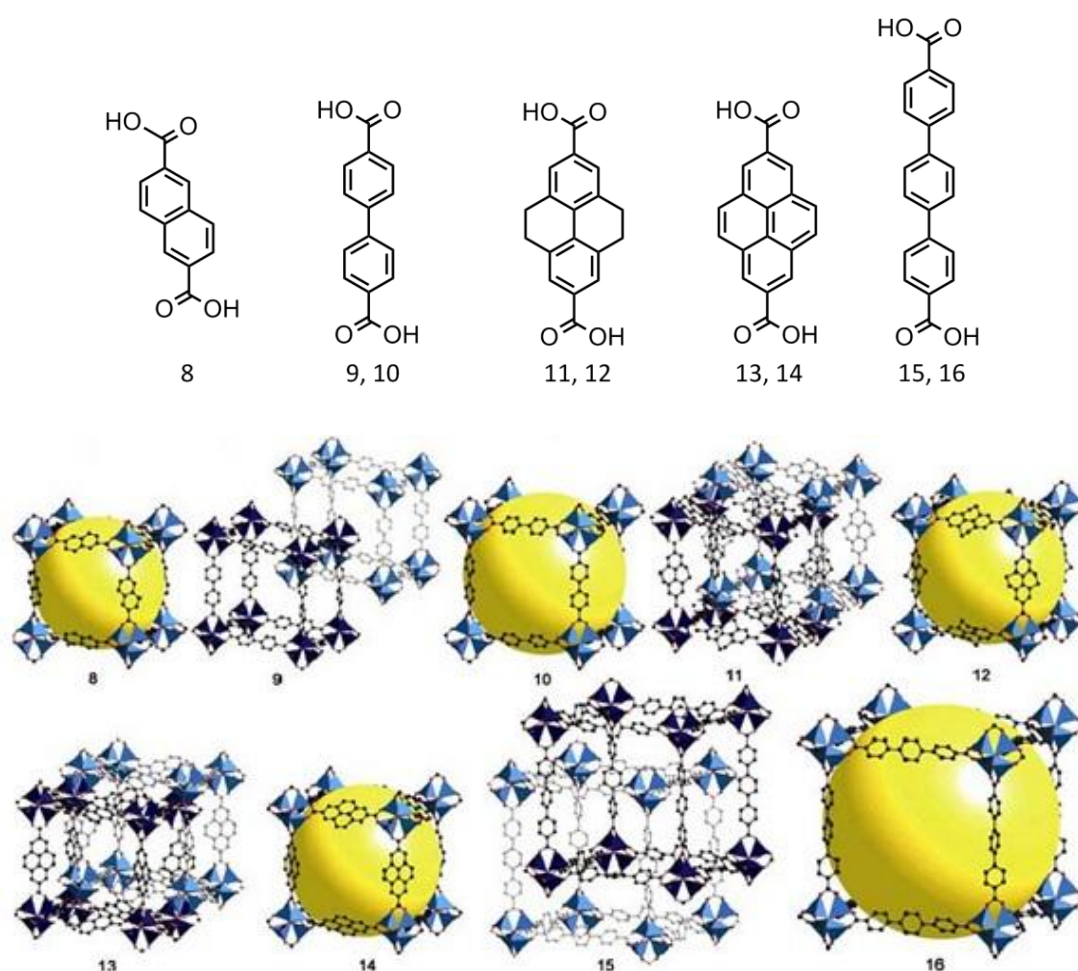


**Figure 14.** Diagram of the longer linkers used in the synthesis of isorecticular MOFs; numbering identifying the related IRMOFs below. The yellow spheres represent the void spaces contained in the primitive cubic lattices. Reproduced from ref. 20.

It is of particular note that concomitant with increasing linker length is the increased likelihood of the interpenetration of the networks. Initial attempts to synthesise open frameworks with the potential organic linkers biphenyl-4,4'-dicarboxylic acid (H<sub>2</sub>BPDC), 4,5,9,10-tetrahydropyrene-2,7-dicarboxylic acid (H<sub>2</sub>HPDC), pyrene-2,7-dicarboxylic acid (H<sub>2</sub>PDC) and triphenyldicarboxylic acid (H<sub>2</sub>TPDC), using similar reaction conditions and molar quantities of reactants that were employed in the preparation of the other members of the isoreticular series, gave the doubly interpenetrated structures denoted IRMOF-9, IRMOF-11, IRMOF-13 and IRMOF-15 respectively. The effect of this interpenetration on the pore size of the resultant material is profound, with free diameters of 10.6, 9.0, 10.2 and 8.1 Å reported for these four structures compared to the non-interpenetrated equivalents, obtained under the same reaction conditions but with lower reactant concentrations, IRMOF-10, IRMOF-12, IRMOF-14 and IRMOF-16, which exhibit free diameters of 15.4, 13.0, 13.8 and 19.1 Å.

Tranchemontagne *et al.* have to date reported 131 potential SBUs based on transition metal-carboxylate binding motifs observed in the formation of discrete and extended molecules, as reported in the Cambridge structural database.<sup>21</sup> The variability of these SBUs is enormous, with potential nodes bearing between 3 and 22 points of extension, demonstrating the almost limitless possibilities for materials designed using this concept of reticular synthesis.

### **1.1.3. The pillar/layer technique**

Another frequently employed technique for the rational design of MOFs bearing large pores involves the use of neutral pillaring linkers in conjunction with ligand/metal systems which would otherwise only form 2D sheets, or layers. Occupying metal coordination sites above and below the plane of the sheets, neutral ligands such as those detailed in figure 15 act as cross-linkers, giving 3D framework structures.

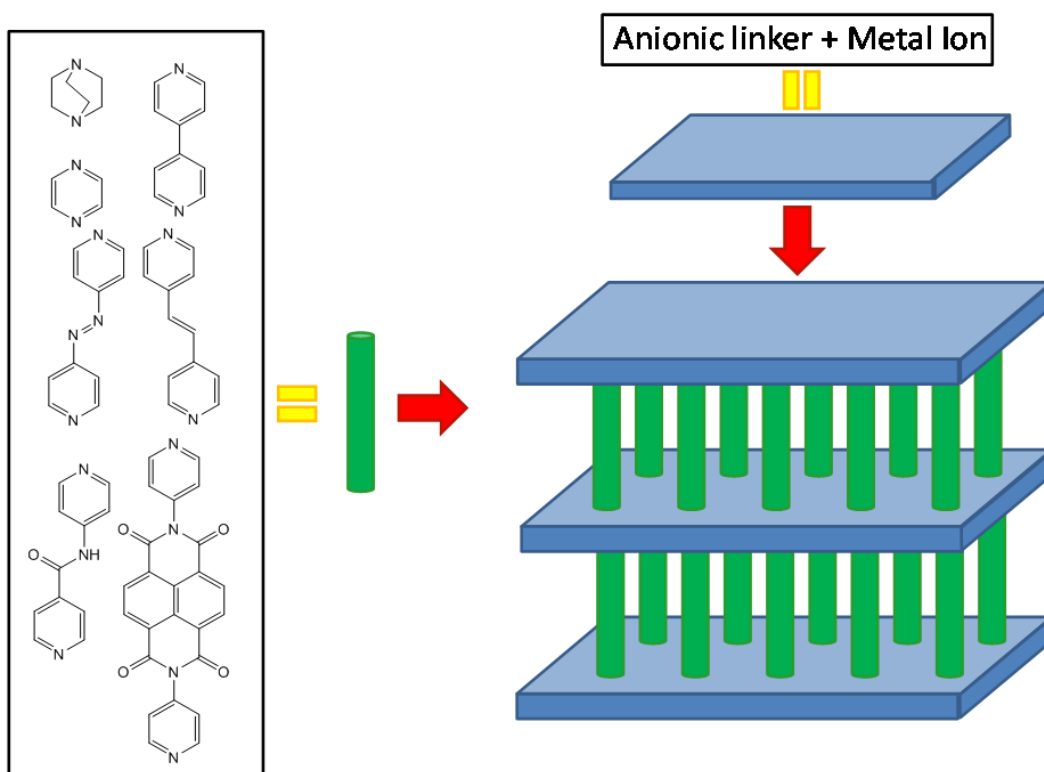


**Figure 15.** Schematic representation of the pillar/layer technique in MOF synthesis

The advantages of a synthetic strategy based on the use of these pillaring linkers are numerous. Through the use of different linker lengths, very small adjustments to pore size can be achieved. The use of two organic linkers allows for greater and more varied functionalisation. Lastly, the use of 2D sheets which bear no large cavities precludes the formation of interpenetrated networks offering greater control over the pore size of the resulting materials.

The flexibility of this technique was first suggested by Russell *et al.* by the synthesis of hydrogen-bonded guanidine layers intercalated by chemical species' bearing two divergent sulfonate groups, giving distinctive pillar-layer structures bearing channels inhabited by guest solvent molecules.<sup>22</sup> Through the use of disulfonate species of varying lengths it was shown that the dimensions of the channels could be altered while maintaining the general topology of the structures, demonstrating that the deliberate design of crystalline solids could be achieved. The lack of strong covalent or coordinate bonds between the building units of these structures however, gave materials which showed no stability towards the removal of the guest molecules. Employment of the same technique using coordination polymers, which bear far

stronger linkages between building units, has led to the prevalence of these types of structure in the literature.

The series of MOFs bearing the general formula  $[\text{Cu}_2(\text{pzdc})_2(\text{L})]_n$  (where pzdc = pyrazine-2,3-dicarboxylate, and L = pyrazine, 4,4'-bipy or N(4-pyridyl)isonicotinamide) as reported by Kitagawa *et al.* are representative of such structures.<sup>23</sup> Prepared by the reaction of  $\text{Cu}(\text{ClO}_4)_2 \cdot 6\text{H}_2\text{O}$  with the disodium salt of pyrazine-2,3-dicarboxylic acid and pyrazine, the first of these structures comprises 2D sheets of pzdc units chelated to  $\text{Cu}^{\text{II}}$  through one nitrogen atom and one carboxylate oxygen, with the second carboxylate moiety binding in a monodentate fashion to two other  $\text{Cu}^{\text{II}}$  centres, giving a neutral 2D sheet of around 7.5 Å thickness situated in the *ac* crystallographic plane.

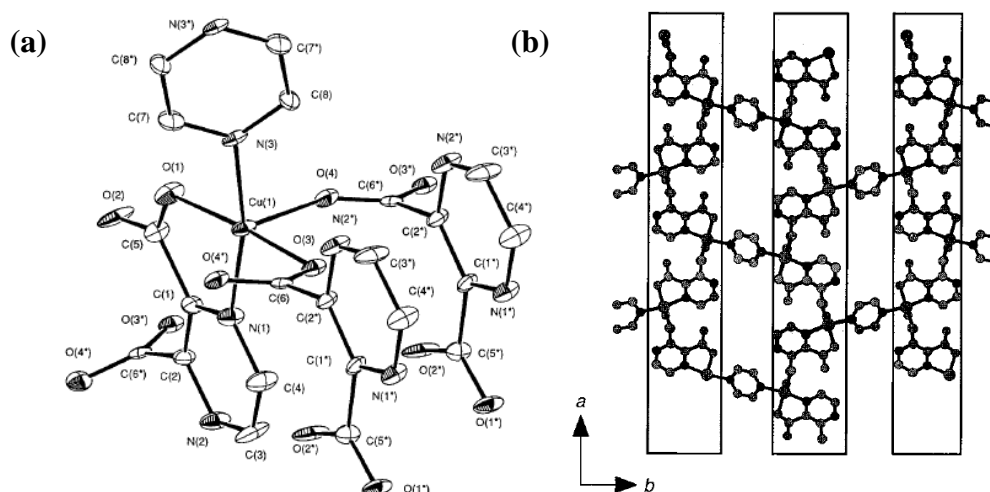


**Figure 16.** Diagrams of  $[\text{Cu}_2(\text{pzdc})_2(\text{L})]_n$  showing (a) the coordination environment around the metals centres and (b) the extended structure as viewed along the *c* axis, with boxes drawn to indicate the 2D sheets. Pillaring pyrazine units are visible between the sheets. Hydrogen atoms are omitted. Reproduced from ref. 23.

The 2D sheets are cross-linked by pyrazine units bound to the copper atoms above and below the plane of the sheet, giving a distorted square pyramidal coordination environment around the  $\text{Cu}^{\text{II}}$  centres. Due to the intercalation of these pyrazine units, the separation between sheets is estimated to be around 3 Å, with extended channels of 4 x 6 Å containing guest water molecules observed running along the crystallographic *c* axis. The substitution of the pillaring pyrazine linker with 4,4'-bipy and N(4-pyridyl)isonicotinamide) gives rise to two analogous structures,

bearing the same Cu-pzdc-L binding motif, but due to the increased length of the pillaring linker, elongated channels inhabited by guest water molecules, with dimensions of 9 x 6 Å and 10 x 6 Å respectively. The thermal stability of these networks is confirmed by TGA, revealing the loss of water from the pores at temperatures up to 100 °C, with no thermal decomposition of the anhydrous frameworks observed until 260 °C. Powder X-ray diffraction patterns collected on the anhydrous species' reveal the stability of these networks to guest removal, offering evidence of the successful synthesis of three permanently porous materials. Further evidence of this permanent porosity is provided by their methane adsorption properties, with type I isotherms collected for all three members of this series. It is of note that the increasing pore size achieved by the intercalation of larger pillaring linkers leads to increased methane adsorption capabilities.

The application of this principle of MOF construction to the previously described  $\{[\text{Zn}(\text{BDC})].(\text{DMF})(\text{H}_2\text{O})\}_n$  framework has also been documented, with the addition of 1,4-diazabicyclo[2.2.2]octane (dabco) to the reaction mixture affording the 3D framework  $\{[\text{Zn}(\text{BDC})(\text{dabco})_{0.5}].(\text{DMF})_4(\text{H}_2\text{O})_{0.5}\}_n$ , in which the apically bound water molecules are substituted with the neutral pillaring linker.<sup>24</sup> Analogous copper structures are reported by Seki and Mori, with the use of a variety of rigid dicarboxylate linkers giving the isostructural MOFs  $[\text{Cu}(\text{BDC})(\text{dabco})_{0.5}]_n$ ,  $[\text{Cu}(\text{FMA})(\text{dabco})_{0.5}]_n$ ,  $[\text{Cu}(\text{SDC})(\text{dabco})_{0.5}]_n$  and  $[\text{Cu}(\text{BPDC})(\text{dabco})_{0.5}]_n$  (where FMA = fumarate and SDC = styrene dicarboxylate).<sup>25</sup> The robustness of this technique is also demonstrated by the preparation of a variety of isomorphous mixed metal MOFs bearing the formulas  $[\text{Zn}_{1-x}\text{Cu}_x(\text{BDC})(\text{dabco})_{0.5}]_n$ .<sup>26</sup> The reaction of the longer neutral pillaring linker 4,4'-bipy with zinc nitrate and benzene dicarboxylic acid predictably gives the primitive cubic framework  $\{[\text{Zn}(\text{BDC})(4,4'\text{-bipy})_{0.5}].(\text{DMF})(\text{H}_2\text{O})_{0.5}\}_n$ .<sup>27</sup> It is of particular interest that the desolvated framework has been used with great success in the chromatographic separation of natural gas, and of *n*-pentane from *n*-hexane, 2-methylbutane from *n*-pentane and 2-methylpentane from 2,2-dimethylbutane and *n*-hexane. These applications have particular relevance in petroleum refining, and stem from the size of the intersecting 1D pores exhibited by this MOF. At 4 x 4 Å, these pores are perfectly suited to the separation of linear and branched alkanes on a size exclusion basis.

The structure  $[\text{Zn}_2(\text{BDC})_2(\text{dpNDI})]_n$  is a further example of the advantages of the pillar/layer strategy in MOF synthesis.<sup>28</sup> Utilising the pillaring linker *N,N'*-di(4-pyridyl)-1,4,5,8-naphthalenediimide (dpNI), this framework bears even larger separations between the 2D  $[\text{Zn}(\text{BDC})]_n$  sheets. Due to the open nature of the sheets the framework exhibits two-fold interpenetration of the networks, and while this dramatically reduces its internal pore volume, the material shows interesting dynamicity on guest adsorption, and displays chemical sensing properties which will be discussed further later in this chapter.

The systematic synthesis and analysis of gas uptake behaviours of pillar/layer MOFs deliberately designed to prevent the interpenetration of the networks is reported by Bu and co-workers.<sup>29</sup> In these examples, the solvothermal reaction of 1,1'-biphenyl-2,2',6,6'-tetracarboxylic acid ( $\text{H}_4\text{-btpa}$ ) with zinc nitrate gives rise to the formation of sheets bearing no large apertures which would facilitate the catenation of the nets, figure 17, hence the inclusion of pillaring linkers of increasing size can be expected to yield a series of isostructural MOFs with varying pore dimensions.

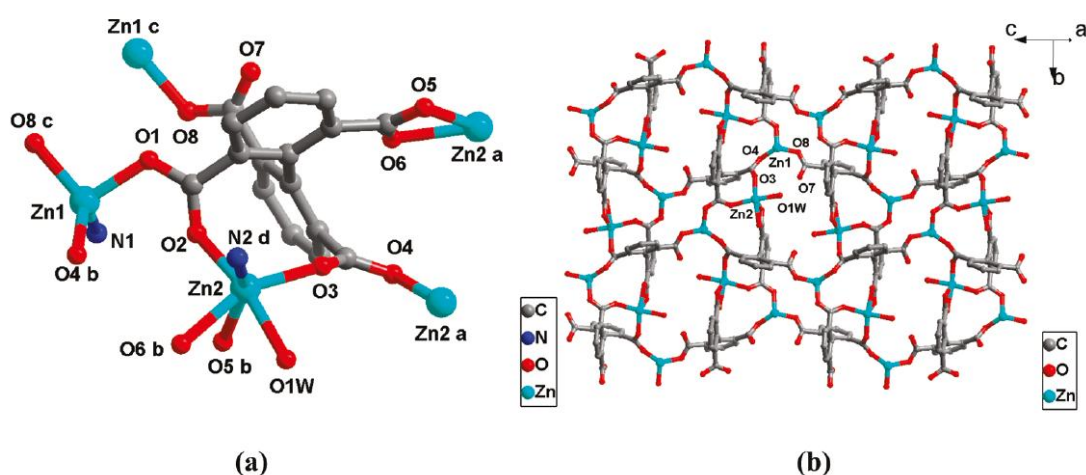


**Figure 17.** Diagram showing (a) the coordination environment of  $\text{Zn}^{2+}$  and  $\text{btpa}^{4-}$  ions in  $\{[\text{Zn}_4(\text{btpa})_2(4,4'\text{-bipy})_2(\text{H}_2\text{O})_2]\cdot 3\text{DMF}\cdot 3\text{H}_2\text{O}\}_n$ ,  $\{[\text{Zn}_4(\text{btpa})_2(4,4'\text{-azopy})_2(\text{H}_2\text{O})_2]\cdot 4\text{DMF}\cdot 3\text{H}_2\text{O}\}_n$  and  $\{[\text{Zn}_4(\text{btpa})_2(\text{dipytz})_2(\text{H}_2\text{O})_2]\cdot 4\text{DMF}\cdot 3\text{H}_2\text{O}\}_n$ , and (b) the 2D layer observed in the *b/c* plane. Hydrogen atoms are excluded. Reproduced from ref. 29.

The intercalation of the neutral pillaring linkers 4,4'-bipy, 4,4'-azopyridine (4,4'-azopy) and di-3,6-(4-pyridyl)-1,2,4,5-tetrazine (dptz) gives three isostructural

frameworks of the formulae  $\{[\text{Zn}_4(\text{bpta})_2(4,4'\text{-bipy})_2(\text{H}_2\text{O})_2]\cdot 3\text{DMF}\cdot 3\text{H}_2\text{O}\}_n$ ,  $\{[\text{Zn}_4(\text{bpta})_2(4,4'\text{-azopy})_2(\text{H}_2\text{O})_2]\cdot 4\text{DMF}\cdot 3\text{H}_2\text{O}\}_n$  and  $\{[\text{Zn}_4(\text{bpta})_2(\text{dipytz})_2(\text{H}_2\text{O})_2]\cdot 4\text{DMF}\cdot 3\text{H}_2\text{O}\}_n$ , which demonstrate the close control of pore size offered by this technique. The use of 4,4'-bipy in  $\{[\text{Zn}_4(\text{bpta})_2(4,4'\text{-bipy})_2(\text{H}_2\text{O})_2]\cdot 3\text{DMF}\cdot 3\text{H}_2\text{O}\}_n$  gives pillared 2D sheets exhibiting 1D channels running parallel to the *b* and *c* axes containing guest DMF and water molecules. The presence of  $\text{btpa}^{4-}$  phenyl units blocks the entrances to these channels, giving encapsulated void spaces occupying 29.4 % of the total volume of the framework, figure 18.

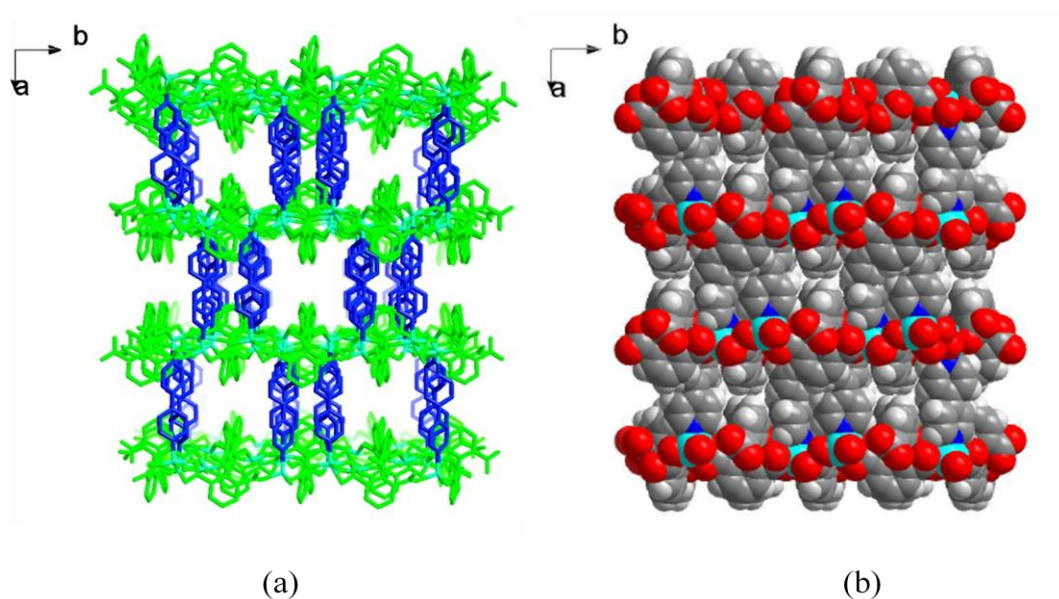


**Figure 18.** Diagrams of  $\{[\text{Zn}_4(\text{bpta})_2(4,4'\text{-bipy})_2(\text{H}_2\text{O})_2]\cdot 3\text{DMF}\cdot 3\text{H}_2\text{O}\}_n$  viewed along the *c* axis showing the (a) the pillar layer structure of the extended solid, with 2D  $[\text{Zn}_2(\text{btpa})]_n$  sheets coloured green, and intercalated 4,4'-bipy molecules coloured blue and (b) a space filling representation of the MOF demonstrating the closure of the pore entrance by  $\text{btpa}^{4-}$  phenyl units. Carbon, nitrogen, oxygen and zinc atoms are coloured grey, blue, red and light blue respectively. Reproduced from ref. 29.

The increased length of the 4,4'-azopy linker in the isostructural  $\{[\text{Zn}_4(\text{bpta})_2(4,4'\text{-azopy})_2(\text{H}_2\text{O})_2]\cdot 4\text{DMF}\cdot 3\text{H}_2\text{O}\}_n$  gives increased interlayer distance, hence the  $\text{btpa}^{4-}$  phenyl rings are no longer large enough to close the entrances to the pores, giving channels of  $3.6 \times 3.7 \text{ \AA}$  in the *b* direction intersecting with channels of  $6.0 \times 3.7 \text{ \AA}$  in the *c* direction, with an increased accessible pore volume of 36.8 %, figure 19. This pattern is followed with the use of the longer dptz linker, with the increased

interlayer layer distance for  $\{[\text{Zn}_4(\text{bpta})_2(\text{dipytz})_2(\text{H}_2\text{O})_2]\cdot 4\text{DMF}\cdot 3\text{H}_2\text{O}\}_n$  being confirmed by powder X-ray diffraction data. Analysis of the gas uptakes behaviours of these three isostructural MOFs reveal the affect of such close control of pore size on the properties of the framework. The desolvated form of  $\{[\text{Zn}_4(\text{bpta})_2(4,4'\text{-bipy})_2(\text{H}_2\text{O})_2]\cdot 3\text{DMF}\cdot 3\text{H}_2\text{O}\}_n$ , shows no uptake of  $\text{N}_2$  or  $\text{O}_2$  due to the kinetic diameters of these molecules of 3.64 Å and 3.46 Å respectively, however an appreciable uptake of  $\text{H}_2$  (57 cm<sup>3</sup> g<sup>-1</sup> at 77 K and 1.2 atm) is achieved, with the smaller kinetic diameter of this molecule (2.40 Å) allowing its diffusion through the partially closed pore entrances.

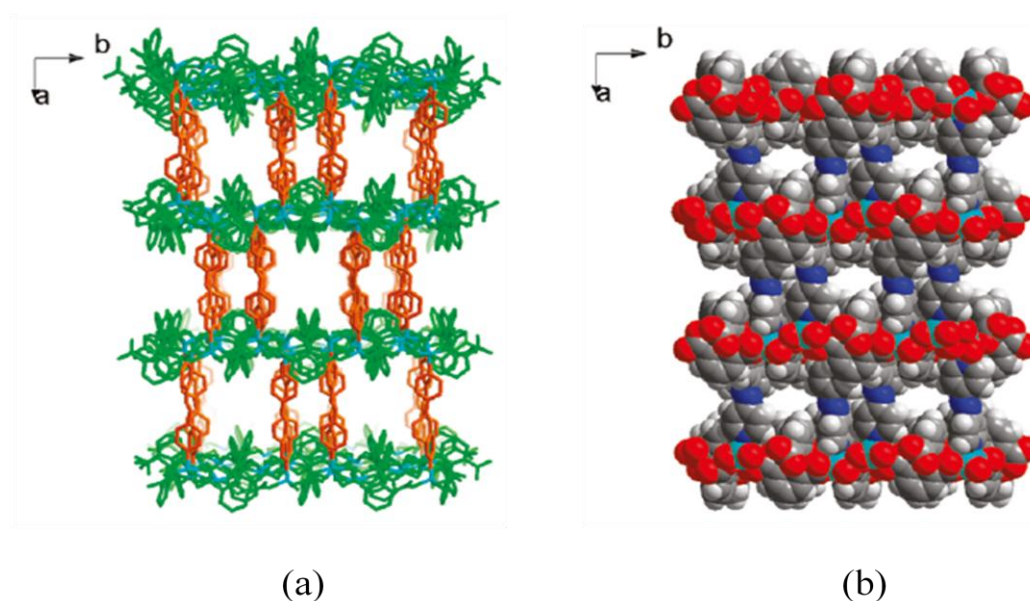


**Figure 19.** Diagrams of  $\{[\text{Zn}_4(\text{bpta})_2(4,4'\text{-azopy})_2(\text{H}_2\text{O})_2]\cdot 4\text{DMF}\cdot 3\text{H}_2\text{O}\}_n$  as viewed along the c axis, showing (a) the pillar layer structure of the extended solid, with 2D  $[\text{Zn}_2(\text{btpa})]_n$  sheets coloured green, and intercalated 4,4'-azopy molecules coloured orange and (b) a space filling representation of the MOF showing the narrowed but accessible pores. Carbon, nitrogen, oxygen and zinc atoms are coloured grey, blue, red and light blue respectively. Reproduced from ref. 29.

Partially and completely desolvated  $\{[\text{Zn}_4(\text{bpta})_2(4,4'\text{-azopy})_2(\text{H}_2\text{O})_2]\cdot 4\text{DMF}\cdot 3\text{H}_2\text{O}\}_n$  and  $\{[\text{Zn}_4(\text{bpta})_2(\text{dipytz})_2(\text{H}_2\text{O})_2]\cdot 4\text{DMF}\cdot 3\text{H}_2\text{O}\}_n$  were prepared *via* heating to 50 and 150 °C, giving the dehydrated and guest-free frameworks respectively. Due to larger pore sizes all four structures demonstrate  $\text{N}_2$  and  $\text{O}_2$  adsorption, allowing the calculation of the Langmuir and BET internal surface areas. Unusually, these reveal a smaller internal surface area for both dehydrated and guest-free

$\{[\text{Zn}_4(\text{bpta})_2(\text{dipytz})_2(\text{H}_2\text{O})_2]\cdot 4\text{DMF}\cdot 3\text{H}_2\text{O}\}_n$  compared to the 4,4'-azopy analogues, which is attributed to the bulkiness of the dipytz linker. With this in mind,  $\text{H}_2$  adsorption uptake data follow the expected pattern with the 4,4'-azopy analogues demonstrating larger uptakes ( $102 \text{ cm}^3 \text{ g}^{-1}$  and  $103 \text{ cm}^3 \text{ g}^{-1}$  at 77 K and 1 atm) than the dipytz ( $90 \text{ cm}^3 \text{ g}^{-1}$  and  $65 \text{ cm}^3 \text{ g}^{-1}$  at 77 K and 1 atm).

#### 1.1.4. Post-synthetic modification

The ability for a chemical species to diffuse through the pores of a MOF and affect a chemical change on the constituents of the framework without inducing its collapse was predicted by Hoskins and Robson at the outset of research in this field, however it was not until seventeen years later that examples of this post-synthetic modification (PSM) appeared in the literature. Though the modular nature of MOF synthesis demonstrates remarkable flexibility toward ligand functionalisation with numerous examples of linkers bearing  $-\text{NH}_2$ ,  $-\text{Br}$ ,  $-\text{OH}$  moieties as well as much larger pendant groups, there are limitations to this 'pre-functionalisation'. In order to successfully synthesise a MOF, the functional group must be non-coordinating and demonstrate stability toward the elevated temperatures and pressures required for solvothermal syntheses. The possibility of modification of the organic linkers post-synthesis removes these limitations, enabling the synthetic chemist to exploit a range of chemical reactions to further tailor the environment within the pores. The first example of PSM in this manner, *via* the heterogeneous reaction of a chemical species with the organic linker, was reported by Wang and Cohen utilising the well documented IRMOF-3.<sup>30</sup> This cubic MOF displays cylindrical pores of 9.6 Å diameter with uncoordinated  $-\text{NH}_2$  groups lining the interior of the pores. Following solvent exchange with chloroform, crystals of IRMOF-3 were suspended in dichloromethane and treated with two equivalents of acetic anhydride at room temperature for several days giving the acetylated framework IRMOF3-AM1, figure 20.

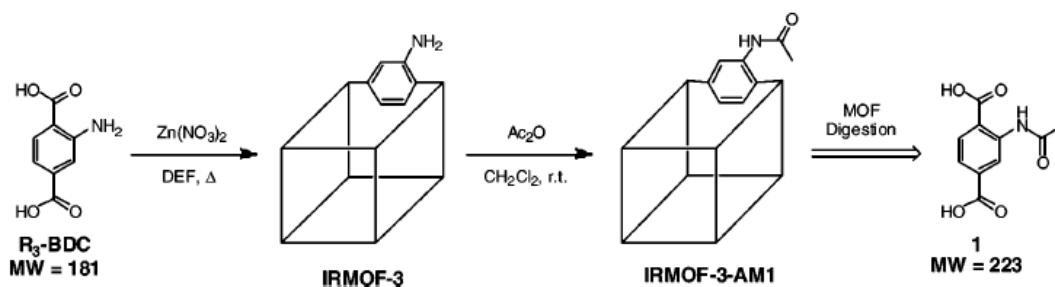


**Figure 20.** Schematic representation of the post-synthetic modification of IRMOF-3. Reproduced from ref. 30.

The presence of the acetylated product was confirmed by the digestion of the material in dilute acid and DMSO, followed by the analysis of the samples by electrospray ionisation mass spectrometry.  $^1\text{H}$  NMR studies performed on the digested samples reveal that after five days the material had undergone around 80 % conversion to the acetylated IRMOF3-AM1 species. Interestingly, a control experiment run concurrently using 2-amino-1,4-benzene dicarboxylic acid and acetic anhydride in dichloromethane demonstrated negligible conversion to the acetylated species over the same period. Subsequent studies on the reaction of IRMOF-3 with a range of linear alkyl anhydrides of the general formula  $(\text{O}(\text{CO}(\text{CH}_2)_n\text{CH}_3)_2$  (where  $n = 1$  to 18) reveal the correlation between the size of the diffusing species and the degree to which conversion to the corresponding amide species has been achieved, with increasing chain length giving reduced conversion due to the steric hindrance of alkyl anhydride.<sup>31</sup>

This approach to PSM, utilising the covalent reaction of the organic linker with a diffusing species has been termed covalent modification. A second approach, termed coordinate covalent modification, can be achieved either through the interaction of chemical species with coordinatively unsaturated metals centres comprising the SBU or through the metallation of the unbound functional groups of the organic linker. An example of the first of these techniques is reported by Hupp *et al.*<sup>32</sup> The solvothermal reaction of 1,2,4,5,-tetrakis(4-carboxyphenyl)benzene with zinc nitrate tetrahydrate in DMF gives a MOF of the formula  $[\text{Zn}_2(\text{tcpb})(\text{DMF})_2]_n$  comprising the square planar zinc paddlewheel SBU linked through the carboxylate functions of the organic linker, with DMF molecules bound to the zinc in the axial positions of the SBU. Thermogravimetric analysis conducted on the MOF reveal

mass losses at 100 and 175 °C which are attributed to the loss of the bound DMF molecules from the lattice, with the resulting evacuated species maintaining structural stability up to 425 °C. PSM reactions conducted on the evacuated species, by immersion in dichloromethane followed by the introduction of a variety of pyridinyl ligands, give five analogous MOFs bearing pyridinyl ligands bound to the axial sites of the Zn paddlewheel, figure 21. TGA data confirm the porosity of the modified MOFs and reveal increased binding energies for pyridine-Zn interactions compared to DMF-Zn, requiring temperatures in the range of 260-375 °C for their removal. The modified MOFs also show enhanced selectivity to CO<sub>2</sub> over N<sub>2</sub> adsorption.

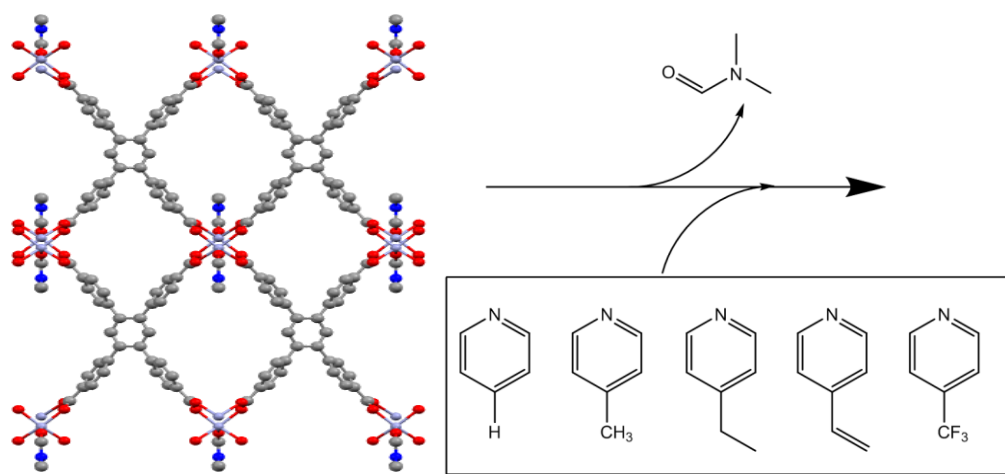


**Figure 21.** Schematic representation of the PSM reactions performed on  $[\text{Zn}_2(\text{tcpb})(\text{DMF})_2]_n$ .<sup>32</sup>

The lithiation of the unbound -OH groups in the pillar-layer structure DO-MOF as reported by Mulfort *et al.* gives an example of a coordinate covalent modification of the second kind.<sup>33</sup> The solvothermal reaction of 1,2,4,5,-tetrakis(4-carboxyphenyl)benzene and 1,2-di(4-pyridyl)-1,2-ethanediol with zinc nitrate tetrahydrate in DMF leads to the assembly of a cubic framework bearing unbound -OH moieties on the pillaring linkers, figure 22. Reaction of this MOF with lithium *tert*-butoxide in CH<sub>3</sub>CN/THF leads to the deprotonation of these unbound alcohol groups, and the formation of the lithium alkoxide, with Li:Zn ratios for the resulting modified framework being controlled through reaction time.

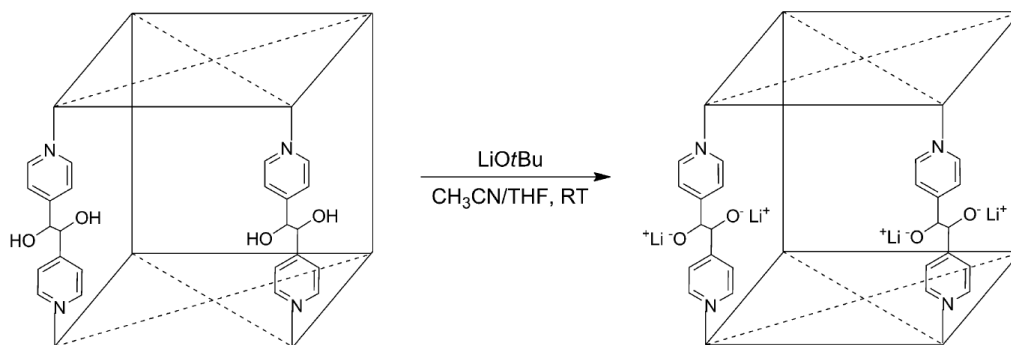


**Figure 22.** Schematic representation of the post-synthetic modification of DO-MOF. Reproduced from ref. 35.

In many cases, the desired post-synthetic modification can only be achieved through the application of these techniques in tandem. In the example reported by Tanabe and Cohen, the decoration of the pore walls of UMCM-1-NH<sub>2</sub> with 3-hydroxyphthalic anhydride and 2,3-pyrazinedicarboxylic anhydride *via* covalent modification to give the structures, UMCM-1-AMsal and UMCM-1-AMpz was achieved.<sup>34</sup> These modified MOFs, were treated with [Fe(acac)<sub>3</sub>] and [Cu(acac)<sub>2</sub>] with this second coordinate covalent modification giving two new materials bearing Fe<sup>3+</sup> and Cu<sup>2+</sup> ions coordinated to the appended groups, the former demonstrating catalytic activity for the Mukaiyama-aldol reaction. The diagram at figure 23 illustrates the strategies employed in the post-synthetic modification of MOFs.<sup>35</sup>

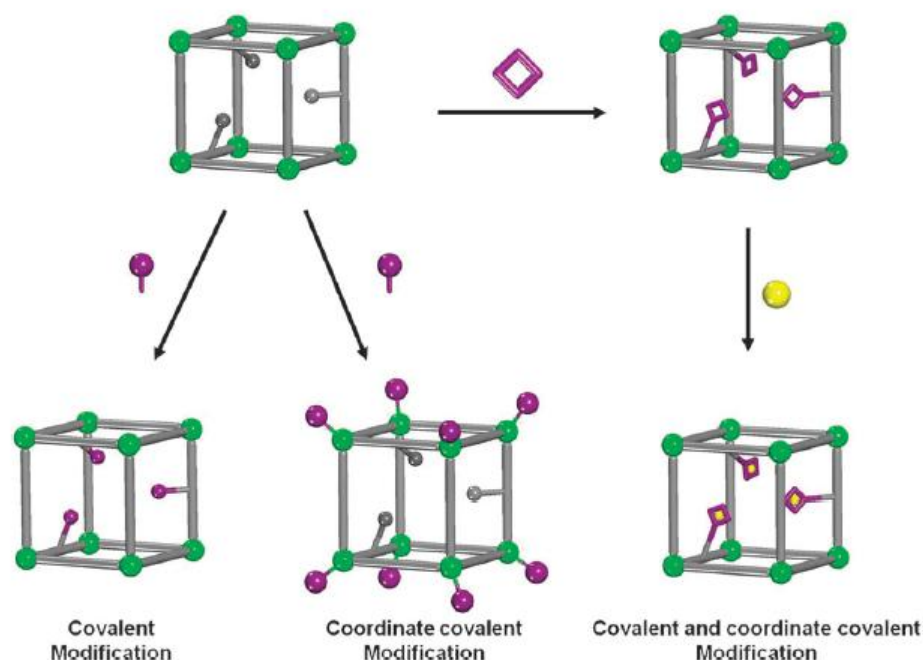


**Figure 23.** Schematic of the strategies employed in the post-synthetic modification of MOFs. Reproduced from ref. 35.

### 1.1.5. Interpenetration and dynamic MOFs

The design of pore size in MOFs from a 'bottom-up' basis through the selection of building units which bear the desired geometry has can be achieved through a number of techniques, as described previously, however the inability to predict whether the self-assembly of the components will lead to the interpenetration of these networks, and to what extent this interpenetration will affect the pore size of the resulting MOF is a major stumbling block in the rational design of crystalline materials. In those examples where interpenetration does occur, it has been shown that the pore size is reduced significantly with the usefulness of the resulting materials being governed by serendipity. Though this phenomenon may be avoided either by the reduction of reactant concentration, or through the use of pillared 2D sheets, there are examples where this interpenetration has lead to the synthesis of MOFs which show dynamic behaviour on guest molecule removal, with independent networks able to move in relation to each other due to the weak inter-network associations.

An example of a MOF which undergoes dynamic change on guest adsorption by the shearing of interpenetrated networks is offered by Chen and co-workers.<sup>36</sup> In this example, the solvothermal reaction of H<sub>2</sub>NDC (where H<sub>2</sub>NDC = 2,6-naphthalenedicarboxylic acid) and DPE with zinc nitrate in DMF affords  $\{[\text{Zn}(\text{NDC})(\text{DPE})_{0.5}].2.25\text{DMF}.0.5\text{H}_2\text{O}\}_n$  as doubly interpenetrated primitive cubic nets, with the spacing between networks governed by the presence of guest DMF molecules, figure 24

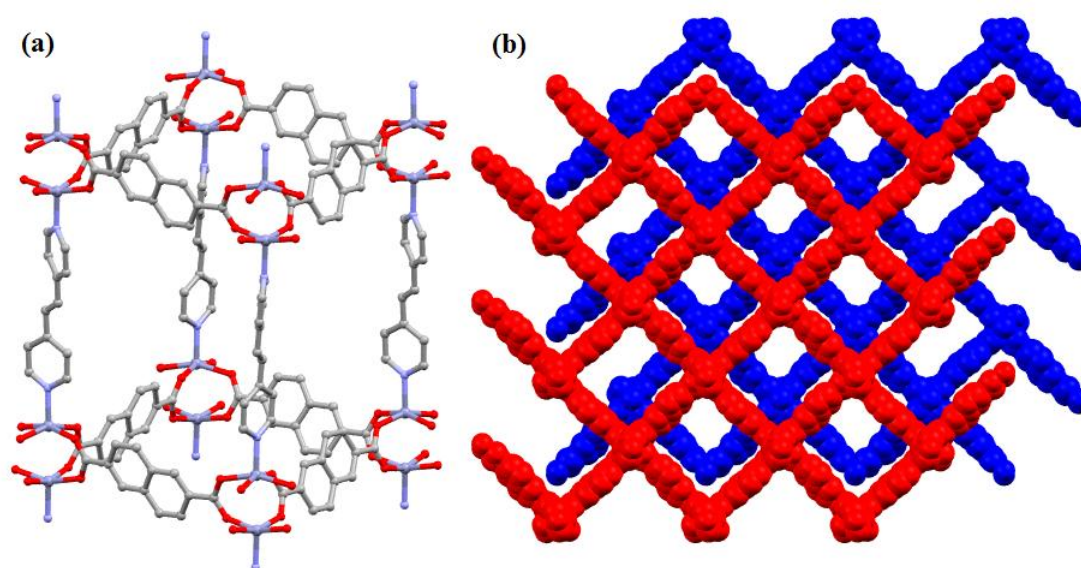


**Figure 24.** Diagram of  $[\text{Zn}(\text{NDC})(\text{DPE})_{0.5}]_n$  showing (a) the primitive cubic net, with carbon oxygen nitrogen and zinc atoms are coloured grey, red blue and purple respectively, and (b) a space filling representation as viewed along the a axis, with independent nets coloured red and blue for clarity.<sup>36</sup>

Solvent exchange performed on the as-synthesised framework with methanol and acetone, and the subsequent analysis of the solvent exchanged species by powder X-ray diffraction reveal reduced  $d$  spacing, offering evidence of crystal to crystal transformation, with the quantity and identity of guest molecules confirmed by TGA analyses. The recorded N<sub>2</sub> adsorption isotherm for the desolvated framework offers more evidence of the dynamic nature of this material, allowing an internal surface area of only 303 m<sup>2</sup> g<sup>-1</sup> to be calculated, compared to 484 m<sup>2</sup> g<sup>-1</sup> for the triply interpenetrated cobalt analogue  $[\text{Co}(\text{NDC})(\text{DPE})_{0.5}]_n$ .<sup>37</sup> This data demonstrates that in the absence of guest molecules, the pore size of this material is further decreased. Many examples of this form of reversible structural deformation exist,<sup>38</sup> including

the previously described  $\{[\text{Zn}(\text{BDC})(4,4'\text{-bipy})_{0.5}]\cdot\text{DMF}\cdot\text{H}_2\text{O}\}_{0.5}\}_n$ ,<sup>25</sup> though the nature of dynamic changes exhibited by MOFs are not limited to this phenomenon. The ability for frameworks to distort through the rotational freedom of organic linker to metal coordinate bonds is also reported. MIL-53(Cr) offers an ideal example of a MOF which undergoes fully reversible structural deformation of this type.<sup>39</sup> Synthesised by the hydrothermal reaction of H<sub>2</sub>BDC with chromium nitrate the extended structure of MIL-53(Cr) is composed of 1D [Cr(OH)]<sub>n</sub> chains linked *via* bridging carboxylate functions from BDC units giving a 3D microporous material of the formula  $\{[\text{Cr}(\text{OH})(\text{BDC})]\cdot 0.75\text{H}_2\text{BDC}\}_n$  with templating H<sub>2</sub>BDC molecules situated in large pores observed along the *a* axis. Removal of the templating molecules by calcination is accompanied by the opening of the pores giving a guest free species with a unit cell volume of 1480 Å<sup>3</sup> compared to 1440 Å<sup>3</sup> for the as-synthesised framework. The most striking change occurs on the introduction of water molecules to the guest free species, which leads to a decrease in the unit cell volume to 1012 Å<sup>3</sup>, due to the formation of hydrogen bonds between the guest molecules and the coordinated -OH groups and the onset of  $\pi$ - $\pi$  interactions between the benzyl groups of the organic linker with the flexing facilitated by the rotation of the carboxylate to metal bonds, figure 25.

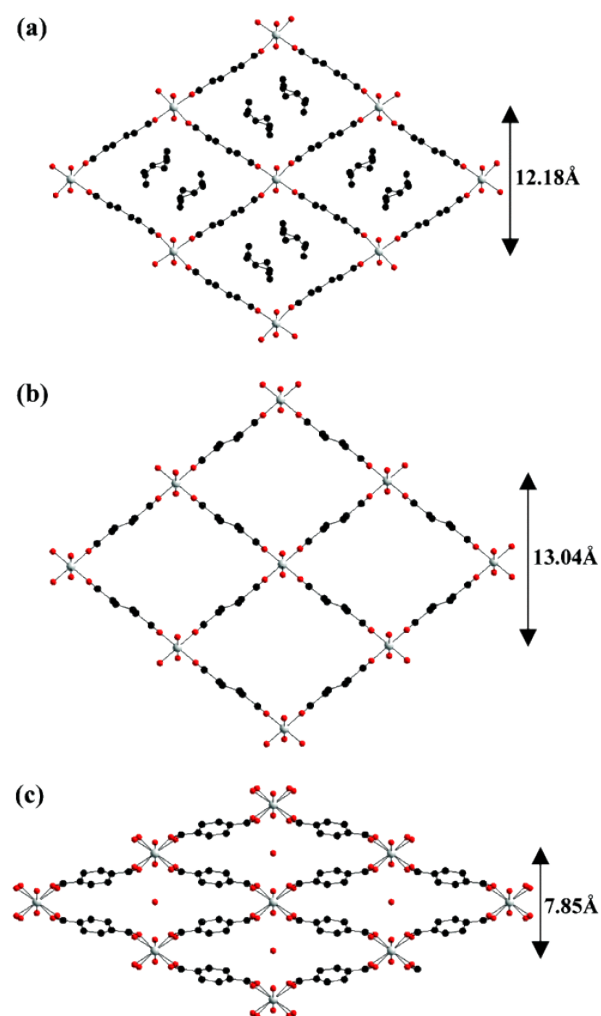


**Figure 25.** Diagram of MIL-53(Cr) showing (a) the as synthesised MOF containing disordered templating H<sub>2</sub>BDC molecules, (b) the guest-free framework and (c) the hydrated framework. The reduction in pore volume is illustrated by measurements of the separation between Cr<sup>2+</sup> centres along vertical axis. Carbon, oxygen and chromium atoms are coloured black, red and grey respectively. Reproduced from ref. 39.

An example of a MOF which undergoes structural deformations of both types is the previously mentioned pillar/layer MOF [Zn<sub>2</sub>(bdc)<sub>2</sub>(dpNDI)]<sub>n</sub>.<sup>28</sup> Prepared solvothermally by the reaction of H<sub>2</sub>BDC and dpNI with zinc nitrate, the as-synthesised material demonstrates doubly interpenetrated networks, with void spaces situated at sites A and B containing 4 DMF molecules per formula unit, figure 26 (a, b).

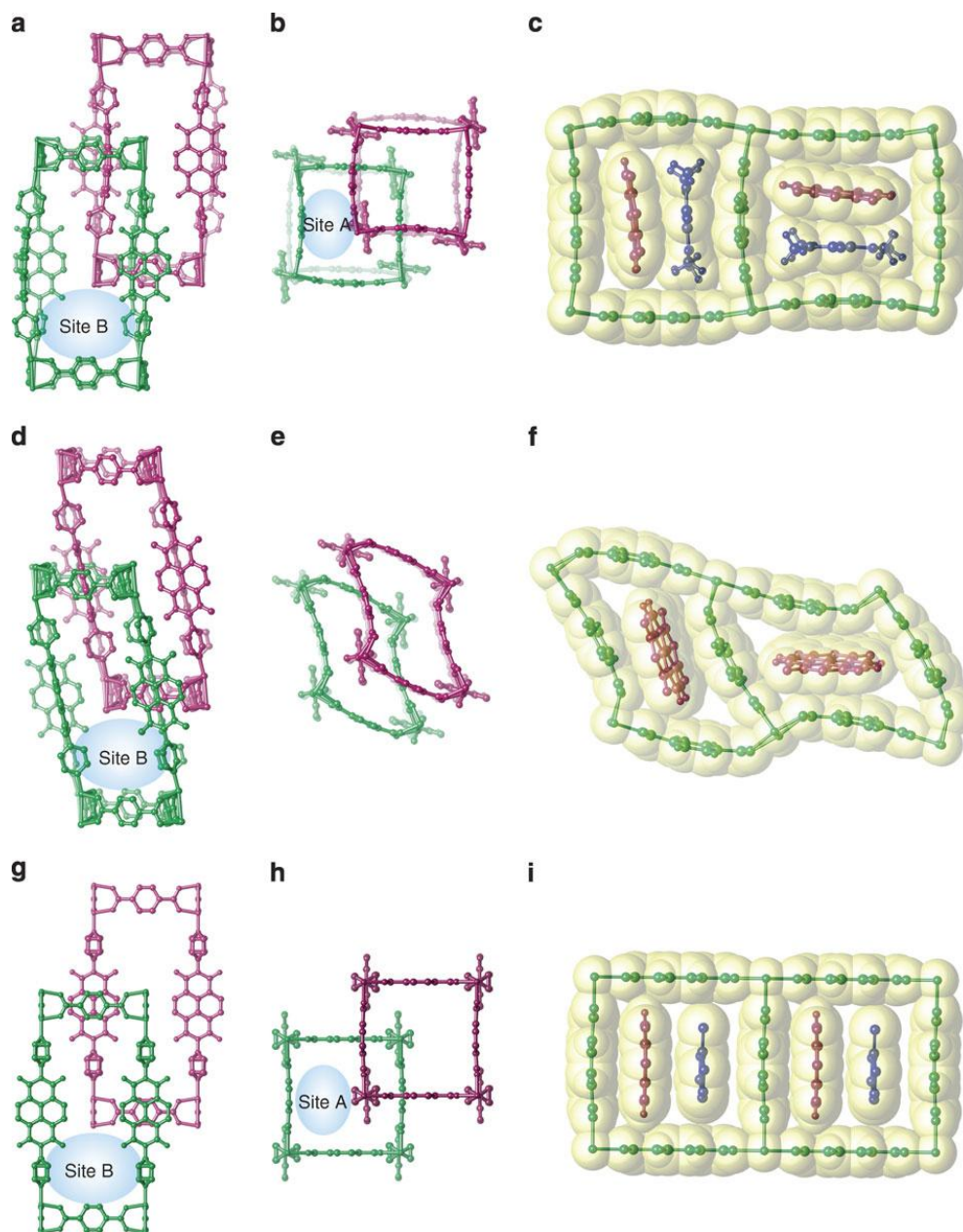


**Figure 26.** Diagram of the pillar/layer MOF  $[\text{Zn}_2(\text{bdc})_2(\text{dpNDI})]_n$  showing views along a) the BDC linker and b) the dpNDI pillar, with void spaces A and B identified. c) the view along the dpNDI linker showing the guest DMF molecule located at site A; Van der Waals surfaces are highlighted in yellow. d-f) show the shearing of the networks on guest removal and the bent configuration adopted by the linkers. g-i) show the same views of the network on the adsorption of toluene. Reproduced from ref. 28.

Removal of two guest DMF molecules from site A leads to the distortion of the framework by the shearing of the networks, with both the BDC and dpNI units adopting a bent configuration to minimise the void space at site A, figure 22 (d-f).

Immersion of the dried MOF in toluene induces a further structural transformation, giving a third species bearing the formula  $\{[\text{Zn}_2(\text{bdc})_2(\text{dpNDI})].2.5\text{toluene}\}_n$ , figure 22 (g-i). Due to proximity of the guest toluene molecules to the photoactive 1,4,5,8-naphthalenediimide moiety, the inclusion of these guest molecules is accompanied by a measureable change in the fluorescence wavelength of the MOF, which is not observed in the non-interpenetrated analogue. Similar shifts in emission spectra are observed on the incorporation of benzene, benzonitrile, *o*-xylene, *m*-xylene, *p*-xylene, anisole and iodobenzene, demonstrating the potential for this material as a chemosensor for these atmospheric pollutants.

### 1.1.6. Classification of porous structures

Due to the vast quantity of MOFs which now appear in the literature some means of classification of these structures based on their physical and structural properties is required. One such form of classification is through the identification of the structure of the pores. On this basis, porous materials can be separated into four categories, those which bear 0 D dots, those which bear 1D channels, 2D layers and 3D intersecting channels, figure 27.<sup>40</sup>

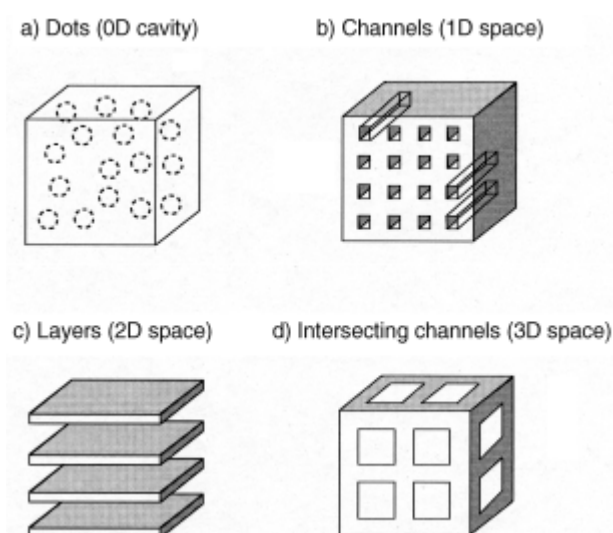


**Figure 27.** Representation of the different types of porosity exhibited by MOFs. Reproduced from ref. 40.

Progress in the development of these structures, and the enormous diversity of physical properties exhibited by MOFs however, requires a form of classification which takes these properties into account and is not based not solely on the nature of

porosity. Consequently, it has been suggested that 3 generations of MOF now exist.<sup>41</sup> Those frameworks which are not stable towards solvent removal are identified as 1<sup>st</sup> generation MOFs. Those which are stable to the removal of solvent and show permanent porosity are classified as 2<sup>nd</sup> generation. 3<sup>rd</sup> generation MOFs are permanently porous, stable to solvent removal and demonstrate dynamic frameworks which respond to external stimuli and are able to change their channels or pores reversibly, figure 28.

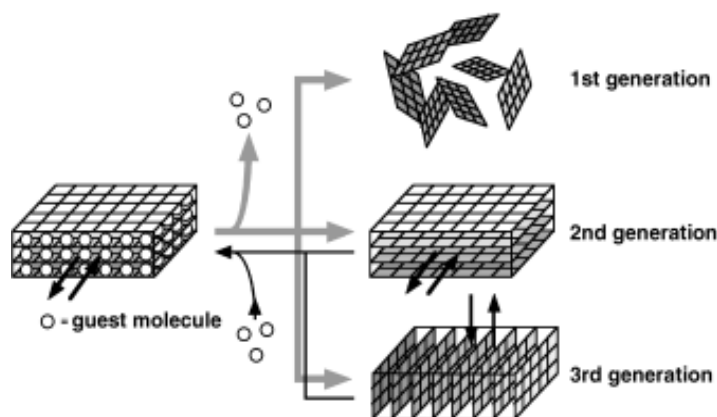


**Figure 28.** Diagram of the 3 generations of MOF classified by their structural properties on guest removal. Reproduced from ref. 41.

MOFs which fall under the third title can be further classified by the characteristics of this dynamic change. In those examples where the removal of guest solvent gives rise to a crystalline to amorphous transformation, which is fully reversible on the re-introduction of guest solvent molecules, the label CAT, 3rd-I can be applied. Those materials which exhibit a crystal to crystal transformation on the removal or exchange of guest solvent molecules are categorised CCT, 3rd-II, with two further sub-categories identifying those materials which retain crystallinity on guest removal and those which retain crystallinity on guest exchange, figure 29.

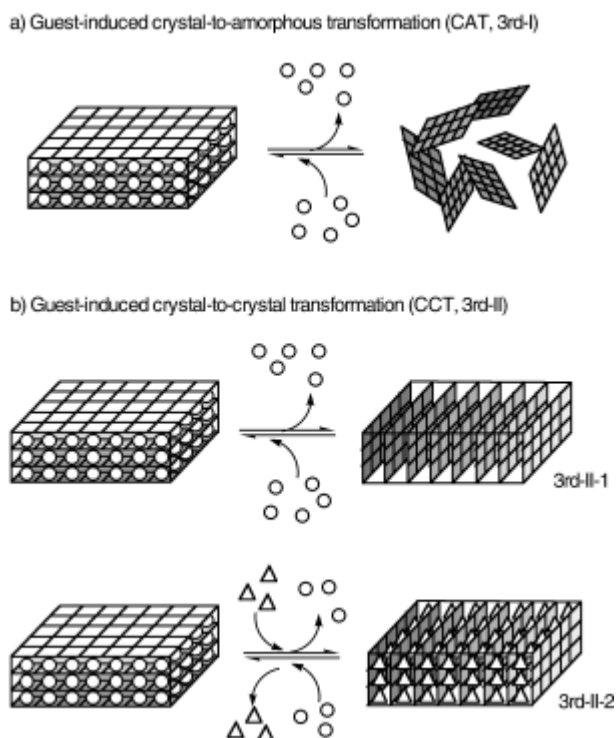


**Figure 29.** Representation of the three sub-classes of dynamic MOF. Reproduced from ref. 41.

## 1.2. Hydrogen storage in MOFs

In recent times, the dependence of the global economy on hydrocarbon based energy carriers such as gasoline/petroleum and diesel has been subject to numerous ecological and economic concerns. Dwindling reserves of the fossil fields from which these fuels are derived and the discovery of the environmentally harmful effects of the combustion of hydrocarbons have revealed the need for a cleaner, more sustainable energy economy. With a mass energy density of  $120 \text{ MJ Kg}^{-1}$  compared to  $44.4 \text{ MJ Kg}^{-1}$  for gasoline, molecular hydrogen would appear to be the ideal candidate for a new energy carrier.<sup>42</sup> It is with this in mind that vast amounts of capital have been invested in the research and development of molecular hydrogen powered fuels cells.

The so-called Hydrogen Economy has numerous benefits over the current hydrocarbon economy. Not only is hydrogen the third most abundant element in our environment, answering the sustainability issues from which the hydrocarbon economy is at risk, but also the combustion of hydrogen in its molecular form has none of the associated environmental concerns, releasing only water as a waste

product. There are however many areas in which research is required in order to make molecular hydrogen a viable replacement for hydrocarbon fuels, chiefly among these is storage. Though the gravimetric energy density of molecular hydrogen is almost three times that of gasoline, its density at ambient conditions (300 K, 1 atm) is only  $0.08 \text{ Kg m}^{-3}$ , giving a volumetric energy density of  $10.7 \text{ KJ L}^{-1}$  compared to  $31.1 \text{ MJ L}^{-1}$  for gasoline.<sup>40</sup>

Due to the comparatively very low volumetric energy density of molecular hydrogen at ambient conditions compared to its hydrocarbon counterparts, it follows that some means of increasing the density at which hydrogen is stored is required. High pressure or cryogenic tanks to store molecular hydrogen in its gas or liquid form respectively are expensive and prohibitively bulky for use in the automotive industry. With the U.S. Department of Energy (DoE) target of 9 wt% or  $81 \text{ g L}^{-1}$  at near ambient conditions for onboard storage for a viable transport system, giving a range of 300 miles (500 Km) with comparative cost, safety and performance to current hydrocarbon powered vehicles, the mass of cooling and regeneration equipment must be minimised.<sup>43</sup> It is with this in mind that the storage of this potential energy carrier *via* chemisorption and physisorption has attracted so much research funding over the last two decades.

Storage of hydrogen through chemisorption requires the formation of chemical bonds between the materials and the hydrogen. The binding energies of the adsorbate to the adsorbent in these systems are therefore high, typically 1-10 eV, allowing for the uptake of substantial quantities of molecular hydrogen at close to ambient conditions. In most cases however, these high binding energies lead to slow uptake kinetics, poor reversibility of the materials, and substantial heat generation during hydrogen loading.<sup>44</sup>

Physisorption on porous materials allows for the storage of high volumes of molecular hydrogen at greatly reduced pressures compared to pure tank-storage methods.<sup>45</sup> As the major factor governing physisorption is weak Van der Waals interactions,  $\text{H}_2$  storage systems should suffer far less from the heat generation and reversibility issues surrounding chemisorption. Concomitant with this, however, are far lower binding energies between the adsorbent and the adsorbate, typically 10-100 meV, hence significant uptake of molecular hydrogen in these materials requires

cryogenic temperatures (77 K).<sup>46</sup> As physisorption is a surface phenomenon, it follows that the development of an optimal sorbent for this purpose should be an exercise in producing materials with greater and greater internal surface areas, and indeed it would appear that those MOFs with the highest surface areas also demonstrate some of the highest uptakes of molecular hydrogen. The ideal example of this is MOF-177, figure 30.<sup>47</sup>

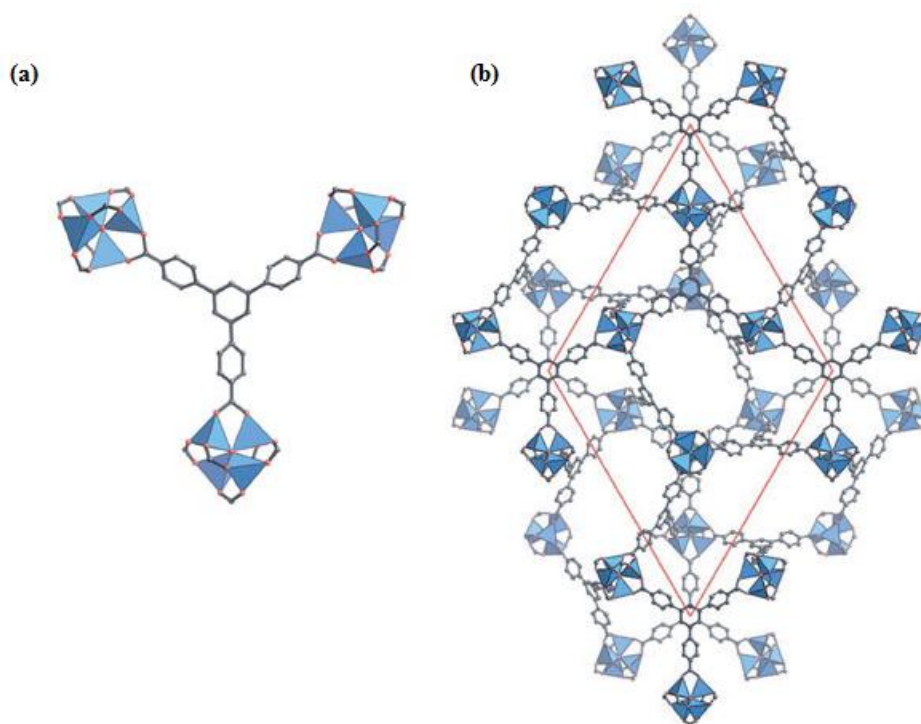


**Figure 30.** The structure of MOF-177 showing (a) a BTB unit linked to three basic zinc acetate SBUs, (b) the structure as viewed along [001]. Carbon and oxygen atoms are coloured grey and red, zinc atoms are represented by blue tetrahedra. Hydrogen atoms are omitted. Reproduced from ref. 47.

Prepared by the solvothermal reaction of 4, 4', 4''-benzene-1,3,5-tri-benzoic acid ( $H_3BTB$ ) with zinc nitrate hexahydrate in DEF, the material displays the basic zinc acetate SBU commonly observed in MOF synthesis. This SBU acts as an octahedral node *via* the formation of coordinate bonds to six independent 4,4',4''-benzene-1,3,5-tri-benzoate (BTB) molecules by the di-monodentate binding of the carboxylate groups. The metal binding motif is repeated at each of the three carboxylate moieties of the BTB unit, giving the formula unit  $Zn_4O(BTB)_2$ . The Langmuir and BET surface areas of this material, determined by  $N_2$  adsorption studies are calculated as  $5640 \text{ m}^2 \text{ g}^{-1}$  and  $4750 \text{ m}^2 \text{ g}^{-1}$  with pore volumes of  $1.59 \text{ cm}^3$

$\text{g}^{-1}$  calculated using the Dubinin-Radushkovich equation. Initial hydrogen uptake isotherms recorded up to 90 bar pressure at 77 K, reveal that this material has a saturation hydrogen uptake of 7.5 wt% or  $32 \text{ g L}^{-1}$  approaching the targets set by the US DoE,<sup>48</sup> however, subsequent studies performed at 298 K at pressures up to 100 bar give an uptake of only 0.62 wt%.<sup>49</sup> Bearing an even larger BET surface area of  $6143 \text{ m}^2 \text{ g}^{-1}$  with pore volumes of  $2.82 \text{ cm}^3 \text{ g}^{-1}$ , NU-100, prepared *via* the reaction of the hexacarboxylate ligand in figure 31a, with copper, shows similar behaviour with excess hydrogen uptake at 77 K and 56 bar of 9.95 wt%.<sup>50</sup> At ambient pressure however, this uptake is dramatically reduced, with an excess hydrogen uptake of only 1.82 wt%.

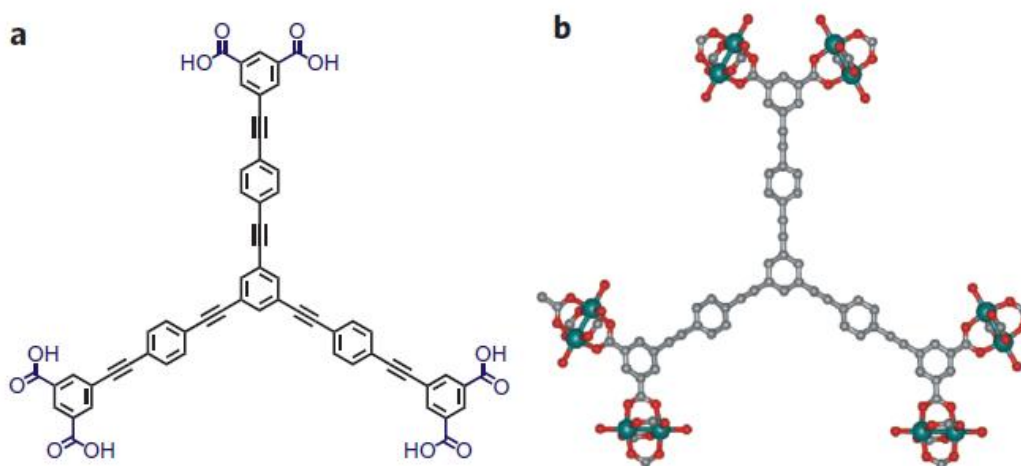


**Figure 31.** Diagram of a) the hexacarboxylic acid linker and b) location of paddlewheel SBUs on each of the carboxylate moieties in NU-100. Reproduced from ref. 50.

The highest internal surface area of any MOF so far reported is that of NU-110E.<sup>51</sup> Determined experimentally using the nitrogen isotherm, the BET surface area is  $7140 \text{ m}^2 \text{ g}^{-1}$  with a pore volume of  $4.40 \text{ cm}^3 \text{ g}^{-1}$ . Though excess hydrogen uptake measurements have yet to be reported on this framework, due to the similarities in structure between this framework at that of NU-100, the results are expected to follow the same pattern as the previous two examples, with high pressure, low temperature uptakes far in excess of those recorded at ambient pressure and temperature. Thus, the challenge for the synthetic chemist remains to be the optimisation of such systems to maximise the uptake of molecular hydrogen at close to ambient conditions.

### 1.2.1. Pore optimisation for hydrogen uptake

The high uptake of molecular hydrogen observed in the *Soc*-MOF material prepared by Liu and co-workers, at close to ambient pressure offers clues to the form that this optimisation should take.<sup>52</sup> Prepared by the solvothermal reaction of the organic linker azobenzene-3,3',5,5'-tetracarboxylic acid with indium nitrate dihydrate in the presence of piperazine and nitric acid, the structure exhibits an oxo-centred indium trimer bound to the carboxylate groups of six independent organic linkers in a dimonodentate fashion, with water molecules coordinated to the indium centres in the apical positions. The resulting cationic SBU can be considered a trigonal prismatic unit bearing six points of extension. This binding motif is repeated at each of the carboxylate moieties of the organic linker, giving a material with the molecular formula  $\{[\text{In}_3\text{O}(\text{abtc})_{1.5}(\text{H}_2\text{O})_3(\text{NO}_3)].3\text{H}_2\text{O}\}_n$  (where abtc = azobenzene-3,3',5,5'-tetracarboxylate) exhibiting a square octahedral connectivity net, with the cationic SBU being charge balanced by the presence of one nitrate anion per formula unit, figure 32.

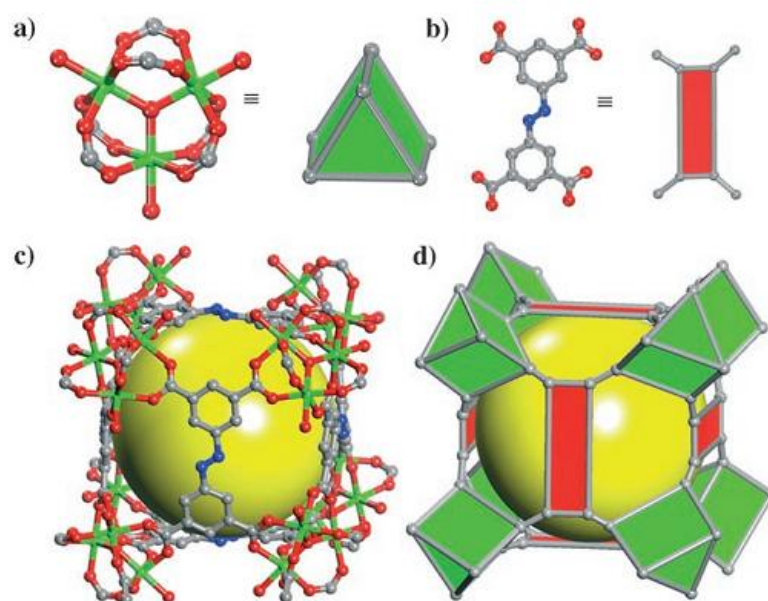


**Figure 32.** Diagram of  $\{[\text{In}_3\text{O}(\text{abtc})_{1.5}(\text{H}_2\text{O})_3(\text{NO}_3)].3\text{H}_2\text{O}\}_n$  showing a) the trigonal prismatic SBU, b) the abtc linker and c, d) the square octahedral lattice, with the yellow sphere identifying the void space. Carbon, nitrogen, oxygen and indium atoms are coloured grey, blue, red and green respectively. Reproduced from ref. 52.

Hydrogen adsorption studies performed on the evacuated material at 78 K and 1.22 bar give an uptake of 2.61 wt%, with no hysteresis observed on desorption. Due to the relatively low Langmuir surface area ( $1417 \text{ m}^2 \text{ g}^{-1}$ ) and pore volume ( $0.50 \text{ cm}^3 \text{ g}^{-1}$ ) of this material, the remarkable uptake of molecular hydrogen at close to ambient pressure has been attributed to a number of interesting features this MOF exhibits. The material displays two types of narrow channel of around 1 nm diameter, the first of these is hydrophilic containing guest water molecules hydrogen bound to the coordinated water molecules, the second channel is guest free. The charge balancing nitrate anions are situated inside the cubic unit formed by the binding of eight SBUs to six organic linkers. This unit, bearing windows of  $7.651 \times 5.946 \text{ \AA}$ , acts as a carcerand, preventing the escape of the nitrate anions from the framework during solvent removal, figure 33. Finally, the removal of apical water molecules from the SBU during sample evacuation gives a MOF bearing cationic, coordinatively unsaturated metal centres. The result of these factors is the preparation of a framework with narrow pores, which exhibits highly localised charge density. This allows for the adsorption of molecular hydrogen at a density of  $0.05 \text{ g cm}^{-3}$  at 78 K, which approaches the density of  $0.0708 \text{ g cm}^{-3}$  of liquid hydrogen at 20 K.

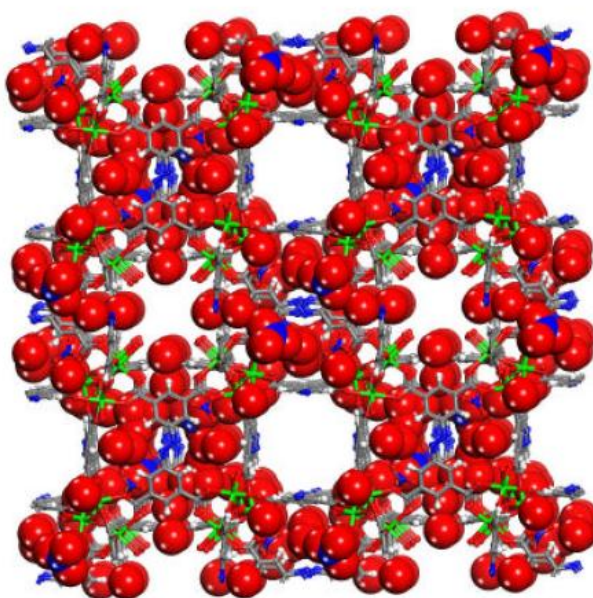


**Figure 33.** Diagram of  $\{[\text{In}_3\text{O}(\text{abtc})_{1.5}(\text{H}_2\text{O})_3(\text{NO}_3)].3\text{H}_2\text{O}\}_n$  showing the structure of the MOF (wireframe), with nitrate anions (space filling) encapsulated by the carcerand unit. Reproduced from ref. 52.

*In silico* calculations performed by Belof *et al.*<sup>53</sup> using the material prepared by Liu offer some insight in to this molecular hydrogen uptake behaviour and reveal the requirement for a molecular hydrogen sorbent to have a high surface area, with a caveat that in those circumstances where this surface area is accompanied by large pore size, giving a very low density material, hydrogen storage potential is actually limited by the lack of strong H<sub>2</sub>-MOF interactions in the middle of the pores. The ideal sorbent should therefore have a large surface area comprising small, interdigitated pores. Significant H<sub>2</sub>-MOF interactions observed at the N=N moiety of the organic linker lead to the conclusion that the interaction of the hydrogen molecules with the internal surface of the MOF can be maximised through the inclusion of heteroatoms which give areas of local polarity, inducing dipole interactions between the MOF and the adsorbed hydrogen molecules. This effect propagates through the pores with the induced dipole-dipole interactions between adsorbed and free hydrogen molecules leading to an increase in the condensation temperature of molecular hydrogen. The presence of cationic indium centres in the SBU and nitrate anions held within the carcerand unit also serve to increase the local charge density in the pores of the MOF and hence the polarisation of molecular hydrogen.

The enhanced excess hydrogen adsorption behaviour of structures bearing N=N moieties is repeated in the uptake behaviours of the MOFs PCN-10 and PCN-11.<sup>54</sup> These analogous frameworks are prepared *via* the reaction of copper nitrate (hemi)pentahydrate with azoxybenzene-3,3',5,5'-tetracarboxylic acid in the first example and *trans*-stilbene-3,3',5,5'-tetracarboxylic acid in the second figure 34.

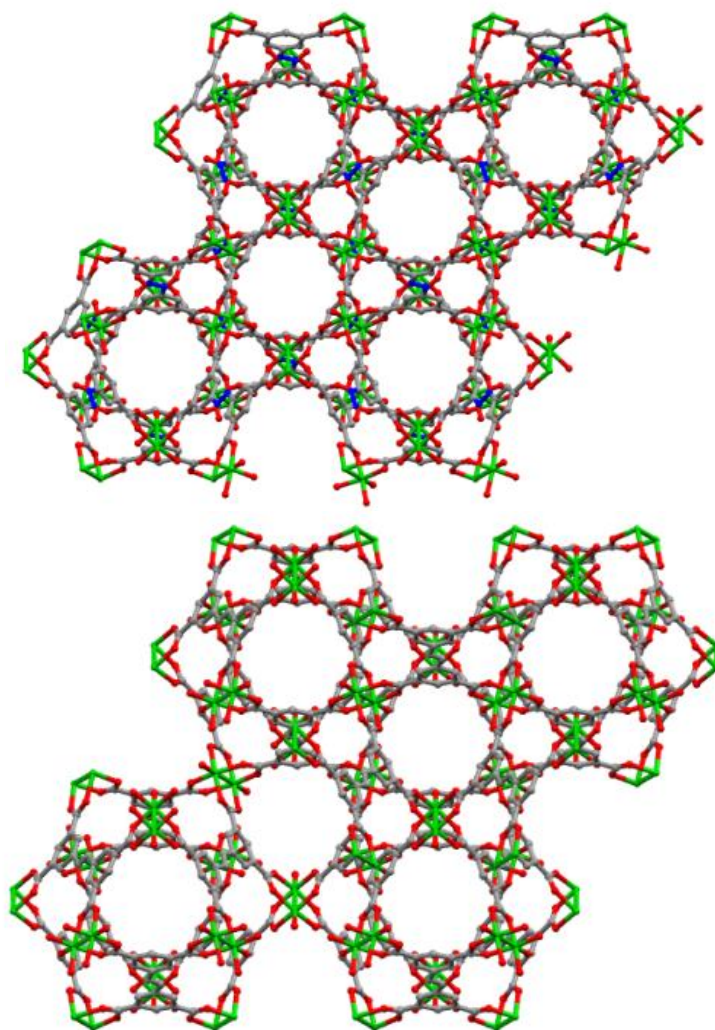


**Figure 34.** Diagram showing PCN-10 (top) and PCN-11 (bottom) as viewed along the  $c$  axes. Carbon, nitrogen, oxygen and copper atoms are coloured grey, blue, red and green respectively. Hydrogen atoms are omitted for clarity.<sup>54</sup>

In the first instance, the solvothermal synthesis conducted in DMA at 80 °C, leads to the *in situ* reduction of the azoxybenzene-3,3',5,5'-tetracarboxylic acid to give azobenzene-3,3',5,5'-tetracarboxylic acid, yielding a MOF with the formula  $\{[\text{Cu}_2(\text{abtc})(\text{H}_2\text{O})_2] \cdot 3\text{DMA}\}_n$ . The MOF exhibits two types of channel, the first visible along the [0, 15, 13] plane has dimensions of 8.13 x 9.26 Å while the second, orientated along the crystallographic  $c$  axis bears dimensions of 8.13 x 8.13 Å. The isostructural PCN-11, is prepared using the same procedure giving the formula  $\{[\text{Cu}_2(\text{sbtc})(\text{H}_2\text{O})_2] \cdot 3\text{DMA}\}_n$  (where sbtc = *trans*-stilbene-3,3',5,5'-tetracarboxylate). Due to the similarity in the lengths of the organic linkers abtc and sbtc, the resulting structures demonstrate very similar pore size with accessible pore volumes of 71.2 %

for PCN-10 and 71.9 % for PCN-11 calculated using PLATON. Langmuir and BET surface areas, of 1779 m<sup>2</sup> g<sup>-1</sup> and 1407 m<sup>2</sup> g<sup>-1</sup> for PCN-10 and 2442 m<sup>2</sup> g<sup>-1</sup> and 1931 m<sup>2</sup> g<sup>-1</sup> for PCN-11, calculated using the nitrogen adsorption isotherms recorded for these structures however, display a marked difference. This is attributed to the reduced thermal stability of the N=N bond in PCN-10 compared to the C=C bond in PCN-11, with solvent removal conducted at elevated temperature leading to the partial decomposition of PCN-10. Low pressure gas adsorption studies performed on these two frameworks reveal a hydrogen uptake of 2.34 wt% for PCN-10 and 2.55 wt% for PCN-11 at 77 K and 1 atm. These figures would suggest that PCN-11 is the better performing material, however the 27.2 % reduction in surface area of PCN-10 compared to PCN-11 is accompanied by only an 8.2 % reduction in hydrogen uptake, due to the increased binding affinity of molecular hydrogen to the N=N moiety.

Though the previous three examples demonstrate that the presence of polar functionality at the organic linker plays a large role in increasing the binding energy and condensation temperature of molecular hydrogen, the presence of coordinatively unsaturated metal centres in these examples cannot be ignored. Research conducted by Long and co-workers using the framework  $\{\text{Mn}_3[(\text{Mn}_4\text{Cl}_3)(\text{BTT})_8(\text{CH}_3\text{OH})_{10}]_2\}_n$  (where BTT = 1,3,5-benzenetristetrazolate) offers evidence that the presence of such centres serves to increase the binding energy of adsorbed hydrogen further through strong metal-H<sub>2</sub> interactions.<sup>55</sup> Formed *via* the solvothermal reaction of H<sub>3</sub>BTT with MnCl<sub>2</sub>·4H<sub>2</sub>O in a DMF/methanol mixture, the structure is comprised of chloride centred [Mn<sub>4</sub>Cl]<sup>7+</sup> square planar units bound to eight BTT linkers *via* the N2 and N3 nitrogens of the tetrazolate moieties. This binding motif is repeated at each of the three tetrazolate groups giving a truncated octahedral unit comprising six [Mn<sub>4</sub>Cl]<sup>7+</sup> squares connected by eight BTT units, with the macroscopic structure of the framework being formed by the linking of these octahedra through the [Mn<sub>4</sub>Cl]<sup>7+</sup> squares. The as-synthesised structure bears water molecules coordinated at the apical position of each of the Mn<sup>2+</sup> centres giving an anionic structure with the formula  $\{[(\text{Mn}_4\text{Cl})_3(\text{BTT})_8(\text{H}_2\text{O})_{12}]^{3-}\}_n$  which is charged balanced by the presence of extra-framework cationic [Mn(DMF)<sub>6</sub>]<sup>2+</sup> units situated inside the truncated octahedra, figure 35.

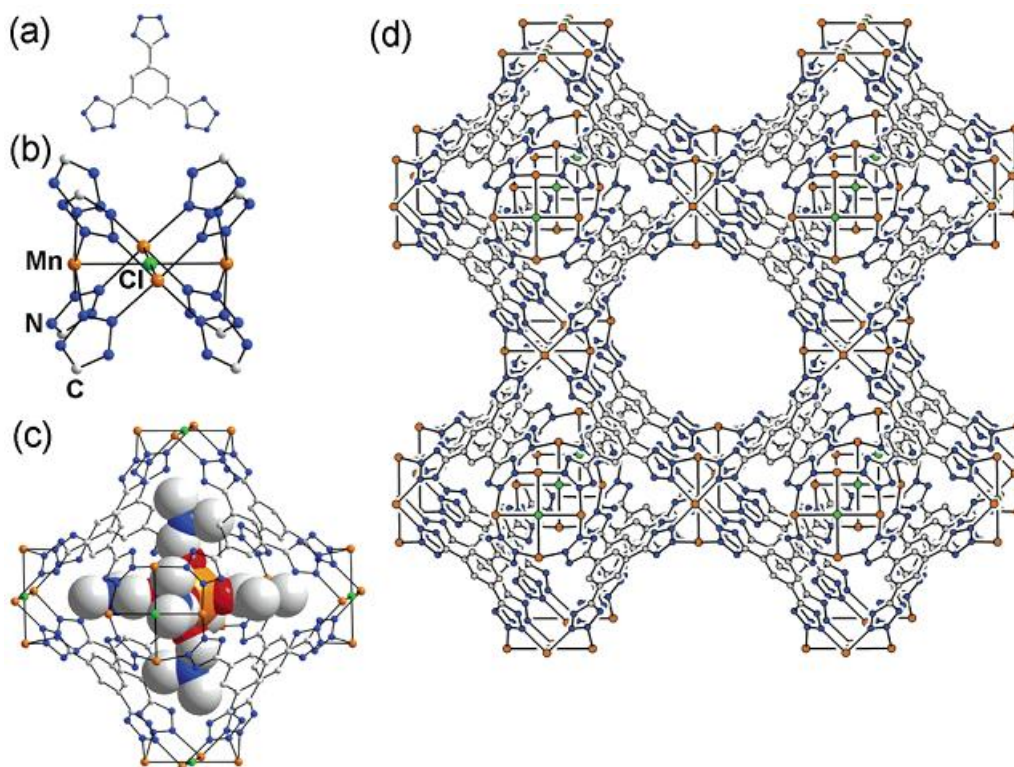


**Figure 35.** Diagram showing a) the 1,3,5-benzenetristetrazolate linker, b) the coordination environment around the metal centres in  $\{\text{Mn}_3[(\text{Mn}_4\text{Cl}_3)(\text{BTT})_8(\text{CH}_3\text{OH})_{10}]_2\}_n$ , c) the truncated octahedral unit (ball and stick) containing  $[\text{Mn}(\text{DMF})_6]^{2+}$  units (space-filling) and d) the extended structure of the MOF. Carbon, nitrogen, oxygen, manganese and chlorine atoms are coloured grey, blue, red, brown and green respectively. Reproduced from ref. 55.

Heating the structure to 150 °C under dynamic vacuum for 2 h gives the partially desolvated species  $\{[\text{Mn}(\text{DMF})_6]_3[(\text{Mn}_4\text{Cl}_3)(\text{BTT})_8(\text{DMF})_{12}]_2\}_n$ , which exhibits coordinatively unsaturated framework  $\text{Mn}^{2+}$  atoms due to the removal of the apically coordinated water molecules. Gas uptake studies performed on this partially desolvated species allow the BET isotherm to be calculated, giving an internal surface area of  $1100 \text{ m}^2 \text{ g}^{-1}$ , with an excess hydrogen uptake of 1.7 wt% at 77 K and 1.2 bar, with no hysteresis observed on desorption. Due to the relatively low internal surface area of this MOF, the high uptake of molecular hydrogen at low pressure is attributed to the strongly  $\text{H}_2$  binding  $\text{Mn}^{2+}$  sites. At pressures up to 50 bar the MOF has a saturation hydrogen uptake of only 3.9 %, demonstrating that at high pressures the major factor governing hydrogen uptake is the surface area of the pores rather than the affinity of particular binding sites to molecular hydrogen.

Solvent exchange performed on the as-synthesised structure using methanol, followed by the removal of this methanol by heating to 150 °C under dynamic vacuum for 48 h gives a second partially desolvated structure,  $\{\text{Mn}_3[(\text{Mn}_4\text{Cl}_3)(\text{BTT})_8(\text{CH}_3\text{OH})_{10}]_2\}_n$  in which the previously DMF coordinated extra-framework  $\text{Mn}^{2+}$  atoms are coordinated to the N1 and N4 nitrogen atoms of the tetrazolate moieties, figure 36. Single crystal diffraction studies performed on this evacuated species show the coordination of methanol to only 83 % of the framework  $\text{Mn}^{2+}$  atoms, giving evidence that this species contains both framework and extra-framework coordinatively unsaturated metals centres.

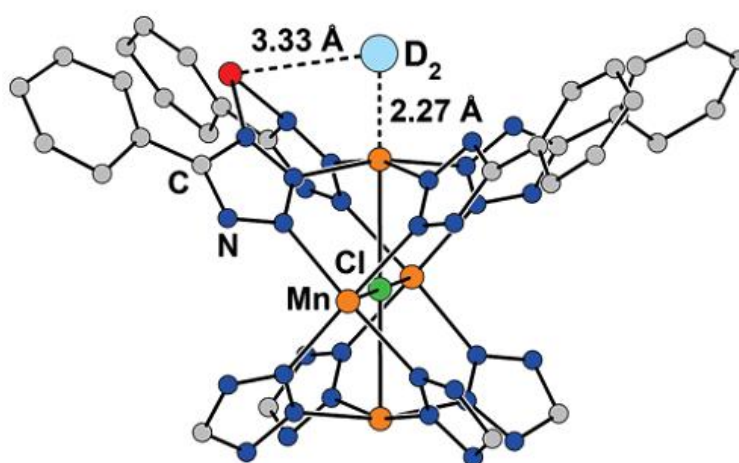


**Figure 36.** Diagram of the coordination environment around metals centres in  $\text{Mn}_3[(\text{Mn}_4\text{Cl}_3)(\text{BTT})_8(\text{CH}_3\text{OH})_{10}]_2$  showing the strongest binding site for guest  $\text{D}_2$  molecules as a light blue circle. The extra framework  $\text{Mn}^{2+}$  ion is coloured red, with framework  $\text{Mn}^{2+}$  ions coloured orange. Carbon and nitrogen atoms are coloured grey and blue respectively. Reproduced from ref. 55.

Gas uptake studies performed on this species allow a BET surface area of  $2100 \text{ m}^2 \text{ g}^{-1}$  to be calculated, demonstrating that the removal of the coordinated DMF molecules from the extra framework  $\text{Mn}^{2+}$  leads to an almost two-fold increase in the available surface area. Excess molecular hydrogen uptake is recorded as 2.2 wt% at 77 K and 1.2 bar, with the increase in uptake compared to the non-solvent exchanged structure being attributed to the greater number of available coordinatively unsaturated  $\text{Mn}^{2+}$  binding sites. Neutron powder diffraction data collected on this species at low loadings of  $\text{D}_2$  allow a Rietveld profile analysis to be conducted, revealing that the strongest binding site in this structure is  $2.27 \text{ \AA}$  from the framework  $\text{Mn}^{2+}$  atom,

figure 36. The proximity of this site to the extra-framework  $\text{Mn}^{2+}$  confirms the assertion that the increase in  $\text{H}_2$  uptake at low pressure for this species is due to the increased quantity of unsaturated metal centres, and leads to the conclusion that some cooperative effect exists between these two coordinatively unsaturated metal centres. At pressures up to 90 bar this species has a saturation hydrogen uptake of only 6.9 wt%, again demonstrating that as the pressure of molecular hydrogen increases the selectivity of binding sites becomes secondary to the internal surface area.

*Ab initio* calculations have shown that the uptake of molecular hydrogen in MOFs can also be dramatically increased through the doping of the frameworks with lithium. Grand canonical ensemble Monte Carlo (GCMC) simulations performed on lithium doped isorecticular MOFs composed of the organic linkers at figure 37, bound to the  $\text{Zn}_4\text{O}(\text{O}_2\text{CR})_6$ , or basic zinc acetate, SBU have been studied by Goddard and Han, and reveal an increased affinity to molecular hydrogen over the parent structures.<sup>56</sup>

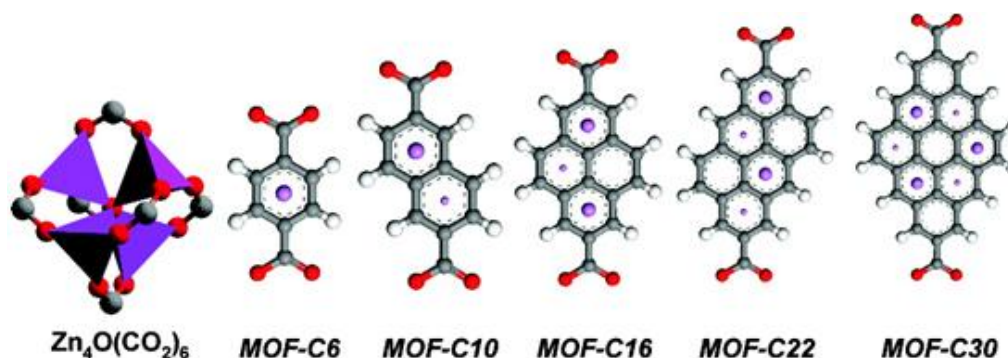


**Figure 37.** Diagram of the basic zinc acetate SBU, and the organic linkers used for simulation. The purple spheres represent the location of lithium ions with large and small spheres indicating the location in front or behind the plane of the linker respectively. Reproduced from ref. 56.

The validity of the GCMC model is confirmed by the simulations performed on MOF-C6 and MOF-C10 (previously published as IRMOF-1 and IRMOF-8)<sup>18</sup> with hydrogen uptakes of 1.28 wt% and 1.62 wt% respectively at 77 K and 1 bar comparing well with the experimentally derived results of 1.32 wt% and 1.50 wt%. Simulated and experimental results at 300 K and 60 bar for MOF-C6 also compare favourably with figures of 0.35 wt% (simulated) and 0.45 wt% (experimental), and

for MOF-C10 at 300 K and 30 bar of 0.3 wt% (simulated) and 0.4 wt% (experimental). The graph in figure 38 shows the simulated excess hydrogen uptakes for the un-doped and doped MOFs at 300 K and pressures up to 100 bar, and whilst all of the lithium doped structures show dramatically increased uptakes the most striking result is that of Li-MOF-C30, which at 50 bar has an uptake of 4.56 wt%, an order of magnitude higher than that of the parent structure of 0.56 wt% under the same conditions. Similar findings are reported by Blomqvist *et al.* using lithium doped IRMOF-1, with predicted binding energies of 12 kJ mol<sup>-1</sup> compared to 5 kJ mol<sup>-1</sup> for pure IRMOF-1, giving a potential uptake of 2.0 wt% at 300 K and 1 bar.<sup>57</sup>

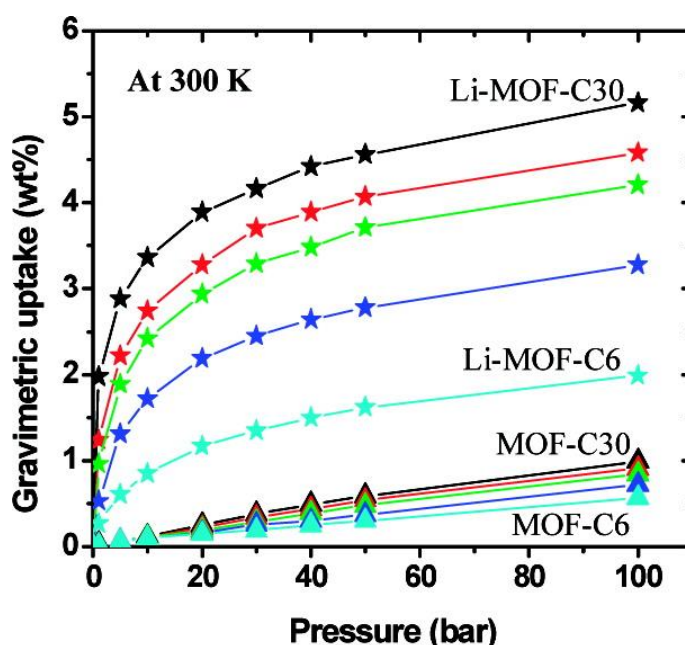


**Figure 38.** Graph of the simulated gravimetric H<sub>2</sub> uptakes for a series of MOFs and their lithium doped counterparts. Parent structures are represented by triangles, with the doped counterparts identified by stars of the same colour. Reproduced from ref. 56.

Simulations of the enhanced hydrogen uptake of lithium doped structures compared to the pure parent structures are borne out by the research conducted by Mulfort and Hupp.<sup>58</sup> Post-synthetic modification of the previously reported MOF [Zn<sub>2</sub>(NDC)<sub>2</sub>(dpNI)]<sub>n</sub><sup>59</sup> via the *in situ* reduction of the neutral pillaring linker by lithium metal gave the structure [Zn<sub>2</sub>(NDC)<sub>2</sub>(dpNILi<sup>+</sup>)]<sub>n</sub>. Excess hydrogen uptakes recorded for this and the parent framework at 77 K and 1 bar of 1.63 wt% and 0.93

wt% respectively, while modest in comparison to many other MOFs, demonstrate an almost two-fold increase in hydrogen uptake for the lithiated material.

### 1.3. Carbon dioxide sequestration in MOFs

The goal of an energy economy based on clean and renewable fuels is still far from achievable at our current technological level, and though advances in energy production through solar, wind and other highly renewable, clean sources continue to be made, our reliance on the burning of fossil fuels for the production of electricity and for industrial manufacturing is likely to continue and increase in line with the rapidly increasing global population for the foreseeable future. The environmental effects of our current energy economy are well known, with the vast quantities of carbon dioxide produced by coal-fired power stations and other fossil fuel dependant industries being identified as the major component of anthropogenic greenhouse gases. It follows then that some means of minimising the release of carbon dioxide from these processes into the environment must be employed. Three such techniques are currently being developed, pre-combustion CO<sub>2</sub> capture, oxyfuel combustion and post-combustion CO<sub>2</sub> capture, figure 39.

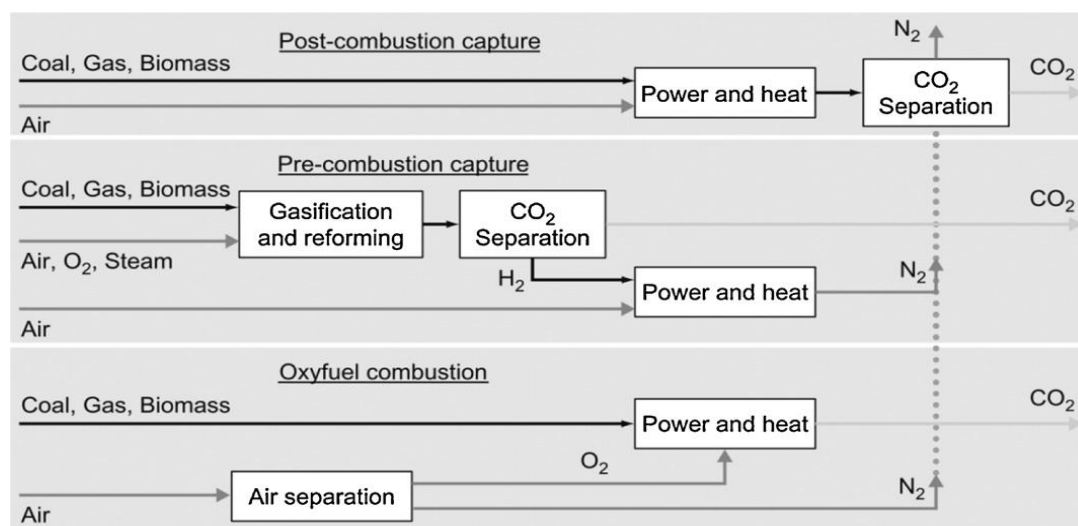


**Figure 39.** Schematic of the three options for CO<sub>2</sub> capture from power generation plants. Reproduced from ref. 60.

Pre-combustion CO<sub>2</sub> capture involves the gasification of existing fossil fuels through their reaction with air or oxygen to produce a mixture of H<sub>2</sub> and CO known as syngas. Separation of the H<sub>2</sub> is followed by the catalysed reaction of CO with steam

giving more H<sub>2</sub> and CO<sub>2</sub> which must undergo further separation, the resulting pure H<sub>2</sub> gas is then used as fuel. Oxyfuel combustion depends on the complete combustion of fossil fuel through the introduction of pure oxygen, giving only CO<sub>2</sub> as a waste product which can be directly sequestered. Both of these techniques have high associated costs due to the requirement of cryogenic gas separation systems, and the construction of new power generation facilities. Separation of CO<sub>2</sub> from the post-combustion flue gases from existing power plants is a far cheaper option, requiring only the retrofitting of these facilities with gas separation systems, though the requirement for advancements in this field is apparent and is common to all three of these processes. Currently, the most mature process for industrial CO<sub>2</sub> separation is scrubbing using aqueous alkanolamine solutions,<sup>61</sup> however due to the high temperatures required for the recycling and regeneration of the alkanolamines and the associated cost, this technology is still far from meeting the US DoE target of 90 % CO<sub>2</sub> capture with less than a 35 % increase in the cost of power generation.<sup>62</sup> All technologies based on chemisorptive processes suffer from similar issues, with the parasitic power requirement for their regeneration leading to a prohibitive increase in the cost of power generation. In contrast to this, technologies based on physisorption such as porous carbons, zeolites and MOFs are far more efficient, with the lack of chemical bonds between the adsorbant and adsorbate giving low regeneration costs. Though the poor selectivity of porous carbons to CO<sub>2</sub> over N<sub>2</sub> and the low CO<sub>2</sub> loadings demonstrated by zeolites prevent their application in an industrial setting, MOFs have already demonstrated record CO<sub>2</sub> uptakes, and have been shown to be highly selective to particular target molecules.

### 1.3.1. CO<sub>2</sub> loading capacity in MOFs

As with hydrogen storage the limiting factor for the total gas uptake for porous materials at high pressures is the internal surface area. At 50 bar and 298 K, the previously described MOF-177 has a gravimetric uptake of 60.8 wt% with a volumetric uptake of 320 cm<sup>3</sup>(STP)/cm<sup>3</sup>, a density nine times higher than that of the same quantity of CO<sub>2</sub> stored under the same conditions in the absence of the MOF. Performances exceeding this have been reported for materials with higher surface areas with the highest recorded uptakes thus far being reported by Furukawa *et al.* for MOF-200 and MOF-210.<sup>63</sup> The first of these examples is prepared by the solvothermal reaction of 4,4',4''-(benzene-1,3,5-triyl-tris(benzene-4,1-

diyl))tribenzoic acid ( $H_3BBC$ ) with zinc nitrate giving a structure of the formula  $[Zn_4O(BBC)_2(H_2O)_3]_n$ , which is isoreticular to MOF-177, figure 40. Langmuir and BET surface areas for this material are incredibly high at  $10400\text{ m}^2\text{ g}^{-1}$  and  $4530\text{ m}^2\text{ g}^{-1}$  respectively, with  $CO_2$  uptake on a gravimetric basis of 73.9 wt% at 50 bar and 298 K.

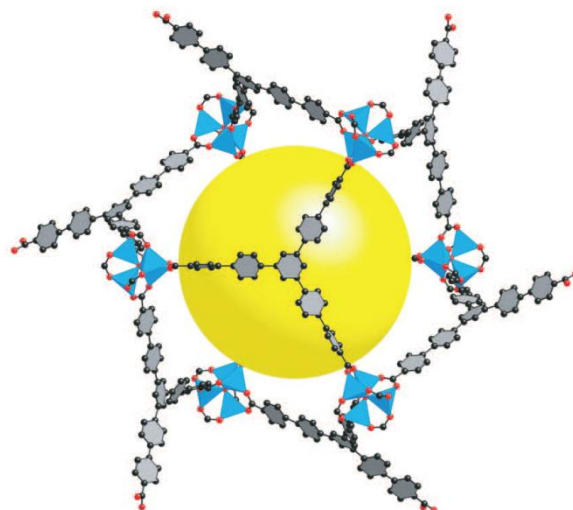


**Figure 40.** Diagram of a section of MOF-200. The yellow sphere represents the void space encapsulated by the lattice. Carbon, and oxygen atoms are coloured black and red respectively, with phenyl rings filled in grey. Zinc atoms are represented by blue tetrahedra. Reproduced from ref. 63.

MOF-210 is a mixed linker framework derived from the solvothermal reaction of 4,4',4''-(benzene-1,3,5-triyl-tris(ethyne-2,1-diyl))tribenzoic acid ( $H_3BTE$ ) and biphenyl-4,4'-dicarboxylic acid ( $H_2BPDC$ ) with zinc nitrate. The resulting structure bearing the formula  $[Zn_4O(BTE)_{4/3}(BPDC)]_n$  is formed by the stacking of cages of two distinct morphologies, figure 41. This structure has Langmuir and BET surface areas of  $10400\text{ m}^2\text{ g}^{-1}$  and  $6240\text{ m}^2\text{ g}^{-1}$ , exceeding those of MOF-200, with a  $CO_2$  uptake of 74.2 wt% at 50 bar and 298 K.

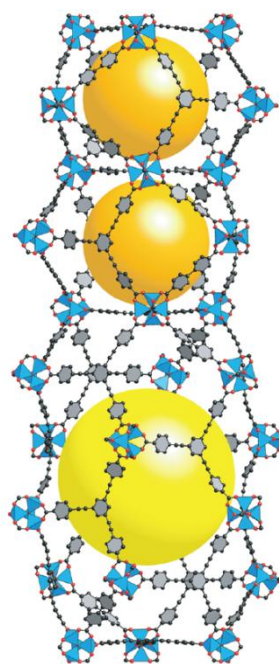


**Figure 41.** Diagram of a section of MOF-210. The yellow spheres represent the void spaces defined by the cages. Carbon, and oxygen atoms are coloured black and red respectively, with phenyl rings filled in grey. Zinc atoms are represented by blue tetrahedra. Reproduced from ref. 63.

These incredible CO<sub>2</sub> uptakes at pressures up to 50 bar make high surface area MOFs of this type the ideal candidates for applications in CO<sub>2</sub> transport and short term storage, however the pressure range at which flue gases are expelled is typically around 1 bar, a region in which the uptakes exhibited by these structures are negligible. Materials designed for the capture of CO<sub>2</sub> from flue gases must therefore contain features which these high surface area materials do not, namely high affinity binding sites which increase the adsorption enthalpy of CO<sub>2</sub>. Tailoring of the pore environment to include such sites can be achieved in a number of ways and mirrors findings for the optimisation of materials for hydrogen uptake. The first method is through the use of organic linkers bearing non-coordinating heteroatoms, specifically those which bear nitrogen based functionalities such as the azo and amine moieties. Two such materials are [Zn<sub>2</sub>(abtc)(DMF)<sub>2</sub>]<sub>n</sub> and [Cu<sub>2</sub>(abtc)(H<sub>2</sub>O)<sub>2</sub>]<sub>n</sub> (referred to as SNU-4 and SNU-5' respectively).<sup>64</sup> Prepared *via* the solvothermal reaction of the organic linker 1,1'-azobenzene-3,3',5,5'-tetracarboxylic acid with the respective metal nitrate hydrate these MOFs exhibit isomorphous 3D structures formed by the linking of organic linker units by paddlewheel SBUs at each of the carboxylate

functions, with DMF (SNU-4) and water (SNU-5') molecules inhabiting the apical coordination sites, figure 42. The as-synthesised SNU-4 bears two large cavities per unit cell of 9.1 Å and 3.0 Å diameter which contain 4 water and 10 DMF molecules per formula unit as guests, with similarly situated cavities of 10.2 Å diameter in SNU-5' inhabited by 10 DMF and 6 1,4-dioxane guests.

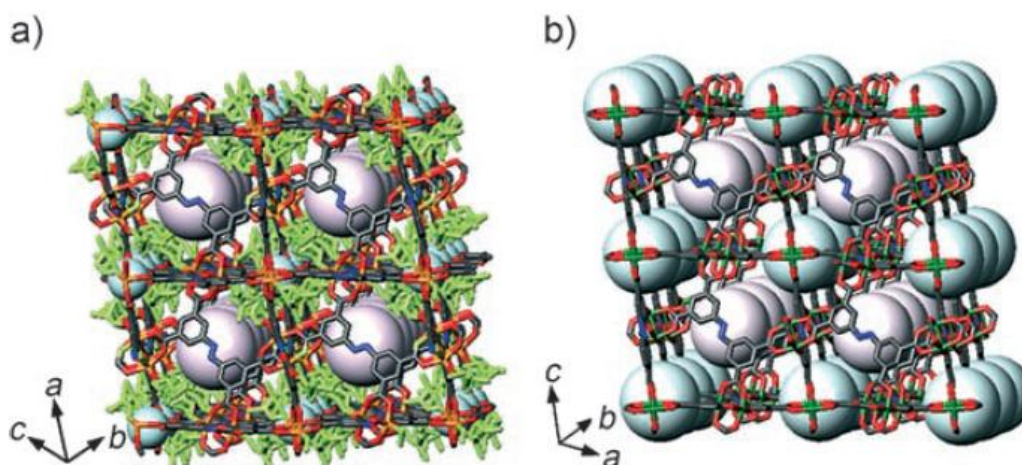


**Figure 42.** Diagrams of a) SNU-4 with coordinated DMF molecules coloured green and b) SNU-5' with coordinated water molecules omitted for clarity. Light blue and grey spheres represent the cavities present in each structure. Carbon, nitrogen, oxygen, zinc and copper atoms are coloured dark grey, blue, red, orange and green respectively. Hydrogen atoms are omitted. Reproduced from ref. 64.

Despite the relatively low Langmuir surface areas reported for these materials of  $1460 \text{ m}^2 \text{ g}^{-1}$  (SNU-4) and  $1260 \text{ m}^2 \text{ g}^{-1}$  (SNU-5'), the removal of guest solvent molecules and subsequent testing for  $\text{CO}_2$  adsorption reveals uptakes of 20.6 wt% for SNU-4 and 19.2% for SNU-5' at 273 K and 1 bar pressure, some of the highest low pressure uptakes reported thus far. Similarly high uptakes at low pressure are reported for CAU-1, a MOF exhibiting amine decorated pores due to the use of the  $\text{H}_2\text{BDCNH}_2$  linker.<sup>65</sup> In this example, the reaction of  $\text{AlCl}_3 \cdot 6\text{H}_2\text{O}$  with the organic linker in methanol gives a porous 3D structure of the formula  $[\text{Al}_4(\text{OH})_2(\text{OCH}_3)_4(\text{BDCNH}_2)_3]_n$ . Once again, a relatively low internal surface area ( $1268 \text{ m}^2 \text{ g}^{-1}$  BET) and pore size ( $3.2 \times 3.3 \times 5.4 \text{ \AA}$ ) belies an uptake of 24.1 wt% (273 K, 1 bar), which is attributed to the inclusion of the Lewis basic amino groups. The enhancement of  $\text{CO}_2$  uptake for MOFs bearing aromatic amine functionalities as compared to their non-functionalised analogues has been reported for many other

examples<sup>66</sup> and may be attributed to the increased acid-base interaction of the functionality with CO<sub>2</sub> or to enhanced electrostatic interactions. Similar enhancements are reported for structures bearing the 1, 2, 3-triazole moiety.<sup>67</sup>

The second method for pore optimisation is the inclusion of coordinatively unsaturated metal centres, with the structure  $\{[\text{Dy}(\text{BTC})(\text{H}_2\text{O})].\text{DMF}\}_n$  acting as an ideal example of the high uptakes achievable through the use of this technique.<sup>68</sup> Prepared by the reaction of H<sub>3</sub>BTC with dysprosium nitrate hydrate in the presence of dibutylamine, this structure is composed of 1D chains of seven coordinate metal ions located along the [001] axis bound to three bridging carboxylate moieties from three independent BTC units. The organic linkers extend in the [100] and [010] directions giving an extended structure bearing 1D circular channels of approximately 7 Å diameter observed in the [001] direction, figure 43.

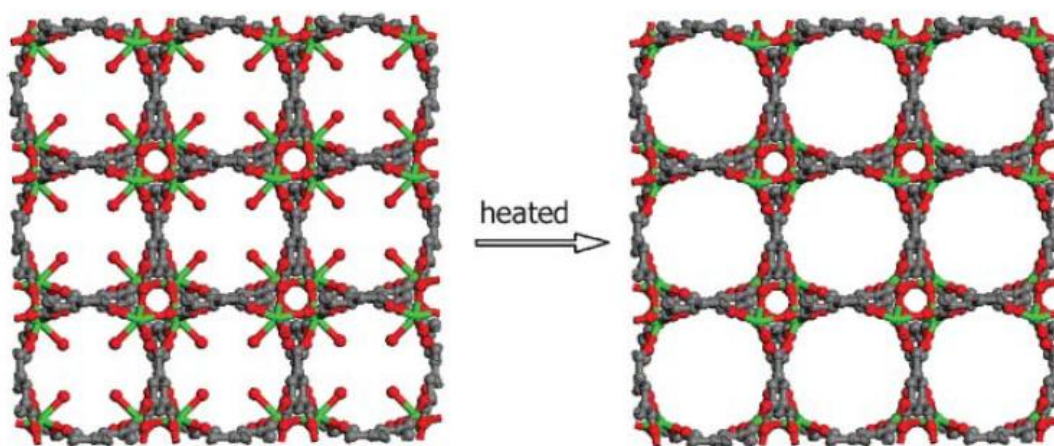


**Figure 43.** Diagram of the structure  $\{[\text{Dy}(\text{BTC})(\text{H}_2\text{O})].\text{DMF}\}_n$  as viewed along the [001] direction. Coordinated water molecules are shown extending in to the pores in the preheated structure. Carbon, oxygen and dysprosium atoms are coloured grey red and green respectively, hydrogen atoms are excluded. Reproduced from ref. 68.

Removal of guest DMF molecules and the coordinated water molecules by heating to 300 °C gives the desolvated framework, bearing available coordinatively unsaturated metal centres lining the pore walls. Adsorption isotherms recorded for N<sub>2</sub> and CO<sub>2</sub> allow a BET surface area 655 m<sup>2</sup> g<sup>-1</sup> to be calculated, and reveal a CO<sub>2</sub> uptake of 27.2 wt% at 273 K and 1 bar.

Another example of coordinative unsaturation in low pressure high uptake MOFs is  $[\text{Mg}_2(\text{dobdc})]_n$  (also referred to as Mg-MOF-74).<sup>69</sup> Prepared by the solvothermal reaction of 2,5-dihydroxybenzene-1, 4-dicarboxylic acid ( $\text{H}_2\text{dobdc}$ ) with magnesium nitrate, this material is part of a series of isostructural MOFs formed by the reaction of the linker with variety of metal nitrates.<sup>70</sup> The MOF is comprised of 1D chains of  $\text{Mg}^{2+}$  ions linked through the bridging coordination of the carboxylate groups of the linker to two metal nodes, with one of the carboxylate oxygens and the deprotonated phenyl oxygen chelating to a third metal centre, with coordinated water molecules giving octahedral geometry. The organic linkers extend in three directions, with neighbouring linkers related to each other by a  $120^\circ$  rotation about the axis of the chains of magnesium ions. The resulting extended 3D framework exhibits a honeycomb structure, with large hexagonal pores of around 12 Å diameter, filled with guest water molecules, extending along the [001] direction, figure 44.

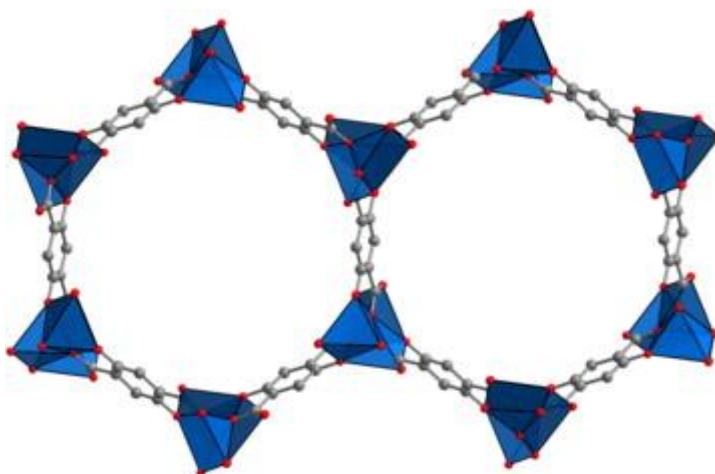


**Figure 44.** The structure of  $[\text{Mg}_2(\text{dobdc})]_n$  as viewed along the [001] direction. Carbon and oxygen atoms are coloured grey and red respectively, magnesium ions are represented by blue tetrahedra. Hydrogen atoms are excluded. Reproduced from ref. 71.

Removal of the guest and coordinated water molecules gives a material with Langmuir and BET surface areas of 1733 and 1174  $\text{m}^2 \text{g}^{-1}$  respectively, with coordinatively unsaturated metal binding sites lining the interior of the pores. The  $\text{CO}_2$  uptake of this material is reported to be 20.6 wt% at 303 K at pressures as low as 0.15 bar,<sup>72</sup> with only a small increase in uptake recorded at 298 K and 1 bar of

27.5 wt%<sup>72</sup> suggesting that these metal binding sites quickly become saturated, which may limit the overall uptake performance of the material.

The use of these two techniques in tandem, as observed in the MOF SNU-5 leads to the highest CO<sub>2</sub> uptake of any material thus far reported at pressures up to 1 bar. This material is isostructural to the previously described SNU-5', however the use of elevated temperatures in the preparation of the material for gas uptake testing gives a structure bearing the formula [Cu<sub>2</sub>(abtc)]<sub>n</sub> in which the removal of apically coordinated water molecules gives coordinative unsaturation and a CO<sub>2</sub> uptake of 38.5 wt% with a Langmuir surface area of only 2850 m<sup>2</sup> g<sup>-1</sup>.<sup>65</sup>

### 1.3.2. Target gas selectivity

The requirements of an adsorbent for the separation of CO<sub>2</sub> from post-combustion flue gases are not limited to high uptakes at low pressures. Typically the composition of waste gases is a mixture of nitrogen, carbon dioxide and water vapour in large volumes with trace quantities of other pollutants, table 1. In order for an adsorbent to meet the criteria set out by the US DoE, it must therefore be water stable and show high selectivity to CO<sub>2</sub> over N<sub>2</sub>.

**Table 1.** Typical post-combustion flue gas composition for a coal fired power plant.<sup>73</sup>

Molecule	Concentration(by volume)
N <sub>2</sub>	73 - 77 %
CO <sub>2</sub>	15 - 16 %
H <sub>2</sub> O	5 - 7 %
O <sub>2</sub>	3 - 4 %
SO <sub>2</sub>	800 ppm
SO <sub>3</sub>	10 ppm
NO <sub>x</sub>	500 ppm
HCl	100 ppm
CO	20 ppm
Hydrocarbons	10 ppm
Hg	1 ppm

Separation based purely on size exclusion is challenging due to the relatively small differences in kinetic diameters between CO<sub>2</sub> (3.30 Å) and N<sub>2</sub> (3.64 Å), though previously described examples have shown that this level of control of pore size is possible. A drawback to separations based on this kinetic property of gases however, is the requirement for the adsorbent to have very small pores, which may restrict the diffusion of gases through the material. The ability to tune the chemical environment of the pores through ligand design offers a second option, allowing the separation of molecules based thermodynamic properties such as polarisability and quadrupolar moment. Once again, this pore optimisation involves the inclusion of nitrogen moieties and coordinatively saturated metals centres, with the highest selectivities so far reported achieved by HKUST-1,<sup>74</sup> mmen-Cu-BTtri<sup>75</sup> and bio-MOF-11.<sup>76</sup> With a Henry's law selectivity of 165 for CO<sub>2</sub> from a mixture of N<sub>2</sub> and CO<sub>2</sub> at 298 K and a pressure relevant to post-combustion, mmen-Cu-BTtri is by far the highest performing of these materials. Prepared by the post-synthetic modification of H<sub>3</sub>[(Cu<sub>4</sub>Cl)<sub>3</sub>(BTtri)<sub>8</sub>(DMF)<sub>12</sub>]<sup>77</sup> with *N,N'*-dimethylethylenediamine (mmen) by coordination of the secondary amine to framework Cu<sup>2+</sup> ions the MOF exhibits pores lined with Lewis basic amine functions, figure 45.

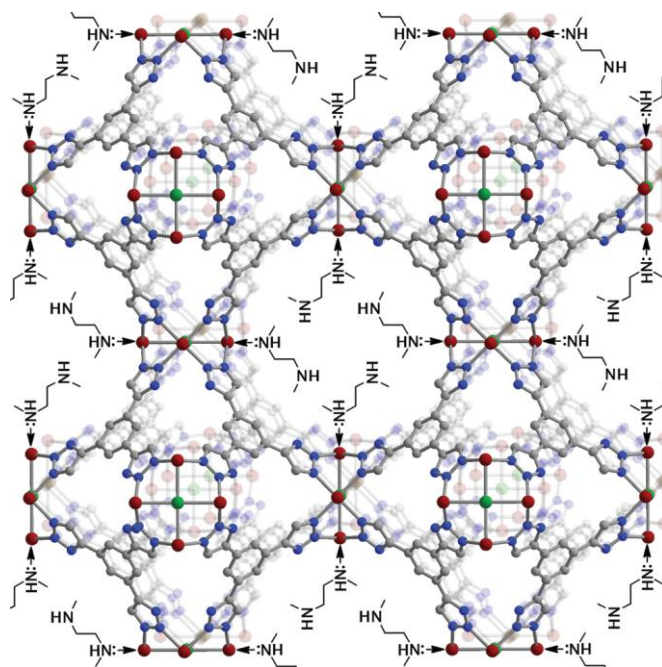


**Figure 45.** Diagram showing the structure of mmen-Cu-BTtri. Carbon, nitrogen chlorine and copper atoms are coloured grey, blue red and green respectively. Hydrogen atoms are omitted. Reproduced from ref. 75.

Bearing coordinatively unsaturated metal centres, the previously described HKUST-1 shows Henry's law selectivity of 101 at 293 K and the same pressure conditions as the previous example, while bio-MOF-11, formed by the solvothermal reaction of cobalt acetate with adenine has a selectivity of 65 at 293 K due to the high density of Lewis basic amine and pyrimidine functions lining the pore walls, figure 46.

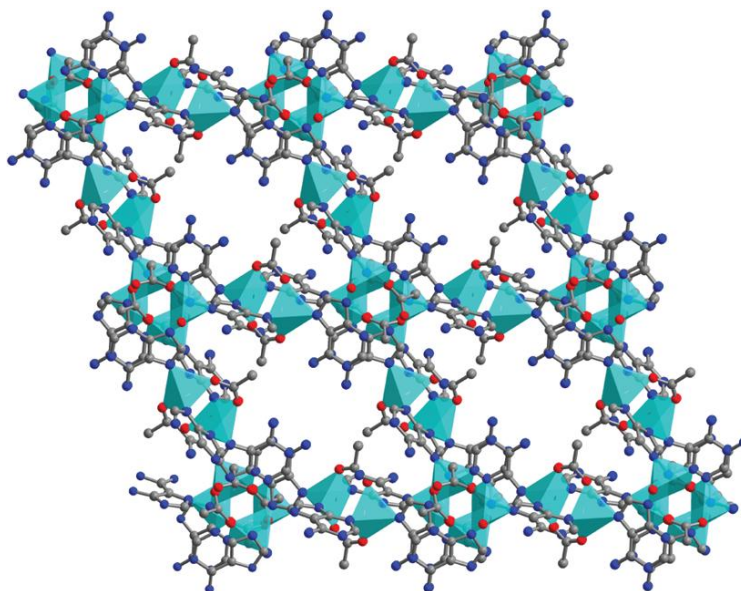


**Figure 46.** A section of the bio-MOF-11 structure showing the high density of nitrogen moieties lining the pores. Carbon, nitrogen and oxygen atoms are coloured grey, blue and red respectively, cobalt ions are represented by turquoise tetrahedra. Hydrogen atoms are omitted. Reproduced from ref. 76.

#### 1.4. Aims of the study

The first aim of this study is to synthesise and structurally characterise a series of new MOFs using the pillar/layer approach and to investigate the potential of these structures as gas storage media.

Previous research using the potential anionic linker 5-aminoisophthalic acid in conjunction with neutral bipyridyl linkers and a variety of late transition metals has shown that this approach can predictably give porous structures which share network topologies, however their gas uptake behaviours have not been probed. It is our belief that structures of this type, bearing large intersecting pores and polar functionalities, will exhibit interesting gas uptake properties. The pillar/layer technique also allows the investigation of pore tuning on the gas adsorption

behaviours of these structures, through the synthesis of isostructural series of MOFs bearing variation at the neutral pillaring linker. The use of 4, 4'-bipyridyl (4, 4'-bipy), 1, 2-Di(4-pyridyl)ethylene (DPE) and 4, 4'-azopyridine (4, 4'-azopy) gives the opportunity to achieve this variation, and allows the investigation of the effect of pore size and polarity on the gas uptake performance of the MOFs.

The use of flexible anionic linkers in MOF synthesis has also been reported, however little research has been conducted on the gas adsorption properties on such structures. It is our belief that linker flexibility will allow for dynamic framework changes to occur on guest adsorption, and that the dynamic nature of these structures will lead to interesting gas uptake behaviours. We have therefore conducted research employing the pillar/layer approach in the synthesis of MOFs comprising the flexible potential linker 4-carboxy-phenylene-methyleneamino-4-benzoic acid in conjunction with rigid neutral pillaring linkers.

The second aim of this study is to synthesise and structurally characterise MOFs using lower-rim acid functionalised calix[4]arene ligands and to investigate their gas uptake properties. The participation of calix[4]arene molecules in host-guest chemistry is well known, with the apolar bowl of the macrocycle able to accommodate various molecules, giving the potential to synthesise MOFs which bear hierarchical porosity. Previous research using upper-rim appended calix[4]arene acids has shown that these molecules can be successfully employed in the construction of multidimensional networks, however access to the calix[4]arene bowl is limited by the presence of sterically bulky coordinating groups. The use of the lower-rim appended analogues in MOF synthesis has not yet been reported and it is our hope that structures based on this potential anionic linker will retain accessibility to the calix[4]arene bowl. We have therefore embarked on a programme of research using 25, 27-bis(methoxycarboxylic acid)-26, 28-dihydroxycalix[4]arene and 25, 27-bis(methoxycarboxylic acid)-26, 28-dihydroxy-4-*tert*butylcalix[4]arene in the construction of MOFs.

## 1.5. Thesis overview

This study focuses on the synthesis of novel metal-organic frameworks for gas storage and separation applications. Various new MOFs have been synthesised and structurally characterised and their gas adsorption behaviours investigated.

**Chapter 2** focuses on the synthesis of MOFs using 4-aminoisophthalic acid and the neutral pillaring linkers 4, 4'-bipy, DPE and 4, 4'-azopy in conjunction with the late transition metal cations zinc(II), cobalt(II), manganese(II) and cadmium(II), with the resulting materials tested for their low pressure carbon dioxide adsorption properties.

**Chapter 3** concerns the synthesis of MOFs with the potential for dynamic change on guest adsorption using the flexible potential linker 4-carboxy-phenylene-methyleneamino-4-benzoic acid in conjunction with rigid neutral pillaring linkers and a source of zinc(II). Again the resulting materials have been tested for their low pressure carbon dioxide uptake properties.

**Chapter 4** moves the focus from the synthesis of MOFs using the pillar/layer technique and concentrates on the use of the potential anionic linker 25, 27-bis(methoxycarboxylic acid)-26, 28-dihydroxycalix[4]arene in the synthesis of multidimensional structures with the potential for hierarchical porosity. The reaction of this molecule with sources of Li(I) and zinc(II) is reported with the resulting structures tested for their H<sub>2</sub>, N<sub>2</sub> and CO<sub>2</sub> adsorption properties.

**Chapter 5** is a continuation of the research presented in chapter 4, with the reaction of the related molecule 25, 27-bis(methoxycarboxylic acid)-26, 28-dihydroxy-4-*tert*butylcalix[4]arene with neutral pillaring linkers 4, 4'-bipy, DPE and 4, 4'-azopy and a source of zinc(II) giving a series of structures whose porosities have been examined using TGA.

**Chapter 6** is the experimental section, containing all synthetic procedures and characterisation data.

## 1.6. References

---

- 1 a) Y. Liu, W. Xuan, Y. Cui, *Adv. Mater.*, 2010, **22**, 4112. b) A. M. Shultz, O. K. Farha, J. T. Hupp, S. T. Nguyen, *J. Am. Chem. Soc.*, 2009, **131**, 4204. c) K. Schlichte, T. Kratzke, S. Kaskel, *Microporous Mesoporous Mater.*, 2004, **73**, 81. d) C. D. Wu, A. Hu, L. Zhang, W. Lin, *J. Am. Chem. Soc.*, 2005, **127**, 8940.
- 2 a) G. F. Qrey, M. Latroche, C. Serre, F. Millange, T. Loiseau, A. Percheron-Guégan, *Chem. Commun.*, 2003, **24**, 2976. b) J. L. C. Rowsell, A. R. Millward, K. S. Park, O. M. Yaghi, *J. Am. Chem. Soc.*, 2004, **126**, 5666.
- 3 a) P. Horcajada, C. Serre, M. Vallet-Regi, M. Sebban, F. Taulelle, G. Ferey, *Angew. Chem. Int. Ed.* 2006, **45**, 5974–5978. b) P. Horcajada, T. Chalati, C. Serre, B. Gillet, C. Sebrie, T. Baati, J. F. Eubank, D. Heurtaux, P. Clayette, C. Kreuz, J. S. Chang, Y. K. Hwang, V. Marsaud, P. N. Bories, L. Cynober, S. Gil, G. Ferey, P. Couvreur, R. Gref, *Nature Mat.* 2010, **9**, 172. c) M. O. Rodrigues, M. V. de Paula, K. A. Wanderley, I. B. Vasconcelos, S. Alves Jr., T. A. Soares, *Int. J. Quant. Chem.*, 2012, **112**, 3346. d) K. M. L. Taylor-Pashow, J. D. Rocca, R. C. Huxford, W. Lin, *Chem. Commun.*, 2010, **46**, 5832.
- 4 C. D. Chudasama, J. Sebastian, R. V. Jasra, *Ind. Eng. Chem. Res.*, 2005, **44**, 1780.
- 5 Y. Y. Li, F. Cunin, J. R. Link, T. Gao, R. E. Betts, S. H. Reiver, V. Chin, S. N. Bhatia, M. J. Sailor, *Science*, 2003, **299**, 2045.
- 6 H. Sohn, S. Letant, M. J. Sailor, W. C. Trogler, *J. Am. Chem. Soc.*, 2000, **122**, 5399.
- 7 a) Y. Zhao, L. Zhao, K. X. Yao, Y. Yang, Q. Zhang, Y. Han, *J. Mater. Chem.*, 2012, **22**, 19726. b) G. P. Hao, W. C. Li, D. Qian, G. H. Wang, W. P. Zhang, T. Zhang, A. Q. Wang, F. Schuth, H. J. Bongard, A. H. Lu, *J. Am. Chem. Soc.*, 2011, **133**, 11378. c) L. Wang and R. T. Yang, *J. Phys. Chem. C.*, 2012, **116**, 1099.
- 8 a) Z. J. Lin, D. S. Wragg, R. E. Morris, *Chem. Commun.*, 2006, **19**, 2021. b) P. Amo-Ochoa, G. Givaja, P. J. S. Miguel, O. Castillo and F. Zamora, *Inorg.*

- 
- Chem. Commun.*, 2007, **10**, 921. c) Z. Ni, R. I. Masel, *J. Am. Chem. Soc.*, 2006, **128**, 12394.
- 9 S. L. James, *Chem. Soc. Rev.*, 2003, **32**, 276.
- 10 B. F. Hoskins, R. Robson, *J. Am. Chem. Soc.*, 1990, **112**, 1546.
- 11 M. Fujita, J. Yazaki, K. Ogura, *J. Am. Chem. Soc.*, 1990, **112**, 5645.
- 12 J. Zhang, R. Liu, P. Feng, X. Bu, *Angew. Chem. Int. Ed.*, 2007, **46**, 8388.
- 13 S. Hasegawa, S. Horike, R. Matsuda, S. Furukawa, K. Mochizuki, Y. Kinoshita, S. Kitagawa, *J. Am. Chem. Soc.* 2007, **129**, 2607-2614.
- 14 H. Li, M. Eddaoudi, M. O'Keeffe, O. M. Yaghi, *Nature*, 1999, **402**, 276.
- 15 M. Eddaoudi, D. B. Moler, H. Li, B. Chen, T. M. Reineke, M. O'Keeffe, O. M. Yaghi, *Acc. Chem. Res.*, 2001, **34**, 319.
- 16 O. M. Yaghi, M. O'Keeffe, N. W. Ockwig, H. K. Chae, M. Eddaoudi, J. Kim, *Nature*, 2003, **423**, 705.
- 17 H. Li, M. Eddaoudi, T. L. Groy, *J. Am. Chem. Soc.*, 1998, **120**, 8571.
- 18 S. S. Y. Chui, S. M. F. Lo, J. P. H. Charmant, A. G. Orpen, I. D. Williams, *Science*, 1999, **283**, 1148.
- 19 a) R. Pech, J. Pickardt, *Acta Crystallogr. C.*, 1988, **44**, 992. b) S. S.-Y. Chui, I. D. Williams, *Acta Crystallogr. C.*, 1999, **55**, 194.
- 20 M. Eddaoudi, J. Kim, N. Rosi, D. Vodak, J. Wachter, M. O'Keeffe, O. M. Yaghi, *Science*, 2002, **295**, 469.
- 21 D. J. Tranchemontagne, J. L. Mendoza-Cortés, M. O'Keeffe, O. M. Yaghi, *Chem. Soc. Rev.*, 2009, **38**, 1257.
- 22 V. A. Russell, C. C. Evans, W. Li, M. D. Ward, *Science*, 1997, **276**, 575.
- 23 M. Kondo, T. Okubo, A. Asami, S. I. Noro, T. Yoshitomi, S. Kitagawa, T. Ishii, H. Matsuzaka, K. Seki, *Angew. Chem. Int. Ed.*, 1999, **38**, 140.
- 24 D. N. Dybtsev, H. Chun, K. Kim, *Angew. Chem. Int. Ed.*, 2004, **43**, 5033.
- 25 K. Seki, W. Mori, *J. Phys. Chem. B*, 2002, **106**, 1380.
- 26 O. Kozachuk, K. Khaletskaya, M. Halbherr, A. Bétard, M. Meilikhov, R. W. Seidel, B. Jee, A. Pöppel, R. A. Fischer. *Eur. J. Inorg. Chem.*, 2012, 1688.
- 27 B. Chen, C. Liang, J. Yang, D. S. Contreras, Y. L. Clancy, E. B. Lobkovsky, O. M. Yaghi, S. Dai, *Angew. Chem. Int. Ed.*, 2006, **45**, 1390.

- 
- 28 Y. Takashima, V. M. Martínez, S. Furukawa, M. Kondo, S. Shimomura, H. Uehara, M. Nakahama, K. Sugimoto, S. Kitagawa, *Nat. Commun.*, 2011, **2**, 168.
- 29 Z. Chang, D. S. Zhang, Q. Chen, R. F. Li, T. L. Hu, X. H. Bu, *Inorg. Chem.*, 2011, **50**, 7555.
- 30 Z. Wang, S. M. Cohen, *J. Am. Chem. Soc.*, 2007, **129**, 12368.
- 31 K. K. Tanabe, Z. Wang, S. M. Cohen, *J. Am. Chem. Soc.*, 2008, **130**, 8508.
- 32 Y.-S. Bae, O. K. Farha, J. T. Hupp, R. Q. Snurr, *J. Mater. Chem.*, 2009, **19**, 2131.
- 33 K. L. Mulfort, O. K. Farha, C. L. Stern, A. A. Sarjeant, J. T. Hupp, *J. Am. Chem. Soc.*, 2009, **131**, 3866.
- 34 K. K. Tanabe, S. M. Cohen, *Angew. Chem. Int. Ed.*, 2009, **48**, 7424.
- 35 K. K. Tanabe, S. M. Cohen, *Chem. Soc. Rev.*, 2011, **40**, 498.
- 36 B. Chen, S. Ma, F. Zapata, E. B. Lobkovsky, J. Yang, *Inorg. Chem.*, 2006, **45**, 5718.
- 37 E. Y. Choi, K. Park, C. M. Yang, H. Kim, J. H. Son, S. W. Lee, Y. H. Lee, D. Min, Y. U. Kwon, *Chem. Eur. J.*, 2004, **10**, 5535.
- 38 S. Ma, X. S. Wang, E. S. Manis, C. D. Collier, H. C. Zhou, *Inorg. Chem.*, 2007, **45** 3432.
- 39 C. Serre, F. Millange, C. Thouvenot, M. Nogues, G. Marsolier, D. Louër, G. Férey, *J. Am. Chem. Soc.*, 2002, **124**, 13519.
- 40 S. Kitagawa, R. Kitaura, S. I. Noro, *Angew. Chem. Int. Ed.*, 2004, **43**, 2334.
- 41 S. Kitagawa, M. Kondo, *Bull. Chem. Soc. Jpn.*, 1998, **71**, 1739.
- 42 US DOE Hydrogen Program 2000 Annual Review May 9-11, 2000, <http://www1.eere.energy.gov/hydrogenandfuelcells/docs/storageoverview.ppt>.
- 43 Targets for Onboard Hydrogen Storage Systems for Light-Duty Vehicles, US Department of Energy, Office of Energy Efficiency and Renewable Energy and The FreedomCAR and Fuel Partnership, 2009, [http://www1.eere.energy.gov/hydrogenandfuelcells/storage/pdfs/targets\\_onboard\\_hydro\\_storage\\_explanation.pdf](http://www1.eere.energy.gov/hydrogenandfuelcells/storage/pdfs/targets_onboard_hydro_storage_explanation.pdf)
- 44 S. I. Orimo, Y. Nakamori, J. R. Eliseo, A. Züttel, C. M. Jensen, *Chem. Rev.*, 2007, **107**, 4111.

- 
- 45 R. E. Morris, P. S. Wheatley, *Angew. Chem. Int. Ed.*, 2008, **47**, 4966.
- 46 R. J. Kuppler, D. J. Timmons, Q. R. Fang, J. R. Li, T. A. Makal, M. D. Young, D. Yuan, D. Zhou, W. Zhuang, H. C. Zhou, *Coord. Chem. Rev.*, 2009, **253**, 3042.
- 47 H. K. Chae, D. Y. Siberio-Pérez, J. Kim, Y. Go, M. Eddaoudi, A. J. Matzger, M. O'Keefe, O. M. Yaghi, *Nature*, 2004, **427**, 523.
- 48 A. G. Wong-Foy, A. J. Matzger, O. M. Yaghi, *J. Am. Chem. Soc.*, 2006, **128**, 3495.
- 49 Y. Li, R. T. Yang, *Langmuir*, 2007, **23**, 1293.
- 50 O. K. Farha, A. O. Yazaydin, I. Eryazici, C. D. Malliakas, B. G. Hauser, M. G. Kanatzidis, S. T. Nguyen, R. Q. Snurr, J. T. Hupp, *Nature Chemistry*, 2010, **2**, 944.
- 51 O. K. Farha, I. Eryazici, N. K. Cheong, B. G. Hauser, C. E. Wilmer, A. A. Sarjeant, R. Q. Snurr, S. T. Nguyen, A. O. Yazaydin, J. T. Hupp *J. Am. Chem. Soc.*, 2012, **134**, 15016.
- 52 Y. L. Liu, J. F. Eubank, A. J. Cairns, J. Eckert, V. C. Kravtsov, R. Luebke, M. Eddaoudi, *Angew. Chem. Int. Ed.*, 2007, **46**, 3278.
- 53 J. L. Belof, A. C. Stern, M. Eddaoudi, B. Space, *J. Am. Chem. Soc.*, 2007, **129**, 15202.
- 54 X. S. Wang, S. Ma, K. Rauch, J. M. Simmons, D. Yuan, X. Wang, T. Yildirim, W. C. Cole, J. J. López, A. de Meijere, H. C. Zhou, *Chem. Mater.*, 2008, **20**, 3145.
- 55 M. Dinca, A. Dailly, Y. Liu, C. M. Brown, D. A. Neumann, J. R. Long, *J. Am. Chem. Soc.*, 2006, **128**, 16876.
- 56 S. S. Han, W. A. Goddard, *J. Am. Chem. Soc.*, 2007, **129**, 8422.
- 57 A. Blomqvist, C. Moyses Araujo, P. Srepusharawoot, R. Ahuja, *Proc. Natl. Acad. Sci. U. S. A.*, 2007, **104**, 20173.
- 58 K.L. Mulfort, J. T. Hupp, *J. Am. Chem. Soc.*, 2007, **129**, 9604.
- 59 J. L. C. Rowsell, O. M. Yaghi, *J. Am. Chem. Soc.*, 2006, **128**, 1304.
- 60 J. R. Li, Y. Ma, M. C. McCarthy, J. Sculley, J. Yu, H. K. Jeong, P. B. Balbuena, H. C. Zhou, *Coord. Chem. Rev.*, 2011, **255**, 1791.
- 61 G. T. Rochelle, *Science*, 2009, **325**, 1652.

- 
- 62 US DOE/NETL's Carbon Capture R&D Program for Existing Coal-Fired Power Plants, DOE/NETL- 2009/1356.
- 63 H. Furukawa, N. Ko, Y. B. Go, N. Aratani, S. B. Choi, E. Choi, A. O. Yazaydin, R. Q. Snurr, M. O'Keefe, J. Kim, O. M. Yaghi, *Science*, 2010, **329**, 424.
- 64 Y. G. Lee, H. R. Moon, Y. E. Cheon, M. P. Suh, *Angew. Chem. Int. Ed.*, 2008, **47**, 7741.
- 65 X. Si, C. Jiao, F. Li, J. Zhang, S. Wang, S. Liu, Z. Li, L. Sun, F. Xu, Z. Gabelica, C. Schick, *Energy Environ. Sci.*, 2011, **4**, 4522.
- 66 a) B. Arstad, H. Fjellvåg, K. O. Kongshaug, O. Swang, R. Blom, *Adsorption*, 2008, **14**, 755. b) R. Vaidhyanathan; S. S. Iremonger; K. W. Dawson, G. K. H. Shimizu, *Chem. Commun.*, 2009, **35**, 5230. c) Y. E. Cheon, J. Park, M. P. Suh, *Chem. Commun.*, 2009, **35**, 5436. d) J. Moellmer, E. B. Celer, R. Luebke, A. J. Cairns, R. Staudt, M. Eddaoudi, M. Thommes, *Microporous Mesoporous Mater.*, 2010, **129**, 345.
- 67 W. Y. Gao, W. Yan, R. Cai, K. Williams, A. Salas, L. Wojtas, X. Shi, S. Ma, *Chem. Commun.*, 2012, **48**, 8898.
- 68 X. Guo, G. Zhu, Z. Li, F. Sun, Z. Yang, S. Qiu, *Chem. Commun.*, 2006, **30**, 3172.
- 69 P. D. C. Dietzel, R. Blom, H. Fjellvåg, *Eur. J. Inorg. Chem.*, 2008, 3624.
- 70 a) N. L. Rosi, J. Kim, M. Eddaoudi, B. Chen, M. O'Keefe, O. M. Yaghi, *J. Am. Chem. Soc.*, 2005, **127**, 1504. b) P. D. C. Dietzel, Y. Morita, R. Blom, H. Fjellvåg, *Angew. Chem. Int. Ed.*, 2005, **44**, 6354. c) P. D. C. Dietzel, R. E. Johnsen, R. Blom, H. Fjellvåg, *Chem. Eur. J.*, 2008, **14**, 2389. d) P. D. C. Dietzel, B. Panella, M. Hirscher, R. Blom, H. Fjellvåg, *Chem. Commun.*, 2006, **9**, 959.
- 71 Z. Bao; L. Yu, Q. Ren, X. Lu, S. Deng, *J. Colloid Interface Sci.*, 2011, **353**, 549.
- 72 J. A. Mason, K. Sumida, Z. R. Herm, R. Krishna, J. R. Long, *Energy Environ. Sci.*, 2011, **4**, 3030.
- 73 E. J. Granite, H. W. Pennline, *Ind. Eng. Chem. Res.* 2002, **41**, 5470.
- 74 P. Aprea, D. Caputo, N. Gargiulo, F. Iucolano, F. Pepe, *J. Chem. Eng. Data*, 2010, **55**, 3655.

- 
- 75 T. M. McDonald, D. M. D'Alessandro, R. Krishna, J. R. Long, *Chem. Sci.*, 2011, **2**, 2022.
- 76 J. An, S. J. Geib, N. L. Rosi, *J. Am. Chem. Soc.*, 2010, **132**, 38.
- 77 A. Demessence, D. M. D'Alessandro, M. L. Foo, J. R. Long, *J. Am. Chem. Soc.*, 2009, **131**, 8784.

## **Chapter 2**

### **Pillared metal-organic frameworks based on 5- aminoisophthalic acid**

## 2.1. Introduction

The construction of MOFs using more than one type of organic linker continues to receive a huge amount of attention due to the vast structural diversity offered by this technique.<sup>1</sup> The control of pore size achievable by the variation of a single component of a multi-linker framework exceeds that of single-linker systems, in which a small change in linker size has a cumulative effect. The potential for the generation of multi-functional frameworks is also increased through the ability to select linkers which bear differing and potentially useful functionalities. Three such combinations of linker are currently known, anionic-anionic,<sup>2</sup> neutral-neutral<sup>3</sup> and neutral-anionic,<sup>4</sup> though due to the ability to generate charge balanced networks without the inclusion of counter-ions, and the stability to guest removal exhibited by such structures, the prevalence of the anionic-anionic and neutral-anionic combinations in the literature is understandable, with applications ranging from gas storage<sup>5</sup> and separation<sup>6</sup> to catalysis.<sup>7</sup>

As discussed in the previous chapter, a multitude of neutral organic linkers are commonly observed in the literature, in conjunction with di- and tri-carboxylate anionic linkers, however of particular interest to this project is the use of linear dipyridyls in conjunction with benzene dicarboxylic acids. Mixed ligand systems employing benzene-1,4-dicarboxylic acid (H<sub>2</sub>BDC) with a variety of neutral organic linkers are one of the most extensively studied of the mixed ligand systems, with early research by Yaghi *et al.* revealing the stability of the square planar net resulting from the solvothermal reaction of H<sub>2</sub>BDC with zinc nitrate to the removal of axially coordinated water molecules.<sup>8</sup> Follow up research conducted by Seki and co-workers using the copper analogue of this 4,4 net in conjunction with 4,4'-bipyridyl revealed the intercalation of the neutral organic linker, with neighbouring sheets being linked *via* coordinate bonds between each of the nitrogen atoms of the neutral linker and the metal centres, at the axial coordination sites of the copper paddlewheel SBU, giving a cubic net.<sup>9</sup> This binding motif was also observed in the structure reported by Hupp *et al.*<sup>10</sup> using the zinc analogue, in conjunction with 4,4'-bipyridyl and *N,N*-di(4-pyridyl)-1,4,5,8-naphthalenetetracarboxydiimide. It is of note that all of these examples exhibit hysteresis on adsorption and desorption of guest molecules, indicating that reversible structural transformations occur during this process. This phenomenon has been attributed to the two-fold network interpenetration exhibited

by these structures, and the ability of these nets to move in relation to each other on guest adsorption.

The effect of functionalisation of the BDC linker has also been extensively researched. The solvothermal reaction of 2-hydroxybenzene-1,4-dicarboxylic acid with copper acetate in the presence of 4,4'-bipyridyl afforded an analogous cubic net bearing the formula  $[\text{Cu}_2(\text{BDC-OH})_2(4,4'\text{-bipy})]_n$ . (where BDC-OH = 2-hydroxybenzene-1,4-dicarboxylate).<sup>11</sup> This structure bears intersecting pores of  $4.1 \times 7.8 \text{ \AA}^2$  observed along the *b* axis and  $3.7 \times 5.1 \text{ \AA}^2$  along the *c* axis, which are lined with uncoordinated -OH moieties. Strong interactions observed between these functional groups and guest ethylene and carbon dioxide molecules give zero coverage adsorption enthalpies of  $39.5 \text{ kJ mol}^{-1}$  and  $40.6 \text{ kJ mol}^{-1}$ , respectively. The lack of such interactions with guest methane molecules gave a far lower adsorption enthalpy of  $13.6 \text{ kJ mol}^{-1}$ , and rise to Henry's law selectivities of 55.6 for ethylene/methane and 24.2 for carbon dioxide/methane at 296 K. These selectivities are among the highest reported to date, revealing the potential for target molecule specificity through the selection of appropriate linker functionality.

Similar selectivity has been reported by Fischer *et al.*<sup>12</sup> using alkoxy and bis(methoxyethoxy) functionalised BDC. The reactions of zinc nitrate hexahydrate with 4,4'-bipyridyl and 2,3-bis(methoxyethoxy)benzene-1,4-dicarboxylic acid in the first example and 2,5-dimethoxybenzene-1,4-dicarboxylic acid in the second afforded two cubic networks bearing the same network topology and structural formula of  $[\text{M}_2\text{L}_2\text{P}]_n$  (where M = metal, L = dicarboxylate linker and P = neutral pillaring linker) as in the previously described examples. Analogous reactions using  $\text{H}_2\text{BDC}$  bearing ethoxy, propoxy and butoxy and methoxyethoxy groups at the 2- and 5- positions and methoxyethoxy groups at the 2- and 6- positions however, afforded five MOFs bearing the same structural formula but exhibiting honeycomb-like structures, figure 47.

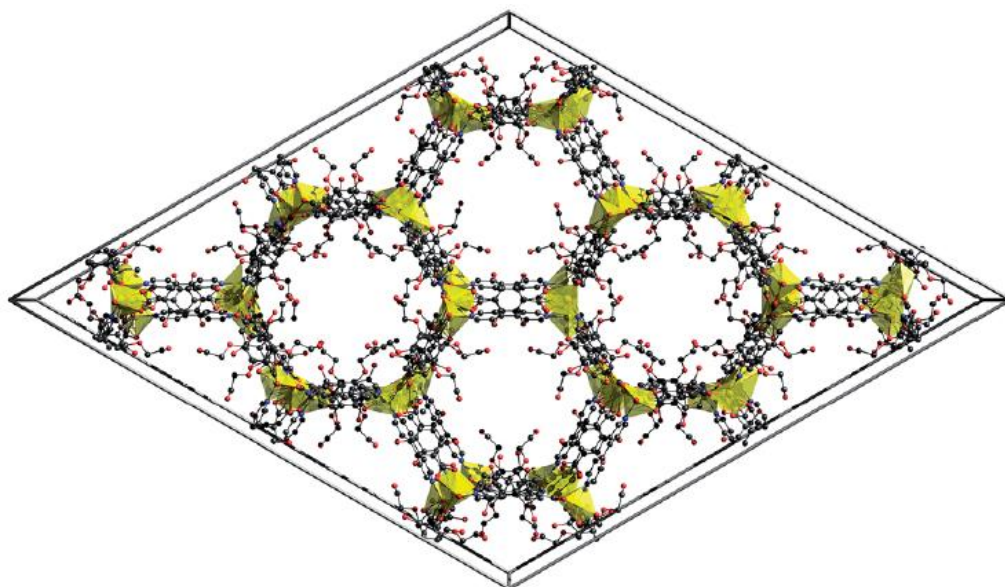


**Figure 47.** Diagram showing the honeycomb structure of  $[\text{Zn}_2(2,5\text{-bis}(2\text{-methoxyethoxy})\text{-1,4-benzenedicarboxylate})_2(\text{bipy})]_n$ . Carbon, nitrogen and oxygen atoms are coloured black, blue and red respectively. Yellow polyhedra are used to identify the coordination environment around the zinc centres. Hydrogen atoms are excluded for clarity. Reproduced from ref. 12.

This topological isomerisation results from the steric bulk of the substituents present, with larger groups forcing the carboxylic moieties to adopt a twisted conformation, moving them out of the plane of the phenyl rings and facilitating the assembly of the honeycomb structure. Gas uptake studies performed on the evacuated honeycomb structures revealed enhanced selectivity for  $\text{CO}_2$  over  $\text{CH}_4$  for those structures bearing methoxy head groups compared to those bearing alkoxy substituents. This was attributed to the weakly Lewis basic nature of the groups, and the subsequent increase in interaction strength with the polar  $\text{CO}_2$  molecule.

The use of the related anionic linker benzene-1,3-dicarboxylic acid (*m*- $\text{H}_2\text{BDC}$ ) has also received a great deal of attention. Due to the similarities between these two potential linkers, the preparation of an isorecticular series of MOFs using *m*- $\text{H}_2\text{BDC}$  with dipyrityls is expected to be facile, though the difference in the angle between the coordinating carboxylates should give very different topologies. Concomitant with this is the ability to include functionality at the 5- position without steric interaction with the coordinating groups. Thus, greater variation of functionality should be possible within the isorecticular series, however comparatively little

research has been done in this area. Initial research using the unfunctionalised *m*-H<sub>2</sub>BDC ligand in mixed linker systems was reported by Sun and co-workers.<sup>13</sup> The solvothermal reaction of this potential linker with 4,4'-bipyridyl and cobalt nitrate gives the 2D coordination polymer [Co(*m*-BDC)(4,4'-bipy)]<sub>*n*</sub>, figure 48.

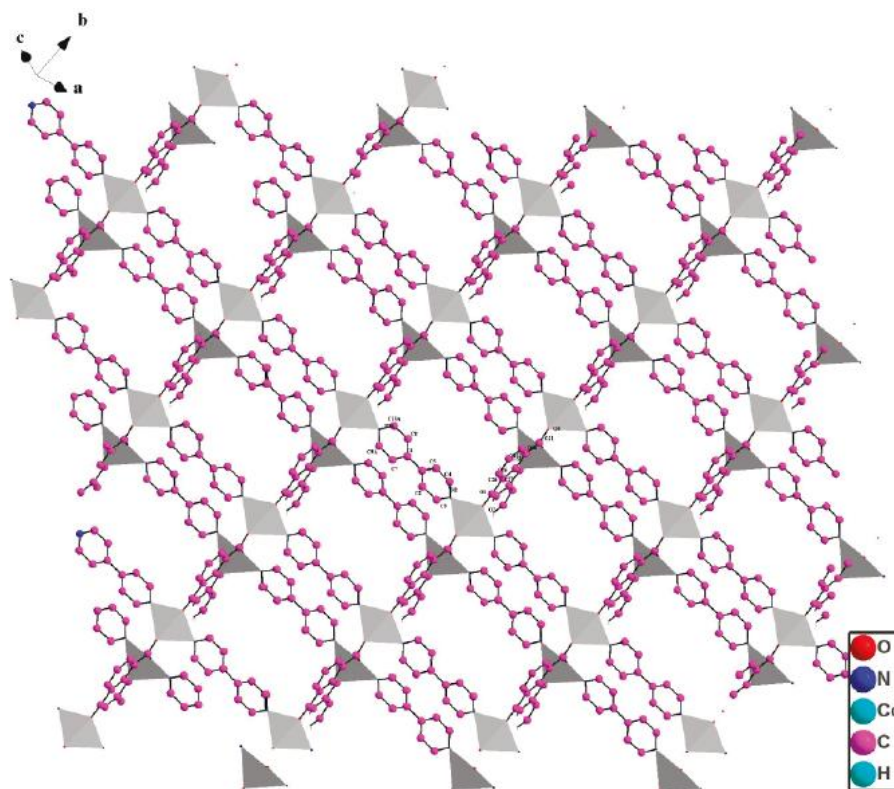


**Figure 48.** Diagram showing the 2D coordination polymer [Co(*m*-BDC)(4,4'-bipy)]<sub>*n*</sub>. 1D Co(*m*-BDC) chains are observable along the *b* axis. Grey polyhedra are used to identify the coordination environment around the cobalt centres. Hydrogen atoms are excluded for clarity. Reproduced from ref. 13.

Two types of metal carboxylate binding are observed in this structure. Each *m*-BDC unit chelates to a single metal centre *via* the first carboxylate function, whilst the second carboxylate bridges two further metal centres in a di-monodentate fashion. Pairs of Co<sub>2</sub>(*m*-BDC)<sub>2</sub> units orient along the *b* axis with the bridging carboxylates linking these pairs in to 1D chains. These chains, which can be described as a series of linked 16 membered macrometallo-cycles, are linked in to extended 2D sheets *via* the 4,4'-bipyridyl linkers, with N-donor bonds observed above and below the plane of the Co(*m*-BDC) pairs giving distorted octahedral coordination geometry about the metal centres, figure 49.

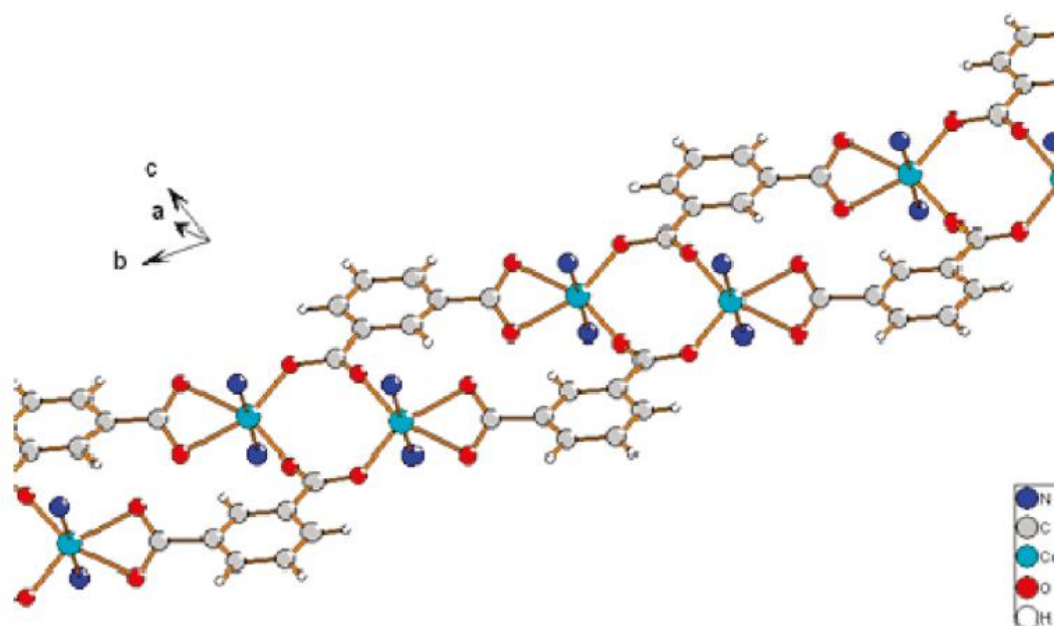


**Figure 49.** Diagram showing the commonly observed metal-carboxylate binding motif in mixed ligand systems involving the *m*-BDC unit. Pyridinyl nitrogens are shown in blue. Reproduced from ref. 13.

Many similar 2D structures have been reported which feature the metal *m*-BDC binding mode detailed in figure 48, linked *via* a variety of bis(pyridinyl) pillaring linkers.<sup>14</sup> A variety of structures were reported by Huo *et al.* using the *m*-H<sub>2</sub>BDC linker in conjunction with the flexible neutral pillaring linkers *N*-(pyridin-3-ylmethyl)pyridin-2-amine (PMP2A) and *N*-(pyridin-3-ylmethyl)pyridin-3-amine (PMP3A) and various transition metal nitrates, and give examples of 2D and 3D frameworks bearing different topologies.<sup>15</sup> The use of milder reaction conditions (120 °C, solvothermal) afforded a series of 2D structures, however the binding motifs in these examples differed from those described previously with 1D chains formed by the coordination of each *m*-BDC to two metal centres being linked in to 4,4 nets by the dipyridyl linker. Distorted octahedral coordination geometries were observed in each of these examples due to the coordination of one or more water molecules. Elevated temperature syntheses, conducted at 140 °C gave rise to increased dimensionality by the elimination of one or more of these coordinated water molecules, and the formation of further metal to linker coordinate bonds.

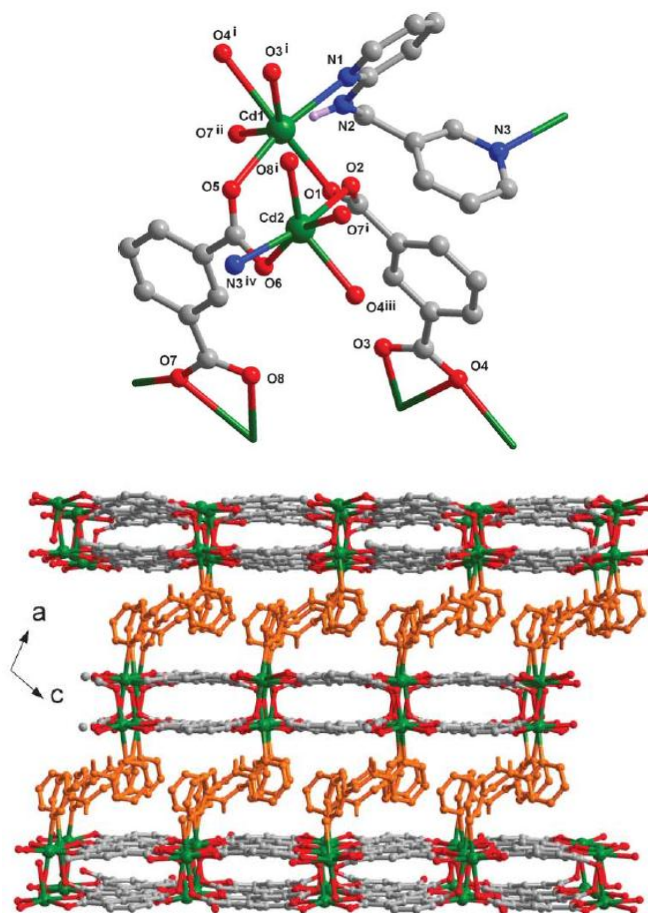


**Figure 50.** Diagram of the  $[\text{Cd}_2(m\text{-BDC})_2\text{PMP2A}]_n$  structure showing the asymmetric unit (top) and the extended 3D structure (bottom). Carbon, oxygen, nitrogen and cadmium atoms are coloured grey, red, blue and green respectively. Dipyriddy linkers are coloured orange in the packing diagram. Hydrogen atoms are excluded for clarity. Reproduced from ref. 15.

The first of these examples was prepared by the hydrothermal reaction of  $m\text{-H}_2\text{BDC}$  and PMP2A with cadmium nitrate tetrahydrate. These conditions afforded a 3D framework formed by the cross-linking of  $[\text{Cd}(m\text{-BDC})]_n$  bilayer sheets by the neutral dipyriddy linker, giving the structural formula  $[\text{Cd}_2(m\text{-BDC})_2\text{PMP2A}]_n$  figure 50.

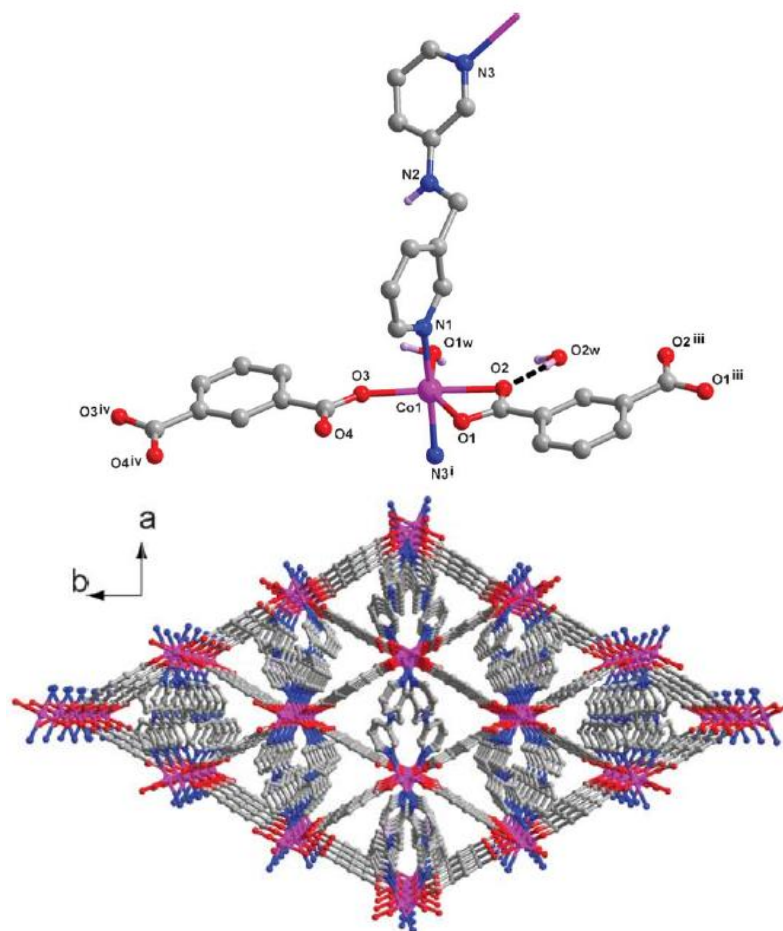


**Figure 51.** Diagram of the  $[\text{Co}(m\text{-BDC})\text{PMP3A}(\text{H}_2\text{O})]_n \cdot n\text{H}_2\text{O}$  framework showing the asymmetric unit (top) and the extended structure (bottom). Carbon, oxygen, nitrogen and cobalt atoms are coloured grey, red, blue and purple respectively. Hydrogen atoms are excluded for clarity. Reproduced from ref. 15.

The reaction of the organic linkers *m*-BDC and PMP3A with cobalt nitrate hexahydrate or nickel nitrate hexahydrate under the same conditions afforded two isostructural 3D frameworks bearing the formula  $[\text{M}(m\text{-BDC})\text{PMP3A}(\text{H}_2\text{O})]_n \cdot n\text{H}_2\text{O}$  (where  $\text{M} = \text{Co}^{2+}, \text{Ni}^{2+}$ ), figure 51. In these examples 1D chains of  $[\text{M}(m\text{-BDC})]_n$  similar to those reported for the 2D 4,4 net structures were formed by the coordinate bonding of the carboxylates to the metal centres, with each *m*-BDC bridging two metal centres. Each *m*-BDC unit coordinates in a bidentate fashion at the first carboxylate moiety and a monodentate fashion at the second. These chains are linked into an extended 3D structure *via* the coordination of two PMP3A units per metal, with a single coordinated water molecule per metal giving distorted octahedral geometry.

The final example was prepared *via* the reaction of zinc nitrate hexahydrate with *m*-H<sub>2</sub>BDC and PMP3A under the same reaction conditions and again exhibited a different net topology, with three zinc SBU binding to four *m*-BDC and two PMP3A units giving six points of extension, figure 52.

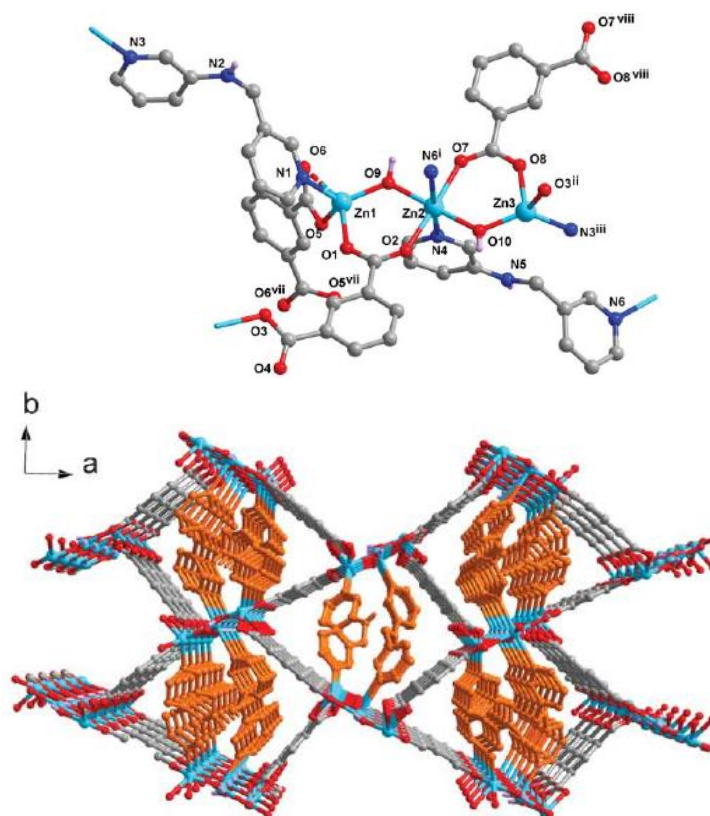


**Figure 52.** Diagram of the  $[Zn_3(m\text{-BDC})_2(OH)_2(PMP3A)_2]_n$  structure showing the asymmetric unit (top) and the extended structure (bottom). Carbon, oxygen, nitrogen and zinc atoms are coloured grey, red, blue and light blue respectively. Dipyriddy linkers are coloured orange in the packing diagram. Hydrogen atoms, except those associated with bound hydroxyl units, are excluded for clarity. Reproduced from ref. 15.

Structures reported using the functionalised anionic linker 5-hydroxybenzene-1,3-dicarboxylic acid (H<sub>2</sub>-5-HIP) in mixed ligand systems revealed a similar split between 2D and 3D frameworks. The reaction of cobalt nitrate hexahydrate with H<sub>2</sub>-5-HIP and 4,4'-bipyridyl by slow diffusion of the reactants gave a 4,4 net topology resulting from the monodentate binding of 5-HIP units to cobalt atoms at each of the carboxylate functions. The resulting chains were linked into a 4,4 sheet *via* the coordination of the neutral linkers with two coordinated water molecules per metal

centre giving octahedral coordination geometry.<sup>16</sup> Use of hydrothermal conditions with the same organic linkers but with the substitution of cobalt nitrate with manganese acetate gives an extended 2D sheets bearing the same binding motif observed in structures using *m*-BDC described in figure 48.<sup>17</sup>

The reactions of zinc nitrate hexahydrate with H<sub>2</sub>-5-HIP and the neutral pillaring linkers 1,2-bis(4-pyridyl)ethane (BPE), 1,2-di(4-pyridyl)ethylene (DPE) and 1,3-bis(4-pyridyl)propane (BPP) as reported by Li *et al.* afforded three multiply interpenetrated 3D diamondoid networks, [Zn(BPE)(5-HIP)]<sub>n</sub>, [Zn(DPE)(5-HIP)]<sub>n</sub> and [Zn(BPP)(5-HIP)(H<sub>2</sub>O)]<sub>n</sub>.<sup>18</sup> In all these examples, tetrahedrally coordinated zinc atoms are bound to two 5-HIP units and two dipyridyl units, with each of the organic linkers bridging two zinc centres. The metal-carboxylate binding modes for [Zn(BPE)(5-HIP)]<sub>n</sub> and [Zn(DPE)(5-HIP)]<sub>n</sub> are identical, with each dipyridyl unit binding in a monodentate fashion at the first carboxylate function, and a bidentate fashion at the second, figure 53.

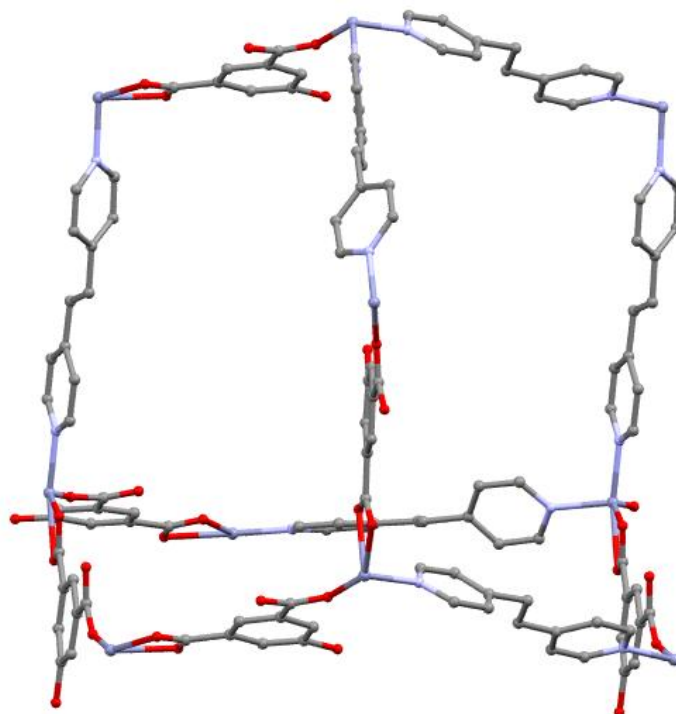


**Figure 53.** Diagram of a single diamondoid cage in [Zn(BPE)(5-HIP)]<sub>n</sub>. Carbon, nitrogen, oxygen and zinc atoms are coloured grey, blue, red and purple respectively. Hydrogen atoms are omitted.<sup>93</sup>

In the case of  $[\text{Zn}(\text{BPP})(5\text{-HIP})(\text{H}_2\text{O})]_n$ , the 5-HIP units bridge two metals centres *via* monodentate bonds at each carboxylate. It is of particular note that the use of the same reaction conditions and neutral linkers in conjunction with *m*-H<sub>2</sub>BDC did not give the analogous structures as may be expected, but rather an amorphous powder. The successful synthesis of the 3D structures is therefore attributed to the templating effect arising from the hydrogen bonding of the anionic linker with solvent molecules.

The huge structural diversity observed in mixed ligand structures based on *m*-BDC and 5-HIP is a major obstacle in the rational design of isorecticular series of MOFs. A common theme for these structures is the formation of 1D chains of 2 metal/2 anionic ligand macrometallo-cycles due to the reduced angle between the carboxylate groups when compared to BDC. The inclusion of a linear ditopic pillaring linker in these systems can therefore only give 2D structures. In order to reliably synthesise a series' of 3D structures from such anionic linkers, the divergence of the coordinating groups must be maintained. In the structures reported by Li and co-workers, this divergence was achieved through the templating effect of solvent molecules H-bonded to the non-coordinating hydroxyl function, though only in these structures does the phenomenon lead to the self-assembly of 3D diamondoid networks. In comparison to the 2D structures reported, those arising from the use of the related ligand 5-aminoisophthalic acid (H<sub>2</sub>-5-AIP) showed very similar binding modes, but with significant differences in the orientation of the 5-AIP units giving rise to 2D sheets which can be further linked in to 3D frameworks by the intercalation of linear dipyriddyis. The reaction of zinc nitrate hexahydrate with H<sub>2</sub>-5-AIP under hydrothermal conditions afforded these 2D sheets comprising 5-AIP units bound to three zinc centres in a monodentate fashion at each of the carboxylate functions and at the amine function. Each zinc binds to three 5-AIP units with terminally coordinated water molecules giving tetrahedral coordination geometry,<sup>19</sup> figure 54.

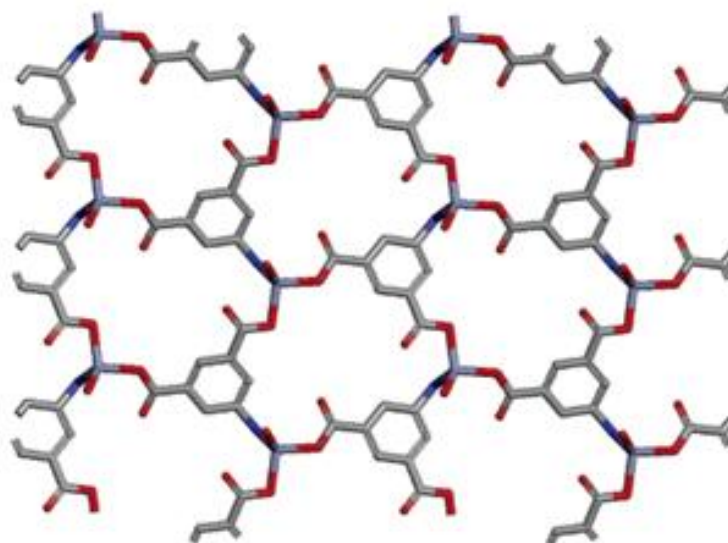


**Figure 54.** Diagram of the 2D sheets resulting from the hydrothermal reaction of H<sub>2</sub>-5-AIP with zinc nitrate under hydrothermal conditions. Carbon, nitrogen, oxygen and zinc atoms are coloured grey, blue, red and purple respectively. Hydrogen atoms are omitted. Reproduced from ref. 94.

With minor changes to the synthetic method, and the addition of the dipyriddyls 4,4'-bipy, 1,2-di-4-pyridylethylene (BPE), 1,2-di-4-pyridylethane (DPA) and 1,2-di-4-pyridylpropane (DPP), Kongshaug and co-workers reported a series of permanently porous bilayer materials with the terminally coordinated water molecules replaced by the neutral pillaring linker,<sup>20</sup> figure 55. In all of these examples the dimensionality of the materials was restricted by the propensity for Zn<sup>2+</sup> to adopt a tetrahedral coordination geometry. By increasing the coordination sphere through the selection of metals ions which preferentially adopt octahedral geometries, further metal-N bonds should allow the coordination of neutral pillaring linkers above and below the plane of the sheets, thereby giving extended 3D structures. Research conducted by Wang *et al* has shown this to be the case.<sup>21</sup> The solvothermal reactions of the nitrates of cadmium, cobalt, and copper with H<sub>2</sub>-5-AIP and 4,4'-bipy afforded a series of isostructural 3D frameworks exhibiting significant differences in binding modes to the bilayer structures reported by Kongshaug.

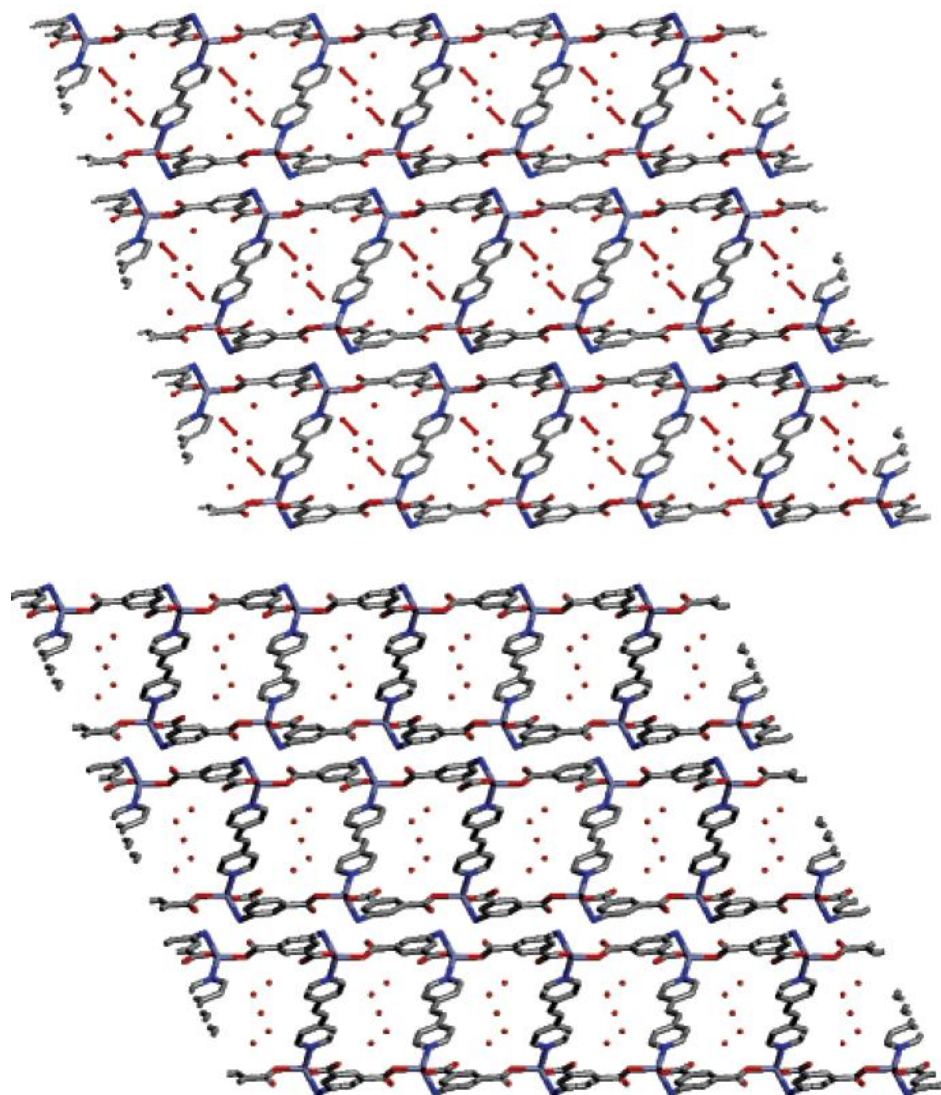


**Figure 55.** Diagram showing the stacked 2D bilayer sheets  $\{[\text{Zn}(5\text{-AIP})(4,4'\text{-bipy})_{0.5}]\cdot 3\text{H}_2\text{O}\}_n$  (top) and  $\{[\text{Zn}(5\text{-AIP})(\text{BPE})_{0.5}]\cdot 2.5\text{H}_2\text{O}\}_n$  (bottom) viewed along [100]. Carbon, nitrogen, oxygen and zinc atoms are coloured grey, blue, red and purple respectively. Hydrogen atoms are omitted. Guest solvent molecules are visible within the pores. Reproduced from ref. 95.

The metal-carboxylate binding motif in these examples was akin to those reported using *m*-BDC and 5-HIP, as detailed in figure 48, in which each 5-AIP unit bridges three metal centres, however the differences observed in the orientation of the 5-AIP units gave divergent tetratopic building units. The 2D sheets resulting from this binding motif can be described as a series of linked 32 membered macrometallo-cycles, figure 56.

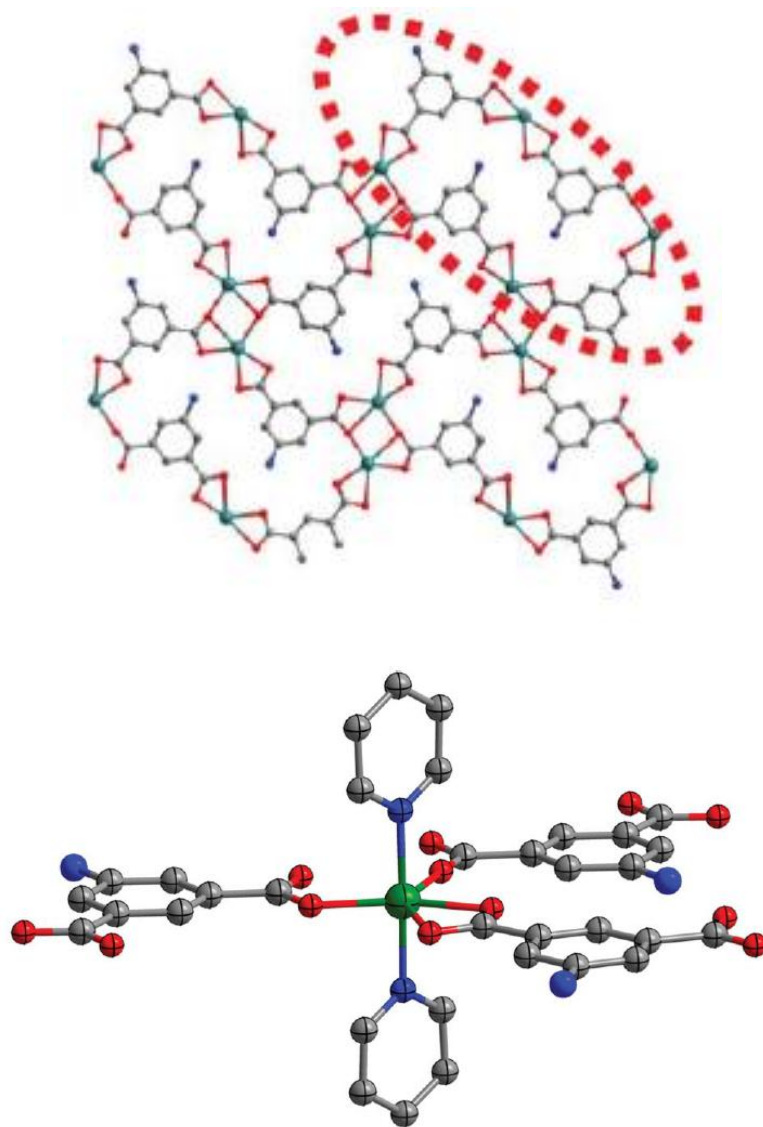


**Figure 56.** Diagram of  $\{[\text{Cu}(5\text{-AIP})(4,4'\text{-bipy})].1.3\text{DMA}\}_n$  showing the 2D sheets, with the 32 membered macrometallocycle identified using a dotted red line (top), and the coordination environment around the metal centres in  $\{[\text{M}(5\text{-AIP})(4,4'\text{-bipy})].1.3\text{DMA}\}_n$  (where  $\text{M} = \text{Co}, \text{Cu}$ ) (bottom). Carbon, nitrogen, oxygen and the metal atoms are coloured grey, blue, red and green respectively. Hydrogen atoms are omitted for clarity.

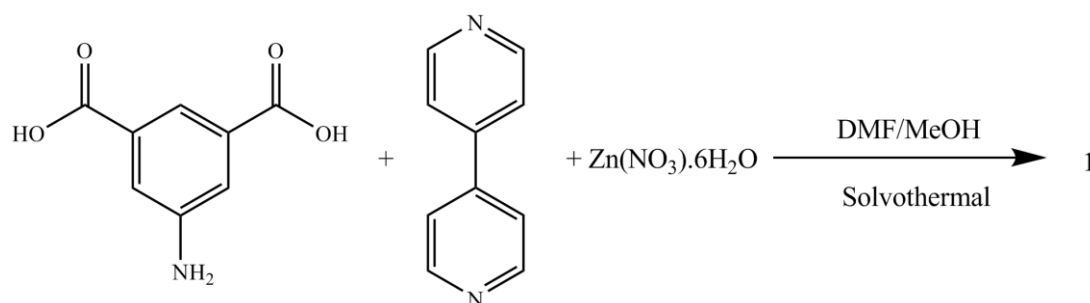
Coordination of the 4,4'-bipyridyl units, perpendicular to the plane of these sheets gave extended 3D frameworks bearing the formulae  $\{[\text{Cd}(5\text{-AIP})(4,4'\text{-bipy})].1.5\text{DMA}\}_n$ ,  $\{[\text{Co}(5\text{-AIP})(4,4'\text{-bipy})].1.6\text{DMA}\}_n$  and  $\{[\text{Cu}(5\text{-AIP})(4,4'\text{-bipy})].1.3\text{DMA}\}_n$ . Only in the case of  $\{[\text{Cd}(5\text{-AIP})(4,4'\text{-bipy})].1.5\text{DMA}\}_n$ , does the metal-carboxylate binding mode differ, the larger metal ion accommodating chelation from two carboxylate groups, with a third carboxylate forming a di-

monodentate-bridging coordination mode between two metal centres, giving a pentagonal bipyramidal coordination environment. The solvent accessible volumes of all three structures were determined using PLATON, giving 51 %, 51 % and 49 % for the cadmium, cobalt and copper analogues respectively, with intersecting 1D channels of 7.65 x 11.714 Å and 6.982 x 11.098 Å reported for {[Cd(5-AIP)(4,4'-bipy)].1.5DMA}<sub>n</sub>, 6.875 x 11.714 Å and 6.798 x 11.371 Å for {[Co(5-AIP)(4,4'-bipy)].1.6DMA}<sub>n</sub> and 7.373 x 11.371 Å and 7.51 x 11.098 Å for {[Cu(5-AIP)(4,4'-bipy)].1.3DMA}<sub>n</sub> without taking in to account the Van der Waals radius of the atoms. No gas uptake data was reported for these structures, however their stability toward guest removal and porosity was confirmed by the reversible adsorption of I<sub>2</sub>.

The advantages of a synthetic strategy based on the use of the amine functionalised ligands are therefore four-fold. The preparation of extended 3D structures *via* the pillaring of linked 32 membered macrometallo-cycles is common to all of the examples reported by Wang, it is therefore expected that syntheses using the similar ligands BPE and 4,4'-azopy with a range of transition metals will afford isostructural materials, giving the opportunity to probe the effect of ligand length, functionality and metal centre on the gas uptake properties of the resultant materials. The inclusion of a polar functionality on the linker which is not involved in coordination has been shown to increase the adsorption enthalpies of guest molecules, and in particular the inclusion of a Lewis basic functionality has been shown to increase the selectivity of materials to CO<sub>2</sub> over CH<sub>4</sub>, also the use of amines in carbon dioxide sequestration is well known.<sup>22</sup> The interaction of the metal centres with the 5-AIP unit affords 2D sheets which bear no cavities large enough to allow the catenation of networks; hence a degree of control can be expressed over the porosity of the prepared materials. Finally the inclusion of amine groups at the 5- position gives the possibility for further pore tuning *via* post-synthetic modification. It is with these factors in mind that we have embarked on a programme to synthesise and structurally characterise a variety of MOFs based on the solvothermal reaction of H<sub>2</sub>-5-AIP with the neutral pillaring linkers 4,4'-bipy, DPE and 4,4'-azopy with a range of transition metal nitrates, and to explore the CO<sub>2</sub> uptake behaviours of the resulting materials.

## 2.2. Results and Discussion

### 2.2.1. Zinc structures



**Scheme 1.** The synthetic route for the preparation of  $\{[\text{Zn}(\text{5-AIP})(4,4'\text{-bipy})_{0.5}]\cdot\text{DMF}\}_n$  **1**.

The synthesis of **1** was achieved through the solvothermal reaction of zinc nitrate hexahydrate with  $\text{H}_2\text{-5-AIP}$  and 4,4'-bipyridyl in a DMF/MeOH mixture following the procedure detailed in scheme 1, which afforded colourless hexagonal prisms of sufficient quality to perform single crystal X-ray diffraction. Structural elucidation of **1** revealed a hybrid covalent/H-bonded 3D network bearing the formula  $\{[\text{Zn}(\text{5-AIP})(4,4'\text{-bipy})_{0.5}]\cdot\text{DMF}\}_n$ . In this example, 2D sheets formed by the bridging of three zinc centres by each 5-AIP unit, *via* monodentate bonds at each carboxylate moiety and an N donor bond from the amino group, are linked into bilayers by 4, 4'-bipyridyl units, giving rise to tetrahedral coordination geometry, figure 57.

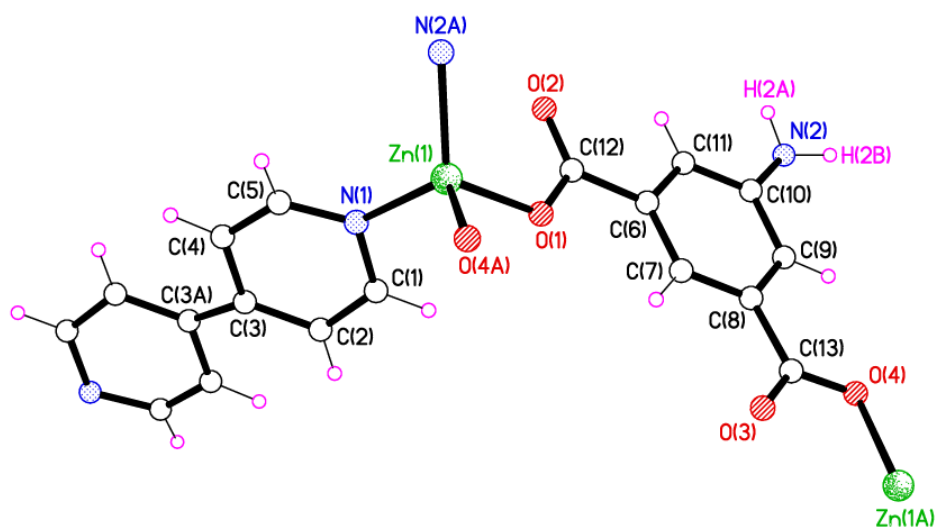


**Figure 57.** Diagram of  $\{[\text{Zn}(\text{5-AIP})(4,4'\text{-bipy})_{0.5}]\cdot\text{DMF}\}_n$  **1**, showing the coordination environment around the zinc centres.

Extensive hydrogen bonding observed between the amine hydrogens of each sheet and the non-coordinated carboxylate oxygen of the neighbouring sheet gives the 3D structure, figure 58.

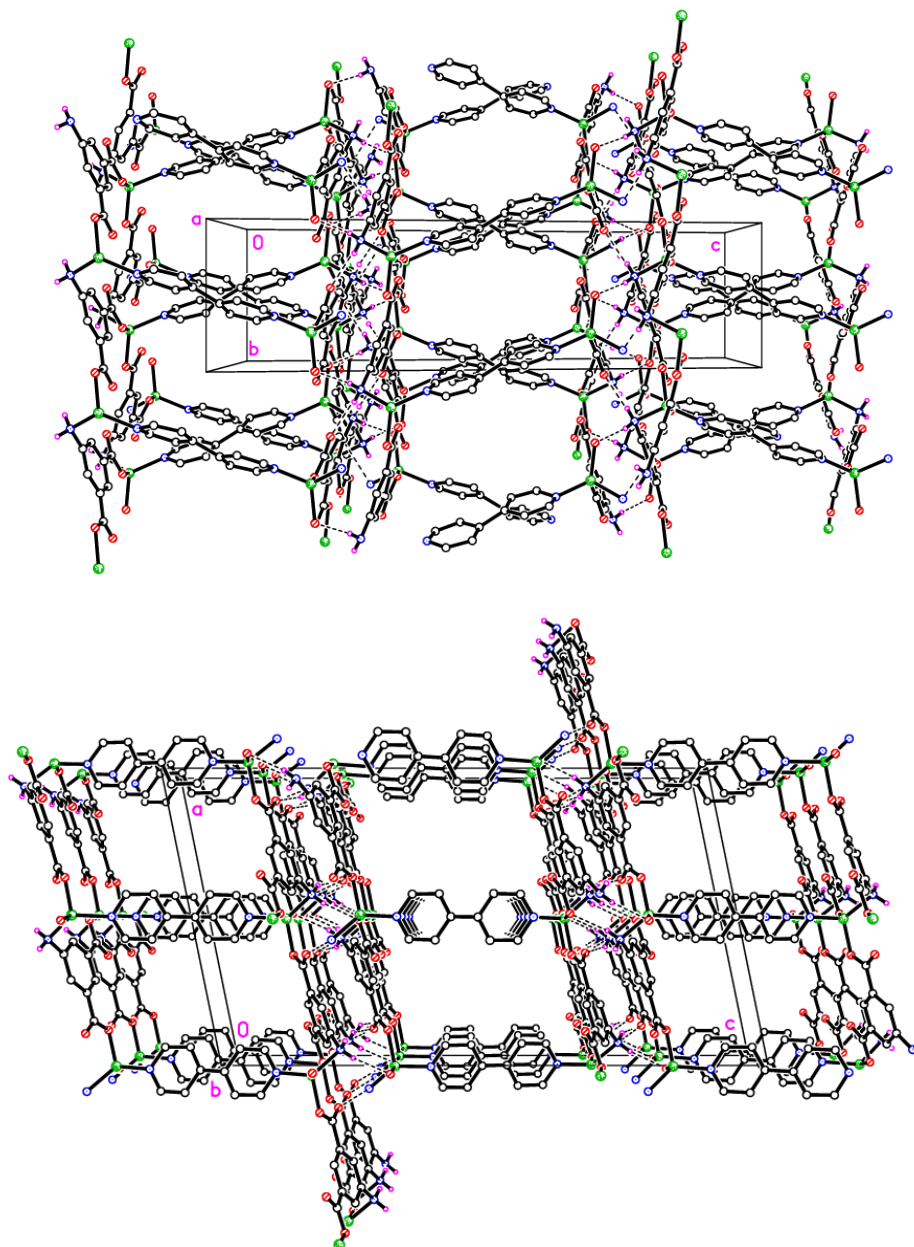
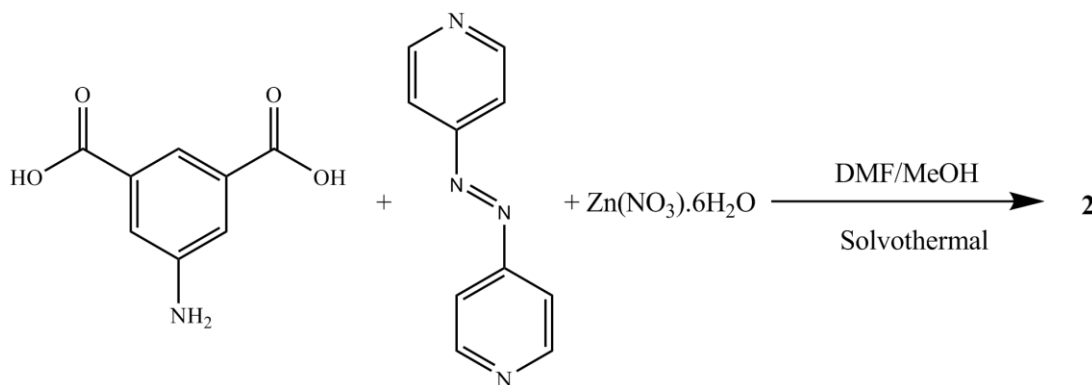


**Figure 58.** Diagram of the extended structure of **1** as viewed along the *a* axis (top) and the *b* axis (bottom). Carbon atoms are represented by empty circles. Nitrogen, oxygen and zinc atoms are coloured blue red and green respectively. Hydrogen atoms, except those involved in hydrogen bonding, are omitted.

The PLATON squeeze procedure was used to model diffuse electron density in the voids of this framework, giving a total of 301 electrons per unit cell. This corresponds to a total of 8 DMF molecules per unit cell, or 1 per formula unit, which inhabit intersecting 1D channels situated parallel to the *a* and *c* axes, with no bonding interactions observed between the guest molecules and the framework.

The binding motif observed in this structure is analogous to the framework reported by Kongshaug *et al.* In that example, the reaction of H<sub>2</sub>-5-AIP with 4,4'-bipyridyl and zinc nitrate hexahydrate in a DMF/H<sub>2</sub>O mixture gave a very similar structure bearing the formula  $\{[\text{Zn}(5\text{-AIP})(4,4'\text{-bipy})_{0.5}]\cdot 3\text{H}_2\text{O}\}_n$ , however no hydrogen bonding was observed between the bilayers. Also reported were the analogous structures  $\{[\text{Zn}(5\text{-AIP})(\text{DPE})_{0.5}]\cdot 2.5\text{H}_2\text{O}\}_n$ ,  $\{[\text{Zn}(5\text{-AIP})(\text{DPA})_{0.5}]\cdot 2.5\text{H}_2\text{O}\}_n$  and  $\{[\text{Zn}(5\text{-AIP})(\text{DPP})_{0.5}]\cdot 3\text{H}_2\text{O}\}_n$  (where DPE = 1,2-di-4-pyridyl ethylene, DPA = 1,2-di-4-pyridylethane and DPP = 1,2-di-4-pyridylpropane). It is of particular interest that the use of neutral linkers of increasing length in this example does not have a profound effect on pore size. Due to the fixed orientation of the zinc tetrahedra on opposing walls of the bilayers, the longer dipyridyls are forced to adopt a bent conformation, and while this leads to a minor increase in the size of the small channels running parallel to the *a* axis, the large channels observed along the *b* axis exhibited dimensions of 3.5 x 6.7 Å<sup>2</sup> in all four examples. Nitrogen adsorption isotherms recorded at 77 K showed no uptake for any of the structures, which can be explained by taking in to account the kinetic diameter of N<sub>2</sub> molecules. At 3.64 Å diameter, nitrogen molecules are too large to diffuse into the structure. Low hydrogen uptakes (< 0.2 wt% at 77 K and 1 bar) however were reported for the four structures.

The lack of pore size modification with increasing linker length prompted our investigation of linker functionality in the CO<sub>2</sub> uptake behaviour of these structures *via* the use of the neutral linker 4,4'-azopy. With the kinetic diameter of 3.3 Å for CO<sub>2</sub> and 3.84 Å for CH<sub>4</sub>, these structures are good candidates for the separation of CO<sub>2</sub> from mixtures of these gases on a size exclusion basis, therefore the use of a neutral pillaring linker bearing the N=N moiety, which has been shown to increase the adsorption enthalpies of polar gases, should give increased uptake and selectivity.



**Scheme 2.** The synthetic route for the preparation of  $\{[\text{Zn}(5\text{-AIP})(4,4'\text{-azopy})_{0.5}]\cdot 1.5\text{DMF}\}_n$  **2**.

The preparation of **2** was achieved using the same reaction conditions as with **1**, however the substitution of 4,4'-bipy for 4,4'-azopy, as detailed in scheme 2, led to the formation of **2** as orange prisms. The crystals were of suitable quality for single crystal X-ray diffraction, however due to a twinning component which could not be resolved the data collected were of sufficient quality to only determine connectivity. Comparison of the collected powder X-ray diffraction pattern for this structure with the simulated pattern for **1** reveals distinct similarities in line spacing and intensity. TGA and gas adsorption data also show similar behaviours, offering good evidence of the isostructurality of **1** and **2**. The framework, bearing the formula  $\{[\text{Zn}(5\text{-AIP})(4,4'\text{-azopy})_{0.5}]\cdot 1.5\text{DMF}\}_n$ , exhibits the same binding motif between the zinc centres and the organic linkers as **1**, with tetrahedrally coordinated zinc atoms forming bonds to two carboxylate oxygens from independent 5-AIP molecules, the amine nitrogen of a third 5-AIP molecule, and the pyridinyl nitrogen of a 4,4'-azopy molecule, figure 59. Each 5-AIP molecule links three zinc centres *via* the monodentate coordination of each of the carboxylate groups and the amine nitrogen, forming infinite 2D sheets observed in the *b/c* plane. The sheets are linked into pairs along the *a* axis by the coordination of the 4,4'-azopy linker to zinc centres at each of the pyridinyl nitrogens, figure 60.



Due to the quality of the data set the amine hydrogen atoms could not be located, however the proximity of the N(3) atoms to the O(2') and O(4') of neighbouring sheets (2.99 Å) offers evidence of strong hydrogen bonding interactions between the bilayer sheets, giving a 3D hybrid H-bonded/covalent network analogous to that of **1**. As with the examples reported by Kongshaug *et al.* the use of the longer neutral pillaring linker has little effect on the size of the large pores, in this example situated parallel to the *b* axis, with the spacing between the 4,4'-azopy molecule dictated by the distance between the zinc atoms in the [Zn(5-AIP)]<sub>*n*</sub> sheets. When viewed along the *c* axis, however, the narrowing of the small pores by the orientation of the 4,4'-azopy molecules is revealed, figure 61.

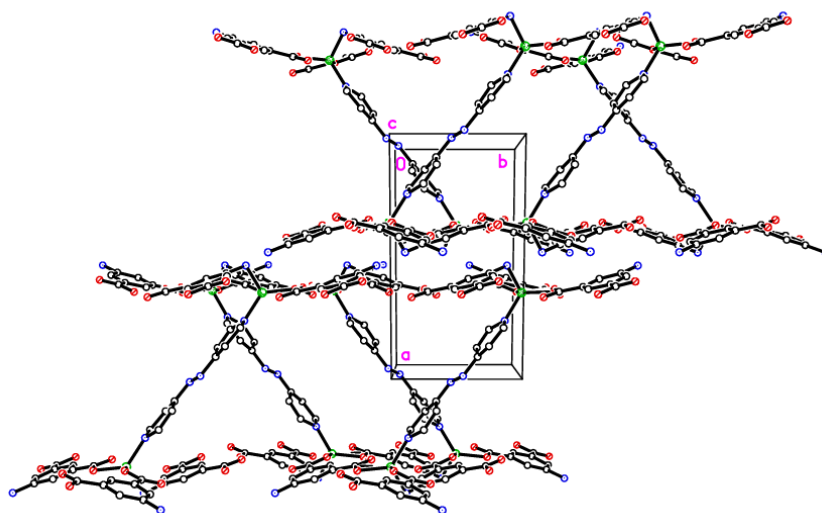
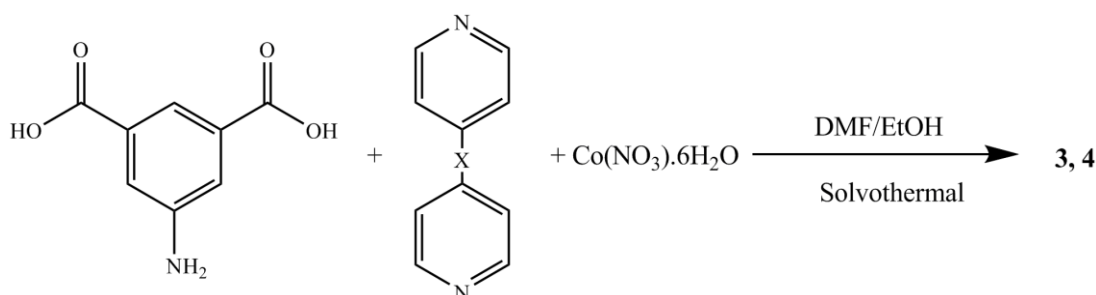


**Figure 61.** Diagram of **2** as viewed along the *c* axis showing the orientation of the 4,4'-azopy linkers, and concomitant narrowing of pores.

Again, due to the quality of the data set, guest solvent molecules could not be resolved by point atoms observations and were modelled as areas of diffuse electron density by the PLATON squeeze procedure, giving 3 DMF molecules located in two small voids per unit cell, equating to 1.5 DMF molecules per formula unit.

### 2.2.2. Cobalt structures



**Scheme 3.** The synthetic route for the preparation of **3** and **4** [where X = nothing (**3**), CH=CH (**4**)].

The solvothermal reactions of cobalt nitrate hexahydrate with H<sub>2</sub>-5-AIP and the bipyridyls 4,4'-bipyridyl, DPE and 4,4'-azopyridyl in a DMF/EtOH mixture, following the procedure detailed in scheme 3, afforded two novel metal organic frameworks, bearing the structural formulae  $\{[\text{Co}_2(\text{NO}_3)_2(5\text{-AIP})(4,4'\text{-bipy})_2] \cdot 2\text{EtOH}\}_n$  (**3**) and  $\{[\text{Co}(5\text{-AIP})(\text{DPE})] \cdot 3\text{DMF}\}_n$  (**4**). Structure **3** was synthesised as purple prisms of suitable quality to perform single crystal X-ray diffraction. The structure is comprised of distorted octahedrally coordinated  $\text{Co}^{2+}$  ions bound in a monodentate fashion to two carboxylate functions, two pyridinyl nitrogens and a chelating nitrate molecule, figure 62.

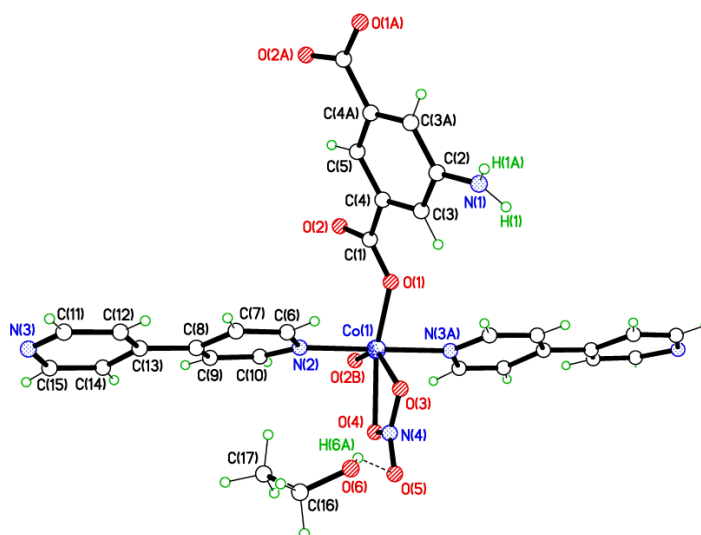


**Figure 62.** Diagram of  $\{[\text{Co}_2(\text{NO}_3)_2(5\text{-AIP})(4,4'\text{-bipy})_2] \cdot 2\text{EtOH}\}_n$  **3**, showing the coordination environment around the metal centre. Carbon atoms are represented by empty circles. Nitrogen, oxygen and cobalt atoms are coloured blue red and dark blue respectively.

Each carboxylate function forms a di-monodentate bridging coordination mode between two crystallographically equivalent  $\text{Co}^{2+}$  ions, and unlike the examples previously reported by Wang and co-workers, this metal-carboxylate binding motif is observed at both carboxylate functions of the 5-AIP linker, with  $180^\circ$  rotation of successive 5-AIP units giving extended 1D chains. These chains are linked to their four nearest neighbours through the coordination of 4,4'-bipyridyl units which are approximately parallel to the  $a$  axis, but in two different mutually angled orientations, giving a herringbone motif and linking the chains in to a 3D structure figure 63.

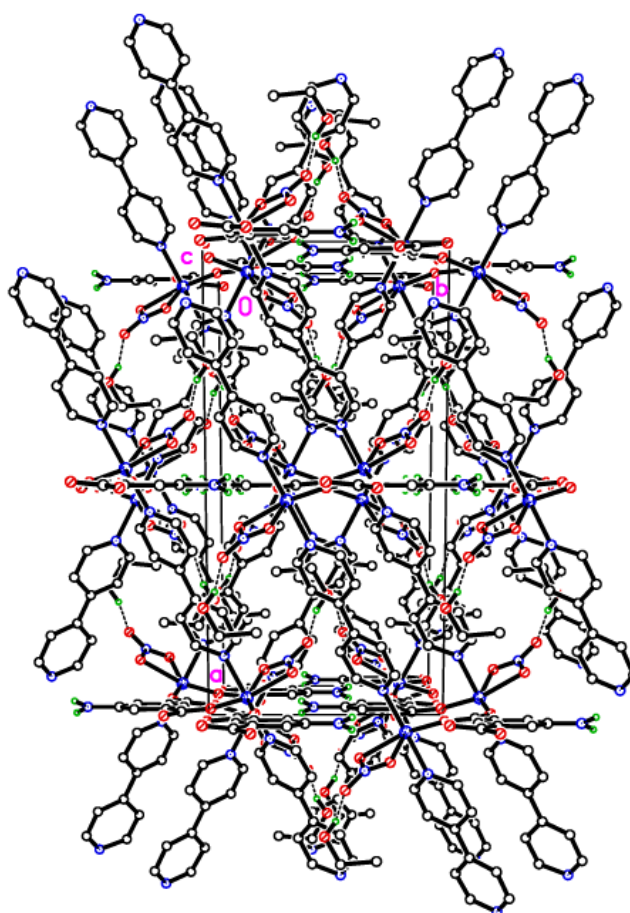


**Figure 63.** Diagram of the extended structure of **3** as viewed along the  $c$  axis, showing the herringbone motif of coordinated 4,4'-bipy units. Carbon atoms are represented by empty circles. Nitrogen, oxygen and cobalt atoms are coloured blue red and dark blue respectively. Hydrogen atoms, except those involved in hydrogen bonding to guest solvent molecules, are omitted.

Chelated nitrate molecules lie out of plane with the 5-AIP units, extending into 1D channels bearing dimensions of 7.08 x 4.18 Å observed parallel to the *b* axis, with each nitrate unit forming a hydrogen bond to guest ethanol molecules, figure 64

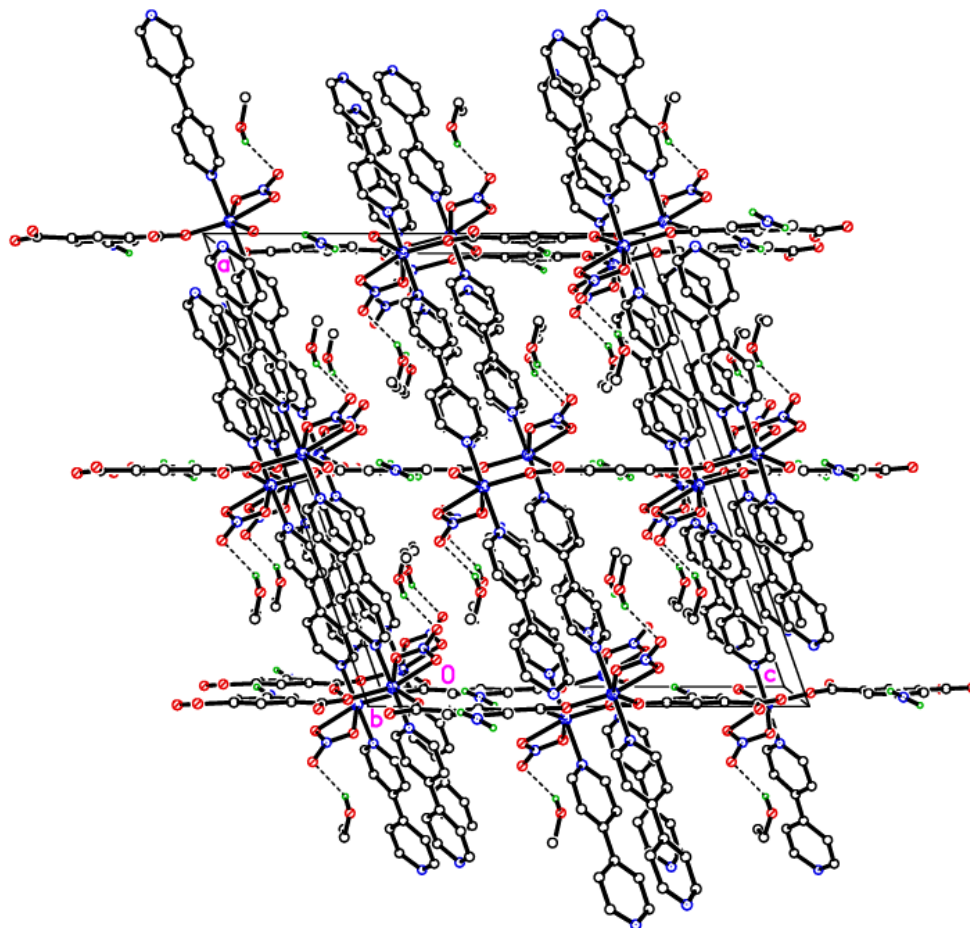


**Figure64.** Diagram of the extended structure of **3** as viewed along the *b* axis. Chelated nitrate anions extend in to the pores of the framework forming hydrogen bonds with guest ethanol molecules. Carbon atoms are represented by empty circles. Nitrogen, oxygen and cobalt atoms are coloured blue red and dark blue respectively. Hydrogen atoms, except those involved in hydrogen bonding to guest solvent molecules, are omitted.

Structure **4** was also synthesised as purple prisms, however due to a twinning component, the single crystal X-ray diffraction data collected was sufficient only to establish connectivity. Similarities observed in the powder X-ray patterns collected for this structure and the related **7** confirmed that they were isostructural and that the synthesis of the 3D framework  $\{[\text{Co}(5\text{-AIP})(\text{DPE})].3\text{DMF}\}_n$  had been successful.

This assertion is also supported by the similarities between the TGA data collected for this and the related structures and by elemental analysis. The structure of **4** is comprised of 6-coordinate, distorted octahedral  $\text{Co}^{2+}$  nodes coordinated to a single chelating carboxylate group, two monodentate carboxylate oxygens from different molecules and two pyridinyl nitrogens, figure 65.

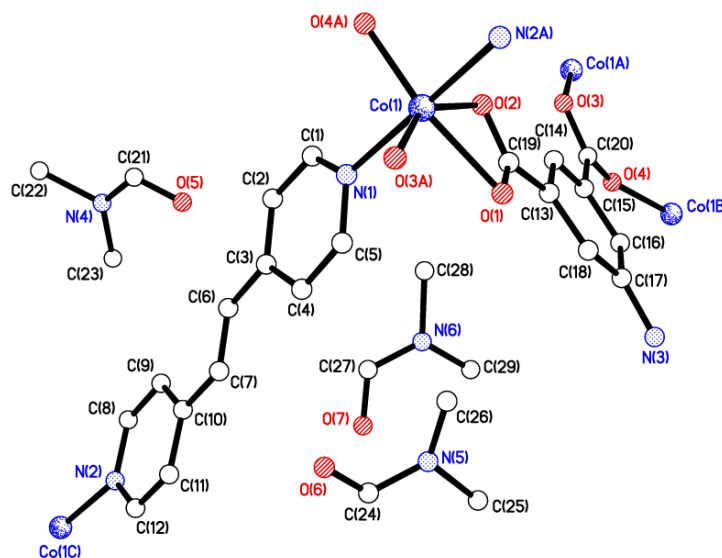


**Figure 65.** Diagram of  $\{[\text{Co}(5\text{-AIP})(\text{DPE})].3\text{DMF}\}_n$ , **4**, showing the coordination environment around the  $\text{Co}^{2+}$  centres and the location of guest DMF molecules around the DPE linker. Hydrogen atoms are omitted for clarity.

The metal-carboxylate binding mode observed in this example is analogous to those reported by Wang *et al.*, with 2D sheets formed by the interaction of the 5-AIP linker with the  $\text{Co}^{2+}$  nodes exhibiting the 32 membered macrometallo cycles previously described, located in the  $b/c$  plane. Additionally the proximity of N(3) to O(1') (2.83 Å) clearly indicates the presence of hydrogen bonding supporting the covalent bonding in this plane. Pillaring DPE linkers extend in the  $a$  direction giving the 3D structure, figure 66. It is of particular note that the larger void spaces resulting from the use of a longer dipridyl linker allows the inclusion of more guest molecules than **3**, with three disordered DMF molecules per formula unit inhabiting intersecting 1D channels observed parallel to the  $b$  and  $c$  axes.

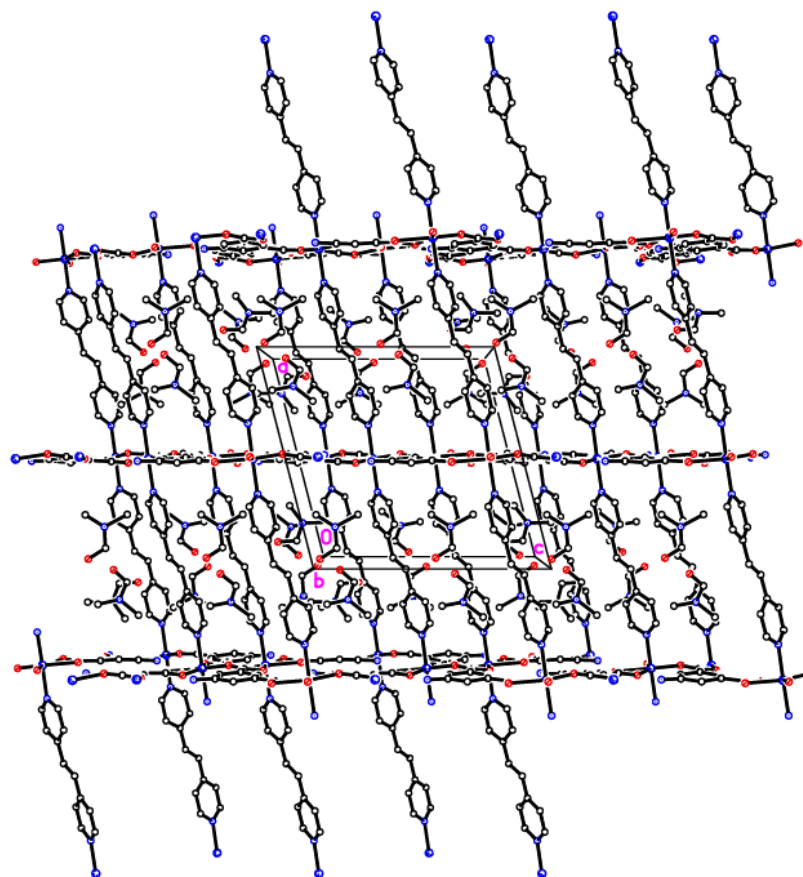
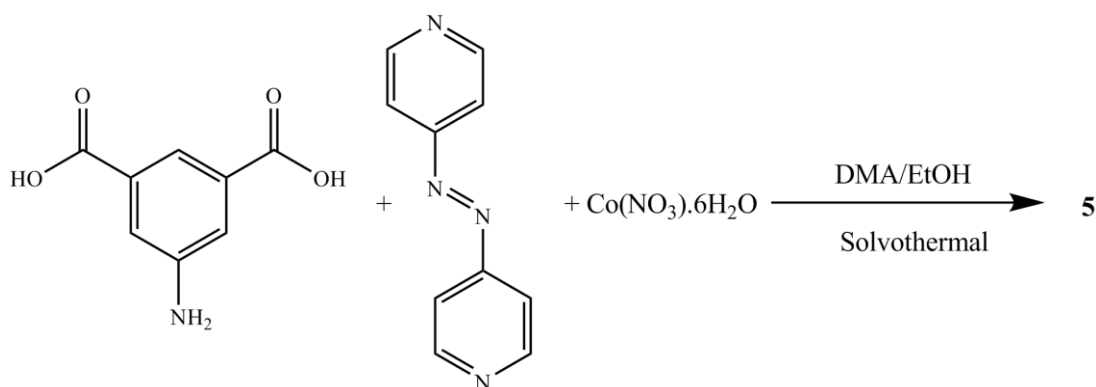


**Figure 66.** Diagram of the extended structure of **4** as viewed along the *b* axis. Guest DMF molecules are visible around the DPE linkers. Carbon atoms are represented by empty circles. Nitrogen, oxygen and cobalt atoms are coloured blue red and dark blue respectively. Hydrogen atoms are omitted for clarity.



**Scheme 4.** The synthetic route for the preparation of  $\{[\text{Co}(5\text{-AIP})(4,4'\text{-azopy})].2\text{DMA}\}_n$  **5**.

The solvothermal reaction of H<sub>2</sub>-5-AIP with cobalt nitrate hexahydrate with 4,4'-azopy in a DMA/EtOH mixture, following scheme 4, afforded **5** as dark red prisms of suitable quality for structural elucidation by single crystal X-ray diffractometry. This reveals a 3D MOF of the formula {[Co(5-AIP)(4,4'-azopy)].2DMA}<sub>n</sub> which is isostructural to **4**, bearing the same carboxylate binding motif, with both groups adopting bidentate coordination modes, one chelating to a single cobalt centre and the other exhibiting bridging behaviour between two metal nodes figure 67.

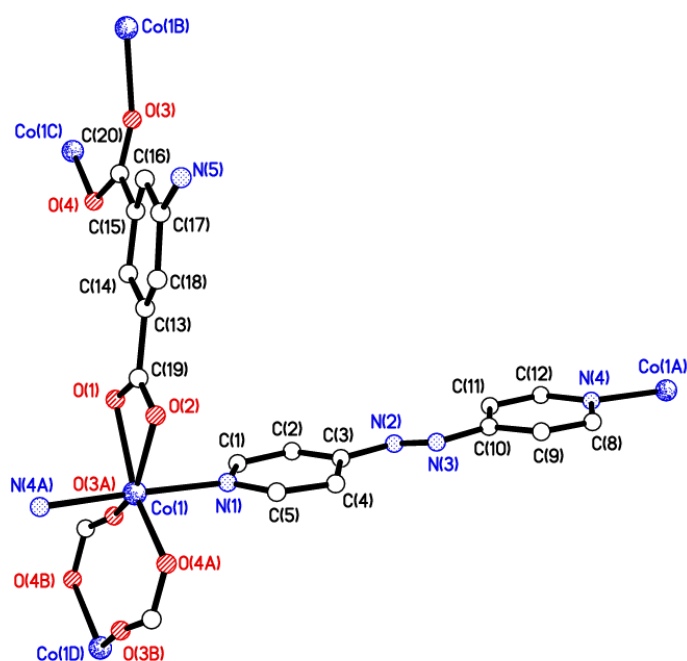


**Figure 67.** Diagram of {[Co(5-AIP)(4,4'-azopy)].2DMA}<sub>n</sub> (**5**), showing the coordination environment around the Co<sup>2+</sup> nodes. Hydrogen atoms are omitted.

As with **4** the proximity of the amine nitrogen N(5) to the carboxylate oxygens O(2A) and O(4B) clearly indicates the presence of hydrogen bonding interactions within the Co(5-AIP) sheets, figure 68.

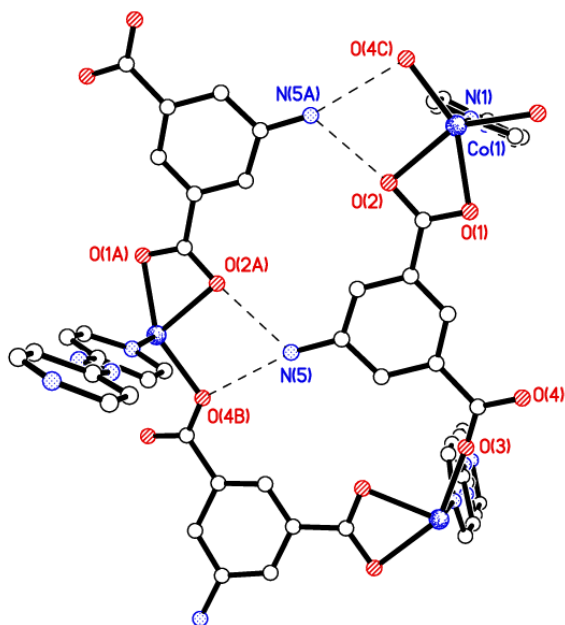


**Figure 68.** Diagram of the 2D sheets in **5** showing the hydrogen bonding interactions, represented by dotted lines between the amine functions and carboxylate groups of neighbouring 5-AIP units. Carbon atoms are represented by empty circles. Hydrogen atoms are excluded for clarity.

Coordination of the 4,4'-azopy linker above and below the plane of the the Co(5-AIP) sheets gives the extended 3D structure which bears intersecting channels of  $7.47 \times 9.80 \text{ \AA}$  and  $3.38 \times 9.80 \text{ \AA}$  observed parallel to the *b* and *c* axes, figure 69. In the as-synthesised MOF these channels contain highly disordered DMA molecules. These could not be refined using point atom observations, hence the PLATON squeeze procedure was performed, recovering 399 electrons per unit cell. This equates to 8 DMA molecules per unit cell, or 2 per formula unit.

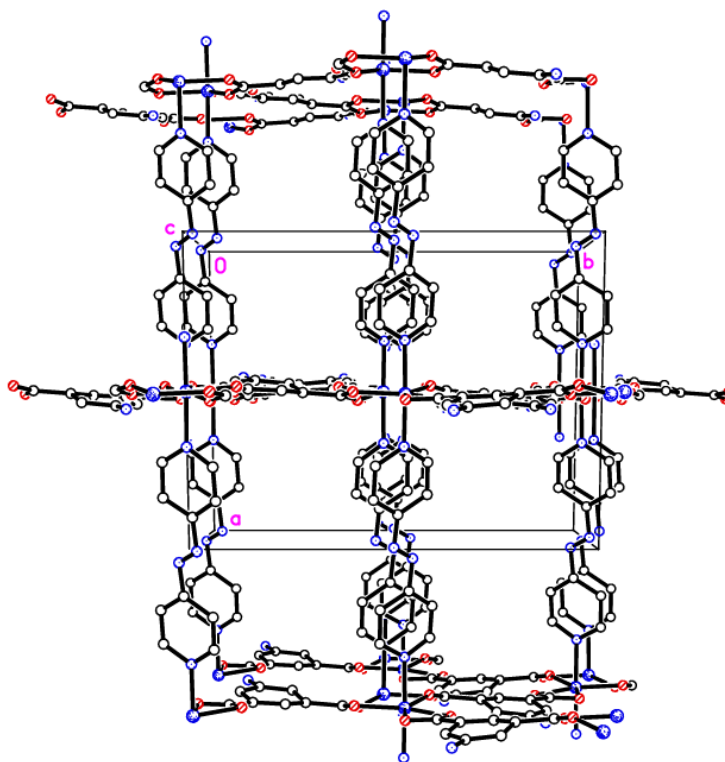
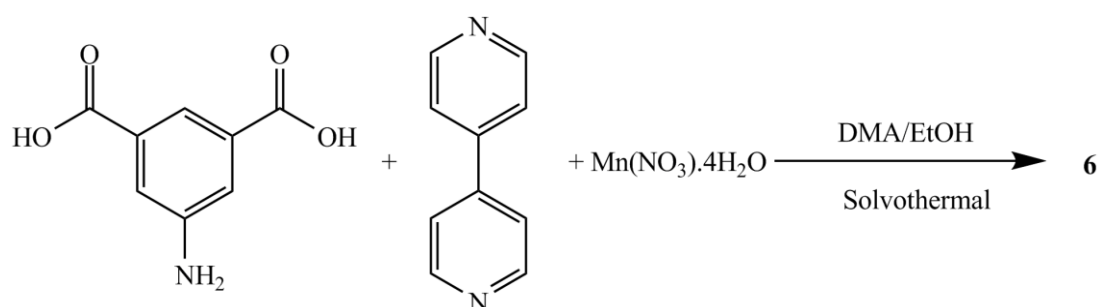


**Figure 69.** Diagram of the extended structure of **5** as viewed along the *c* axis. Carbon atoms are represented by empty circles, nitrogen, oxygen and cobalt atoms are represented by small blue spheres, red spheres and large blue spheres respectively. Hydrogen atoms are omitted.

### 2.2.3. Manganese structures



**Scheme 5.** The synthetic route for the preparation of  $\{[\text{Mn}(5\text{-AIP})(4,4'\text{-bipy})]\cdot 2\text{DMA}\}_n$  **6**.

The solvothermal reaction of  $\text{H}_2\text{-5-AIP}$  with 4,4'-bipyridyl and  $\text{Mn}(\text{NO}_3)_2\cdot 4\text{H}_2\text{O}$  in a DMA/ethanol mixture was conducted following the procedure detailed in scheme 5, affording yellow prisms of suitable quality for single crystal X-ray diffraction.

Structural elucidation revealed an extended 3D framework of the formula  $\{[\text{Mn}(5\text{-AIP})(4,4'\text{-bipy})]\cdot 2\text{DMA}\}_n$ , **6** which is isomorphous to the previously described  $\{[\text{Co}(5\text{-AIP})(\text{DPE})]\cdot 3\text{DMF}\}_n$  (**4**) and  $\{[\text{Co}(5\text{-AIP})(4,4'\text{-azopy})]\cdot 2\text{DMA}\}_n$  (**5**) structures, figure 70.

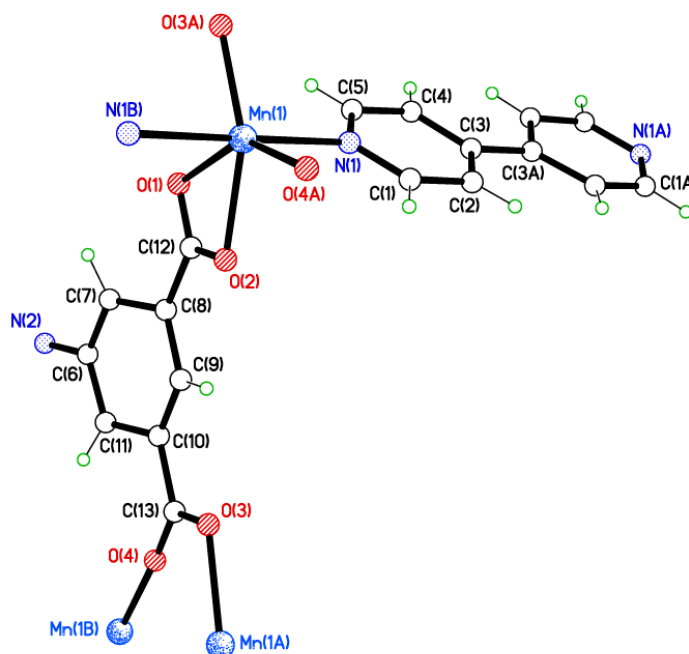


**Figure 70.** Diagram of  $\{[\text{Mn}(5\text{-AIP})(4,4'\text{-bipy})]\cdot 2\text{DMA}\}_n$  **6**, showing the coordination environment around the  $\text{Mn}^{2+}$  nodes.

In this example, the 5-AIP unit links  $\text{Mn}^{2+}$  ions in the  $a/b$  plane, with 4,4'-bipyridyl units linking these sheets in the  $c$  direction. A minor twinning component is observed in the X-ray diffraction data, hence atoms N(2), C(6), C(7) and C(11) were modelled as disordered across the mirror in the  $a/b$  plane, figure 71. As with **4**, the proximity of the N(2) atom to O(1') (2.91 Å) clearly indicates the presence of a hydrogen bonding interaction. Disordered DMA molecules were modelled using the PLATON squeeze procedure which recovered 410 electrons in one large void per unit cell. Given the point atom observations, 8 DMA molecules per unit cell, or two per formula unit, were considered reasonable, located in intersecting channels of 2.67 x 8.21 Å and 1.38 x 8.21 Å observed along the  $a$  and  $b$  axes respectively.

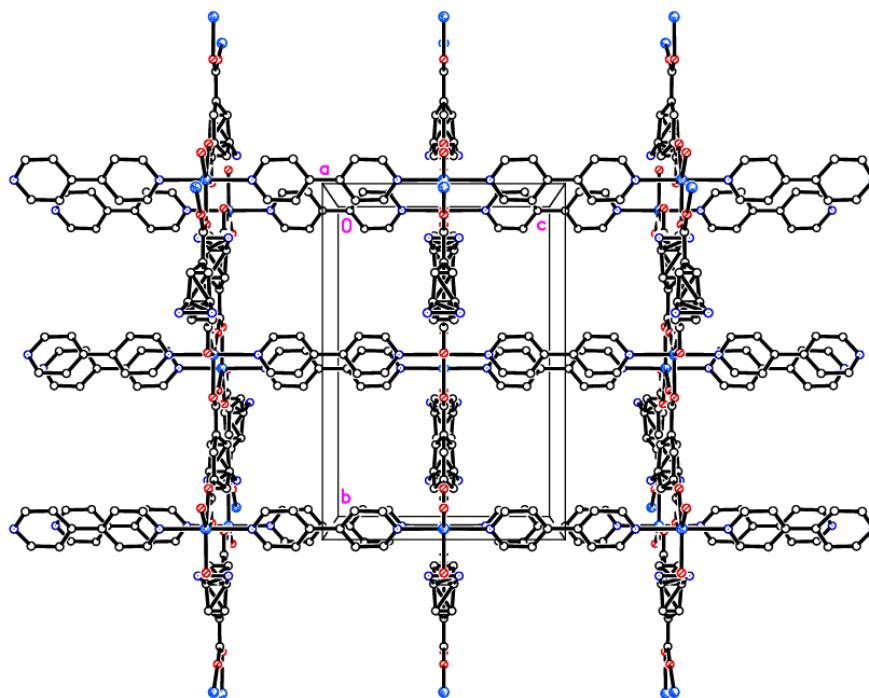
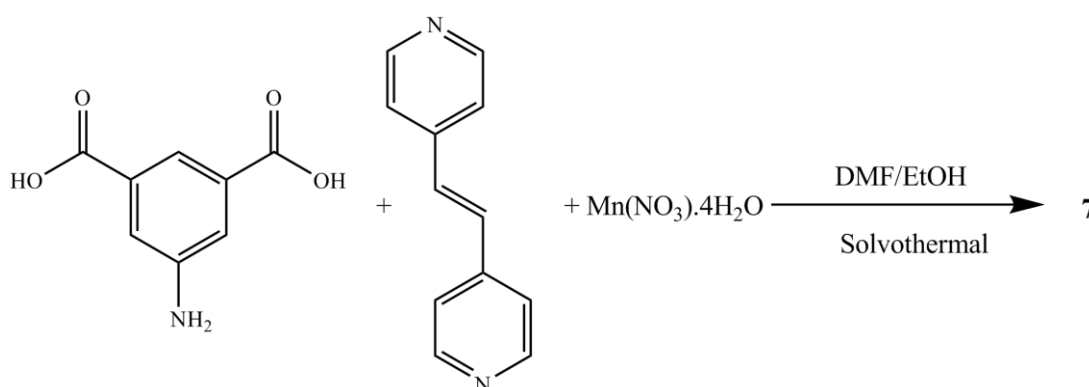


**Figure 71.** Diagram of the extended structure of **6** as viewed along the *a* axis. The 5-AIP is modelled across two positions due to a minor twinning component. Carbon atoms are represented by empty circles. Nitrogen, oxygen and manganese atoms are coloured blue red and dark blue respectively. Hydrogen atoms are omitted for clarity.



**Scheme 6.** The synthetic route for the preparation of  $\{[\text{Mn}(\text{5-AIP})(\text{DPE})] \cdot 1.5\text{DMF}\}_n$  **7**.

The solvothermal reaction of  $\text{H}_2\text{-5-AIP}$  with DPE and  $\text{Mn}(\text{NO}_3)_2 \cdot 4\text{H}_2\text{O}$  was performed according to scheme 6, also affording yellow prisms of suitable quality for single crystal X-ray diffraction. Structure **7** is isostructural to **4**, **5**, and **6** with 2D

sheets of Mn(5-AIP) observed in the *b/c* plane being linked *via* the dipyriddy unit, giving the structural formula  $\{[\text{Mn}(5\text{-AIP})(\text{DPE})].1.5\text{DMF}\}_n$ , figure 72.

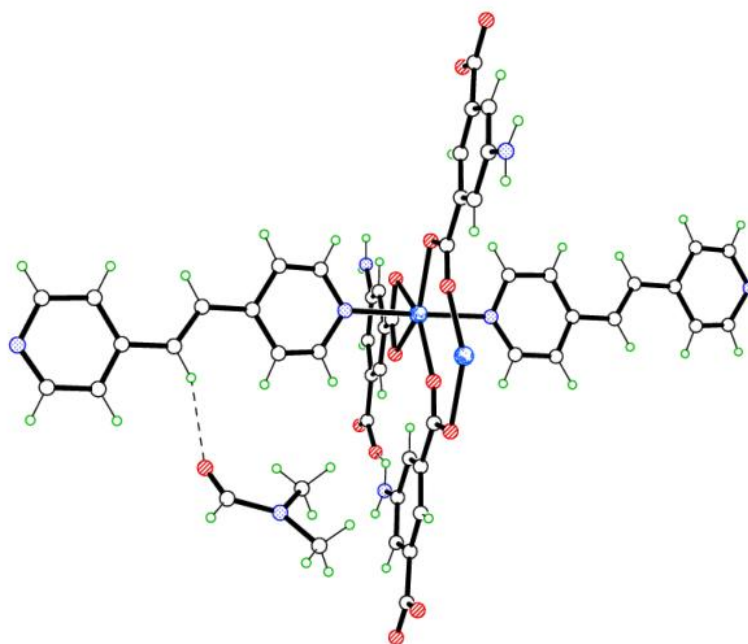


**Figure 72.** Diagram of **7** showing the coordination environment around the  $\text{Mn}^{2+}$  nodes. The hydrogen bond between the dipyriddy linker and the DMF molecule represented by a dotted line. Carbon atoms are represented by empty circles. Nitrogen, oxygen and manganese atoms are coloured blue red and dark blue respectively.

As with **4**, the use of a longer dipyriddy linker gives rise to the elongation of the pores in the *a* direction, giving intersecting 1D channels of  $10.98 \times 5.84 \text{ \AA}$  and  $10.98 \times 3.51 \text{ \AA}$ . However unlike **4**, this does not lead to the incorporation of a greater quantity of guest solvent molecules. A total of six DMF molecules are observed per unit cell, or 1.5 per formula unit. The first of these is well defined, due to the hydrogen bonding interaction of the aldehydic oxygen with the ethylene linkage of the dipyriddy unit and is refined as point atoms, however the remaining five are disordered and are modelled using the PLATON squeeze procedure as diffuse areas of electron density. As with the isostructural frameworks, the intersecting 1D channels containing these guest DMF molecules are visible along the *b* and *c* axes, figure 73.

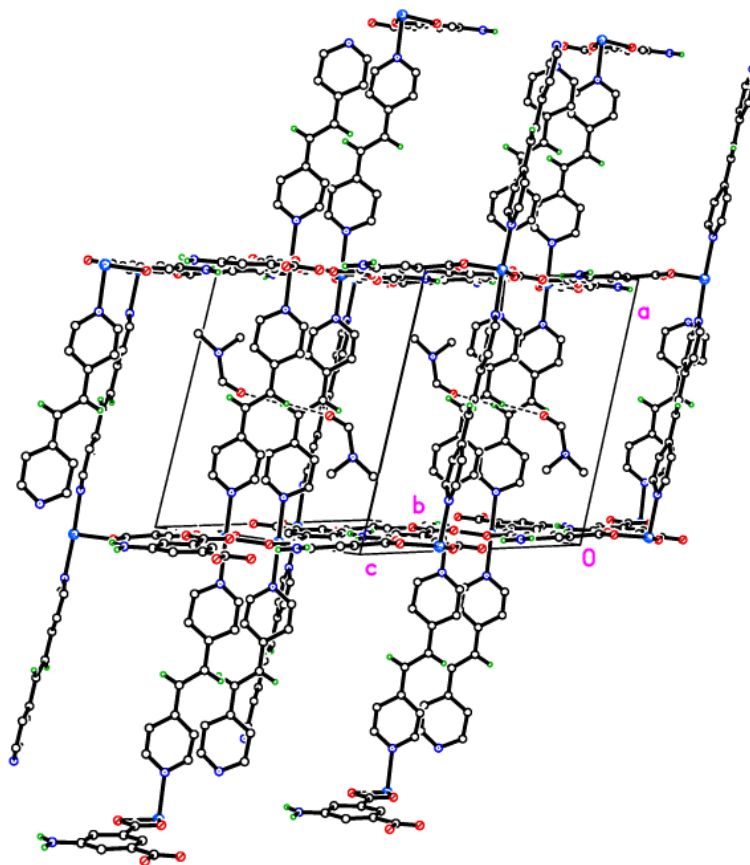
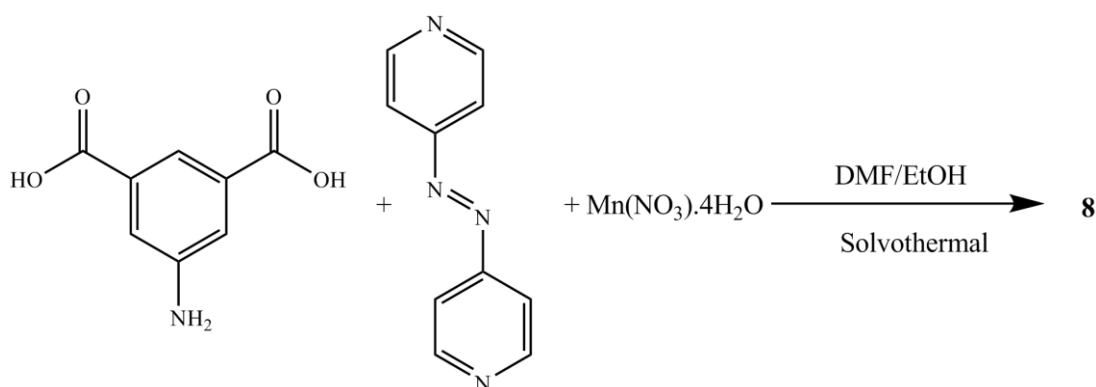


**Figure 73.** Diagram of the extended structure of **7** showing the hydrogen bond DMF molecules situated inside the pores. Carbon atoms are represented by empty circles. Nitrogen, oxygen and manganese atoms are coloured blue, red and dark blue respectively. Hydrogen atoms are omitted for clarity.

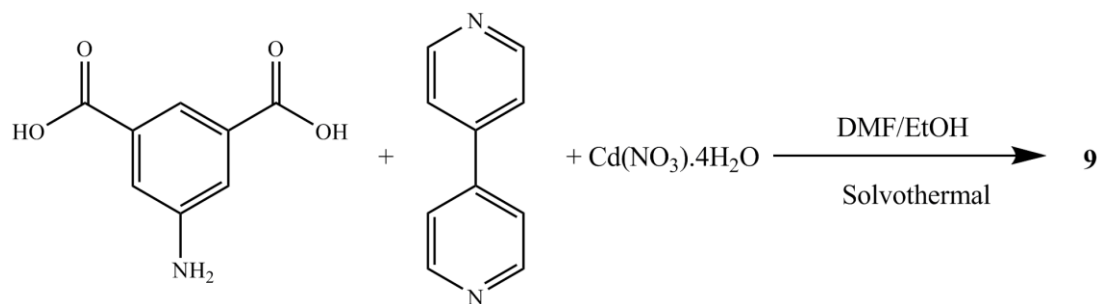


**Scheme 7.** The synthetic route for the preparation of  $\{[\text{Mn}(5\text{-AIP})(4,4'\text{-azopy})]\cdot\text{DMF}\}_n$  **8**.

The reaction of  $\text{H}_2\text{-5-AIP}$  and 4,4'-azopy with  $\text{Mn}(\text{NO}_3)_2\cdot 4\text{H}_2\text{O}$  under solvothermal conditions, following scheme 7, also afforded a crystalline solid in good yield,

however in this example the red prisms were not of adequate quality to collect data by single crystal X-ray diffraction. Multiple attempts to re-synthesise **8** gave poor X-ray data due to extensive twinning, which could not be resolved. Elemental analyses conducted on samples of the crystals which had been dried by heating to 120 °C under dynamic vacuum for 12 h gave the formula  $\{[\text{Mn}(5\text{-AIP})(4,4'\text{-azopy})]\}$ , with the powder X-ray pattern collected for **8** mirroring the pattern simulated for the cobalt analogue of this structure **5**, with similar line spacing and intensities observed for both structures. This data combined with TGA and gas sorption data, which also exhibit similar behaviours, offer good evidence of the isostructurality of **8** with the previous four examples. A weight loss of 15% in the 30-200 °C range as determined by thermogravimetric analyses, equates to the loss of one DMF molecule per formula unit giving a formula of  $\{[\text{Mn}(5\text{-AIP})(4,4'\text{-azopy})]\cdot\text{DMF}\}_n$  for structure **8**.

#### 2.2.4. Cadmium structures



**Scheme 8.** The synthetic route for the preparation of  $\{[\text{Cd}(5\text{-AIP})(4,4'\text{-bipy})]\cdot 3\text{DMF}\}_n$  **9**.

Employment of the same reaction conditions used in the preparation of **7** with the substitution of the metal nitrate with cadmium nitrate tetrahydrate, following scheme 8, afforded **9** as colourless prisms. Elucidation of the structure of **9** by single crystal X-ray diffractometry reveals the isostructurality of this framework with the five described previously, however minor differences are observed in the coordination modes of the carboxylate groups. In this example the larger coordination sphere arising from the use of  $\text{Cd}^{2+}$  allows the chelation of carboxylate moieties from two different 5-AIP units to each metal node, with the O(4) atoms of each of these units bridging to a second  $\text{Cd}^{2+}$  centre. In this manner each metal centre bonds to three 5-AIP units in the *a/b* plane, with pyridinyl nitrogens bound in the apical positions giving heptacoordinate metal centres exhibiting distorted pentagonal bipyramidal

geometry, figure 74. Although the hydrogen atoms associated with each  $\text{-NH}_2$  group could not be resolved satisfactorily due to the disorder of their parent molecules over two positions, it is clear that these groups are involved in hydrogen bonding with the  $\text{O}(1')$  and  $\text{O}(3'')$  atoms of the neighbouring 5-AIP units due to the proximity to  $\text{N}(3)$  of 2.94 and 3.0 Å respectively. The disorder observed in the 5-AIP units can in fact be attributed to these H-bonding interactions, as the preferred pyramidal geometry of the  $\text{-NH}_2$  group can be achieved by its approach to the carboxylate oxygens from either side of the  $a/b$  plane.

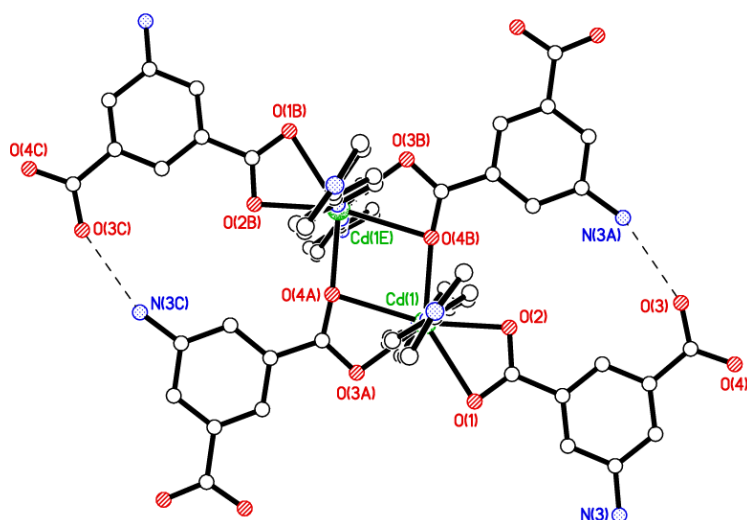


**Figure 74.** Diagram of  $\{[\text{Cd}(5\text{-AIP})(4,4'\text{-bipy})].3\text{DMF}\}_n$ , **9**, showing the coordination environment around the  $\text{Cd}^{2+}$  nodes. Hydrogen bonding interactions are represented by dotted lines. Carbon atoms are represented by empty circles and nitrogen atoms are coloured blue. Hydrogen atoms are omitted for clarity.

The extended structure of **9** is formed by the coordination of 4,4'-bipy units in the apical positions of the metal nodes. These neutral linkers, observed parallel to the  $c$  axis, link 2D  $[\text{Cd}(5\text{-AIP})]_n$  sheets in to an extended 3D framework exhibiting intersecting 1D pores of 3.21 x 8.30 Å and 3.96 x 8.30 Å, figure 75. Badly disordered guest molecules situated inside these pores could not be resolved satisfactorily, however the PLATON squeeze procedure recovered 488 electrons situated in one void per unit cell, situated around the 4,4'-bipy linkers. This data, in conjunction with point atom observations lead to the conclusion that twelve DMF molecules per unit cell, or three per formula unit are present in the as synthesised framework.

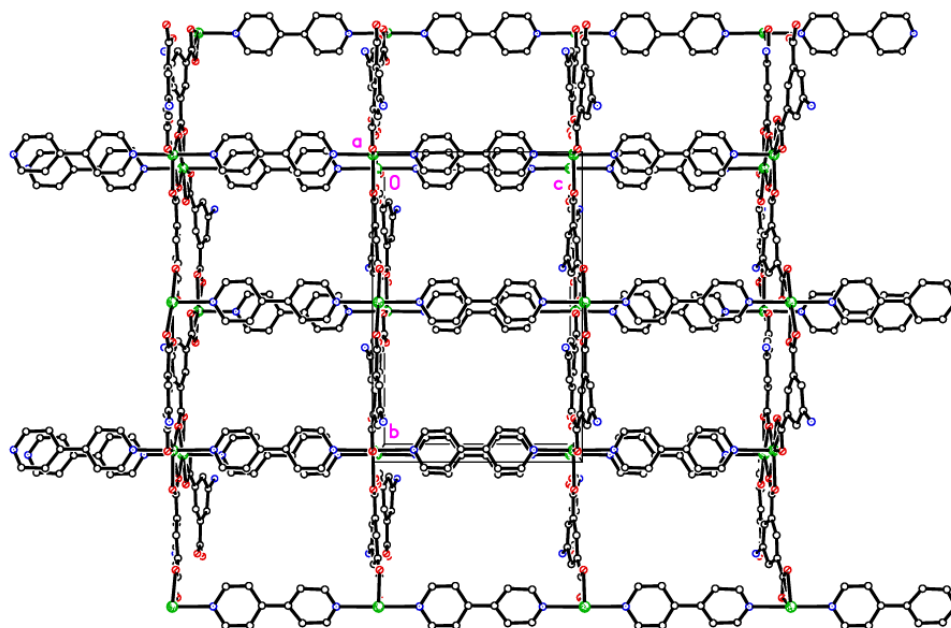
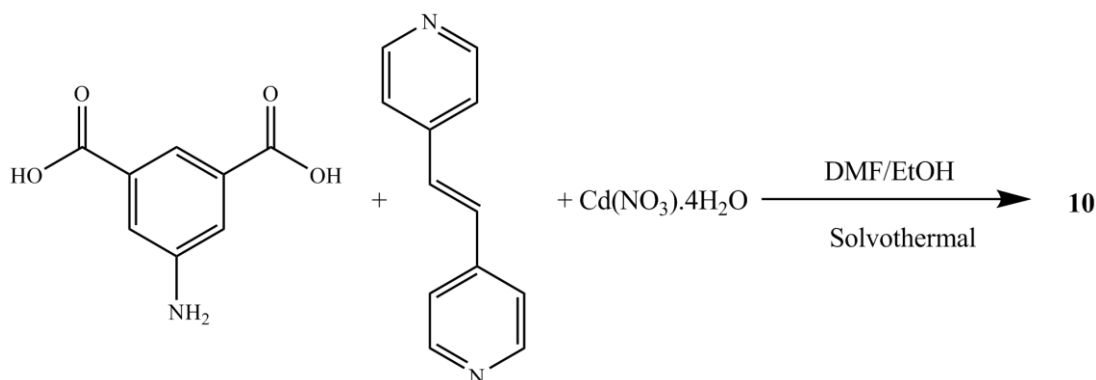


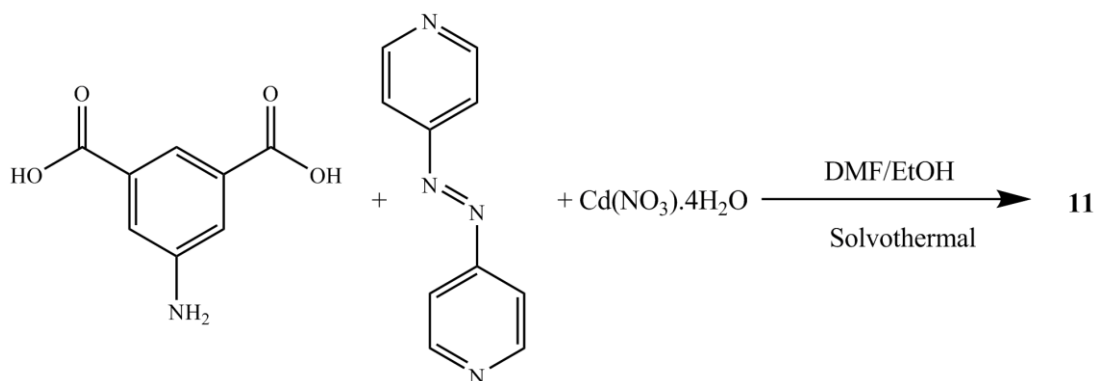
**Figure 75.** Diagram of **9** showing the extended structure as viewed along the *a* axis. Carbon atoms are represented by empty circles. Nitrogen, oxygen and cadmium atoms are coloured blue, red and green respectively. Hydrogen atoms are omitted for clarity.



**Scheme 9.** The synthetic route for the preparation of  $\{[\text{Cd}(\text{DPE})(4,4'\text{-bipy})].1.7\text{DMF}\}_n$  **10**.

The reaction of  $\text{H}_2$ -5-AIP and DPE with  $\text{Cd}(\text{NO}_3)_2 \cdot 4\text{H}_2\text{O}$  following scheme 9, afforded a large quantity of pale yellow needles on which multiple attempts to collect single crystal X-ray diffraction data were made. These attempts failed to provide a data set of suitable quality for structural elucidation due to extensive twinning, which could not be resolved. Elemental analyses performed on samples of the crystals which had been dried by heating to  $120\text{ }^\circ\text{C}$  under dynamic vacuum for 12

h gave the formula  $[\text{Cd}(\text{DPE})(4,4'\text{-bipy})]$ , with powder X-ray diffraction patterns collected for the as-synthesised compound showing almost identical line spacing and intensities as the simulated pattern for **7**. These data, combined with the similarities between the TGA and gas adsorption behaviours of this structure and the previous six examples confirm the isostructurality of **10**.



**Scheme 10.** The synthetic route for the preparation of  $\{[\text{Cd}(5\text{-AIP})(4,4'\text{-azopy})]\cdot\text{DMF}\}_n$  **11**.

The solvothermal reaction of H<sub>2</sub>-5-AIP and 4,4'-azopyridine with  $\text{Cd}(\text{NO}_3)_2\cdot 4\text{H}_2\text{O}$  was conducted following scheme 10, affording **11** as red prisms, which were of suitable quality for single crystal X-ray diffraction. Elucidation of the structure revealed very different topology to the frameworks detailed previously. In this example, each  $\text{Cd}^{2+}$  node has a pentagonal bipyramidal geometry, coordinating to two chelating carboxylate groups from different molecules and a pyridinyl nitrogen in the pentagonal plane, and to a DMF molecule and an amine nitrogen in the axial plane, figure 76.

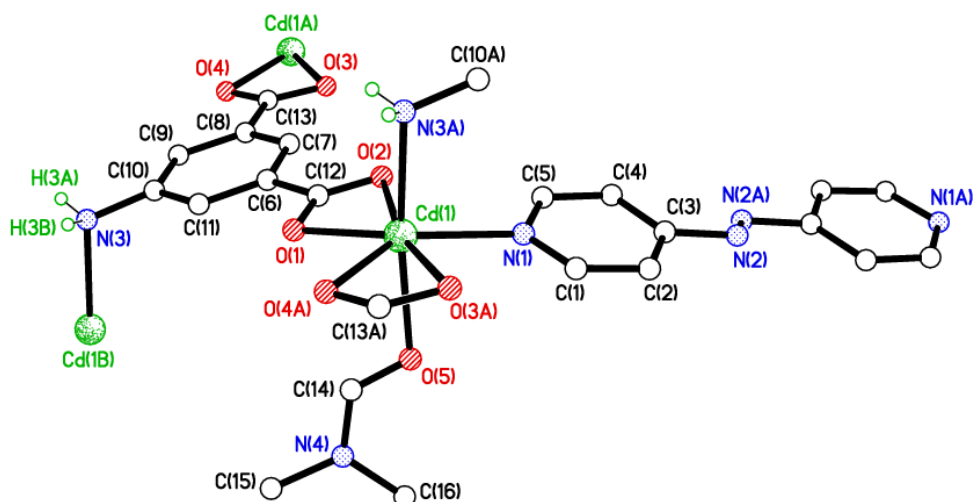


**Figure 76.** Diagram of  $\{[\text{Cd}(\text{5-AIP})(\text{4,4'-azopy})].\text{DMF}\}_n$ , **11**, showing the coordination environment around the metal nodes. Hydrogen atoms, except those involved in hydrogen bonding are omitted for clarity.

Covalent bonding propagates in the  $a/c$  plane, forming bilayer sheets of Cd(5-AIP) linked *via* the coordinate bonding of the dipyridyl. As with the 3D hybrid covalent/H-bonded frameworks **1** and **2**, significant hydrogen bonding interactions between the bilayer sheets, in this example between the  $\text{NH}_2$  groups and O(1) and O(4), link them in to the extended 3D structure, figure 77, however unlike these examples there are no large voids filled with disordered solvent. Only one DMF molecule per formula unit is observed in this structure, located in the intersecting 1D channels of dimensions  $3.89 \times 6.54 \text{ \AA}$  and  $3.77 \times 7.18 \text{ \AA}$  extending in the  $a$  and  $b$  axes respectively, and coordinated to the  $\text{Cd}^{2+}$  centre *via* the aldehydic oxygen.

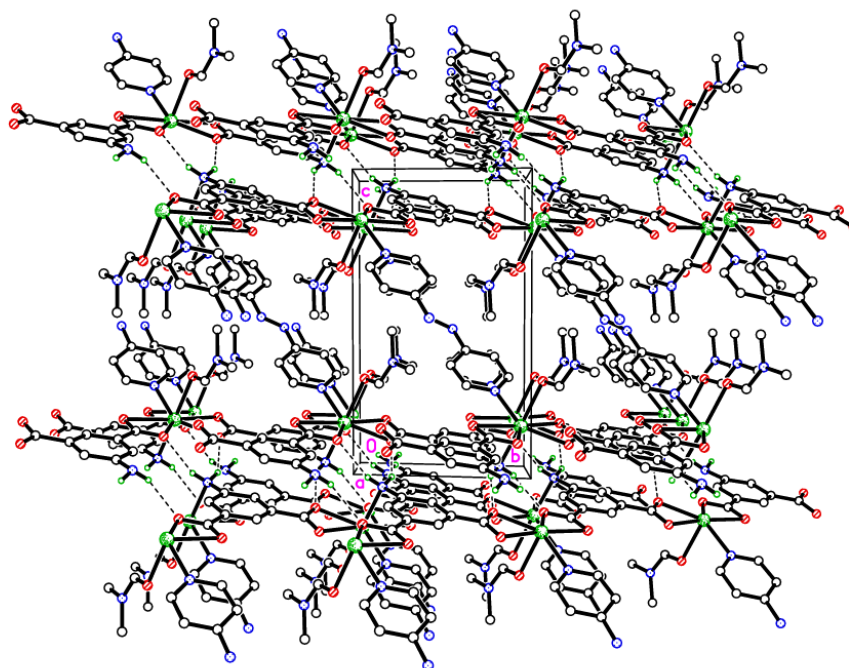


**Figure 77.** Diagram of the extended structure of **11** as viewed along the *a* axis. Coordinated DMF molecules are visible between the 4,4'-azopy units. Hydrogen bonding is represented as dotted lines between the bilayer sheets. Carbon atoms are represented by empty circles. Nitrogen, oxygen and cadmium atoms are coloured blue, red and green respectively. Hydrogen atoms, except those involved in hydrogen bonding, are omitted for clarity.

### 2.2.5. Thermogravimetric analysis

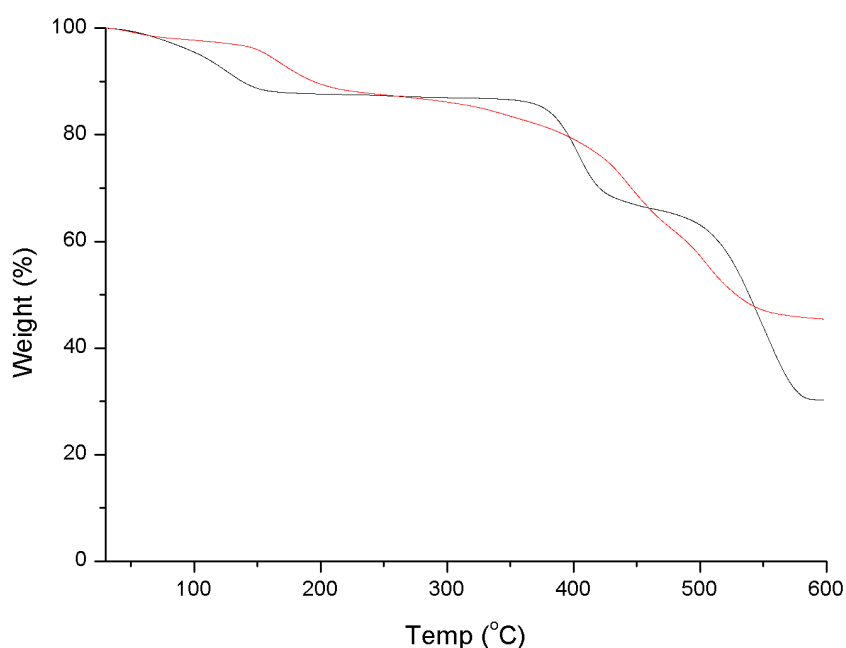


**Figure 78.** Recorded TGA data for Structures **1** (black) and **2** (red).

Thermogravimetric analyses of all the frameworks reported herein were performed between 30 and 600 °C under an inert carrier flow (N<sub>2</sub>) in order to further examine their structural properties. Analysis of structure **1**, revealed a single stage weight loss of *ca.* 12 % between 30-180 °C which can be attributed to the loss of one DMF molecule per formula unit from the pores. The framework then maintains structural stability up to 380 °C at which point a second weight loss of *ca.* 20% indicates the thermal decomposition of one of the organic linkers. This decomposition continued at temperatures in excess of 450 °C with another large weight loss of *ca.* 35 % indicating the complete thermal decomposition of the framework. Analysis of structure **2** revealed a similar weight loss in the range of 150-250 °C with the loss of *ca.* 12 % attributed to the removal of one DMF molecule per formula unit from the pores, however the continuous and rapid weight loss associated with thermal decomposition commences at around 280 °C and continues to 550 °C, figure 78. It is of note that this decomposition occurs almost immediately after the removal of the guest solvent molecules, suggesting the reduced structural stability of the desolvated **2** compared to **1**.

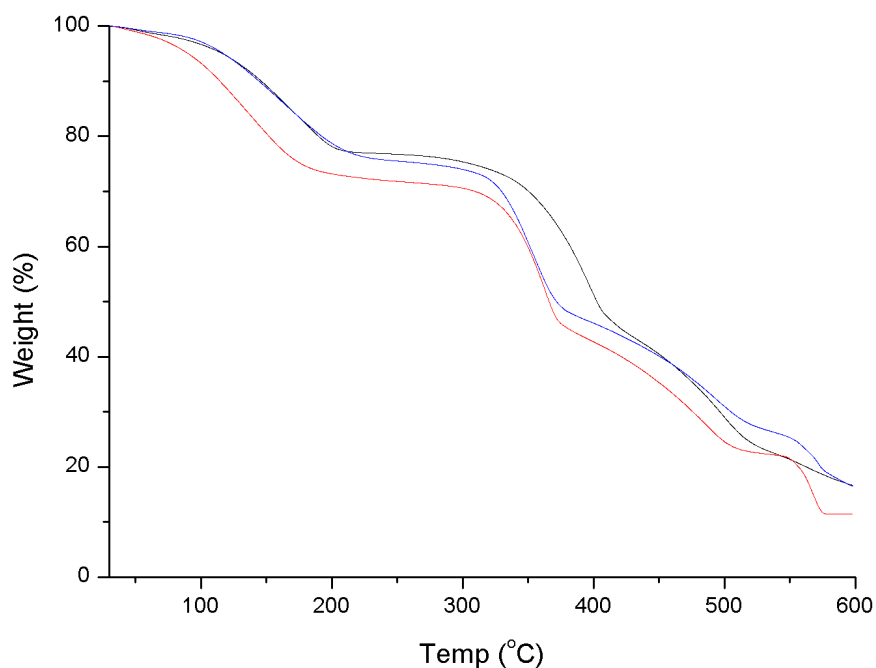


**Figure 79.** Recorded TGA data for structures **3** (black), **4** (red) and **5** (blue).

TGA analyses performed on structures **3-5** revealed weight losses for all three structures in the same region, figure 79. For structure **3**, the initial weight loss of *ca* 23 % between 30 and 230 °C can be attributed to the removal of 4 ethanol guest molecules per formula unit from the pores (calculated 20.1 %). Whilst only two ethanol molecules are resolved satisfactorily in the single crystal X-ray diffraction data, the presence of further guest molecules in the pores is suggested by microanalyses performed on the framework. The MOF then maintained stability up to 300 °C at which point a second loss of *ca* 22 % in the 300-400 °C range can be ascribed to the thermal decomposition of one of the organic linkers. Above 400 °C, the rapid onset of weight loss is indicative of the complete thermal decomposition of the framework. A similar pattern was observed for structure **4** with an initial weight loss of *ca* 28 % in the 30-230 °C region attributable to the removal of 3 DMF molecules per formula unit (calculated 34.0 %). Again the desolvated framework maintains stability up to 300 °C, at which point the thermal decomposition of the framework proceeds in two stages. Structure **5** follows the same pattern with a 24 % weight loss in the 30-230 °C range attributed to the loss of 2 DMA molecules per formula unit (calculated 29.2 %), with the thermal decomposition of the framework beginning at 300 °C. It is of interest that **4** and **5** begin to decompose at a slightly

lower temperature than **3**, due to the decreased thermal stability of the neutral pillaring linkers.

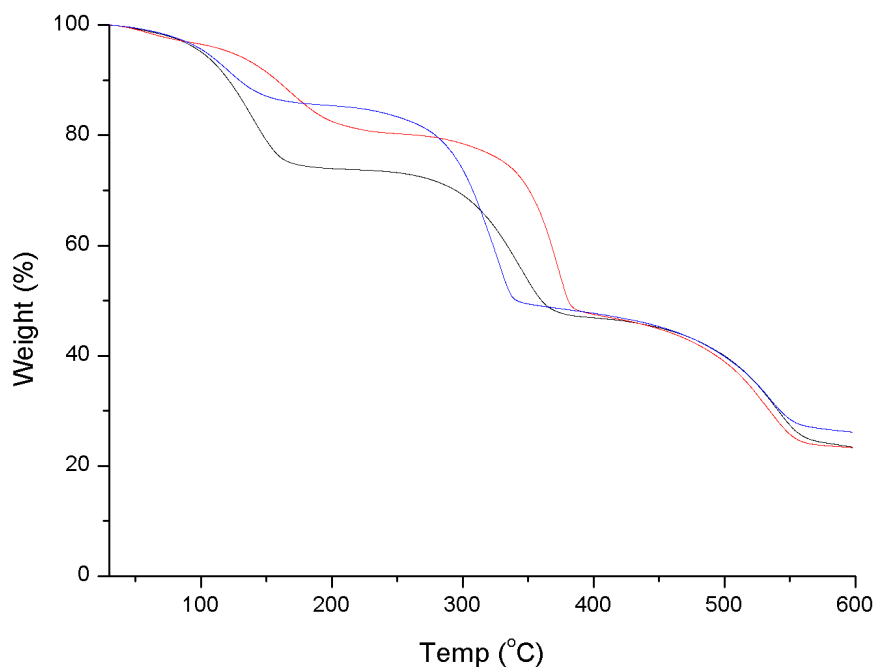


**Figure 80.** Recorded TGA data for structures **6** (black), **7** (red) and **8** (blue).

Analogous weight losses to those observed in structures **3-5** are seen in the TGA data collected for structures **6-8**, figure 80. For structure **6** an initial weight loss of *ca.* 27 % in the range 100-160 °C was attributed to the loss of the 2 DMA molecules resolved by X-ray diffraction (calculated 31.0 %), with the commencement of thermal decomposition accounting for the *ca.* 23 % loss in the range 250-370 °C. Structure **7** undergoes an initial loss of ~20 % in the 80-220 °C range equating to the loss of the 1.5 DMA molecules per formula unit (calculated 20.8 %), with thermal decomposition proceeding at temperatures in excess of 300°C. For structure **8** a smaller weight loss of *ca.* 15 % in the 30-200 °C temperature range equates to the loss of one DMF molecule per formula unit (calculated 14.9 %), with the onset of thermal decomposition occurring at 250 °C.

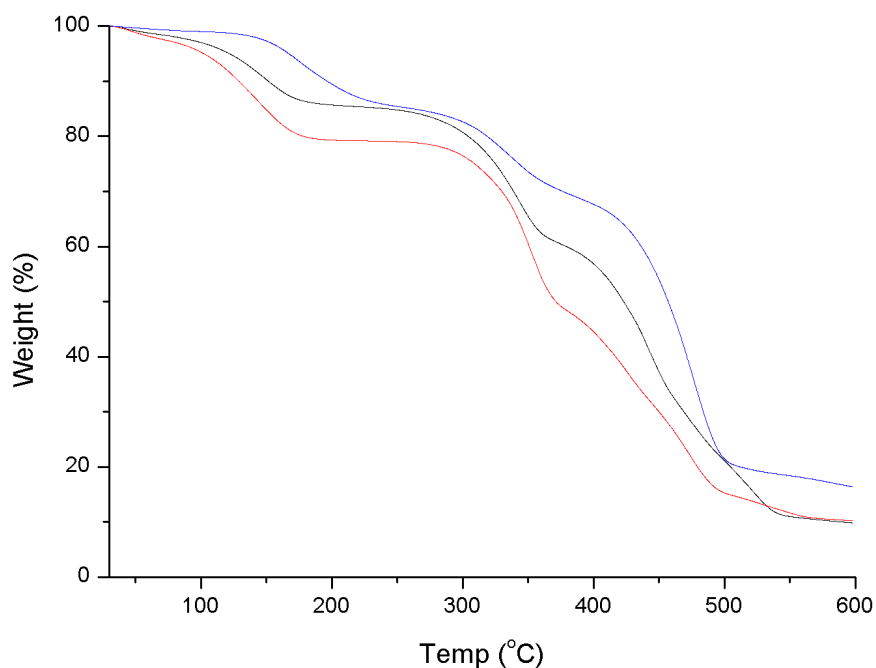


**Figure 81.** Recorded TGA data for structures **9** (black), **10** (red) and **11** (blue).

TGA data recorded for **9**, **10** and **11** follow a similar pattern to those described previously albeit with smaller percentage losses recorded for all three structures, figure 81. Structure **9** undergoes an initial weight loss of 14.3 % in the 30-200°C range, which accounts for only 1 of the 3 DMF guest molecules per formula unit suggested by crystallographic analysis (calculated 14.4 %), Elemental analyses conducted on the as-synthesised **9** match the TGA data, suggesting that **9** contains only one DMF molecule per formula unit, giving the formula  $\{[\text{Cd}(5\text{-AIP})(4,4'\text{-bipy})].\text{DMF}\}_n$ . At 250 °C the thermal decomposition of **9** commences, with the step-wise weight loss observed in excess of this temperature arising from the decomposition of each constituent of the framework in turn. Structure **10** undergoes a larger loss of 20.7 % in the same region, equating to the loss of 1.7 DMF molecules per formula unit (calculated 20.7 %). Structure **11** demonstrated a weight loss of *ca* 13% in the 150-250 °C range which can be ascribed to the removal of a single DMF molecule per formula unit (calculated 13.4 %). The elevated temperature required to remove this molecule compared to **9** and **10** is expected due to the coordination of the DMF to the  $\text{Cd}^{2+}$  centre. Thermal decomposition for all three structures begins at 270 °C and continues up to 600 °C mirroring the data collected for the manganese structures **6-8**.

### 2.2.6. Gas adsorption behaviour

CO<sub>2</sub> uptake behaviours for structures **1-11** were recorded at 273 K at pressures up to 1 atmosphere. All samples were prepared for CO<sub>2</sub> adsorption studies *via* solvent exchange, by immersion in chloroform for 2 weeks, during which time the solvent was replaced four times. Samples were activated prior to testing by heating to 120 °C for 12 h under dynamic vacuum.

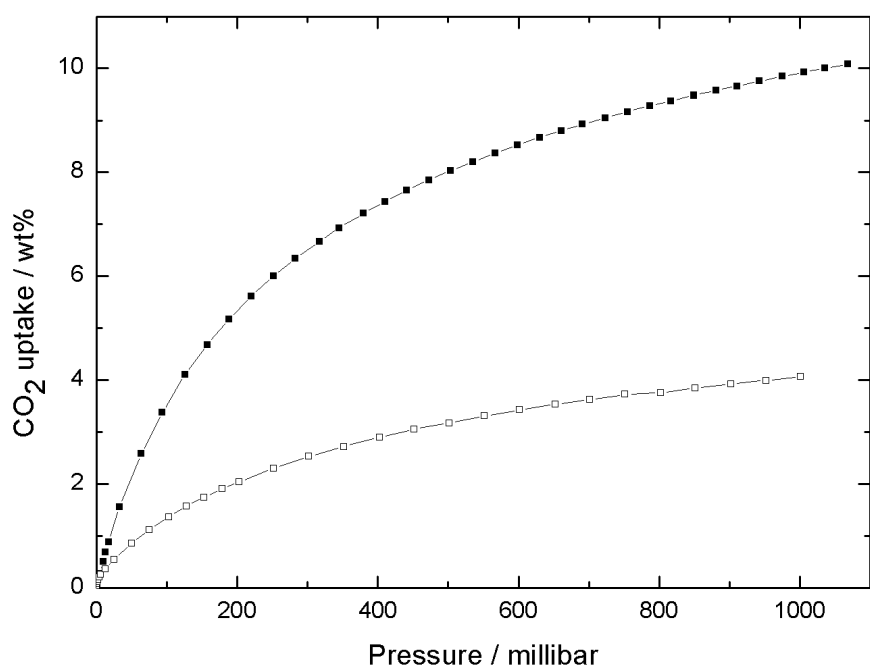


**Figure 82.** CO<sub>2</sub> adsorption isotherms recorded for **1** (filled squares) and **2** (empty squares) at 273 K.

The CO<sub>2</sub> adsorptions recorded for **1** and **2** follow the type I isotherm as defined by the IUPAC classification, offering evidence of the permanent microporosity of these two structures. **1** showed markedly increased CO<sub>2</sub> uptake of 10.08 % compared to 4.00 % at 273 K and 1 atm for **2**, figure 82. Though **2**, comprising pillaring linkers bearing the N=N moiety, was expected to exhibit enhanced CO<sub>2</sub> binding properties, this is not the case. The difference can however be explained by the reduced structural stability of **2**, as demonstrated by TGA. It can therefore be concluded that the removal of guest solvent molecules from **2** led to the partial collapse of the framework and a concomitant loss of porosity. It is of particular note that at pressures up to 1 atm the plateau associated with complete Langmuir monolayer

surface coverage is not observed, indicating that these structures are capable of binding larger quantities of CO<sub>2</sub> at higher pressures.

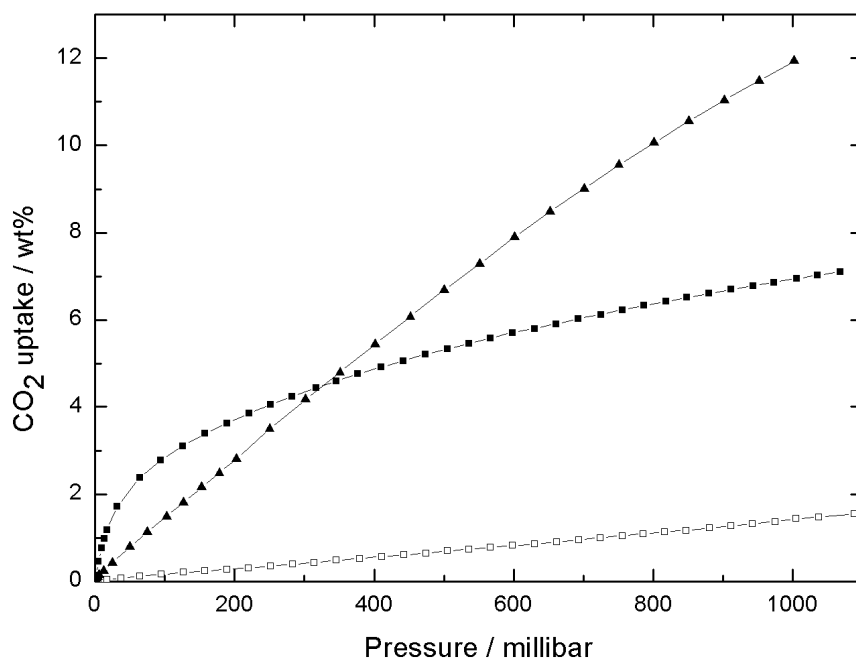


**Figure 83.** CO<sub>2</sub> adsorption isotherms recorded for **3** (filled squares) and **4** (empty squares) and **5** (filled triangles) at 273 K.

The permanent microporosity of the structures **3**, **4** and **5** is also evidenced by the type I isotherms recorded for their CO<sub>2</sub> uptake, figure 83. However in these examples, the differences in architecture of the frameworks led to profound differences in their gas uptake behaviour. **3** exhibited rapid CO<sub>2</sub> adsorption at pressures up to 100 mbar, with an uptake of *ca* 3 wt% recorded in this region. This rate however decreased with increasing pressure giving a maximum uptake of 7.04 wt% at 1067 mBar. Structures **4** and **5** are isostructural, and displayed similar patterns for CO<sub>2</sub> uptake, albeit with a large difference in the maximum recorded uptakes of 1.54 wt% at 1067 mBar for **4** and 11.94 wt% at 1001 mBar for **5**. Given the similarities in the lengths of DPE and 4,4'-azopy, this difference is unlikely to be due to differences in pore size.

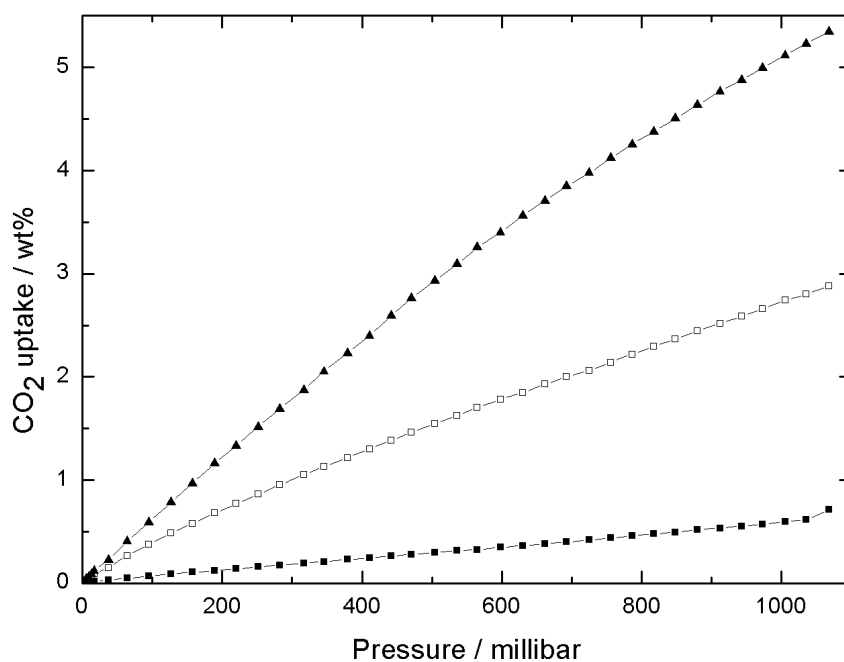


**Figure 84.** CO<sub>2</sub> adsorption isotherms recorded for **6** (filled squares) and **7** (empty squares) and **8** (filled triangles) at 273 K.

The CO<sub>2</sub> adsorption isotherms recorded for structures **7** and **8**, figure 84, also demonstrated type I adsorption, providing evidence for the successful preparation of permanently microporous solids, however the data recorded for **6** followed the type III pattern, suggesting a lack of porosity and giving an uptake of only 0.72 wt%. TGA and crystallographic data collected for this structure demonstrated that it does indeed exhibit porosity, however the intersecting pores of 2.67 x 8.21 Å and 1.38 x 8.21 Å were too small to allow the permeation of CO<sub>2</sub> molecules which bear a kinetic diameter of 3.3 Å. Uptakes of 2.88 and 5.34 wt% at 273 K and 1 atm, for **7** and **8**, whilst modest, followed the expected pattern for this series of isostructural frameworks. The increase in CO<sub>2</sub> uptake observed for **7** in comparison to **6** can be accounted for by the increase in pore size resulting from the use of the longer DPE pillaring linker. In the case of **8**, the increase in uptake was not ascribed to a further increase in pore size, due to the similarity in lengths of the DPE and 4,4'-azopy linker, but rather to the increased affinity of the N=N moiety to polar gases. As with all previous examples, no plateau was observed, indicating that pressures up to 1 atm were insufficient for the formation of a complete Langmuir monolayer on the

internal surface of the pores, hence higher CO<sub>2</sub> uptake is expected at pressures in excess of 1 atm.

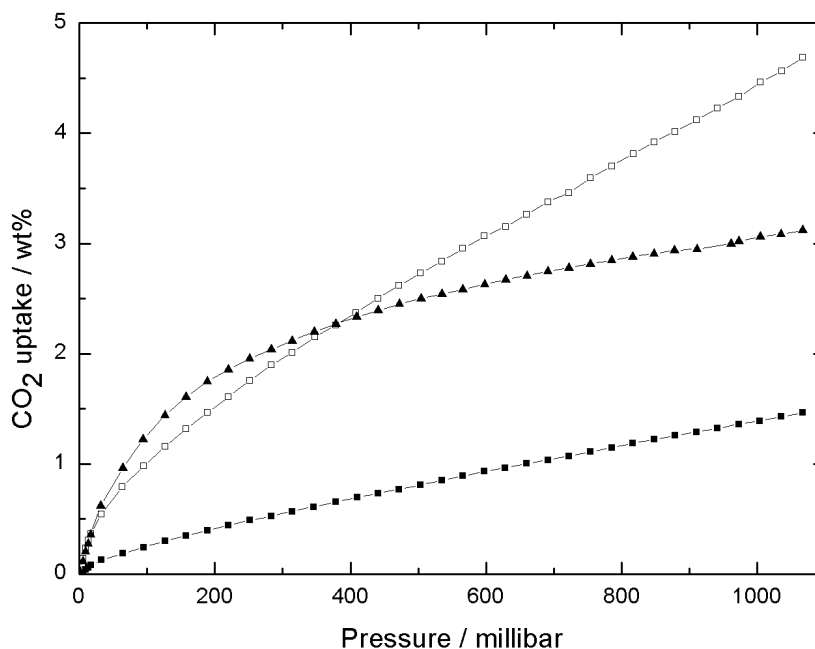


**Figure 85.** CO<sub>2</sub> adsorption isotherms recorded for **9** (filled squares) and **10** (empty squares) and **11** (filled triangles) at 273 K.

CO<sub>2</sub> adsorption isotherms recorded for **9-11** once again exhibit the type I pattern as defined by the IUPAC classification, hence the permanent microporosity of these solids is confirmed. The pattern observed here is similar to the previous examples, with the isostructural frameworks **9** and **10** showing similar patterns for uptakes of CO<sub>2</sub>, adsorbing 1.46 wt% and 4.69 wt% respectively at 1067 mBar and 273 K. Due to the similarities in chemical environments within the pores of these two structures this increase in CO<sub>2</sub> uptake performance can only be ascribed to the increase in pore size resulting from the substitution of the 4,4'-bipy linker with DPE. Comparison of the adsorption data for **10** with the isostructural frameworks **4** and **7**, which also contain the DPE linker reveals interesting behaviour. Due to the use of the same organic-linkers in these three examples very similar chemical environments within the pores are expected, with the close agreement of line spacing in the powder X-ray patterns for these frameworks confirming that these structures bear very similar pore sizes. It would therefore be expected that the uptakes for these frameworks on a

weight percentage basis would follow the pattern  $Mn > Co > Cd$ , however this is not the case. At 4.69 wt% the uptake for **10** is far greater than for **7** (2.88 wt%) and **4** (1.54 wt%), hence the presence of the  $Cd^{2+}$  centre appears to have a positive effect on the  $CO_2$  capacity of the MOF. Structure **11** differs from **9** and **10**, with an increased rate of  $CO_2$  adsorption at pressures below 200 mBar. Above this pressure the rate of  $CO_2$  uptake decreases markedly, with the structure achieving an uptake of only 3.12 wt% at 1067mBar. It is of note that even though desolvated structure bears coordinatively unsaturated  $Cd^{2+}$  centres, and polar  $N=N$  moieties which should increase the binding affinity of polar gas molecules, **11** has a greater density than the previous two examples, bearing a similar bilayer structure to **1** and **2**. Gas adsorption measurements on a weight percentage basis are, therefore, expected to be lower than for **9** and **10**. Concomitant with this are reduced pore dimensions for this structure which, at  $3.89 \times 6.54 \text{ \AA}$  and  $3.77 \times 7.18 \text{ \AA}$ , are only just large enough to allow the diffusion of  $CO_2$  molecules. The presence of high affinity binding sites within narrow pores may therefore explain the behaviour observed in the isotherm, with the fast adsorption of  $CO_2$  molecules to high affinity sites near the surface of the bulk solid blocking access to the rest of the material.

### 2.3. Conclusion

Eleven 2D and 3D MOFs have been synthesised using the solvothermal reaction of 5-aminoisophthalic acid with the nitrates of zinc, cobalt, manganese and cadmium in the presence of the neutral pillaring linkers 4,4'-bipy, DPE and 4,4'-azopy. The MOFs have been structurally characterised, and their porosities and  $CO_2$  adsorption behaviours probed.

In the first two examples the reaction of zinc nitrate with 5-AIP and the pillaring linkers 4,4'-bipy and 4,4'-azopy afforded two isostructural frameworks exhibiting a bilayer motif, with extensive hydrogen bonding between the bilayers giving 3D hybrid H-bonded/covalent structures. Both frameworks adsorb modest quantities of carbon dioxide at pressures up to 1 bar, with the performance of the 4,4'-bipy framework exceeding that of the 4,4'-azopy analogue. Previous research has demonstrated the enhanced uptake of polar gases in MOFs which contain the  $N=N$  moiety versus those which do not, hence this result was not expected. Thermogravimetric analyses however, reveal diminished structural stability for the

desolvated 4,4'-azopy analogue, hence the reduced CO<sub>2</sub> uptake is attributed to the partial collapse of the framework on desolvation, with a concomitant loss of porosity.

The third example, resulting from the reaction of cobalt nitrate with 5-aminoisophthalic acid and 4,4'-bipy, exhibits a porous 3D structure based on the pillaring of Co(5-AIP) sheets with the pyridinyl linker, with the chelation of one nitrate group per metal centre giving a bulk material bearing pores lined with these polar functions. CO<sub>2</sub> uptake for this structure at pressures up to 1 bar is also modest, however comparison of gas adsorption behaviour of this structure with the pillar/layer structures **4-10** reveals the beneficial effect of the presence of coordinated nitrate groups. MOFs **4-10** are isostructural, comprising 2D sheets of 5-AIP coordinated to metal centres, with the neutral linkers pillaring these sheets in to the extended 3D structures. This isostructurality enables the investigation of pore size and functionality on gas uptake behaviour and reveal increased CO<sub>2</sub> uptake for those structures which bear larger pores due to the substitution of 4,4'-bipy with DPE. Gas uptakes are further enhanced by the incorporation of a polar functionality, by the substitution of DPE with 4,4'-azopy. In the case of **3**, however, the presence of coordinated nitrate groups results in far greater gas uptake for the 4,4'-bipy containing structure than for the DPE example, **4**. The last of the structures reported in this chapter results from the reaction of cadmium nitrate with H<sub>2</sub>-5-AIP and 4,4'-azopy and exhibits a bilayer structure reminiscent of **1** and **2**. Despite the fact that this structure has smaller pores and a higher density than **4-10** its CO<sub>2</sub> uptake is comparable, due to the presence of coordinatively unsaturated metal centres and polar N=N moieties.

Although the hydrogen uptake behaviours and gas separation capabilities of these frameworks has not been investigated, the relatively small pores sizes observed in all of the structures and the incorporation of polar functionalities, warrants further research. It is expected that those structures which bear the N=N moiety, coordinated nitrate groups or coordinatively unsaturated metal centres will exhibit the greatest selectivity and hydrogen uptakes, with the narrow pore dimensions having a beneficial effect on the adsorption of molecular hydrogen.

## 2.4. References

- 1 a) K. Koh, A. G. Wong-Foy, A. J. Matzger, *Chem. Commun.*, 2009, **41**, 6162. b) H. Deng, C. J. Doonan, H. Furukawa, R. B. Ferreira, J. Towne, C. B. Knobler, B. Wang, O. M. Yaghi, *Science*, 2010, **327**, 846.
- 2 a) H. Chun, D. N. Dybtsev, H. Kim, K. Kim, *Chem.–Eur. J.*, 2005, **11**, 3521. b) A. D. Burrows, C. G. Frost, M. F. Mahon, C. Richardson, *Angew. Chem. Int. Ed.*, 2008, **47**, 8482.
- 3 B. Yan, R. Ma, Z. Chu, L. Q. Ding, Y. Long, L. L. Chen, X. Q. Lu, F. Bao, *J. Inorg. Organomet. Polym.*, 2010, **20**, 809.
- 4 a) T. Fukushima, S. Horike, Y. Inubushi, K. Nakagawa, Y. Kubota, M. Takata, S. Kitagawa, *Angew. Chem. Int. Ed.*, 2010, **49**, 4820. b) D. N. Dybtsev, H. Chun, K. Kim, *Angew. Chem. Int. Ed.*, 2004, **43**, 5033.
- 5 H. J. Park, M. P. Suh, *Chem. Eur. J.*, 2008, **14**, 8812.
- 6 K. M. L. Taylor-Pashow, J. Della Rocca, Z. Xie, S. Tran, W. Lin, *J. Am. Chem. Soc.*, 2009, **131**, 14261.
- 7 W. Kleist, F. Jutz, M. Maciejewski, A. Baiker, *Eur. J. Inorg. Chem.*, 2009, 3552.
- 8 H. Li, M. Eddaoudi, T. L. Groy, O. M. Yaghi, *J. Am. Chem. Soc.* 1998, **120**, 8571.
- 9 K. Seki, *Phys. Chem. Chem. Phys.*, 2002, **4**, 1968.
- 10 B. Q. Ma, K. L. Mulfort, J. T. Hupp, *Inorg. Chem.*, 2005, **44**, 14.
- 11 Z. Chen, S. Xiang, H. D. Arman, J. L. Mondal, P. Li, D. Zhao, B. Chen, *Inorg. Chem.*, 2011, **50**, 3442.
- 12 S. Henke, A. Schneemann, S. Kapoor, R. Winter, R. A. Fischer, *J. Mater. Chem.*, 2012, **22**, 909.
- 13 L. F. Song, C.H. Jiang, C. L. Jiao, J. Zhang, L. X. Sun, F. Xu, W. S. You, Z. G. Wang, J. J. Zhao, *Cryst. Growth Des.*, 2010, **10**, 12.
- 14 a) M. A. Nadeem, M. Bhadbhade, R. Bircher, J. A. Stride, *Cryst. Growth Des.*, 2010, **10**, 9. b) Y. Hijikata, S. Horike, D. Tanaka, J. Groll, M. Mizuno, J. Kim, M. Takatade, S. Kitagawa, *Chem. Commun.*, 2011, **47**, 7632 .c) Z. Hulvey, J. D. Furman, S. A. Turner, M. Tang, A. K.

- 
- Cheetham, *Cryst. Growth Des.*, 2010, **10**, 5.d) Y. Gong, Y. Zhou, J. Li, R. Cao, J. Qin, J. Li, *Dalton Trans.*, 2010, **39**, 9923.
- 15 Z. P. Deng, Z. Y. Zhang, L. H. Huo, S. W. Ng, H. Zhao, S. Gao, *CrystEngComm*, 2012, **14**, 6548.
- 16 H. Y. He, Y. L. Zhou, Y. Hong, L. G. Zhu, *J. Mol. Struct.*, 2005, **737**, 97.
- 17 R. K. Feller, A. K. Cheetham, *Dalton Trans.*, 2008, 2034.
- 18 X. Li, R. Cao, D. Sun, W. Bi, Y. Wang, X. Li, M. Hong, *Cryst. Growth Des.*, 2004, **4**, 4.
- 19 C. D. Wu; C. Z. Lu; W. B. Yang; H. H. Zhuang, J. S. Huang, *Inorg. Chem.*, 2002, **41**, 3302.
- 20 K. O. Kongshaug, H. Fjellvåg, *Inorg. Chem.*, 2006, **45**, 2424.
- 21 H. N. Wang, X. Meng, C. Qin, X. L. Wang, G. S. Yang, Z. M. Su, *Dalton Trans.*, 2012, **41**, 1047.
- 22 a) R. Idem, M. Wilson, P. Tontiwachwuthikul, A. Chakma, A. Veawab, A. Aroonwilas, D. Gelowitz, *Ind. Eng. Chem. Res.*, 2006, **45**, 8. b) O. F. Dawodu, A. J. Meisen, *Chem. Eng.*, 1996, **74**, 960. c) T. Charkravarty, U. K. Phukan, R. H. Weiland. *Chem. Eng. Prog.*, 1985, **81**, 32.

## **Chapter 3**

### **Pillared metal-organic frameworks based on a reduced Schiff base dicarboxylic acid**

### 3.1. Introduction

The construction of mixed linker MOFs bearing alkylamino, arylamino and pyrimidine moieties is well documented, with enhanced uptakes for molecular hydrogen and carbon dioxide reported for structures of this type in comparison to their parent structures which bear no such functionality. The combination of anionic linkers bearing divergent carboxylate groups with nitrogen containing neutral linkers is a common theme in this research, for the most part however, the field is limited to the use of rigid linkers, which allow a degree of predictability of network topology. The ability to synthesise 'isostructural series' of MOFs, using this technique gives the synthetic chemist a facile means by which to investigate the effect of ligand/metal properties on the behaviour of the resultant material. Conversely the use of flexible linkers has received very little attention. This may be due to the diminished ability to predict network geometry, with an element of flexibility permitting a great deal of structural diversity, therefore complicating the synthesis of isostructural series. There are however advantages to a synthetic strategy based on the use of flexible linkers. The first of these is the potential for greater and more varied dynamic change on guest adsorption. As described in chapter 1, MOFs can undergo these dynamic changes either through the shearing of interpenetrated networks, or through the rotation of metal to organic coordinate bonds. The inclusion of flexible linkers allows a third change, with pores able to expand or contract *via* the twisting of methylene and other bridging groups. The second advantage is the ability to include further functionality as bridging groups between coordinating carboxylate moieties, and in particular secondary amines, due to the enhanced gas adsorption behaviours observed with other nitrogen moieties. It is with this in mind that we have embarked on a programme to synthesise MOFs using dicarboxylate linkers bearing reduced Schiff base functions. Very few examples of multidimensional structures based on reduced Schiff base linkers exist however those that do exhibit varied coordination modes, with the flexibility of the linker leading to some unique structural characteristics. Early research by Ranford and co-workers using the monocarboxylic acid ligand *N*-(2-hydroxybenzyl)-*L*-alanine (H<sub>2</sub>sala) offers a good example of the potential for ligands of this type to form extended multidimensional structures.<sup>1</sup> The reaction of the ligand with zinc chlorate afforded a dimeric complex of the formula  $[\{\text{Zn}(\text{sala})(\text{H}_2\text{O})_2\}_2]\cdot 2\text{H}_2\text{O}$ , in which pairs of zinc atoms are bound to the phenolic

oxygen atoms of both ligands, with these oxygen atoms adopting a bridging coordination mode between the two metal centres. Each metal centre is further coordinated to an amine nitrogen and a single carboxylate oxygen, with a single water molecule per zinc atom giving distorted square pyramidal coordination geometry. Hydrogen bonding of the coordinated water molecule and the amine hydrogen with the carboxylate functions of neighbouring dimeric units give a 3D H-bonded network, figure 86. Following dehydration by heating the complex forms a covalently bonded 3D network, by the coordination of the previously unbound carboxylate oxygen to the metal centre. The resulting structure can be described as a honeycomb network bearing open channels situated along the *c* axis.

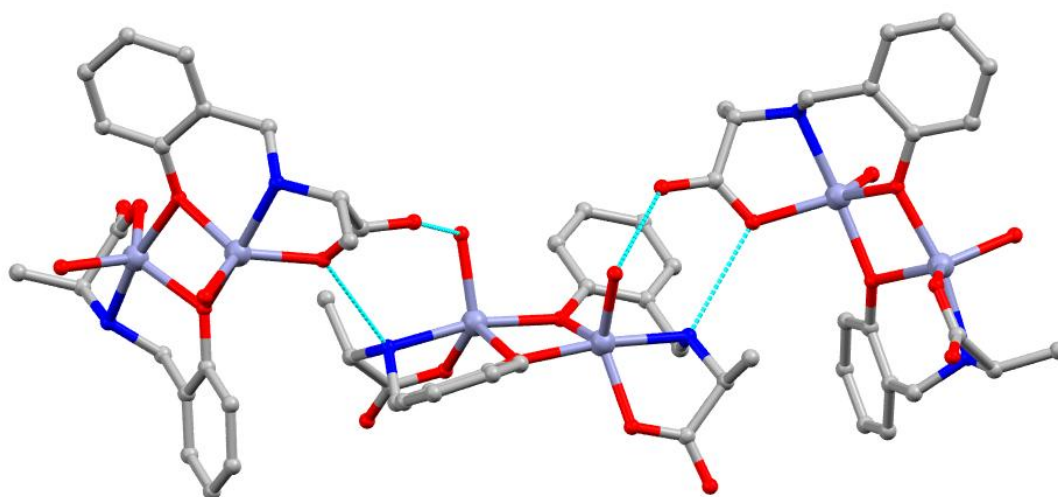


**Figure 86.** Diagram of the H-bonded structure  $[\{Zn(sala)(H_2O)_2\}_2] \cdot 2H_2O$ . Carbon, nitrogen, oxygen and zinc atoms are coloured grey, blue red and purple respectively. Hydrogen bonds are represented by turquoise dotted lines. Hydrogen atoms are omitted.<sup>1</sup>

Analogous structures are reported for the reaction of the ligand with copper acetate in the presence of lithium hydroxide, with a similar crystal to crystal transformation occurring on dehydration, however in this case 1D H-bonded chains transform in to an extended 3D framework which is isostructural to the zinc example.<sup>2</sup> Other examples of multidimensional structures based on ligands of this type exist,<sup>3</sup> however with greatest relevance to this study are those which use linkers of the biphenyl dicarboxylic acid type which bear either reduced Schiff base or amine linkages between the phenyl units such as those in figure 87, due to the similarity of

these ligands to the biphenyl-4,4'-dicarboxylate linker, which has been used with great success in MOF synthesis.

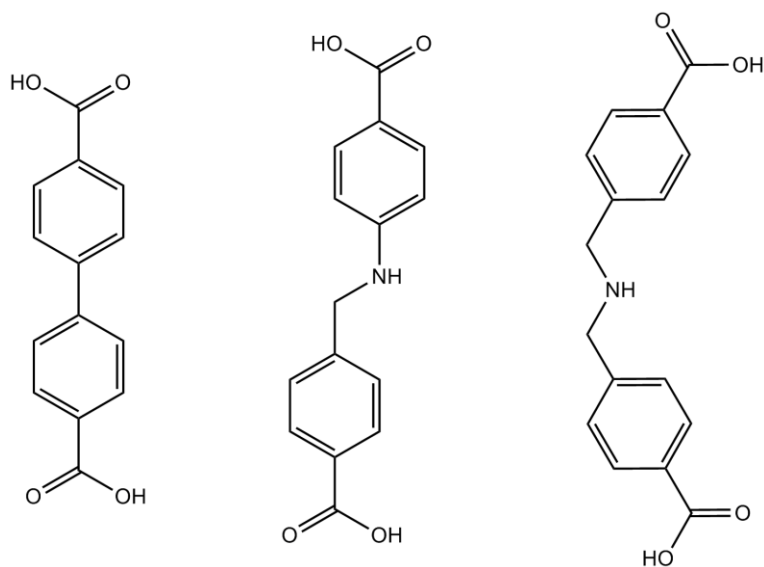


**Figure 87.** The potential anionic linkers biphenyl-4,4'-dicarboxylic acid (H<sub>2</sub>-BPDC), 4-carboxy-phenylene-methyleneamino-4-benzoic acid (H<sub>2</sub>-cpmapb) and bis(4-carboxy-benzyl)amine (H<sub>2</sub>-4-bcba).

Prepared *via* the condensation reaction of terephthalaldehyde with 4-aminomethylbenzoic acid and the subsequent reduction of the imine with sodium cyanoborohydride, the potential anionic linker bis(4-carboxy-benzyl)amine (H<sub>2</sub>-4-bcba) is the first example of the use of a ligand of this type in MOF synthesis.<sup>4</sup> The reaction of the potential linker with copper nitrate in the presence of triethylamine affords a 3D framework of the formula {[Cu(4-bcba)].H<sub>2</sub>O}<sub>n</sub>. As with analogous reactions using the rigid linker BPDC the reaction of the linker with copper nitrate gives the paddlewheel SBU, with each of these metal nodes linking four 4-bcba units *via* the di-monodentate binding of the carboxylate groups in the equatorial positions of the SBU giving extended 2D sheets, however unlike previous examples the axial positions of the SBU are occupied by N atoms from the 4-bcba units of neighbouring sheets. The resulting framework exhibits a Kagomé type structure with two channels of differing dimensions extending along the *c* axis, figure 88.

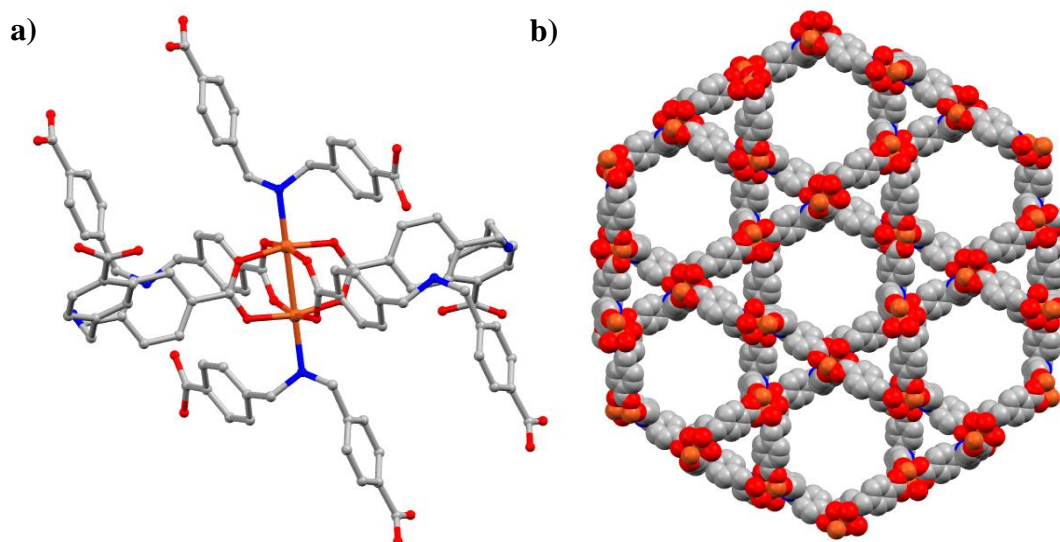


**Figure 88.** Diagrams of  $\{[\text{Cu}(4\text{-bcba})]\cdot\text{H}_2\text{O}\}_n$  showing a) the coordination environment around the metals centres and b) a space-filling representation of the structure viewed along the  $c$  axis showing the two types of pore. Carbon, nitrogen, oxygen and copper atoms are coloured grey blue red and brown respectively. Hydrogen atoms are omitted.<sup>4</sup>

The large hexagonal channels bear dimensions of  $14.3 \times 13.2 \text{ \AA}^2$ , with the smaller triangular pores having dimensions of  $3.3 \times 4.2 \text{ \AA}^2$ , giving an estimated accessible pore volume of 63.9 % of the total crystal volume. Although two sizes of pore are observed in this structure the triangular channel is too small to allow the diffusion of  $\text{N}_2$  and  $\text{CO}_2$  hence isotherms recorded for these gases involve only the large hexagonal channel. A type I adsorption isotherm with no hysteresis on desorption recorded for  $\text{N}_2$ , offers evidence of the permanent porosity of the MOF, while the  $\text{CO}_2$  adsorption isotherm exhibits type IV behaviour suggesting a mesoporous material and the formation of multilayers of adsorbed  $\text{CO}_2$  at 195 K and at pressures up to 1 bar.

Research conducted by Yang *et al.* reveals the variability of structures achievable through the use of the flexible linker ( $\text{H}_2\text{-cpmapb}$ ) and the related reduced Schiff base dicarboxylic acids at figure 89 in conjunction with the flexible neutral pillaring linker 1, 4-bis(1*H*-imidazol-1-yl)butane (bbi) and a variety of late transition metals.<sup>5</sup>

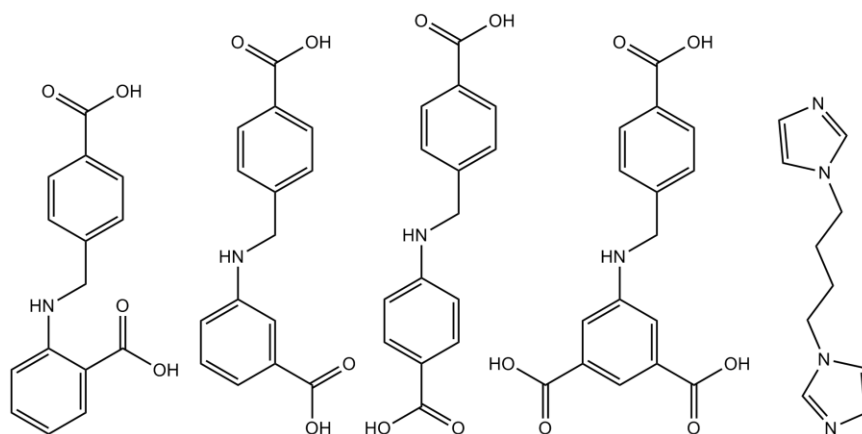


**Figure 89.** Diagram of the Reduced Schiff base linkers 4-carboxy-phenylene-methyleneamino-2-benzoic acid ( $H_2$ -cpmaob), 4-carboxy-phenylene-methyleneamino-3-benzoic acid ( $H_2$ -cpmamb), 4-carboxy-phenylene-methyleneamino-4-benzoic acid ( $H_2$ -cpmapb), 4-carboxy-phenylene-methyleneamino-3,5-dibenzoic acid ( $H_3$ -cpmadb) and 1,4-bis(1*H*-imidazol-1-yl)butane (bbi).

Hydrothermal reactions of the dicarboxylic acid linkers with zinc hydroxide, cobalt carbonate or cadmium hydroxide in the presence of bbi yield nine 2D structures bearing a variety of network topologies. In the first instance the use of  $H_2$ -cpmaob affords three isostructural 2D coordination polymers bearing the formulae  $\{[Zn(cpmaob)(bbi)].0.5H_2O\}_n$ ,  $\{[Co(cpmaob)(bbi)].0.5H_2O\}_n$  and  $\{[Cd(cpmaob)(bbi)].0.5H_2O\}_n$ . These structures are comprised of  $[M(cpmaob)]_n$  chains (where  $M = Zn, Co$  or  $Cd$ ) linked by the coordination of two bbi units per metal centre forming two membered macrometallo cycles. These sheets interpenetrate to form the extended structure, figure 90.

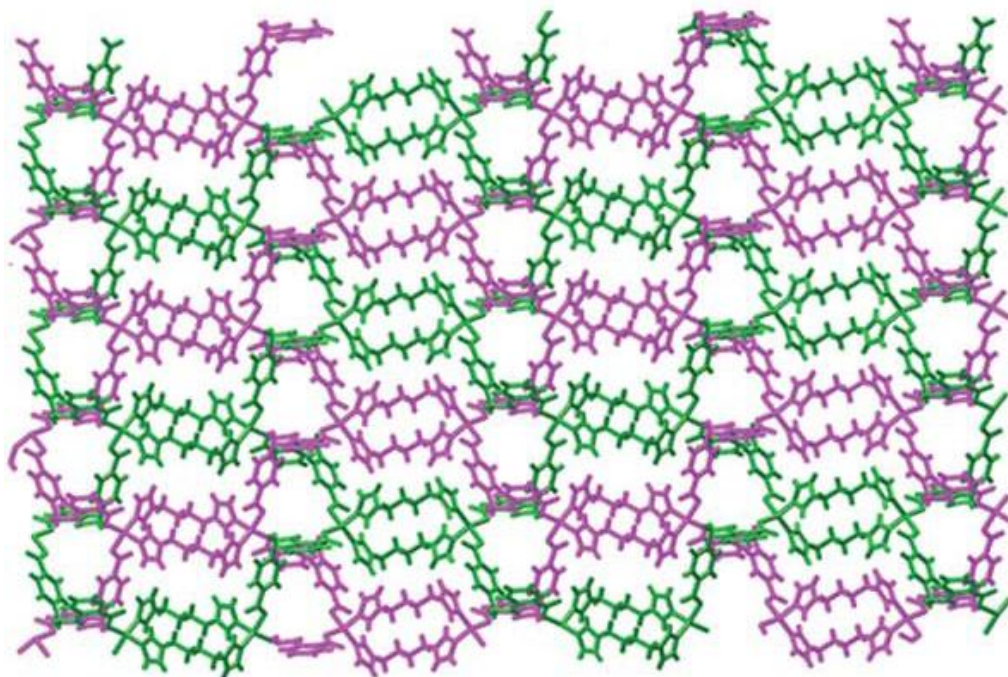


**Figure 90.** Diagram of the extended structure of  $\{[\text{Zn}(\text{cpmaob})(\text{bbi})].0.5\text{H}_2\text{O}\}_n$ . Interpenetrated networks are coloured purple and green for clarity. Reproduced from ref 5.

Similarly linked 1D chains result from the reaction of  $\text{H}_2\text{-cpmamb}$  with cadmium hydroxide in the presence of bbi, however in this example the 1D chains are formed by the coordination of the bbi linker to cadmium centres, with loops formed by the coordination of the anionic linker linking the chains in to an extended 2D sheet of the formula  $[\text{Cd}(\text{cpmamb})(\text{bbi})_{0.5}(\text{H}_2\text{O})]_n$ . The SBU in this example consists of two cadmium atoms, linked *via* the chelation of carboxylate groups from two cpmamb units to each metal centre, with two bidentate bridging carboxylate oxygens generating a  $\text{Cd}_2\text{O}_2$  dimer, figure 91. The networks in this example are interlocked, with the bbi unit from the first sheet passing through the cpmamb loop of the second.

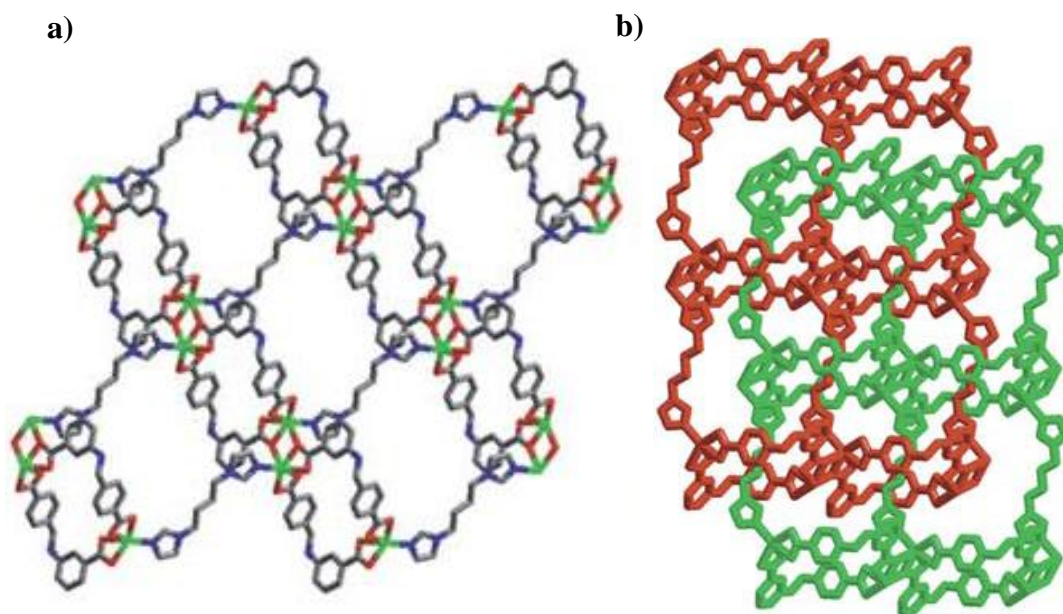


**Figure 91.** Diagram of  $[\text{Cd}(\text{cpmamb})(\text{bbi})_{0.5}(\text{H}_2\text{O})]_n$  showing a) the structure of the 2D sheets, where carbon, nitrogen, oxygen and cadmium atoms are coloured grey, blue, red and green, and b) the interpenetration of the sheets, with independent networks coloured red and green for clarity. Reproduced from ref 5.

The hydrothermal reactions of  $\text{H}_2\text{-cpmamb}$  with zinc hydroxide or cobalt carbonate in the presence of bbi and similar reactions using  $\text{H}_2\text{-cpmapb}$  however, give four undulating 2D sheets of the formulae of  $\{[\text{Zn}(\text{cpmamb})(\text{bbi})] \cdot (\text{H}_2\text{O})\}_n$ ,  $\{[\text{Co}(\text{cpmamb})(\text{bbi})] \cdot (\text{H}_2\text{O})\}_n$ ,  $\{[\text{Zn}(\text{cpmapb})(\text{bbi})] \cdot (\text{H}_2\text{O})\}_n$  and  $\{[\text{Co}(\text{cpmapb})(\text{bbi})] \cdot (\text{H}_2\text{O})\}_n$ . In the first two of these structures, 2D sheets are formed by the monodentate coordination of carboxylate oxygens from two anionic linkers, with the coordination of two bbi nitrogens per metal centre giving tetrahedral geometry. H-bonding interactions between the amine groups of the organic linker and the unbound carboxylate oxygens of neighbouring sheets, give two 3D hybrid covalent/H-bonded networks, figure 92a. Similar coordination environments are observed in the second two examples, however the bidentate binding of one carboxylate moiety per metal centre in these examples gives distorted square pyramidal geometry, with no hydrogen bonding interactions observed between 2D sheets, figure 92b.

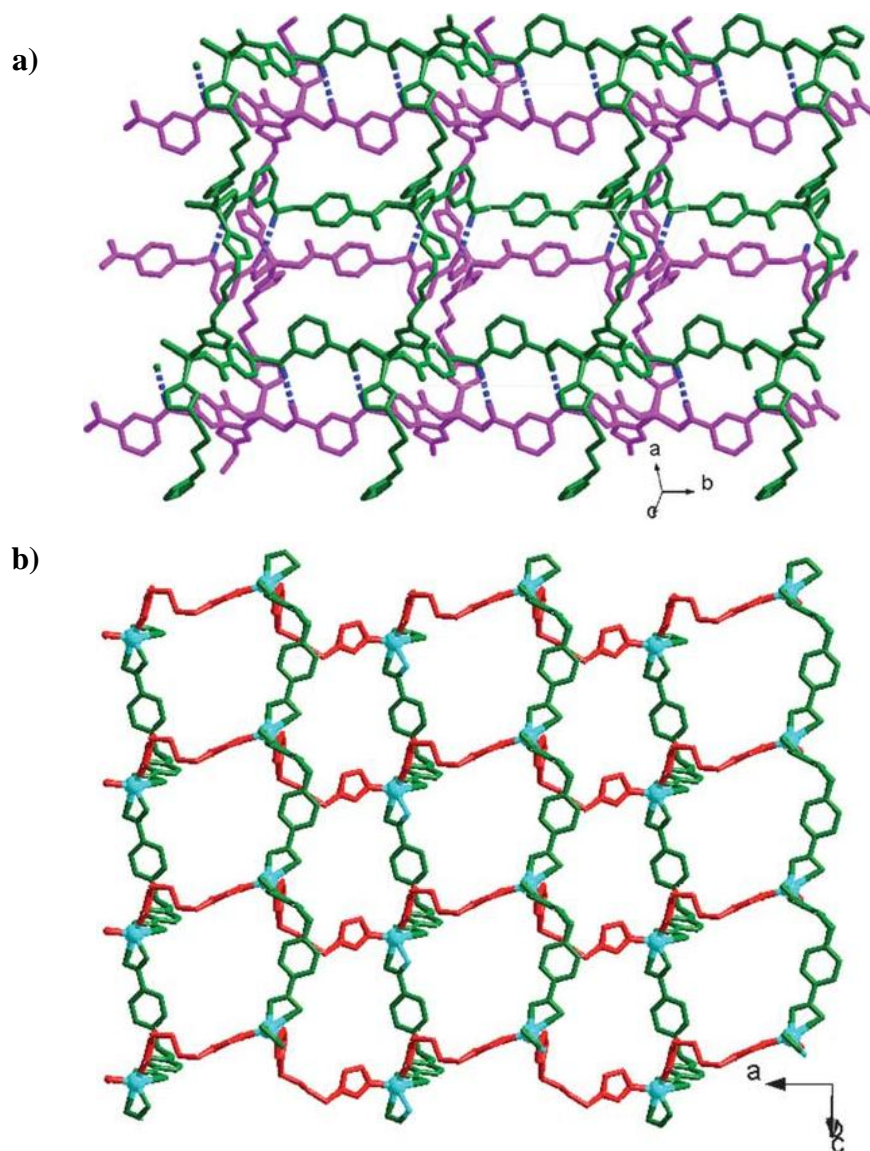


**Figure 92.** Diagrams of a)  $\{[\text{Zn}(\text{cpmamb})(\text{bbi})].(\text{H}_2\text{O})\}_n$  with neighbouring 2D sheets coloured purple and green and H-Bonding interactions represented by dotted blue lines, and b)  $\{[\text{Zn}(\text{cpmapb})(\text{bbi})].(\text{H}_2\text{O})\}_n$  with the zinc ions, anionic linkers and neutral pillaring linkers coloured blue, green and red respectively. Reproduced from ref 5.

The preparation of undulating 2D sheets, is also reported for the reactions of  $\text{H}_2$ -cpmapb with cadmium hydroxide in the presence of bbi and  $\text{H}_3$ -cpmadb with zinc hydroxide in the presence of bbi, however the reaction of the tricarboxylic acid with cadmium hydroxide and bbi under hydrothermal conditions affords the 3D framework  $\{[\text{Cd}(\text{cpmadb})(\text{bbi})(\text{H}_2\text{O})].1.5\text{H}_2\text{O}\}_n$  which exhibits very unusual network topology. Chains of  $\text{Cd}(\text{cpmadb})$  are formed by the bridging of metal ions by 3,5-dibenzoate moieties, with each carboxylate group adopting a bidentate

coordination mode to one metal centre. The anionic linker adopts a bent configuration allowing the coordination of the amine nitrogen to neighbouring chains to form pairs with the parallel packing of these pairs giving layers observed in the *a/c* crystallographic plane. Alternating layers extend perpendicular to their neighbours, with the coordination of the bbi ligands linking the chains in to an extended 3D structure. No bonding interactions are observed between the metal centres and the carboxylic acid group of the 4-carboxy-phenylene-methylene moieties, which extend in to the void spaces between the layers, figure 93.

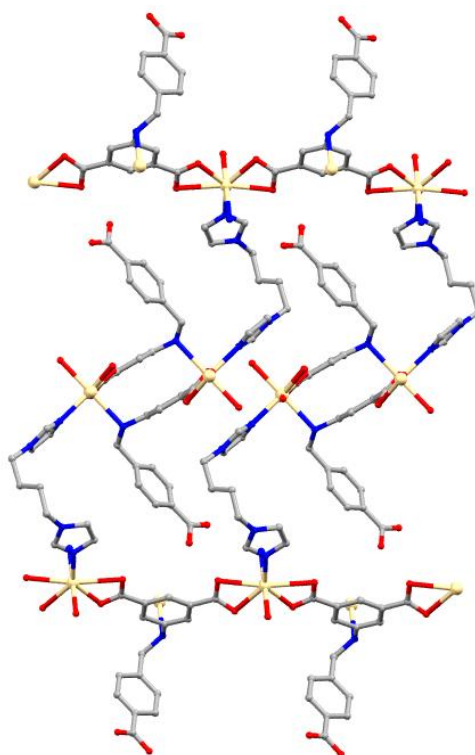
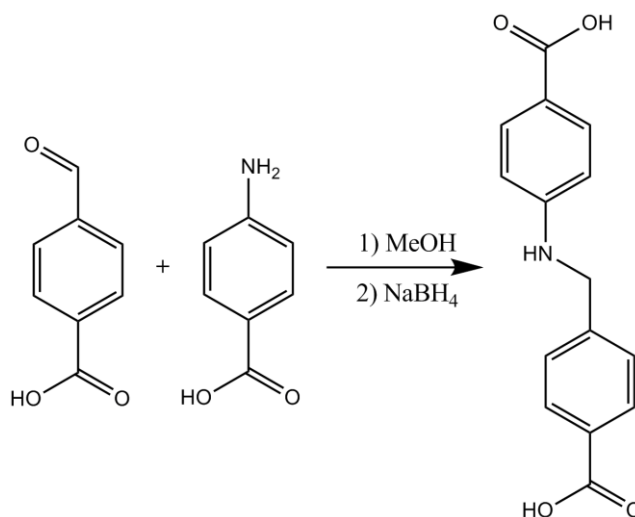


**Figure 93.** The structure of  $\{[\text{Cd}(\text{cpmadb})(\text{bbi})(\text{H}_2\text{O})].1.5\text{H}_2\text{O}\}_n$  viewed along the axis defined by the  $\text{Cd}^{2+}$  ions in the central layer. Carbon, nitrogen, oxygen and cadmium atoms are coloured grey, blue, red and yellow respectively. Hydrogen atoms are omitted.<sup>5</sup>

Though no gas uptake testing is reported for these examples, it is of particular interest that the use of two flexible linkers has such a profound effect on the structure and dimensionality of the reported MOFs. In the previously described examples using rigid linkers, the assembly of 2D metal/anionic linker layers pillared by neutral linkers to give a 3D structure is a common theme, however these examples show a propensity to form either undulating 2D structures or 2D sheets bearing looped

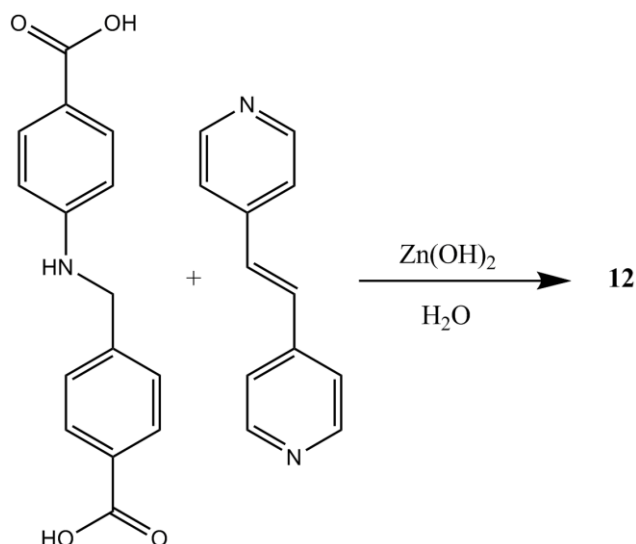
motifs by the bending of one or both of the organic linkers. In only one of these examples, that of  $\{[\text{Cd}(\text{cpmadb})(\text{bbi})(\text{H}_2\text{O})].1.5\text{H}_2\text{O}\}_n$ , does the resulting material demonstrate an extended 3D structure. In order to investigate the use of flexible linkers further we embarked on a programme of research using the flexible reduced Schiff base linker 4-carboxy-phenylene- methyleneamino-4-benzoic acid (henceforth referred to as  $\text{L}^1\text{H}_2$ ) in hydrothermal reactions with zinc hydroxide and the rigid pillaring linkers DPE and 4,4'-azopy. It is hoped that the inclusion of an element of rigidity will provide a backbone around which the flexible linkers can bind, allowing the assembly of 3D structures bearing novel network topologies.

### 3.2. Results and Discussion



**Scheme 11.** Synthetic route for the preparation of  $\text{L}^1\text{H}_2$ .

The synthesis of the reduced Schiff base ligand  $\text{L}^1\text{H}_2$  was achieved following the synthetic procedure at scheme 11. Equimolar quantities of 4-carboxybenzoic acid and 4-aminobenzoic acid were dissolved in methanol and stirred until a bright yellow colour was observed, indicating the formation of the intermediate Schiff base product. The *in situ* reduction of this species to give the target molecule was achieved through the addition of excess  $\text{NaBH}_4$ , with recrystallisation from methanol/water giving  $\text{L}^1\text{H}_2$  in good yield as a beige powder.



**Scheme 12.** Synthetic route for the preparation of  $\{[\text{Zn}_2(\text{L}^1)_2(\text{DPE})]\cdot\text{H}_2\text{O}\}_n$  **12**.

The hydrothermal reaction of equimolar quantities of  $\text{Zn(OH)}_2$  and  $\text{L}^1\text{H}_2$  with half an equivalent of DPE, following scheme 12, afforded the 2D structure **12**. The coordination environment around the metal centres in this structure is reminiscent of the paddlewheel SBU, however due to considerable disorder observed at the O(3) and O(4) oxygens and the appended benzene ring this carboxylate group binds in both a monodentate mode with the O(4) atoms coordinating to the Zn(1A) with a 50.7% contribution and a bridging bidentate mode with a 49.3 % contribution, figure 94.

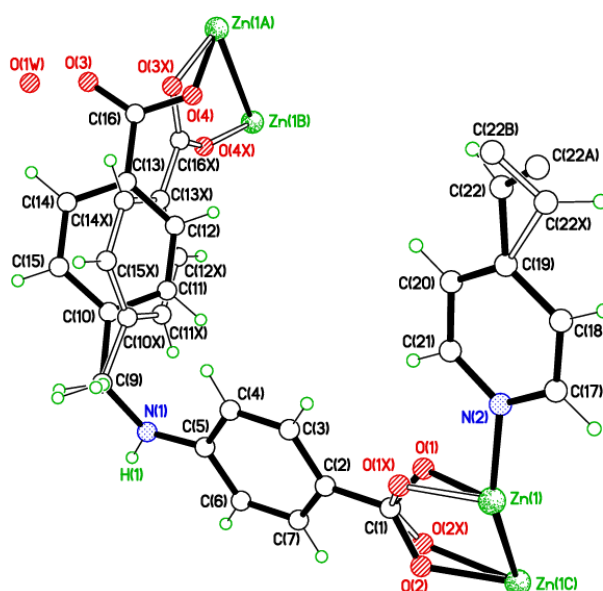


**Figure 94.** The asymmetric unit comprising **12** showing the disordered anionic linker modelled over two positions.

Similarly, the carboxylate group comprising C(1), O(1) and O(2) demonstrates disorder, with the group modelled as disordered over two positions, however in both of these models the carboxylate group exhibits the di-monodentate bridging mode observed in the paddlewheel SBU. Coordination of the pyridinyl nitrogen of the neutral DPE linker above and below the plane of the carboxylate groups gives either four coordinate distorted tetrahedral geometry or five coordinate distorted square-based pyramidal geometry around each zinc centre, figure 95.

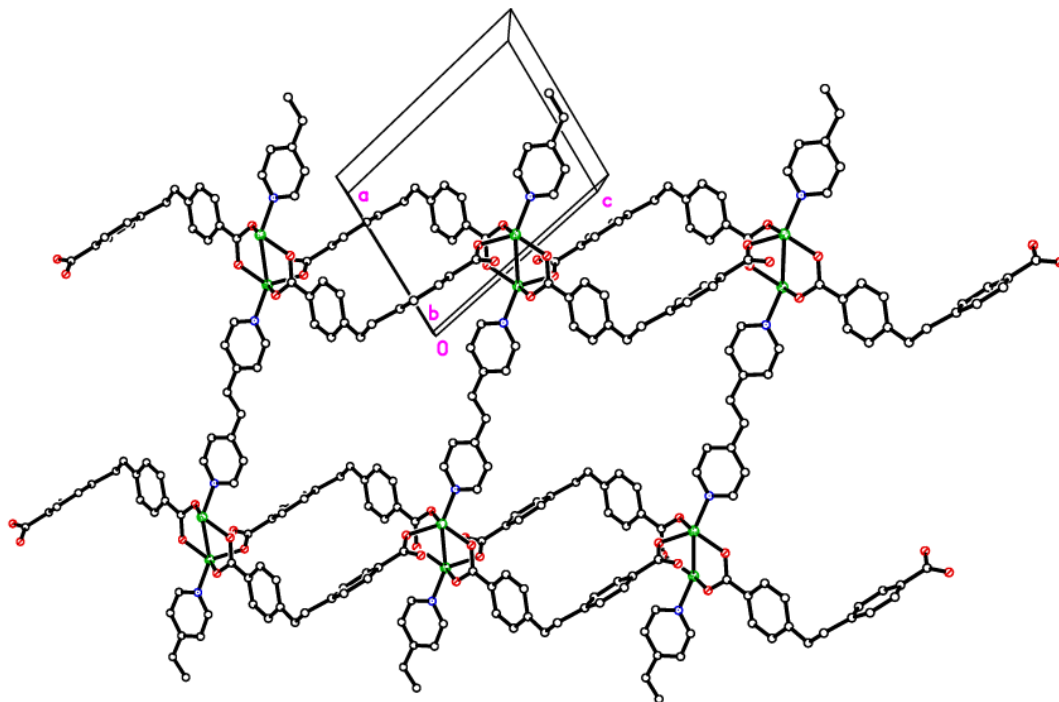


**Figure 95.** Diagram of **12** showing the looped 2D sheets, and the coordination environment around the metal centres. Carbon, nitrogen, oxygen and zinc atoms are represented by empty circles and blue, red and green circles respectively. Hydrogen atoms are omitted for clarity.

Despite the differences in carboxylate binding motifs the extended 2D framework is analogous to the previously described  $[\text{Cd}(\text{L}^1)(\text{bbi})_{0.5}(\text{H}_2\text{O})]_n^5$  comprising loops of  $\text{M}(\text{L}^1)$  (where  $\text{M} = \text{Cd}, \text{Zn}$ ) linked by the coordination of the neutral pillaring linker, however in this example no interpenetration is observed between the sheets. Significant H-bonding interactions are observed between the N(1) atoms of the anionic linker and the O(3) oxygen of neighbouring 2D sheets, giving a close packed hybrid H-bonded/covalent network, figure 96.

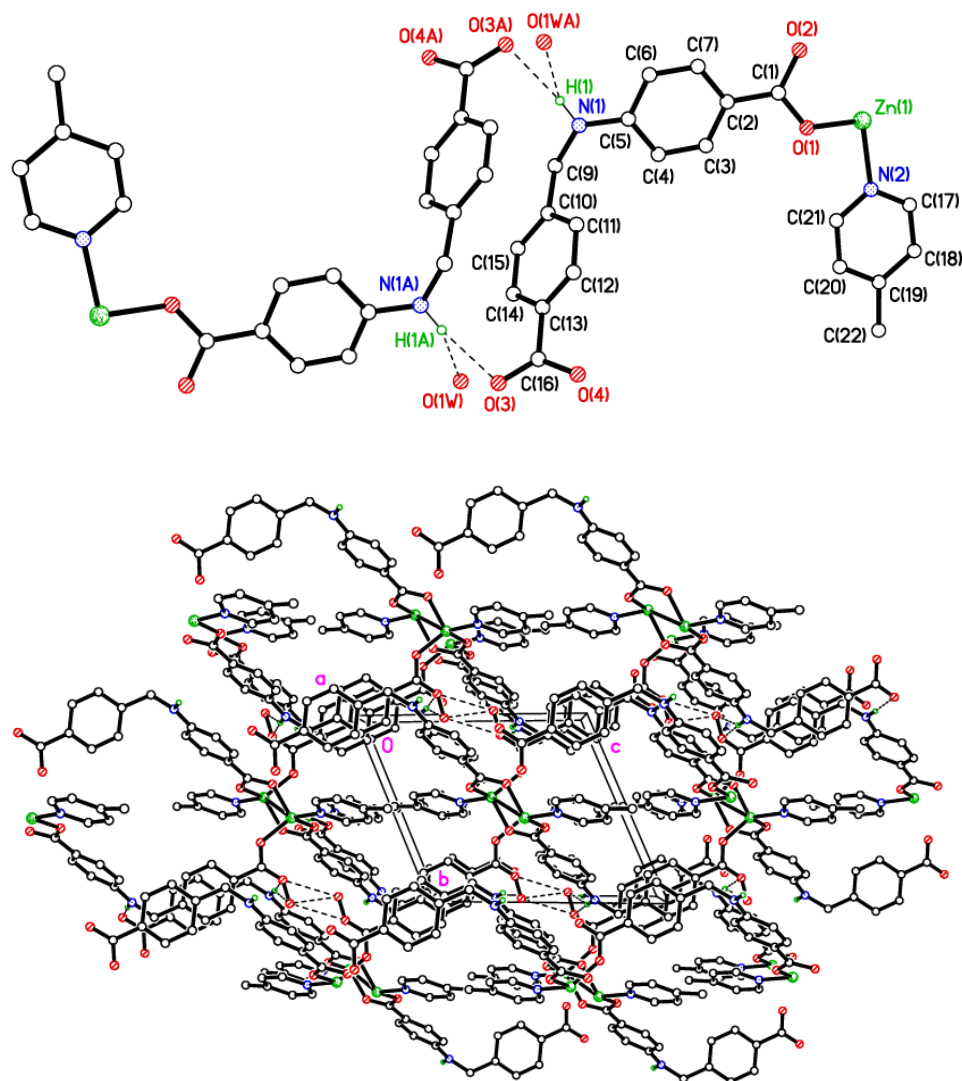
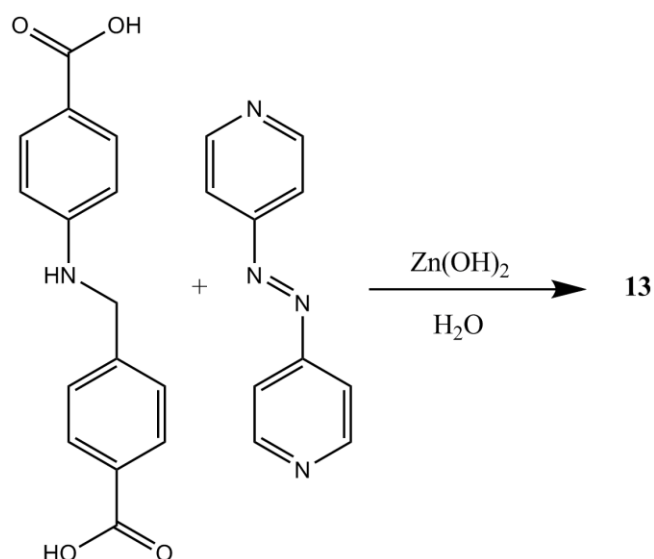


**Figure 96.** Diagram of **12** indicating the H-bonding interactions (dotted lines) between neighbouring 2D sheets (top) and the extended structure as viewed along the *a* axis (bottom). Carbon, nitrogen, oxygen and zinc atoms are represented by empty circles and blue, red and green circles respectively. Hydrogen atoms, except those involved in H-bonding, are omitted for clarity.

In order to be considered a porous material the framework must contain void spaces filled with guest solvent molecules, and demonstrate stability to guest removal. Due to the close packing of the 2D sheets no such void spaces are observed, with less than one guest water molecule per formula hydrogen bonded to the amine function of the anionic linker, it can therefore be concluded that this material is non-porous



**Scheme 13.** Synthetic route for the preparation of  $\{[\text{Zn}_3(\text{L}^1)_3(4,4'\text{-azopy})].7.5\text{H}_2\text{O}\}_n$ , **13**.

Employment of the same quantities of reactants as with structure **12**, but with the substitution of the DPE for 4,4'-azopy, as detailed in scheme 13, gives the 3D structure **13**. The asymmetric unit of this structure comprises 2 zinc atoms, half of the bipyridyl linker and one and a half  $\text{L}^1$  units. The first zinc atom is four coordinate, exhibiting severely distorted tetrahedral geometry by the coordination of three carboxylate oxygens from different  $\text{L}^1$  units, and the pyridinyl nitrogen of a 4,4'-azopy molecule. The second zinc atom is in a six coordinate, distorted octahedral environment through the coordination to six carboxylate oxygens from different dicarboxylate linkers. The SBU comprises three zinc centres forming an hour glass shape by the coordination of carboxylate moieties from six  $\text{L}^1$  units in the di-monodentate bridging mode in the equatorial positions, with 4,4'-azopy units coordinated to the axial positions of the hour glass, figure 97.

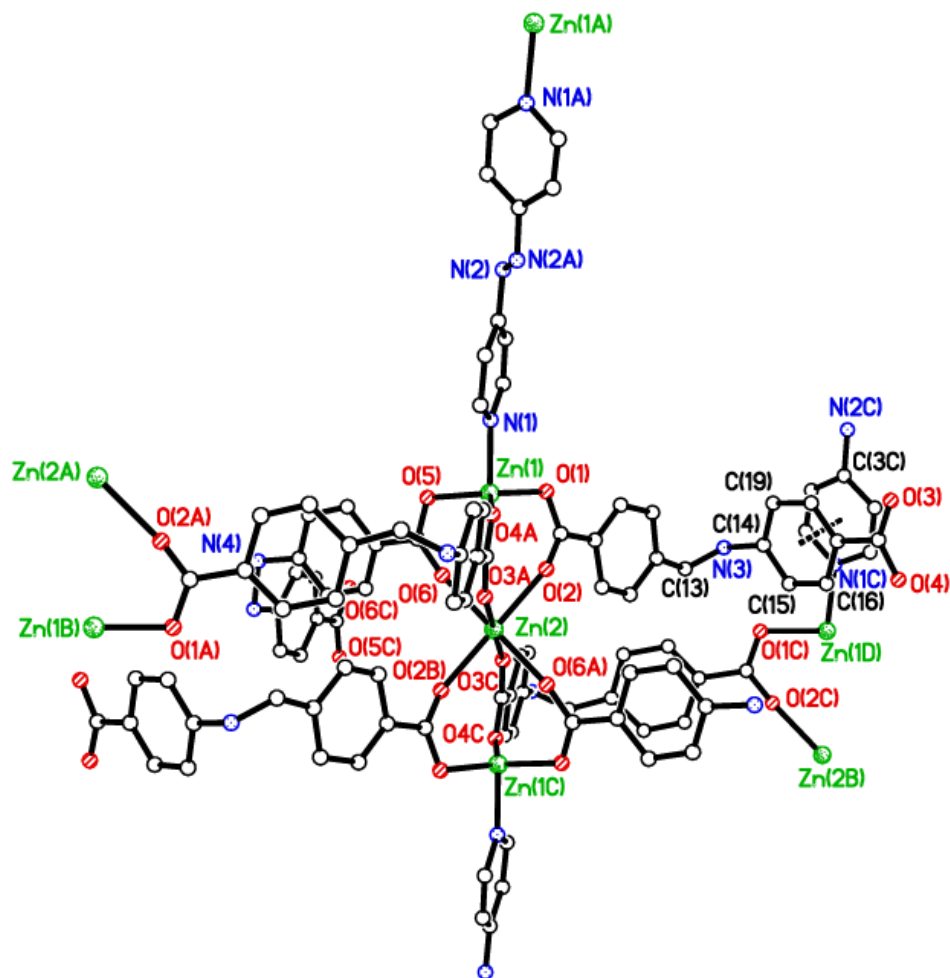


**Figure 97.** The coordination environment around the metal centres in **13**. Carbon atoms represented by empty circles. Hydrogen atoms are omitted.

The  $L^1$  units extend in six directions along the  $a/b$  plane, adopting a bent conformation through the rotation of the amine and methylene bridges, whilst the 4,4'-azopy extend along the  $c$  axis, linking hour glass SBUs in to an extended 3D framework, bearing roughly cylindrical 1D channels of 4.75 Å diameter observed parallel to the  $c$  axis, figure 98. Disordered guest water molecules could not be distinguished by point atom observations and were refined as areas of diffuse electron density using the PLATON squeeze procedure. This procedure found four voids per unit cell, each with a volume of 368 Å<sup>3</sup>. Two of these voids contained 73 electrons with the other containing approximately 78, equating to 30 water molecules per unit cell, or 7.5 per void.

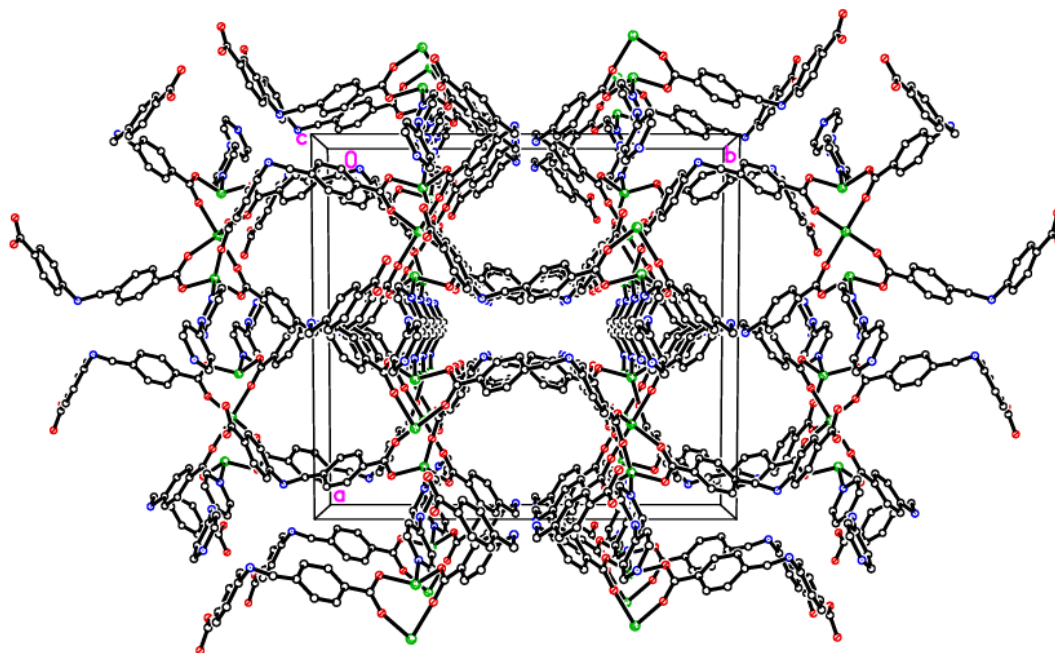


**Figure 98.** Diagram of **13** as viewed along the *c* axis. Carbon, nitrogen, oxygen and zinc atoms are represented by empty, blue, red and green circles respectively. Hydrogen atoms are omitted for clarity.

### 3.2.1. Thermogravimetric analysis

Thermogravimetric analysis of structures **12** and **13** were performed under an inert carrier flow of nitrogen to determine their solid state stabilities.

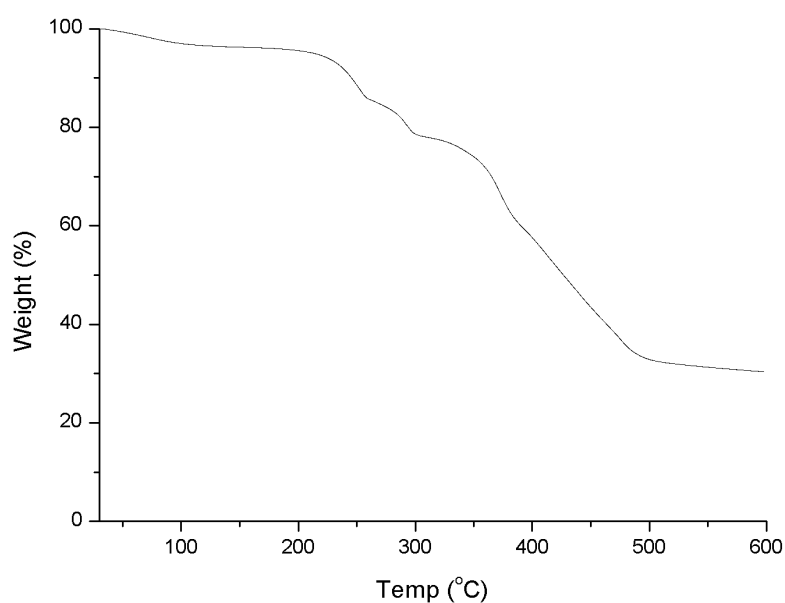


**Figure 99.** Recorded TGA data for **12**.

The graph in figure 99 shows the data collected for **12**, revealing a weight loss of only 4% in the 30-230 °C region. The single crystal X-ray diffraction data reveals the presence of one water molecule per formula unit, the loss of which equates to 2%. It is of note that the broad peak at 3314  $\text{cm}^{-1}$  observed in the IR spectrum of **12** is indicative of the presence of water, though elemental analyses conducted on the as-synthesised structure offered no evidence of its presence. The very minor desolvation observed here supports the assertion that the material is essentially non-porous. The structure maintains stability up to ~230 °C where the onset of thermal decomposition is signalled by the rapid and continuous weight loss from the sample. The step wise weight loss in this region is indicative of the decomposition of each component of the framework in turn.

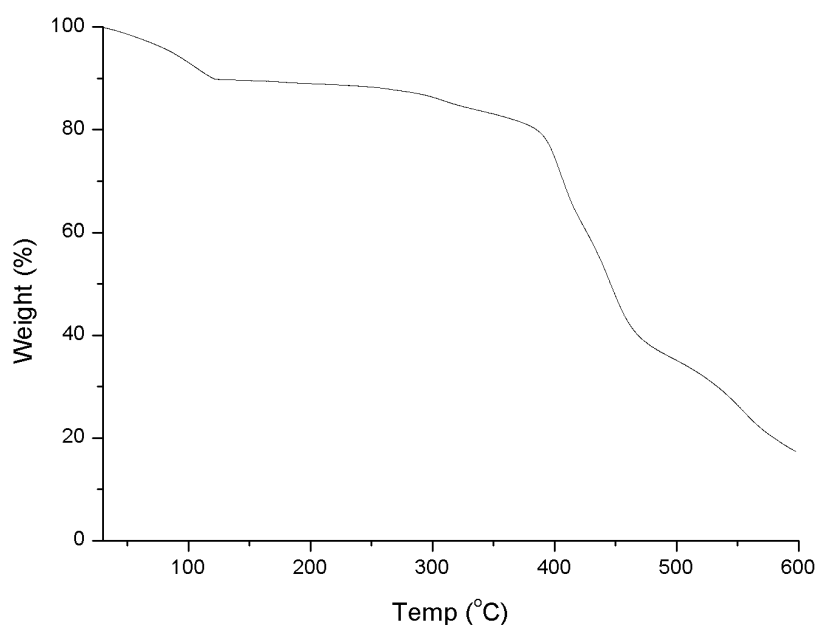


**Figure 100.** Recorded TGA data for **13**.

Analysis of the TGA data collected for **13**, figure 100, reveals a single weight loss of ~10 % in the 30-120 °C temperature range, which is attributable to the loss of 7.5 water molecules per formula unit (calculated 10.2 %). The presence of these guest molecules is also confirmed by elemental analysis. The structure then maintains stability up to 300°C at which point the thermal decomposition of one of the organic linkers commences. This decomposition continues in stages up to 600°C as each of the MOF components loses thermal stability.

### 3.2.2. Gas adsorption behaviour

Gas uptake studies were performed on **13**, with the sample being prepared for CO<sub>2</sub> adsorption studies *via* solvent exchange, by immersion in chloroform for 2 weeks, during which time the solvent was replaced four times. Prior to testing the sample was activated by heating to 120 °C for 12 h under dynamic vacuum, however no such testing was performed on **1** due to the determination of its non-porosity by structural and thermogravimetric analysis. In order to probe the possibility of dynamic change on guest adsorption resulting from the use of a flexible anionic linker, data was recorded for both adsorption and desorption at 273 K and pressure up to 1 atmosphere, figure 101.

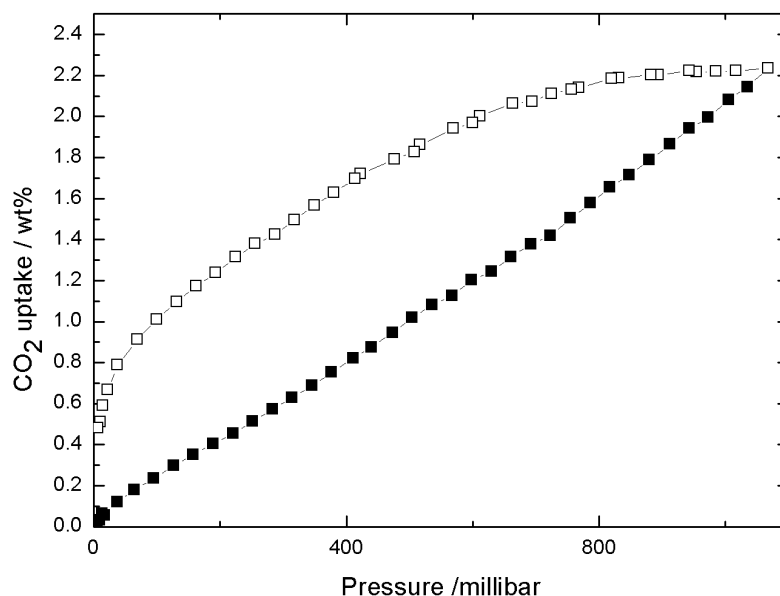


**Figure 101.** The CO<sub>2</sub> isotherm recorded for **13**, showing adsorption (filled squares) and desorption (empty squares).

The CO<sub>2</sub> adsorption isotherm recorded for **13** shows a very modest uptake of 2.24 wt% at 1 atmosphere, and appears to follow the type II isotherm, suggesting a non-porous material, however there are features in both the adsorption and desorption curves which cannot be explained using purely non-porous surface adsorption/desorption behaviour. The first of these is the hysteresis observed on CO<sub>2</sub> desorption. While this phenomenon is not limited to frameworks which exhibit dynamic change on guest uptake/removal, and can also be attributed to high affinity

binding sites on the surface of a non-porous adsorbent, in a system based purely on the physisorption of gas on to a surface it can be expected that at zero pressure there will be zero surface coverage, however in this example that is not the case. Even at zero pressure **2** retains 0.48 wt% of CO<sub>2</sub>. This may be attributed either to the reaction of CO<sub>2</sub> with the amine group of the anionic linker *via* some chemisorptive process, or to the closing of pores at low pressure *via* some dynamic change, which prevents the escape of CO<sub>2</sub> molecules. The second feature is the apparent stepwise adsorption and desorption of CO<sub>2</sub>. At around 440 and 720 millibar the adsorption and desorption curves exhibit a minor step. This phenomenon has also been reported for structures which exhibit dynamic change on guest adsorption, and is attributed to pore opening and closing, with the size of step relating to the magnitude of structural change.<sup>6</sup> In the example of MIL-53 the change from non-porous to porous increases the cell volume by 40% and is accompanied by a large step in the adsorption isotherm as the newly opened pore allows the diffusion of analyte gases.<sup>7</sup> It follows that a small structural change will be accompanied by a small step in the adsorption isotherm, however further investigation is required in order to determine the origins of this MOF's CO<sub>2</sub> uptake behaviour.

### 3.3. Conclusion

Two novel structures have been synthesised using the reaction of the flexible reduced Schiff base linker L<sup>1</sup>H<sub>2</sub> with zinc hydroxide and the pillaring linkers DPE and 4,4'-azopy under hydrothermal conditions, with both structures undergoing full structural characterisation. The first of these is a 3D hybrid H-bonded/covalent structure, bearing no large void spaces capable of accommodating guest solvent molecules, the second is a 3D structure exhibiting 1D channels filled with guest water molecules. Based on these examples the assertion that the use of both rigid and flexible components in the synthesis of MOFs would afford 3D frameworks capable of adsorbing guest molecules is not supported. The self-assembly of the porous 3D structure **13** must, therefore, arise from properties which are particular to this combination of ligands. CO<sub>2</sub> adsorption studies performed on **13** reveal interesting hysteretic behaviour on desorption of the gas, with 0.48 wt% of CO<sub>2</sub> retained even at zero pressure. While further testing is required to determine the origin of this behaviour it is clear that continued research on flexible, reduced Schiff base linkers in the synthesis of MOFs is warranted.

### 3.4. References

---

- 1 J. D. Ranford, J. J. Vittal, D. Wu, *Angew. Chem. Int. Ed.*, 1998, **37**, 1114.
- 2 J. D. Ranford, J. J. Vittal, D. Wu, X. Yang, *Angew. Chem. Int. Ed.*, 1999, **38**, 3498
- 3 a) B. Sreenivasulu, J. J. Vittal, *Angew. Chem. Int. Ed.*, 2004, **43**, 5769. b) L. Jia, N. Tang, J. J. Vittal, *Inorg. Chim. Acta*, 2009, **362**, 2525. c) C. T. Yang, J. J. Vittal, *Inorg. Chim. Acta*, 2003, **344**, 65. d) C. T. Yang, B. Moubaraki, K. S. Murray, J. D. Ranford, J. J. Vittal, *Inorg. Chem.* 2001, **40**, 5934. e) B. Sreenivasulu, J. J. Vittal, *Cryst. Growth Des.*, 2003, **3**, 636. f) A. Garcia-Raso, J. J. Fiola, A. Lopez-Zafra, A. Cabrerob, I. Matab, *Polyhedron*, 1999, **18**, 871.
- 4 S. Horike, S. Hasegawa, D. Tanaka, M. Higuchia, S. Kitagawa, *Chem. Commun.*, 2008, **37**, 4436.
- 5 Y. Y. Liu, Z. H. Wang, J. Yang, B. Liu, Y. Y. Liu, J. F. Ma, *CrystEngComm*, 2011, **13**, 3811.
- 6 a) Y. B. Zhang, W. X. Zhang, F. Y. Feng, J. P. Zhang, X. M. Chen, *Angew. Chem. Int. Ed.*, 2009, **48**, 5287. b) T. K. Maji, G. Mostafa, R. Matsuda, S. Kitagawa, *J. Am. Chem. Soc.*, 2005, **127**, 17152. c) Y. Cheng, A. Kondo, H. Noguchi, H. Kajiro, K. Urita, T. Ohba, K. Kaneko, H. Kanoh, *Langmuir*, 2009, **25**, 4510. d) J. Rabone, Y. F. Yue, S. Y. Chong, K. C. Stylianou, J. Bacsá, D. Bradshaw, G. R. Darling, N. G. Berry, Y. Z. Khimyak, A. Y. Ganin, P. Wiper, J. B. Claridge, M. J. Rosseinsky, *Science*, 2010, **329**, 1053.
- 7 A. Boutin, F. X. Coudert, M. A. Springuel-Huet, A. V. Neimark, G. Férey, A. H. Fuchs. *J. Phys. Chem. C*, 2010, **114**, 22237.

## **Chapter 4**

**1D structures based on a lower-rim acid appended  
calix[4]arene**

## 4.1. Introduction

Though research in the field of porous materials continues to grow, the vast majority of this research is focussed on the construction of extended 3D structures from intrinsically non-porous building units. The porosity of the resulting materials arises from the void spaces encapsulated by the linking of planar organic linkers with metals and metal oxide clusters. The use of organic units bearing void spaces in the construction extended structures using the same principles of coordination chemistry gives the possibility of preparing materials which bear hierarchical porosity, allowing the tailoring of these materials still further. Prepared by the polycondensation of *para*-substituted phenols with formaldehyde, calix[4]arenes are ideal candidates for the development of such hierarchically porous materials due to the 'bowl' shape defined by these macrocyclic compounds and the ease with which these compounds can be selectively functionalised at either the upper or lower-rim, figure 102.

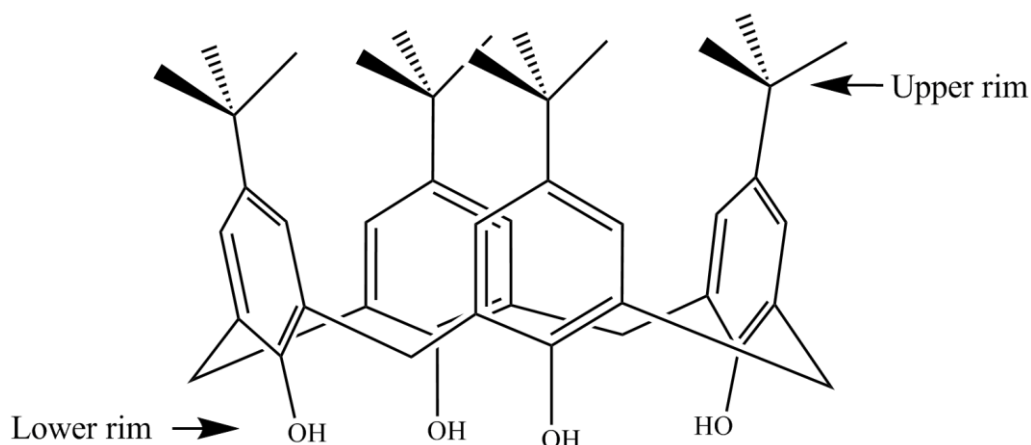


**Figure 102.** *para-tert*-Butylcalix[4]arene. The location of the upper and lower-rims are indicated.

The apolar 'bowl' defined by the phenol units has been shown to readily participate in host-guest chemistry, with clathrates of calix[4]arene with acetone, toluene, chloroform and pyridine being identified in early research on these supramolecules.<sup>1</sup> Crystallographic analysis of apohost calix[4]arene, prepared by the sublimation of the acetone adduct at 300°C reveals interstitial void spaces of around 153 Å<sup>3</sup> which are capable of storing methane and a variety of halomethanes as guests within the intermolecular cavity, at temperatures far in excess of their normal boiling points *via*

only weak Van der Waals interactions.<sup>2</sup> Large cavities, of around 235 Å<sup>3</sup> and 110 Å<sup>3</sup>, visible between the calixarene bilayers in pure sublimed *para-tert-butylcalix[4]arene* and *para-tert-pentylcalix[4]arene* respectively, have been shown to adsorb N<sub>2</sub>, CO<sub>2</sub>, O<sub>2</sub> and CH<sub>4</sub> at 298 K and pressures below 3 atm, with some degree of selectivity. Molecular hydrogen uptake for the sublimed *para-tert-butylcalix[4]arene* has also been observed, with uptakes of 0.2 wt% at 298 K at pressures up to 31 atm, and 0.6 wt% at the same pressure but at a lower temperature of 200 K.<sup>3</sup> More recently, studies conducted on *para-octanoylcalix[4]arene* reveal the adsorption of oxygen, ethylene and the linear alkanes (C1-C4) at room temperature and pressures up to 4 bar.<sup>4</sup>

Density functional theory calculations performed on lithium functionalised *para-tert-butylcalix[4]arene* reveal the potential for greatly enhanced molecular hydrogen uptake. Lithium absorption is possible at four positions on the calixarene, by replacement of one of the phenolic hydrogens, by complexation of the Li<sup>+</sup> cation between the four phenolic oxygens or by the formation of a Li-benzene  $\pi$  complex, with the lithium ion situated either internally or externally to the calixarene bowl. The optimum position for this lithium doping is shown to be the internal face of the bowl, with potential uptakes reported of 10 wt% of hydrogen at temperatures up to 100 K.<sup>5</sup>

The potential for metal-organic frameworks based on calix[4]arenes as gas storage materials is therefore enormous. Selective functionalisation at either rim of the calix[4]arene scaffold gives an almost limitless ligand set with which to perform coordination chemistry, and leads to the prevalence of metallocalix[4]arene structures in the literature, with applications as far reaching as catalysis<sup>6</sup>, single-molecule magnetism<sup>7</sup>, ion sensing<sup>8</sup>, and medicine<sup>9</sup>. Though many examples of multidimensional calix[4]arene structures based on the coordination of transition metals to *para-sulfonatocalix[4]arene* exist,<sup>10</sup> there are few examples of such structures based on carboxylic acid functionalised calix[4]arenes, which are of particular interest to this research due to the prevalence of metal carboxylate bonding in the formation of MOFs.

The first of these structures was reported by Liu *et al.*<sup>11</sup> The reaction of the lower-rim functionalised calix[4]arene, 25,27-bis(hydroxycarbonylmethoxy)-26,28-

dimethoxy-*para-tert*-butylcalix[4]arene ( $H_2L^{C4}$ ) with potassium carbonate and cobalt chloride hexahydrate in refluxing ethanol gives the 3D framework  $[K_3Co_2(L^{C4})_3(EtOH)_6]Cl$ , figure 103.

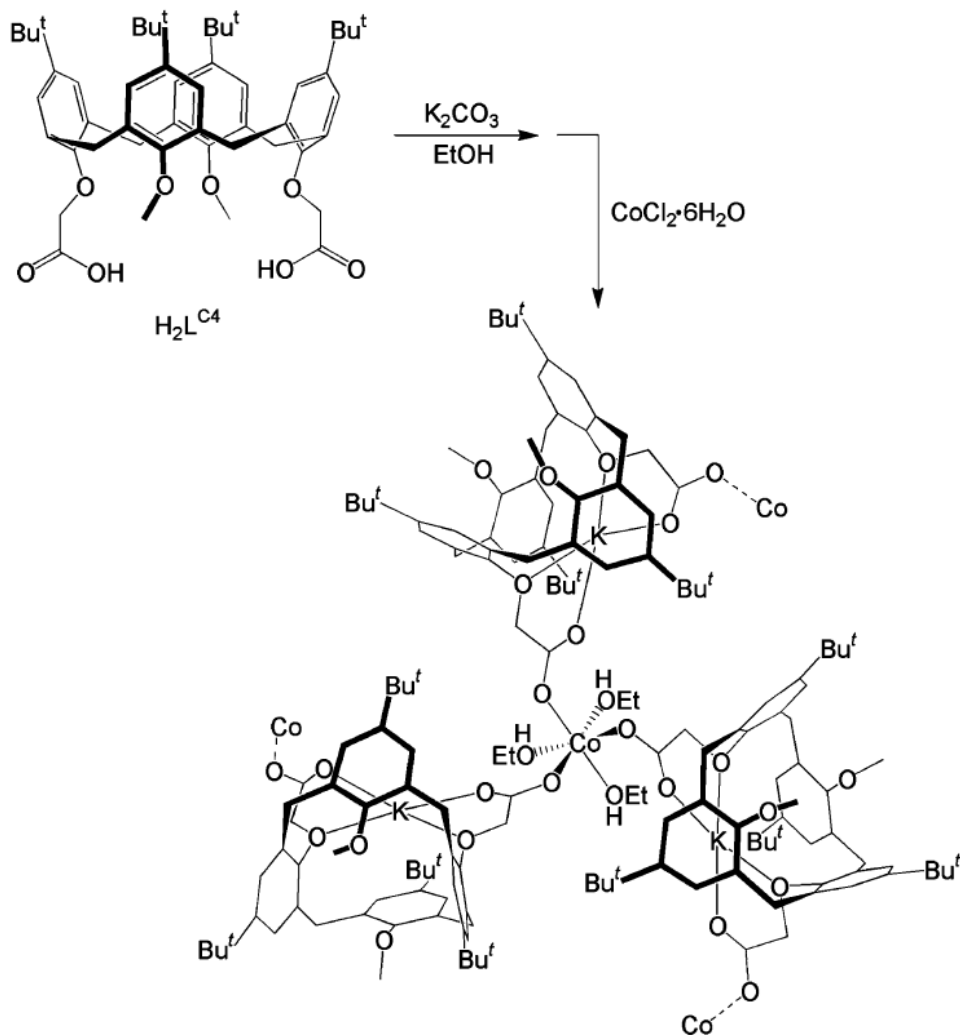


**Figure 103.** The reaction scheme for the formation of  $[K_3Co_2(L^{C4})_3(EtOH)_6]Cl$  from the functionalised calix[4]arene  $H_2L^{C4}$ ,  $K_2CO_3$  and  $CoCl_2 \cdot 6H_2O$ . For clarity the aryl double bonds and charge on the  $[K_3Co_2(L^{C4})_3(EtOH)_6]^+$  unit have been omitted. Reproduced from ref. 11.

In this example the treatment of  $H_2L^{C4}$  with potassium carbonate leads to the deprotonation of the ligand and the coordination of a potassium cation to both the acid functionalised phenolic oxygens and an oxygen atom from each of the two carboxylate moieties. The formation of the 1,3-alternate confirmation of the calixarene is facilitated by considerable interactions observed between the metal centre and the phenyl rings bearing uncoordinated methoxy groups. Subsequent

reaction with cobalt chloride hexahydrate gives a 3D framework by the linking of three calixarene units by coordination of the  $\text{Co}^{2+}$  ion to the unbound acetate oxygens, and the bridging of the calixarene units to two  $\text{Co}^{2+}$  centres. Each  $\text{Co}^{2+}$  centre is further coordinated to three ethanol molecules giving octahedral coordination geometry. The suprastructure of this framework is formed by the bridging of four membered helices by  $[\text{K}(\text{L}^{\text{C}4})]^-$  units to give a (10,3)a net topology, figure 104.

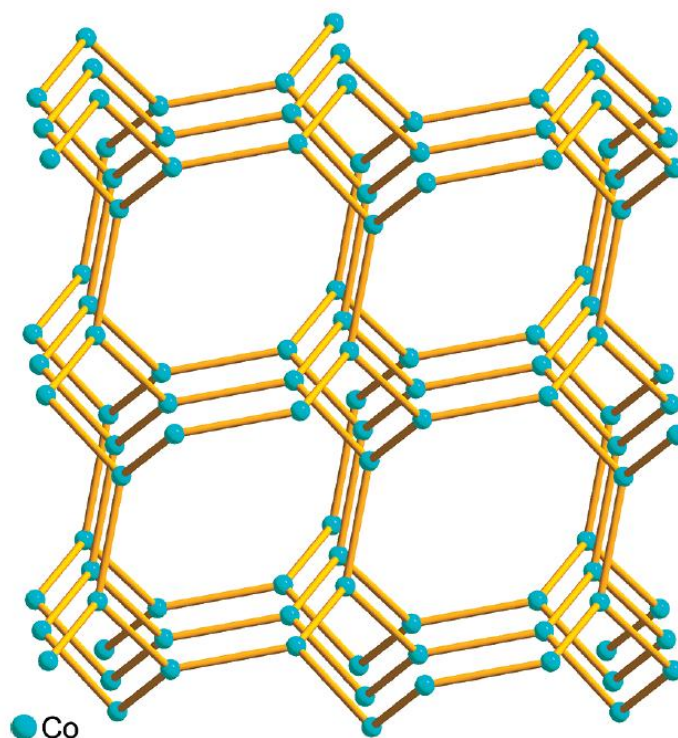


**Figure 104.** Diagram of the (10,3)a net topology exhibited by  $[\text{K}_3\text{Co}_2(\text{L}^{\text{C}4})_3(\text{EtOH})_6]\text{Cl}$ . Cobalt ions are represented by blue spheres, with each  $[\text{K}(\text{L}^{\text{C}4})]^-$  unit represented by a yellow rod. Reproduced from ref. 11.

Thermogravimetric analysis of this framework reveals a small weight loss of 3.4 % in the 25-120 °C range which is attributed to the loss of 4.5 interstitial water molecules per formula unit from the complex. No further change is observed until 230 °C at which point the rapid and continuous weight loss is attributed to thermal decomposition. No gas uptake behaviour has been recorded for this structure.

Research conducted by Brechin and Dalgarno *et al.* using 25, 26, 27, 28-tetrabutoxycalix[4]arene-5, 11, 17, 23-tetracarboxylic acid ( $\text{H}_2\text{L}^{\text{C}4}$ ) offers a second

example of these multidimensional metallocalix[4]arene structures.<sup>12</sup> The reaction of methanol suspensions of the calixarene with methanolic solutions of Ni(NO<sub>3</sub>)<sub>2</sub>, Co(NO<sub>3</sub>)<sub>2</sub> and Mn(NO<sub>3</sub>)<sub>2</sub> hydrates in the presence of pyridine (Py), leads the formation of discrete metal-calixarene dimers which self-assemble in to extended arrays. The nature of these dimers and the extended arrays observed in their crystal structures is dependent on the metal centres involved. The use of Ni<sup>2+</sup> leads to the formation two discrete units bearing the formulas [Ni<sub>2</sub>(μ-H<sub>2</sub>O)(L<sup>1C4</sup>)<sub>2</sub>(Py)<sub>4</sub>] and [Ni<sub>2</sub>(μ-H<sub>2</sub>O)(L<sup>1C4</sup>)<sub>2</sub>(Py)<sub>3</sub>(MeOH)]. These units exhibit the same metal carboxylate-binding motif, with two carboxylate functions per calixarene being involved in coordination to two Ni<sup>2+</sup> centres. The first of these carboxylate moieties binds in a monodentate fashion to the a single metal centre, whilst the second exhibits di-monodentate coordination, bridging two metal centres. Four apically bound pyridine molecules (two per metal centre) in the first of the metallocalixarene dimers, and three pyridine and a methanol molecule in the second give rise to octahedral coordination geometry about the metal centres. The self-assembly of these discrete units leads to the formation of the bilayer array often observed in calix[4]arene crystal structures,<sup>13</sup> with each layer being composed entirely of one of these dimers, figure 105.

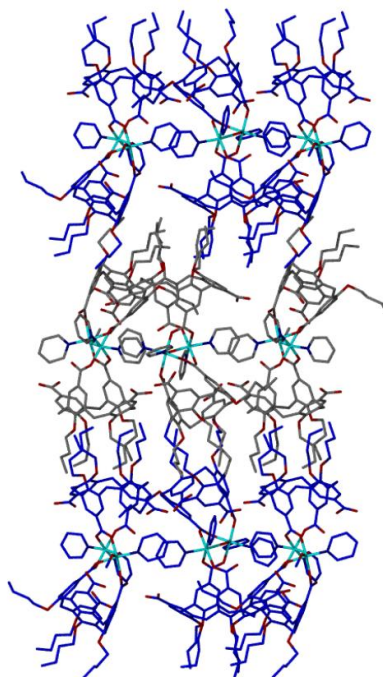


**Figure 105.** Diagram showing the alternating bilayers of [Ni<sub>2</sub>(μ-H<sub>2</sub>O)(L<sup>1C4</sup>)<sub>2</sub>(Py)<sub>4</sub>] (grey) and [Ni<sub>2</sub>(μ-H<sub>2</sub>O)(L<sup>1C4</sup>)<sub>2</sub>(Py)<sub>3</sub>(MeOH)] (blue). Reproduced from ref. 12.

The use of  $\text{Co}^{2+}$  and  $\text{Mn}^{2+}$  gives analogous metalocalixarene dimers, however only one of the previously described complexes, bearing the formula  $[\text{M}_2(\mu\text{-H}_2\text{O})(\text{L}^{1\text{C}4})_2(\text{Py})_4]$  (where  $\text{M} = \text{Co}, \text{Mn}$ ), is observed. In these examples the discrete complexes self-assemble into metal-organic calixarene nanotubes, with the aggregation of eight calixarene molecules defining a central solvent filled channel of around 1.3 nm in diameter, figure 106a

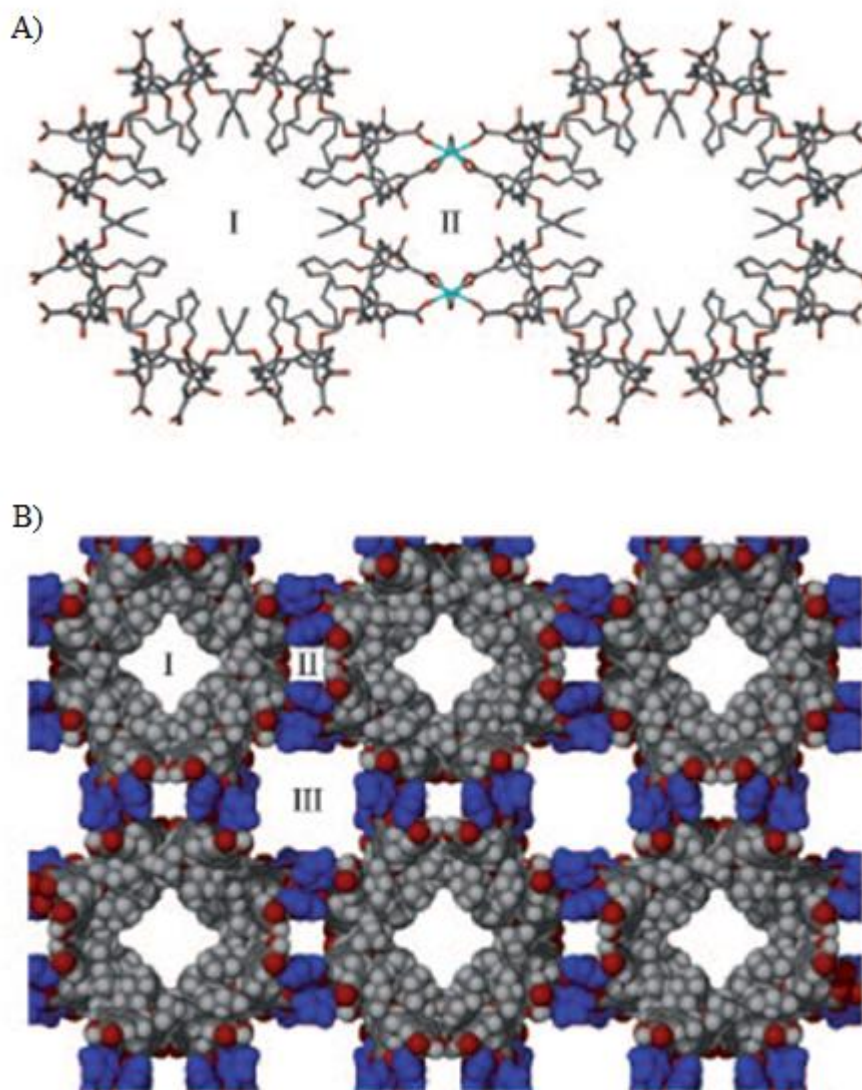


**Figure 106.** Diagrams showing the a) the view down the centre of the nanotubes in  $[\text{M}_2(\mu\text{-H}_2\text{O})(\text{L}^{1\text{C}4})_2(\text{Py})_4]$  and b) a space filling representation of the extended structure, showing the 1.3 nm (I), 0.75 nm (II) and 1.8 nm (III) pores. Coordinated pyridine molecules are coloured blue.

The nanotubes arising from these stacked eight calixarene rings are cross-linked to their four nearest neighbours through the  $[M_2(\mu\text{-H}_2\text{O})(L^{1C4})_2(\text{Py})_4]$  units, giving two further solvent filled channels of 0.75 nm and 1.8 nm, the internal surfaces of which are lined with the uncoordinated carboxylate functions of the calixarene ligands, figure 5b. These factors suggest that these materials would be good candidates for gas adsorption studies, however the lack of strong bonding interactions between the metalocalixarene dimers precludes the removal of guest molecules without the breakdown of the structure, as indicated by microanalyses conducted.

The series of structures reported by Burrows *et al.* using the ligand 25, 26, 27, 28-tetrapropoxycalix[4]arene-5, 17-dicarboxylic acid ( $\text{H}_2\text{L}^{2C4}$ ) are the only literature examples of multidimensional metalocalix[4]arene structures prepared with the gas storage properties of the resultant materials in mind.<sup>14</sup> Solvothermal reactions of the ligand with the nitrates of zinc, copper, cobalt and cadmium in DMF afford four coordination polymers, with the dimensionality of the resulting structures being dependent on the metal centre used. The use of copper and zinc affords two analogous structures bearing the formula  $[M_2(L^{2C4})_2(\text{DMF})_2]_n$ , (where M = Cu, Zn), figure 107. These 2D sheets of single ligand thickness are comprised of calix[4]arene units bound to the metal centres through their carboxylate functions. These structures exhibit the paddlewheel metal-carboxylate binding motif often observed in MOF synthesis. Each paddle wheel unit is comprised of four carboxylate moieties from four different calix[4]arene units bound in a didentate fashion to two metal centres. Apically bound DMF molecules give distorted tetrahedral coordination geometry around the metal centre. This binding motif is repeated at each of the carboxylate moieties giving rise to 2D sheets bearing (4,4) net topology. No binding interactions are observed between the sheets.

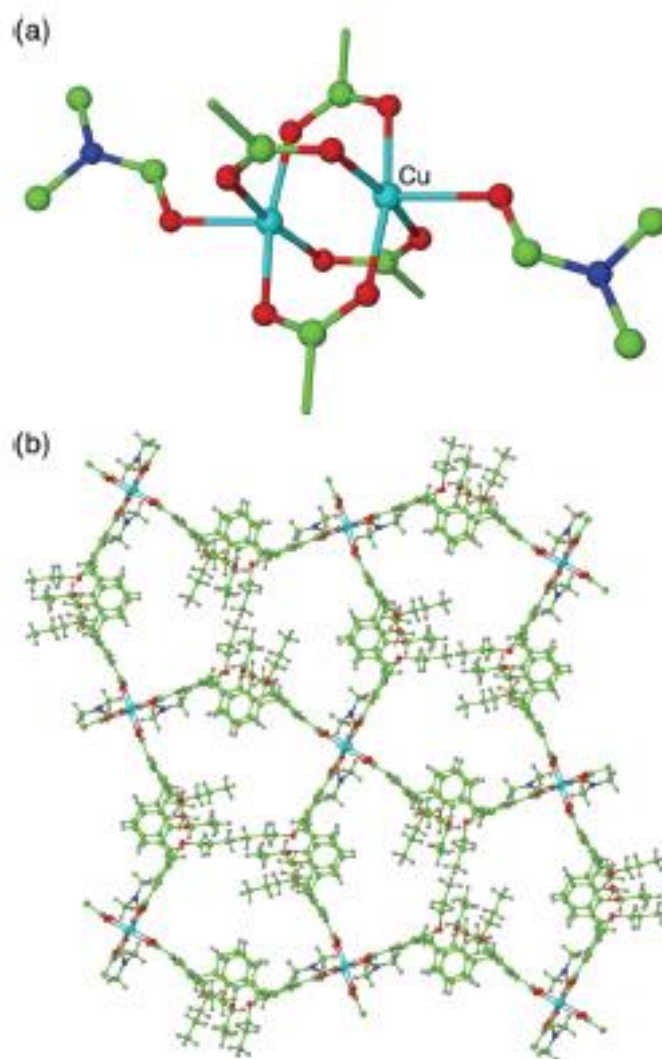


**Figure 107.** The  $[\text{Cu}_2(\text{L}^{2\text{C}4})_2(\text{DMF})_2]_n$  structure showing a) the copper paddlewheel unit with apically bound DMF molecules and b) the (4,4) net formed by the linking of calixarene units *via* the paddlewheel SBU. Reproduced from ref. 14.

The use of cobalt also gives rise to a 2D sheet structure however very different metal-carboxylate binding modes are observed. In this example infinite chains are formed by the interaction of both of the carboxylate moieties of each calixarene unit being bound to a  $\text{Co}_4(\mu_3\text{-OH})_2$  core in an alternate up/down arrangement. The chains are cross-linked by bridging  $\text{Co}(\text{H}_2\text{O})_4(\text{L}^{2\text{C}4})_2$  units, giving extended bilayer sheets of the formula  $\{[\text{Co}_5(\text{L}^{2\text{C}4})_4(\text{OH})_2(\text{H}_2\text{O})_4].8\text{DMF}\}_n$ , exhibiting the previously unreported SBU,  $\text{Co}_4(\mu_3\text{-OH})_2(\text{O}_2\text{CR})_6$ , figure 108.

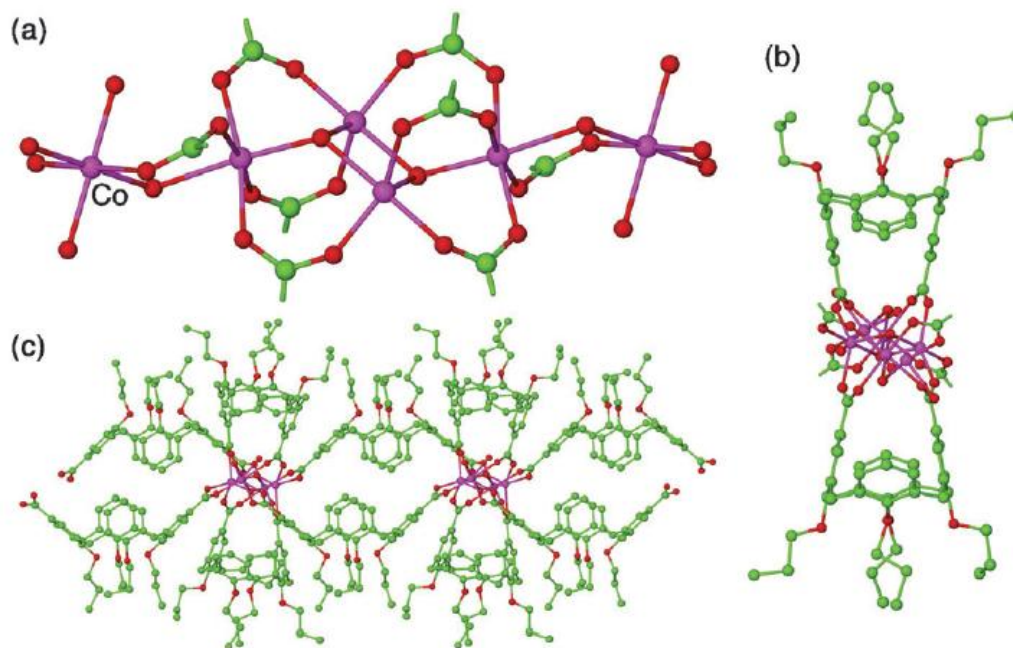


**Figure 108.** The  $\{[\text{Co}_5(\text{L}^{2\text{C}4})_4(\text{OH})_2(\text{H}_2\text{O})_4].8\text{DMF}\}_n$  structure showing a) the alternate  $\text{Co}_4(\mu_3\text{-OH})_2(\text{O}_2\text{CR})_6$  and  $\text{Co}(\text{H}_2\text{O})_4(\text{O}_2\text{CR})_6$  units forming the SBU core of the structure b) the infinite chains formed by the coordination of calixarene units to the SBU and c) the extended structure formed by the cross-linking of the infinite chains by  $\text{L}^{2\text{C}4}$  units. Reproduced from ref. 14.

The use of cadmium leads to the assembly of an extended 3D structure bearing a  $\text{Cd}_4(\text{O}_2\text{CR})_8$  SBU. This structure is comprised of a similar (4,4) net to that observed in the 2D copper and zinc structures previously described, however the enlarged SBU in this example allows for the binding of four additional bridging calixarene units, with two above and two below the plane of the (4,4) net linking neighbouring sheets in to an extended 3D structure of the formula,  $\{[\text{Cd}_2(\text{L}^{2\text{C}4})_2(\text{DMF})_2].3\text{DMF}\}_n$ , figure 109.

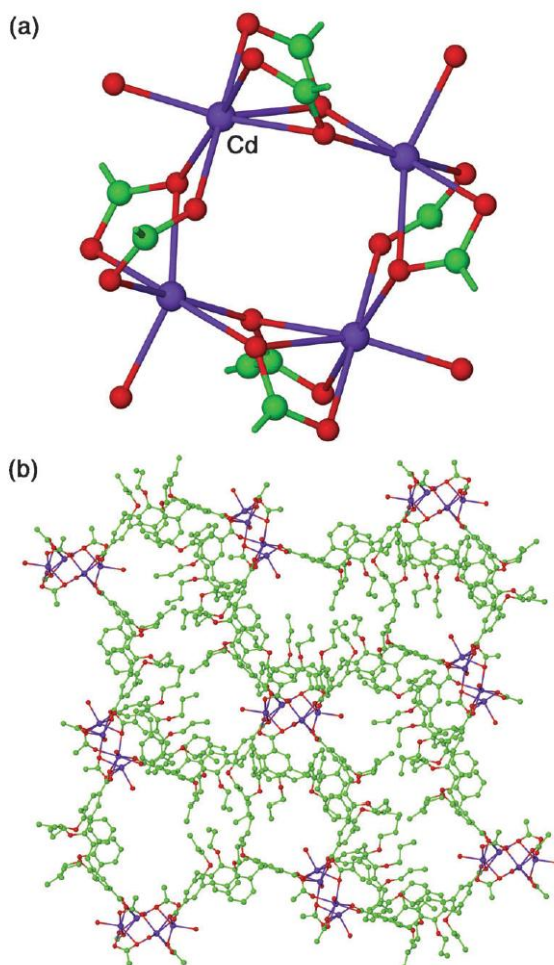
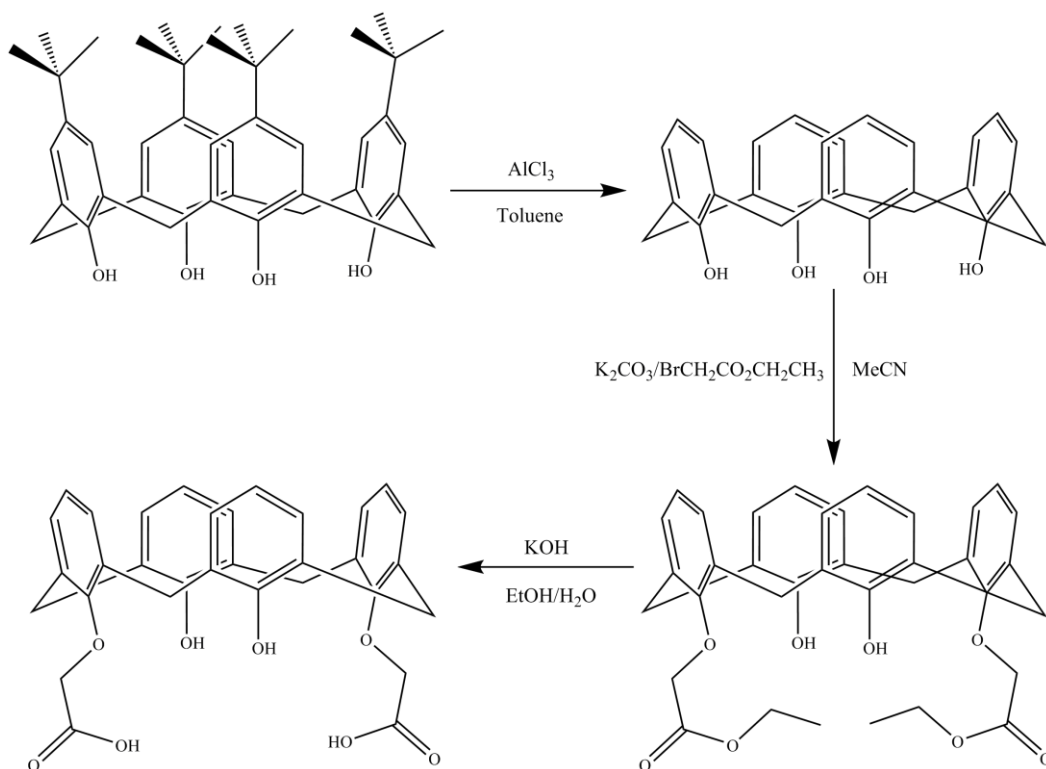


**Figure 109.** The  $\{[\text{Co}_5(\text{L}^{2\text{C}4})_4(\text{OH})_2(\text{H}_2\text{O})_4].8\text{DMF}\}_n$  structure showing a) the  $\text{Cd}_4(\text{O}_2\text{CR})_8$  SBU and b) the extended structure of the framework viewed in the  $b/c$  plane. Reproduced from ref. 14.

The accessible surface areas for these structures, as calculated *via* simulations using an  $\text{N}_2$  probe molecule are reported as  $190 \text{ m}^2 \text{ g}^{-1}$  for  $[\text{Cu}_2(\text{L}^{2\text{C}4})_2(\text{DMF})_2]_n$ ,  $441 \text{ m}^2 \text{ g}^{-1}$  for  $\{[\text{Co}_5(\text{L}^{2\text{C}4})_4(\text{OH})_2(\text{H}_2\text{O})_4].8\text{DMF}\}_n$  and  $410 \text{ m}^2 \text{ g}^{-1}$  for  $\{[\text{Cd}_2(\text{L}^{2\text{C}4})_2(\text{DMF})_2].3\text{DMF}\}_n$ , with experimentally determined values for surface area falling below these. The comparatively low surface areas have been attributed to the inability to remove coordinated DMF molecules without the loss of structural integrity. Further simulations conducted on the gas uptake behaviours of these structures with methane and hydrogen in the absence of solvent molecules reveal interesting selectivity to hydrogen, due to the inaccessibility of the calixarene bowl to methane, suggesting the potential for the use of these structures as gas separation media.

#### 4.1.1. Metal-organic frameworks based on lower-rim acid functionalised calix[4]arenes

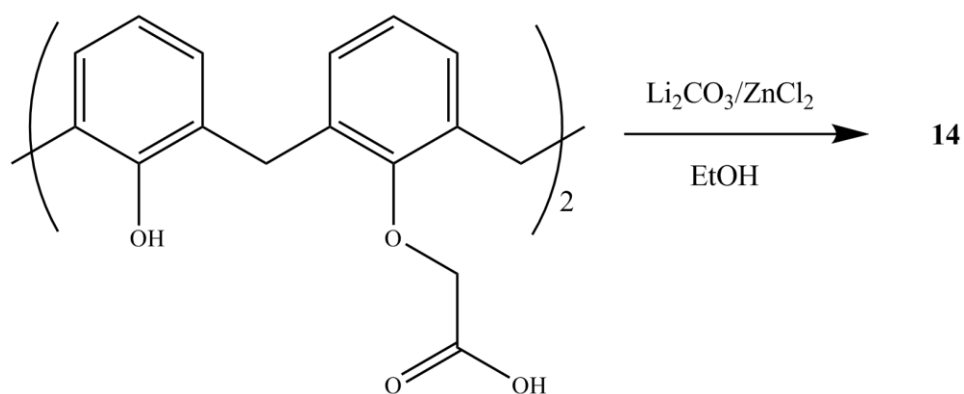
The potential for acid functionalised calix[4]arenes to be utilised as anionic linkers in the synthesis of metal-organic frameworks has been demonstrated by the examples described previously. The design of such frameworks gives the possibility for hierarchically porous materials, with void spaces capable of binding guest molecules arising not only from the secondary structure formed by the coordination of the linkers to metal and metal oxide clusters, but also from the primary structure of the calix[4]arene bowl. This research however also reveals the inherent problems of a research strategy based on upper-rim functionalisation. The classical up/down packing observed in the crystal structures of many functionalised calix[4]arenes is mirrored in the coordination of these upper-rim functionalised calix[4]arenes to transition metals, giving rise to the formation of discrete dimer complexes or extended networks exhibiting upper-rim to upper-rim bonding, effectively forming cavitations from which it is either very difficult to remove guest solvent molecules, or to which there is no access to guest molecules. Though this feature may be desirable in the design of future materials for separation of gases on a size exclusion basis, further research is required to provide such materials. To date, only one literature example of the use of a lower-rim acid functionalised calix[4]arene in the construction of a metal-organic framework exists, however it has been shown to be a viable means by which to maintain access to the calix[4]arene bowl, due to the distance between, and the divergent nature of the bowl and the metal coordination sites. Though the rational design of such frameworks is complicated by the conformational freedom of the appended acetic acid groups the advantages of a research strategy based on lower-rim functionalised calix[4]arenes have prompted our investigation in to the design of MOFs based on the potential linker 25, 27-bis(methoxycarboxylic acid)-26, 28 dihydroxycalix[4]arene ( $L^2H_2$ ). The preparation of this molecule from *para-tert*butylcalix[4]arene is trivial, following the synthetic procedure reported by Iwamoto and Shinkai,<sup>15</sup> scheme 14.



**Scheme 14.** Synthetic route for the preparation of 25,27-bis(methoxycarboxylic acid)-26,28-dihydroxycalix[4]arene ( $L^2H_2$ ) from *para*-*tert*-butylcalix[4]arene.

## 4.2. Results and Discussion

### 4.2.1. Lithium structures



**Scheme 15.** Synthetic route for the preparation of  $[Li_6(L^2)_3]_n$ , **14**.

The preparation of **14** was achieved using a revised version of the method employed by Liu.<sup>11</sup> In that example the use of  $K_2CO_3$  and  $CoCl_2$  lead to the 3D structure described previously. The increased hydrogen uptake behaviour predicted by the lithiation of calix[4]arenes however, prompted the substitution of  $K_2CO_3$  for  $Li_2CO_3$ .

The substitution of  $\text{CoCl}_2$  with  $\text{ZnCl}_2$  was prompted by the prevalence of the zinc paddlewheel SBU in MOF synthesis and the increased thermal and structural stability demonstrated by this metal carboxylate cluster compared to single metal-oxygen bonds.

Treatment of  $\text{L}^2\text{H}_2$  with  $\text{Li}_2\text{CO}_3$  in the presence of  $\text{ZnCl}_2$  in ethanol at reflux, following scheme 15, affords a pink complex (**14**) which crystallises as hexagonal prisms in good yields by slow evaporation of the solvent. The structure of **14** is comprised of calixarene units linked *via* two lithium carboxylate bridges per calixarene into cyclic trimeric units, figure 110.

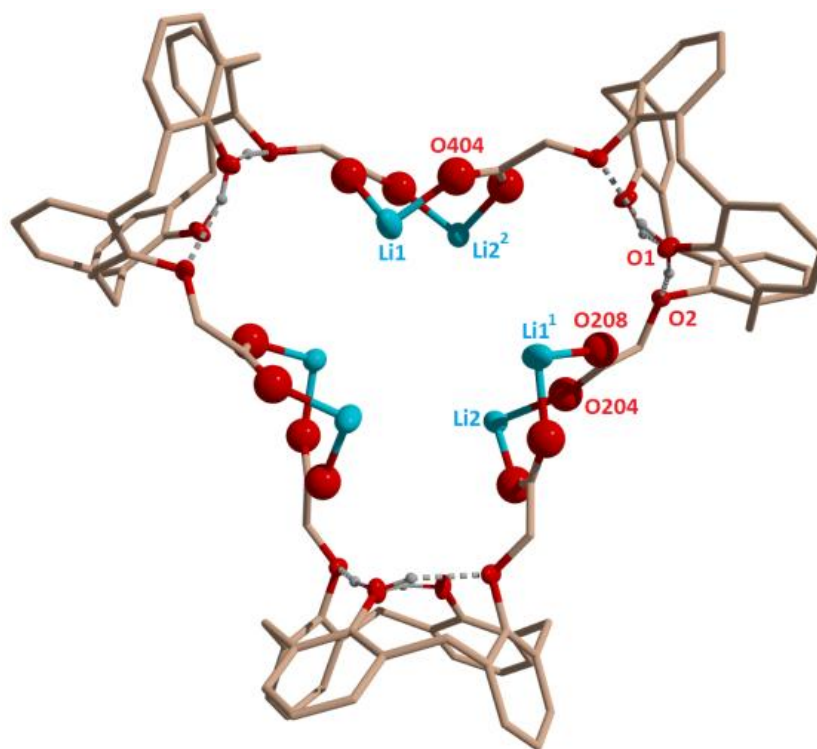


**Figure 110.** Diagram showing the cyclic arrangement of three calixarene units observed in **14**. Calix[4]arene units are linked about a three-fold symmetry axis which is parallel to the crystallographic  $c$  axis. The carboxylate groups (disordered, refined isotropically) shown are of one of several options for each group. Highly disordered solvent atoms in the central core have been omitted.

The trimeric units, related by centres of symmetry, stack in such a way that alternate units are rotated  $60^\circ$  forming helical nanotubes, which pack in a ‘honey-comb’ arrangement, figure 111.

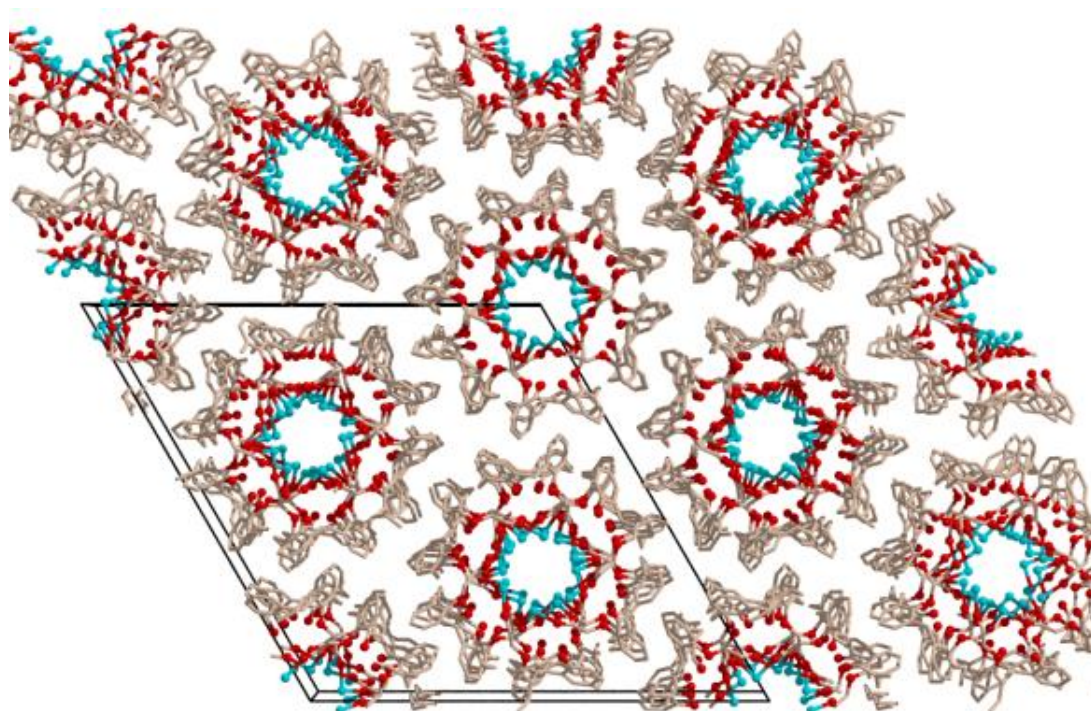


**Figure 111.** The hexagonal packing of individual nanotubes in the extended structure of **14**, when viewed in the *ab* plane.

These cylinders of trimeric units have an outer diameter of 20.36 Å (calculated from the distance between the three-fold symmetry axes through adjacent columns) and an internal diameter of 5.5 Å (calculated from the distance of the innermost non-hydrogen atom, Li(1), from the symmetry axis), figure 112. Due to the absence of zinc from this structure, repeated attempts were made to crystallise **14** from ethanol without the addition of ZnCl<sub>2</sub>, however these attempts were unsuccessful. Though the exact role played by ZnCl<sub>2</sub> in the reaction is unknown the effect of its addition to the polarity of the mother liquor may facilitate the formation of the crystalline species.

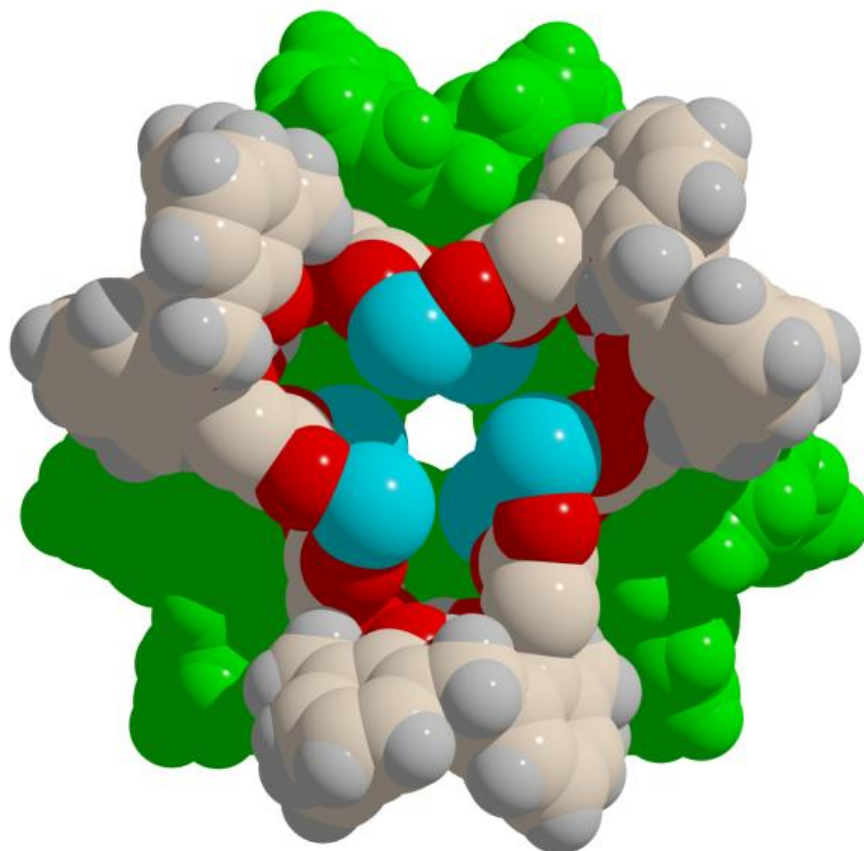
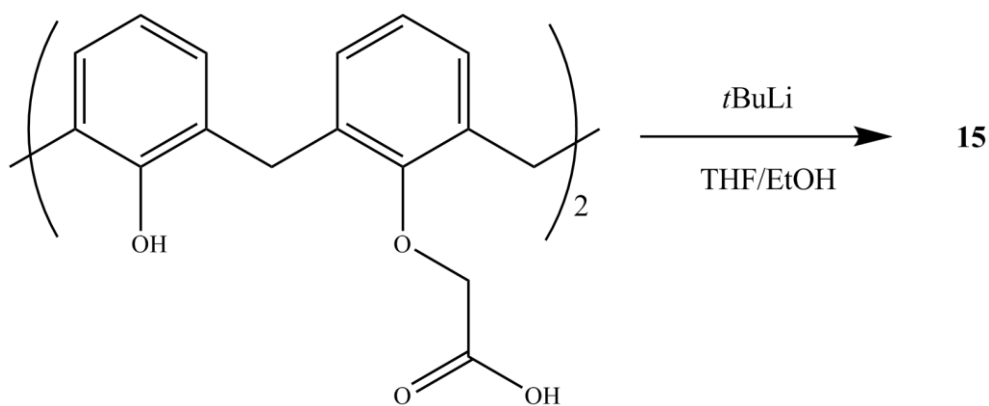


**Figure 112.** Space-filling model of **14**, showing the stacking of trimeric units along the *c* axis. A small, lithium lined void is visible along the length of the resulting nanotube (Li = blue; second trimer = green).

The pattern observed in the structure of **14** is analogous to the structure of the crystallised ligand  $L^2H_2$ , as reported by Coleman and co-workers.<sup>14</sup> In that example, the self-assembly of the supramolecules was attributed to the hydrophobicity of the calix[4]arene bis(methoxycarboxylic acid) bowl, compared to the hydrophilicity of the narrow rim substituents. Crystallisation of the calix[4]arene from methanol/water or chloroform/methanol gave helical nanotubes 20.6 Å in diameter (as defined above) with an internal channel of 6.9 Å in diameter (where the innermost non-hydrogen atom is O(16)). A similar structure was observed for the methyl ester of the calix[4]arene bis(methoxycarboxylic acid), which displayed a diameter of 19.0 Å with an internal channel of 5.5 Å. In both these structures the formation of nanotubes is mediated by hydrogen bonding involving the carbonyl moieties of the pendant groups. It is of note that the ethyl ester of the calix[4]arene bis(methoxycarboxylic

acid) did not follow this trend, but demonstrated the classical up/down packing frequently observed in the crystal structures of substituted calix[4]arenes.<sup>14</sup>

This self-assembly of calix[4]arene supramolecules through hydrophobic/hydrophilic interactions has also been reported by Suwinska *et al.*<sup>16</sup> who showed that the hydrophobicity of the calix[4]arene bowl was increased by the presence of  $\beta$ -carbonyl-*para*-octyl groups on the upper-rim of the calix[4]arene. The aggregation of the calix[4]arene units from non-anhydrous THF affords dodecameric ‘inverse micelles’ with a diameter of 42 Å and an internal void of 1100 Å<sup>3</sup> which contained disordered water molecules. The close proximity (4.6 Å) of the ‘micelles’ allows for the intanglement of the  $\beta$ -carbonyl-*para*-octyl groups between neighbours that gave rise to a second smaller pore of 130 Å<sup>3</sup>. Diffuse electron density in these voids suggests that water molecules are also present here. Many other examples of amphiphilic calix[4]arene structures, mediated by the presence of metal ions exist in the literature, though the majority of these involve the use of *para*-sulfonatocalix[4]arene coordinated to late transition metals. The structure reported herein, is the first example of a calix[4]arene diacid being linked *via* lithium-carboxylate bonds to form helical nanotubes.



**Scheme 16.** Synthetic route for the preparation of  $[\text{Li}_4(\text{L}^2)_2(\text{EtOH})_2]$ , **15**.

In an attempt to achieve a greater degree of lithiation at the lower-rim of  $\text{L}^2\text{H}_2$ , the ligand was reacted with *t*BuLi in THF under anhydrous conditions, followed by crystallisation from dry ethanol, scheme 16. The involvement of the hydroxyl functions of the calix[4]arene dimethoxycarboxylic acid led to the formation of the dimeric structure,  $[\text{Li}_4(\text{L}^2)_2(\text{EtOH})_2]$  (**15**), again with each calixarene bound to two

lithium ions, figure 113. In this case however, one of the lithium atoms is bound to an ethanol molecule, which provides an OH group for intermolecular hydrogen bonding with an acid group of the neighbouring dimer, giving infinite chains, figure 114.

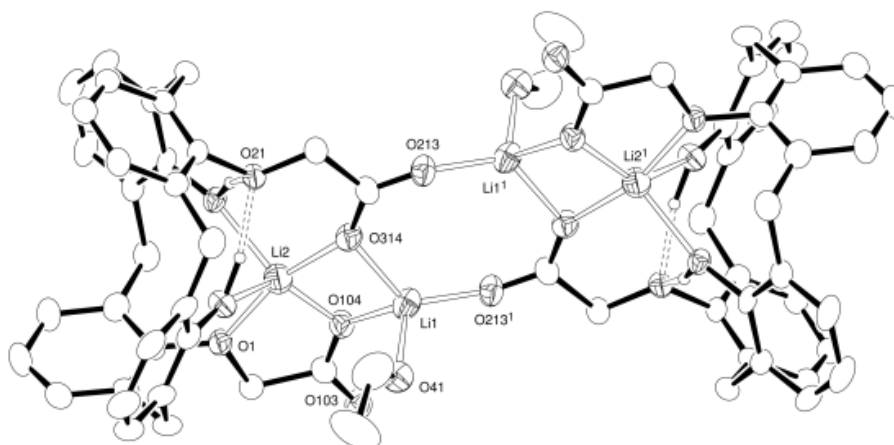


**Figure 113.** ORTEP diagram showing the lithium-calix[4]arene dimer, **15**. Displacement ellipsoids are drawn at the 30% probability level. Hydrogen atoms (except those involved in hydrogen bonding) are omitted for clarity.

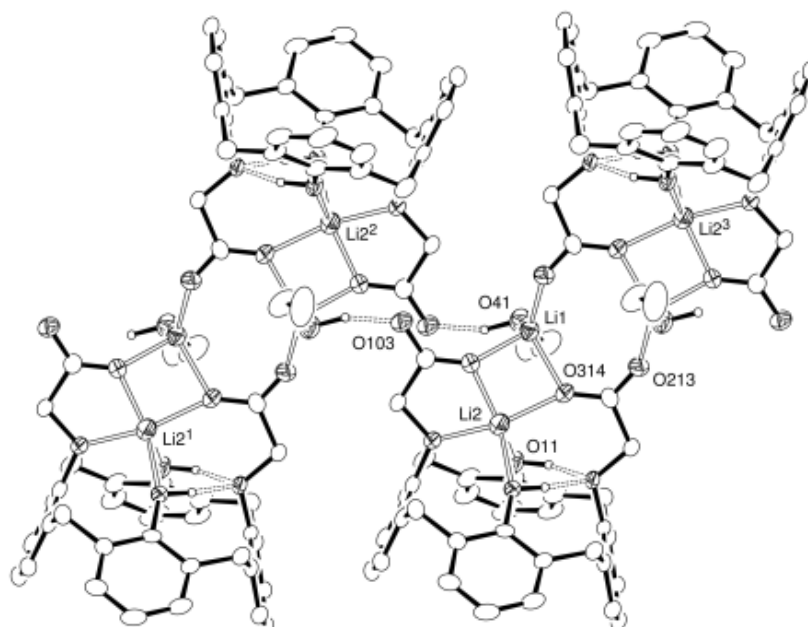
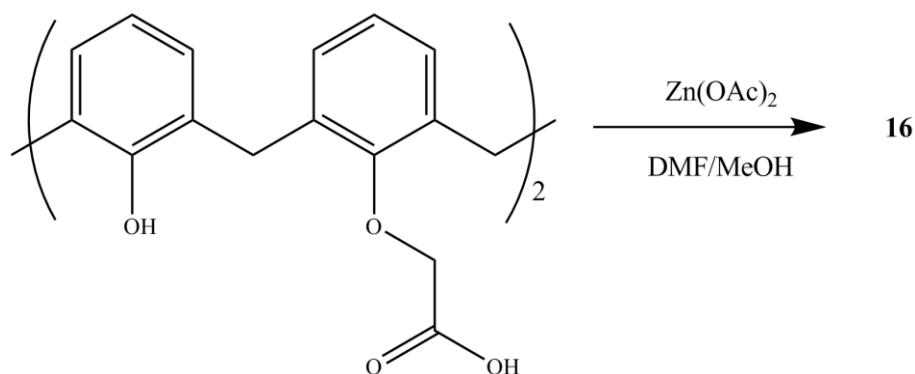


**Figure 114.** ORTEP diagram showing the chains resulting from intermolecular hydrogen bonding between the dimer units in **15**. Hydrogen atoms (except those involved in hydrogen bonding) are omitted for clarity.

#### 4.2.2. Zinc structure



**Scheme 17.** Synthetic route for the preparation of  $[\text{Zn}(\text{L}^2)_2(\text{DMF})(\text{H}_2\text{O})]_n$ , **16**.

The reaction of  $\text{L}^2\text{H}_2$  with zinc acetate under solvothermal conditions following scheme 17, yields the coordination polymer  $[\text{Zn}(\text{L}^2)_2(\text{DMF})(\text{H}_2\text{O})]_n$  (**16**), figure 115. In this example, each metal centre is bound to three calix[4]arene units (*via* acid moieties), a DMF and a water molecule, the latter molecules binding in equatorial positions giving pseudo-trigonal bipyramidal zinc centres.

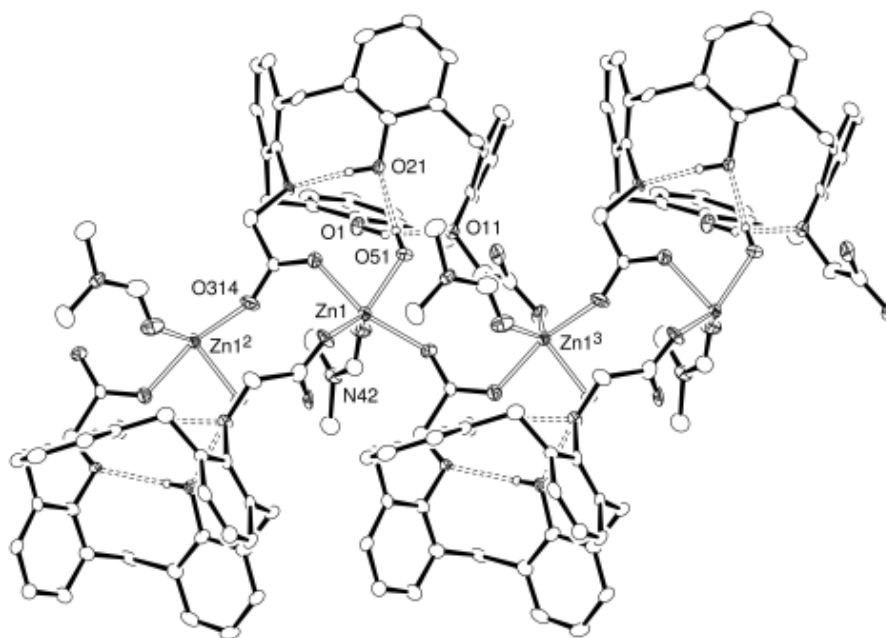


**Figure 115.** ORTEP diagram of  $[\text{Zn}(\text{L}^2)_2(\text{DMF})(\text{H}_2\text{O})]_n$  **16**, as viewed along the *b* axis. Hydrogen atoms have been omitted for clarity.

The carboxylate unit of O(313) and O(314) bridges two metal centres giving infinite chains through the crystal, parallel to the *a* axis. These chains pack in an offset herring-bone pattern with the coordinated DMF molecule dipping into the cavity of the neighbouring calix[4]arene unit. No intermolecular binding is observed between the chains, figure 116.

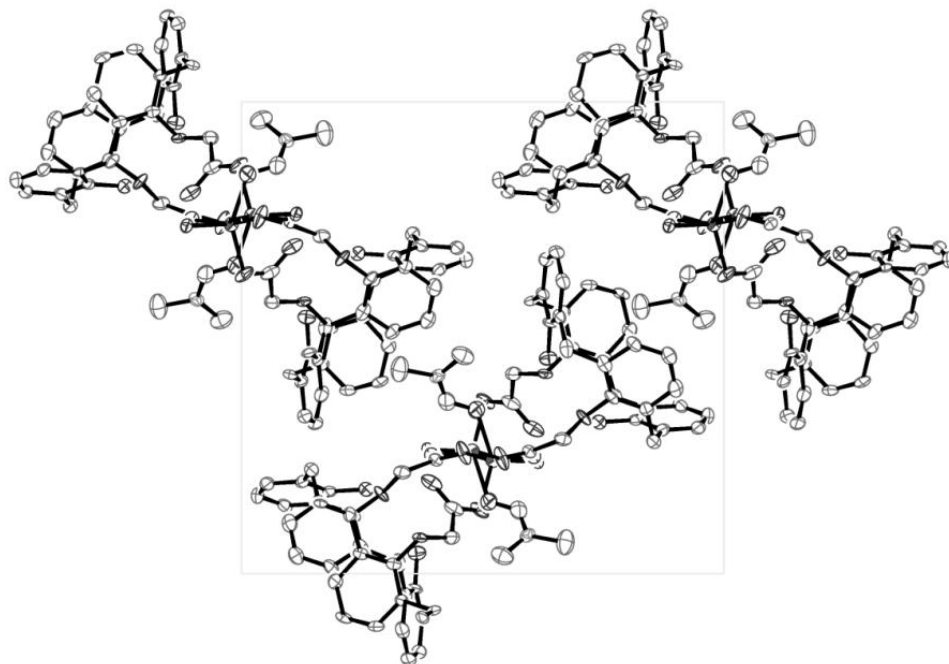


**Figure 116.** ORTEP diagram of **16**, showing the herring-bone packing arrangement of 1D chains. Hydrogen atoms have been omitted for clarity.

### 4.2.3. Thermogravimetric analysis

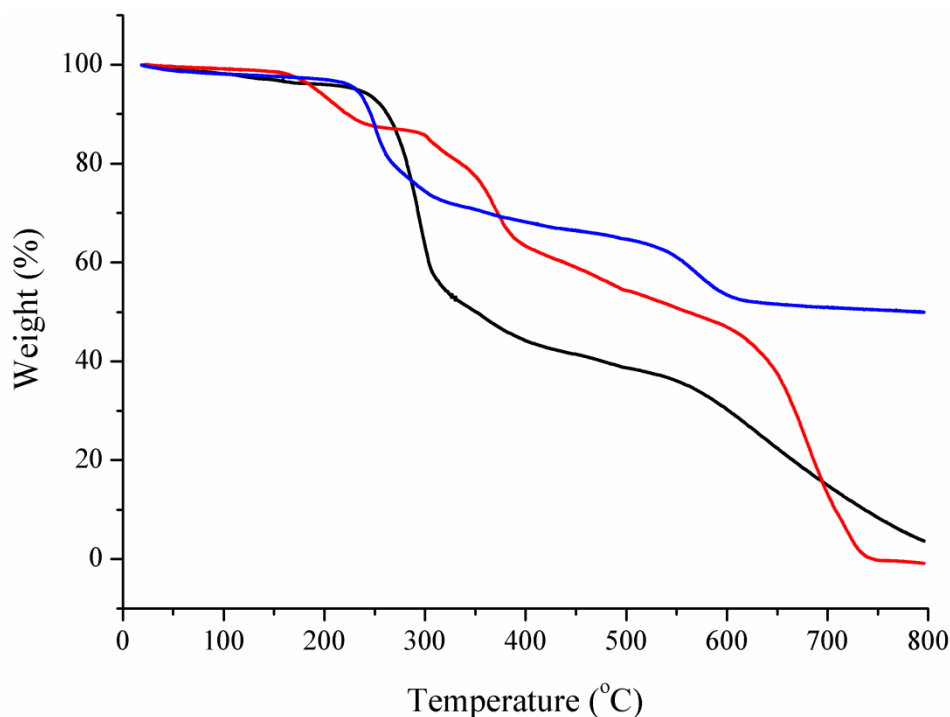


**Figure 117.** Recorded TGA traces for **14** (black), **15** (red) and **16** (blue).

Thermogravimetric analyses (TGA) of **14**, **15** and **16** were performed under an inert carrier flow (He) to further elucidate their solid-state stabilities. Comparison of the TGA traces reveals similar profiles at lower temperature, figure 117. Neither the nanotube material **14**, nor the chain polymer **16**, showed any appreciable mass loss between 25–240 °C that could be ascribed to loss of solvent from pore regions within the lattices. Instead, the onset of continuous structural decomposition was observed in both cases above 250 °C. In the case of **16** this is expected, as the tight packing of the chains prevents the inclusion of unbound solvent molecules. In the case of **14**, however, diffuse electron density suggests the presence of solvent molecules in the lithium lined pores. Structure **15** underwent a localised 12 % mass loss in the range 150–230 °C and was then stable up to 290 °C. This mass loss may be ascribed to the loss of two unbound ethanol and four water molecules per dimer unit. Above 600 °C and even at 800 °C, **16** maintained 52 % total mass. In comparison, major degradation was observed in the Li(I)-containing **14** and **15** that both showed almost complete combustion at 800 °C. This makes sense, since presumably Zn(O) was the major residual component post-decomposition of the organic moieties.

#### 4.2.4. Gas adsorption behaviour

Gas adsorption isotherms were collected for complexes **14-16** after activation of crystalline samples under vacuum ( $10^{-10}$  bar) at 150 °C for 4 h, using various probe adsorbates (H<sub>2</sub>, 78 K; N<sub>2</sub>, 78 K; CO<sub>2</sub>, 196 K). Unfortunately, the materials did not show appreciable uptake of any of these molecules, as predicted by the lack of desolvation from the TGA experiments.

#### 4.3. Conclusion

Three novel coordination polymers based on a lower-rim acid functionalised calix[4]arene have been synthesised and structurally characterised. The self-assembly of two 1D structures results from the reaction of the calix[4]arene with sources of Li<sup>+</sup>, with the morphology of the structures dictated by the strength of the lithiating agent. In the first instance, the use of lithium carbonate afforded helical nanotubes *via* the coordination of one lithium centre per calix[4]arene at the acid moiety. This structure, bearing 1D channels of 5.5 Å diameter through the centre of the nanotubes, is the first example of a structure of this type being reported. The second example, formed by the reaction of <sup>t</sup>BuLi with the acid appended calix[4]arene exhibits a 1D chain structure, formed by the hydrogen bonding of calix[4]arene dimers. Each dimer unit in this example bears four lithium centres, coordinated to the acid moieties and the phenolic oxygens of the calix[4]arene. The third structure was synthesised by the reaction of the functionalised calix[4]arene with zinc acetate under solvothermal conditions, affording a second 1D chain structure, bearing coordinate bonds between the dimeric units.

Thermogravimetric analyses performed on these three structures, reveal a lack of desolvation at elevated temperatures, offering evidence of their non-porous nature. In all of these examples, however, the calix[4]arene exists in the bowl conformation, giving the potential for guest molecules to be adsorbed, though gas uptake studies conducted using a variety of analyte molecules, showed no appreciable uptake for any of the structures. Previously published research has shown that the calix[4]arene bowl readily participates in host-guest chemistry, hence this lack of gas uptake is unexpected, but may be explained by the close-packing of the calix[4]arene units in all three examples preventing access to the bowl. Further research using lower-rim acid functionalised calix[4]arenes should therefore address this issue, employing

techniques to increase both the dimensionality of the structures and the spacing between calix[4]arene units.

#### 4.4. References

- 
- 1 a) C. D. Gutsche, B. Dhawan, K. H. No, R. Muthukrishnan. *J. Am. Chem. Soc.*, 1981, **103**, 3782. b) C. D. Gutsche, *Acc. Chem. Res.*, 1983, **16**, 161. c) R. Ungaro, A. Pochini, G. D. Andreetti, V. Sangermano, *J. Chem. Soc. Perkin Trans. 2*, 1984, 1979.
  - 2 J. L. Atwood, L. J. Barbour, A. Jerga. *Science*, 2002, **296**, 2367.
  - 3 a) J. L. Atwood, L. J. Barbour, A. Jerga, B. L. Schottel, *Science*, 2002, **298**, 1000; b) P. K. Thallapally, T. B. Wirsig, L. J. Barbour, J. L. Atwood, *Chem. Commun.*, 2005, **35**, 4420. c) J. L. Atwood, L. J. Barbour, A. Jerga, *Angew. Chem. Int. Ed.*, 2004, **43**, 2948. d) J. L. Atwood, L. J. Barbour, P. K. Thallapally, T. B. Wirsig. *Chem. Commun.*, 2005, **51**, 5272.
  - 4 G. S. Ananchenko, I. L. Moudrakovski, A. W. Coleman, J. A. Ripmeester, *Angew. Chem.*, 2008, **120**, 5698; *ibid Angew Chem. Int. Ed.*, 2008, **47**, 5616.
  - 5 N.S. Venkataramanan, R. Sahara, H. Mizuseki, Y. Kawazoe, *J. Phys. Chem. C.*, 2008, **112**, 19676.
  - 6 D. M. Homden, C. Redshaw, *Chem. Rev.*, 2008, **108**, 5086
  - 7 a) S. Kennedy, G. Karotsis, C. M. Beavers, S. J. Teat, E. K. Brechin, S. J. Dalgarno, *Angew. Chem. Int. Ed.*, 2010, **49**, 4205 b) A. Wei, S. L. Tripp, J. Liu, T. Kasama, R. E. Dunin-Borkowski, *Supramolecular Chem.*, 2009, **21**, 189.
  - 8 a) I. T. Ho, J. H. Chu, W. S. Chung, *Eur. J. Org. Chem.*, 2011, 1472. b) I. Leray, B. Valeur, *Eur. J. Inorg. Chem.*, 2009, 3525. c) C. Han, H. Li, *Anal. Bioanal. Chem.*, 2010, **397**, 1437.
  - 9 a) K. Langa, J. Mosinger, D. M. Wagnerová, *Coord. Chem. Rev.*, 2004, **248**, 321. b) T. L. Kao, C. C. Wang, Y. T. Pan, Y. J. Shiao, J. Y. Yen, C. M. Shu, G. H. Lee, S. M. Peng, W. S. Chung, *J. Org. Chem.*, 2005, **70**, 2912. c) V. Lamare, J. F. Dozol, S. Fuangswasdi, F. Arnaud-Neu, P. Thuéry, M. Nierlich, Z. Asfari, J. Vicens, *J. Chem. Soc., Perkin Trans.*, 1999, **2**, 271.
  - 10 a) J. L. Atwood, L. J. Barbour, M. J. Hardie, C. L. Raston, M. N. Statton, H. R. Webb, *CrystEngComm*, 2001, **4**, 1. b) J. L. Atwood, G. W. Orr, R. K. Juneja, S. G. Bott, F. Hamada. *Pure Appl. Chem.* 1993, **65**, 1471. c) A. T. Yordanov, O. A. Gansow, M. W. Brechbiel, L. M. Rogers, R. D. Rogers.

- 
- Polyhedron*, 1999, **18**, 1055. d) S. J. Dalgarno, C. L. Raston. *Chem. Commun.*, 2002, **19**, 2216. e) W. Liao, C. Liu, X. Wang, G. Zhu, X. Zhao, H. Zhang. *CrystEngComm*, 2009, **11**, 2282.
- 11 Y.-J. Liu, J.-S. Huang, S. S.-Y. Chui, C.-H. Li, J.-L. Zuo, N. Zhu, C.-M. Che. *Inorg. Chem.*, 2008, **47**, 11514.
- 12 E. J. Brechin, S. J. Dalgarno, S. Kennedy, G. Karotsis, C. M. Beavers, S. J. Teat, *Angew. Chem. Int. Ed.*, 2010, **49**, 4205.
- 13 F. Perret, A.N. Lazar, O. Shkurenko, K. Suwinska, N. Dupont, A. Navaza, A.W. Coleman, *CrystEngComm*, 2006, **8**, 890.
- 14 S. P. Bew, A. D. Burrows, T. Düren, M.F. Mahon, P. Z. Moghadam, V. M. Sebestyen, S. Thurston, *Chem. Commun.*, 2012, **48**, 4824.
- 15 K. Iwamoto, S. J. Shinkai, *J. Org. Chem.*, 1992, **57**, 7066.
- 16 K. Suwinska, B. Lesniewska, M. Wszelaka-Rylik, L. Straver, S. Jebors, A.W. Coleman, *Chem. Commun.*, 2011, **47**, 8766.

## **Chapter 5**

### **Pillared metal-organic frameworks based on a lower-rim acid appended calix[4]arene**

## 5.1. Introduction

The examples described in the previous chapter demonstrate the potential for acid functionalised calix[4]arenes to be used in the construction of multi-dimensional MOFs. The reaction of upper-rim functionalised calix[4]arenes with the late transition metals gives a variety of 2D and 3D frameworks, with the dimensionality of the resulting materials dictated by the nature of the SBU. However, with the exception of the example reported by Liu *et al.* the use of lower-rim acid functionalised analogues lead to the synthesis of only 1D coordination polymers exhibiting nanotube and chain morphologies, with TGA and gas uptake analyses of these structures demonstrating a lack of porosity. In order to synthesise porous frameworks using the lower-rim functionalised calix[4]arene linker, some means of increasing the dimensionality of these structures is required, and it is with this in mind that our attention was drawn to the chain structures **15** and **16**. In both of these examples, the presence of coordinated solvent molecules is reminiscent of the  $[\text{Zn}(\text{BDC})\cdot(\text{DMF})(\text{H}_2\text{O})]_n$  structure and many others, in which the substitution of apically coordinated water molecules with neutral pillaring linkers gives rise to a multitude of porous 3D structures. We therefore embarked on a programme of research involving the reaction of the potential anionic linker 25,27-bis(methoxycarboxylic acid)-26,28-dihydroxy-4-*tert*butylcalix[4]arene with zinc nitrate and the neutral pillaring linkers 4,4'-bipy, DPE and 4,4'-azopy with a view to the synthesis of multi-dimensional porous MOFs. It was hoped that the inclusion of the bipyridyl linkers would give rise to 3D structures exhibiting novel network topologies and hierarchical porosity. While no literature examples exist of the use of neutral pillaring linkers with acid functionalised calix[4]arenes in MOF synthesis, early research conducted by Atwood and Macgillivray reveals the potential for increased dimensionality in hydrogen bound multi-component systems involving the related molecule *C*-methylcalix[4]resorcinarene.<sup>1</sup> The successful synthesis of crystalline *C*-methylcalix[4]resorcinarene(pyridine)<sub>4</sub>·2pyridine, a monomeric species in which four pyridine molecules are hydrogen bonded to the hydroxyl functions of the calix[4]resorcinarene *via* the pyridinyl nitrogens, was followed by the substitution of the pyridine with 4, 4'-bipy. The resulting crystalline product, bearing the formula *C*-methylcalix[4]resorcinarene(4, 4'-bipy)<sub>2</sub> exhibits 1D chains formed by

the H-bonding of two 4, 4'-bipy units per *C*-methylcalix[4]resorcinarene unit in a bridging fashion, figure 118.

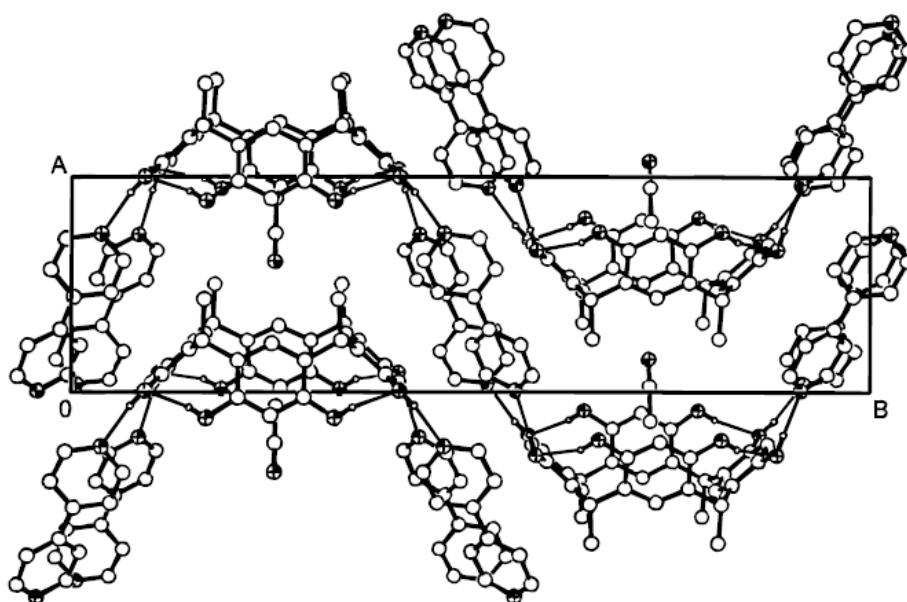
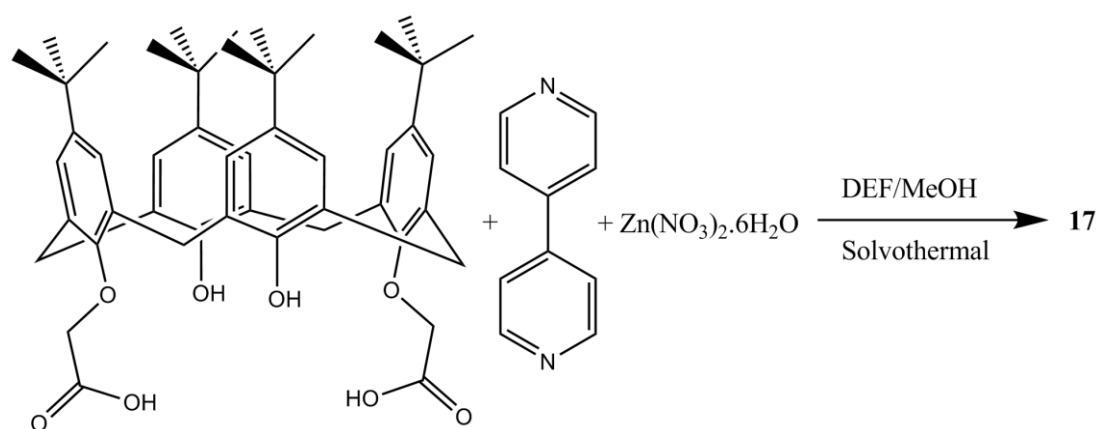


**Figure 118.** The hydrogen-bonded polymer *C*-methylcalix[4]resorcinarene(4, 4'-bipy)<sub>2</sub> viewed along the *c* axis.<sup>1</sup>

Follow-up research by Coppens and co-workers using hydrothermal conditions to explore the H-bonding behaviour of *C*-methylcalix[4]resorcinarene and the bipyridyls 4,4'-bipy and DPE reveals the synthesis of 2 and 3D H-bonded structures,<sup>2</sup> with further examples of multi-dimensional H-bonded networks of this type incorporating longer bipyridyls reported by Nakamura *et al.*<sup>3</sup> In all of these examples, the cavities formed by the interaction of the component molecules are capable of hosting guest molecules, and in many cases, the topology of the H-bonded networks is determined by the size and shape of the guest. It is therefore reasonable to assume that the employment of these principles in a coordination chemistry environment will also afford multi-dimensional structures capable of incorporating guest molecules.

## 5.2. Results and discussion



**Scheme 18.** Synthetic route for the preparation of  $\{[Zn(4,4'\text{-bipy})(L^3)] \cdot 2.25DEF\}_n$ , **17**.

The solvothermal reaction of  $L^3H_2$  with 4,4'-bipy and zinc nitrate in a DEF/methanol mixture following scheme 18 afforded **17** as colourless prisms in good yield. The crystals were of suitable quality for single crystal X-ray diffraction, however requiring the use of synchrotron radiation to provide an adequate data set. Elucidation of the structure reveals the self-assembly of a 2D extended bilayer structure of the formula  $\{[Zn(4,4'\text{-bipy})(L^3)] \cdot 2.25DEF\}_n$  formed by the coordination of 4,4'-bipy molecules to  $Zn_2L^3_2$  dimers. Each of the dimers comprises two calix[4]arene molecules linked through 2 zinc atoms *via* the coordination of their carboxylate groups. These carboxylate groups adopt a monodentate binding mode, the unbound carboxylate oxygen involved in H-bonding to the phenolic -OH groups of the parent calixarene, with two 4,4'-bipy molecules per metal giving a tetrahedral coordination geometry, figure 119.

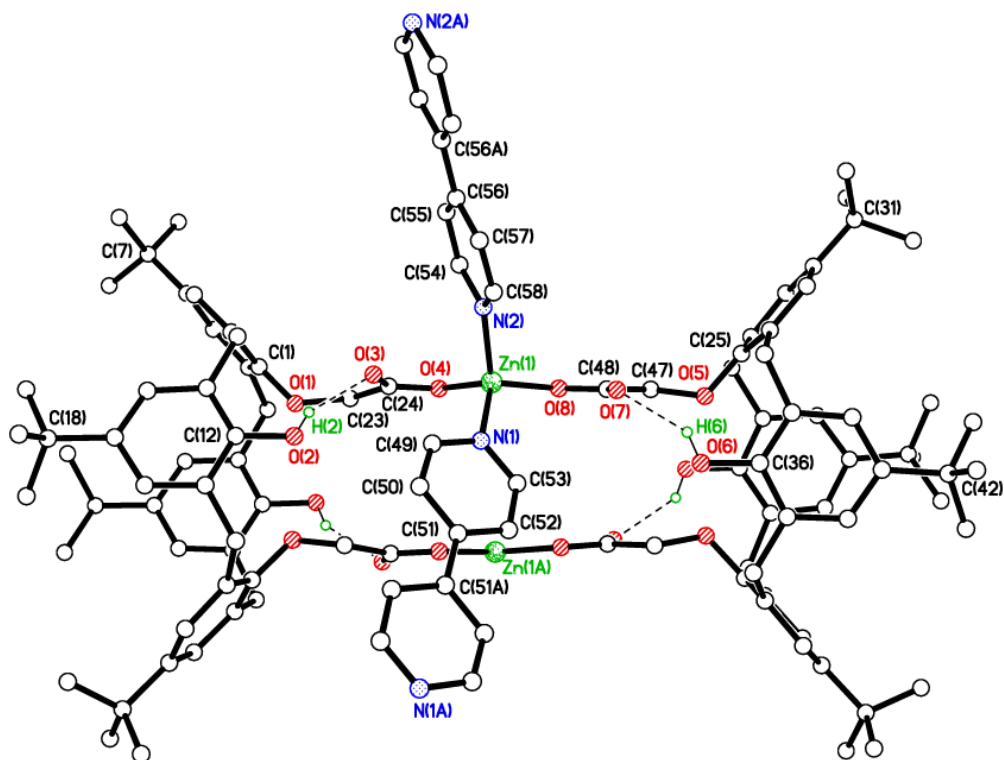


**Figure 119.** Diagram of the  $\text{Zn}_2(\text{L}^3)_2(4,4'\text{-bipy})_2$  dimer comprising **17**, showing the coordination environment around the metal centres. Hydrogen atoms, except those involved in H-bonding interaction are omitted. Hydrogen bonds are represented by dotted lines.

The 4,4'-bipy molecules extend in four divergent directions in the  $a/c$  plane, linking the dimers to their four nearest neighbours to give the extended 2D structure with sheets observed in the  $a/c$  plane, Figure 120. Two large cavities per unit cell, located around the neutral linkers, contain highly disordered solvent molecules which were modelled as areas of diffuse electron density using the PLATON squeeze procedure, giving approximately 9 DEF molecules per void, or 18 per unit cell.

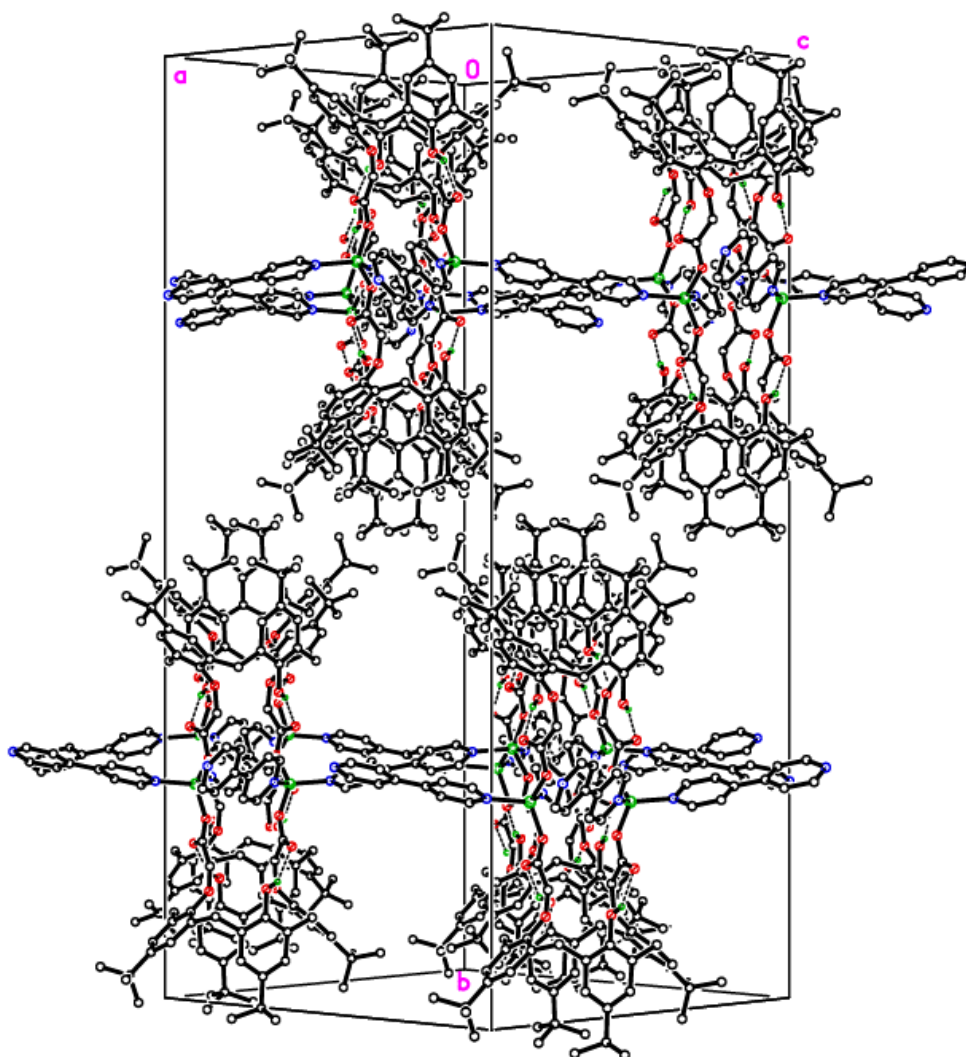


**Figure 120.** Diagram of **17** viewed along the  $a/c$  plane. Carbon atoms are represented by empty circles, with nitrogen, oxygen and zinc atoms coloured blue, red and green respectively. Hydrogen atoms, except those involved in H-bonding, which are represented by small green circles, are omitted.

No guest solvent molecules are observed inside the calix[4]arene bowl, due to the pinched cone conformation adopted by the molecule, figure 121. This conformation may result from the intramolecular H-bonding observed between the H(2)/H(6) hydrogens and the O(3)/O(7) oxygens which reduces the angle between the non-functionalised phenol units, or by the conformation adopted by the acid moieties, which forces the acid appended phenol units to swing outward.

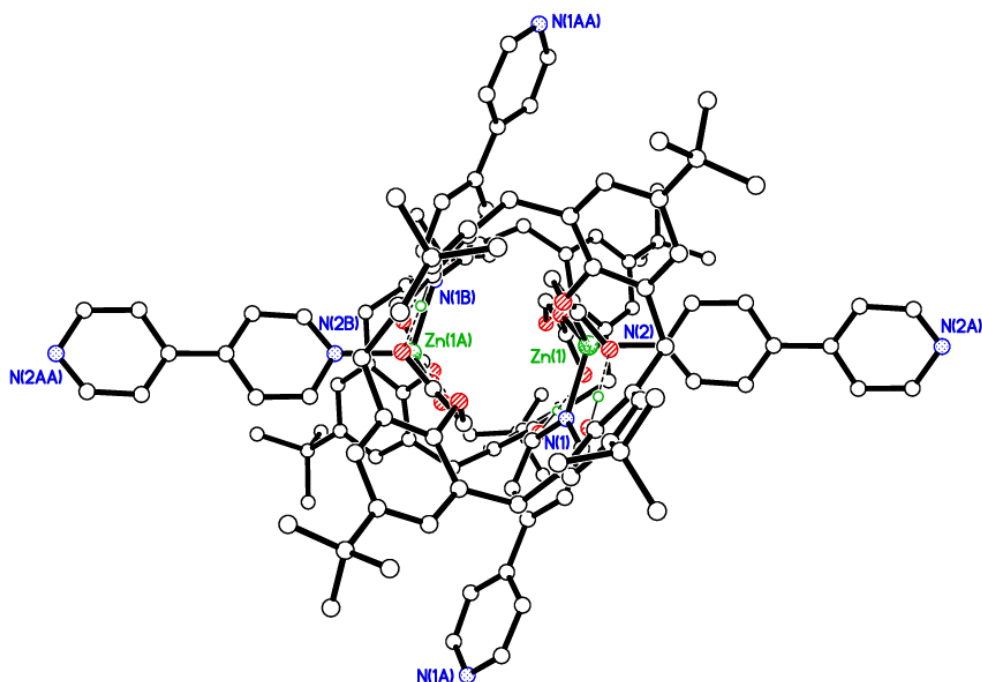
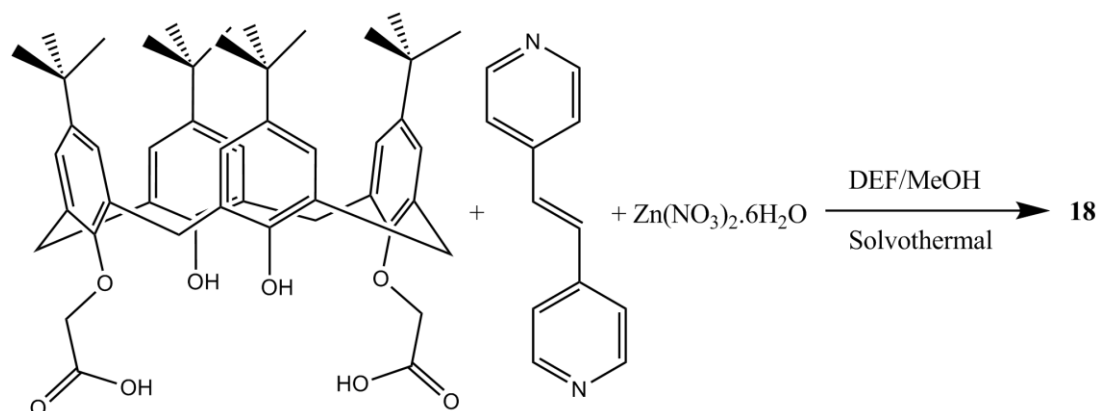


**Figure 121.** Diagram of **17** viewed through the annulus of the calix[4]arene molecule showing the pinched conformation adopted in this structure. Carbon atoms are represented by empty circles, with nitrogen, oxygen and zinc atoms coloured blue, red and green respectively. Hydrogen atoms, except those involved in H-bonding, which are represented by small green circles, are omitted.



**Scheme 19.** Synthetic route for the preparation of  $\{[\text{Zn}_2(\text{L}^3)_2(\text{DPE})].\text{DEF}\}_n$ , **18**.

The solvothermal reaction of  $\text{L}^3\text{H}_2$  with DPE and zinc nitrate in a DEF/methanol mixture following the procedure at scheme 19 afforded **18** as pale yellow prisms in moderate yield. The crystals were of sufficient quality for elucidation by single

crystal X-ray diffraction, revealing a 2D structure of the formula  $\{[\text{Zn}_2(\text{L}^3)_2(\text{DPE})].\text{DEF}\}_n$ . The structure of **18** differs from that of **17** in both carboxylate coordination mode and packing. In this example, four neighbouring calix[4]arene units are linked *via* the coordination of one of the appended acid moieties in a di-monodentate fashion to two zinc centres, giving the paddlewheel SBU, figure 122. This coordination mode is observed at each of the acid moieties, giving infinite chains of the formula  $\text{ZnL}^3$ , observed along the *a* axis.

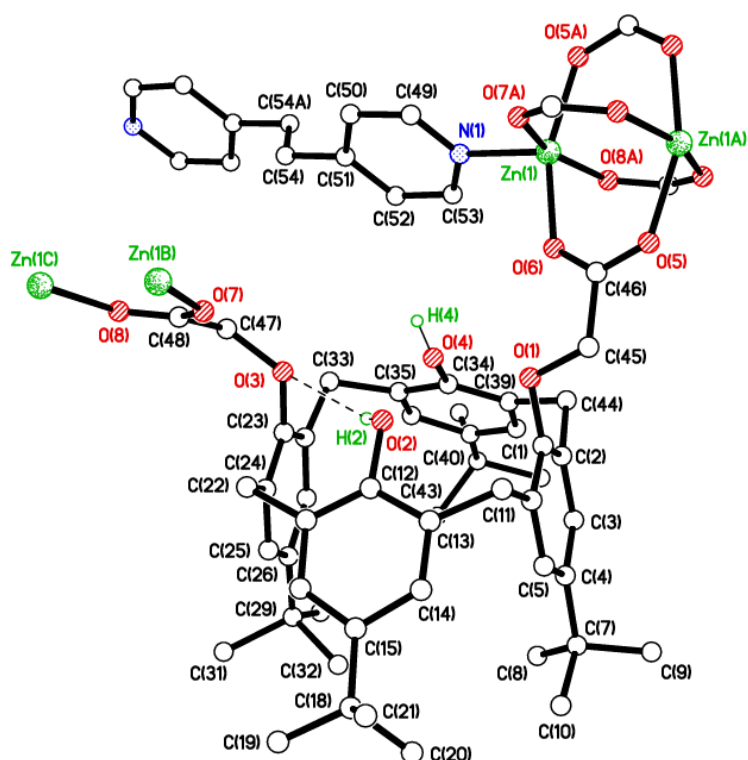


**Figure 122.** Diagram of the coordination environment around the metals centres in **18**. Hydrogen atoms, except those involved in H-bonding have been omitted.

Coordination of the neutral pillaring linker to these paddlewheel SBUs above and below the plane of the carboxylate functions gives a distorted square-based pyramidal coordination geometry around the metal centres, and further links the  $\text{ZnL}^3$  chains in to the extended 2D bilayer structure observed in the *a/b* plane, figure 123. The pyridinyl ligands in this example are disordered over two positions, with only the position of the coordinating N atom common to both components. Likewise, all four tertiary butyl groups per calix[4]arene unit were disordered and modelled over two positions. Guest solvent atoms could not be resolved by point

atom observations due to disorder, hence the PLATON squeeze procedure was performed. This recovered 89 electrons situated in one large void and six much smaller voids per unit cell. As the smaller voids are not large enough to accommodate DEF or MeOH guest molecules their electron contribution was omitted, giving a total of one guest DEF per large void or 1 per formula unit. It is of note that due to the disordered nature of the DPE linker, the dimensions of the large void are subject to variation, hence some may accommodate more than one DEF molecule.

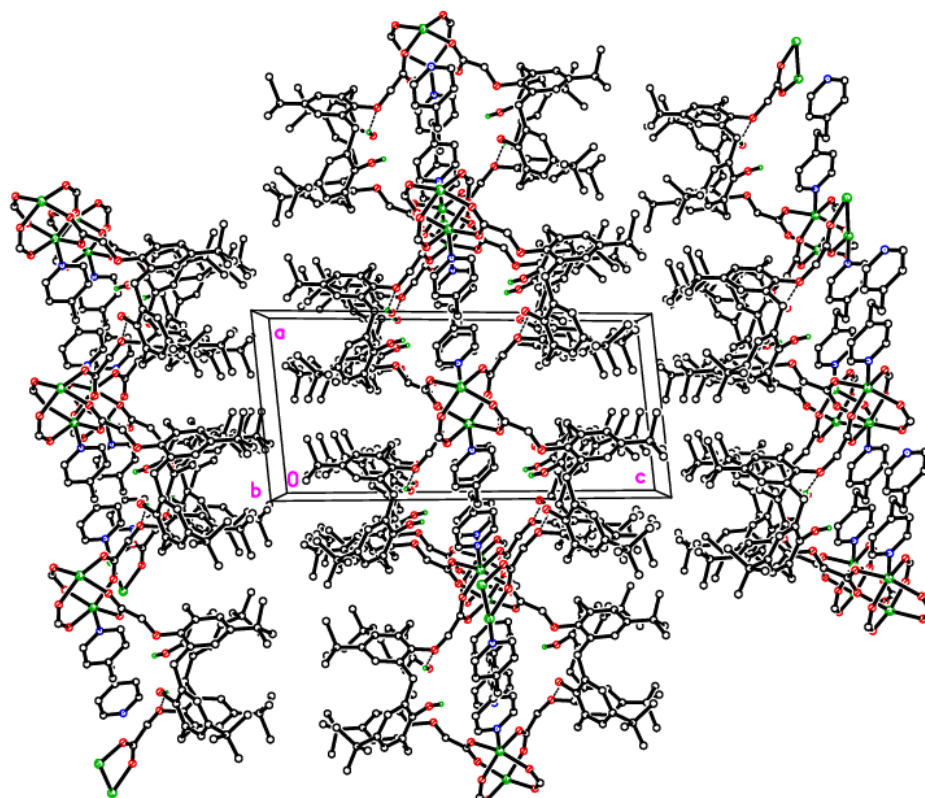


**Figure 123.** Diagram of **18** viewed along the  $b$  axis showing the extended 2D bilayer sheets in the  $a/b$  plane. Carbon atoms are represented by empty circles, with nitrogen, oxygen and zinc atoms coloured blue, red and green respectively. Hydrogen atoms, except those involved in H-bonding, which are represented by small green circles, are omitted.

As with the previous structure, the calix[4]arene adopts a pinched conformation precluding the presence of solvent molecules within the bowl, however in this example it is the acid appended phenol units which are forced to swing inward to allow the acid moiety to participate in binding to the paddlewheel SBU, figure 124.

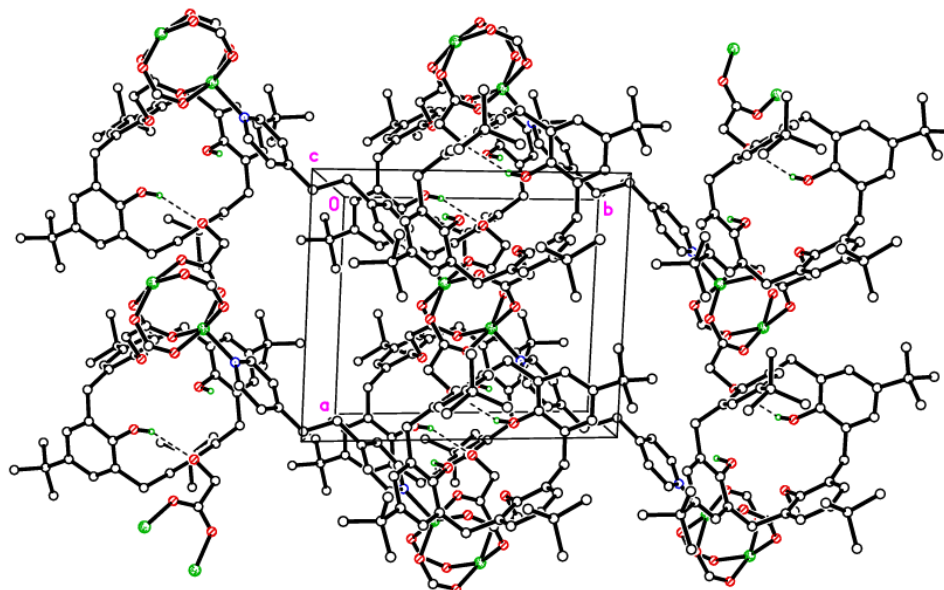
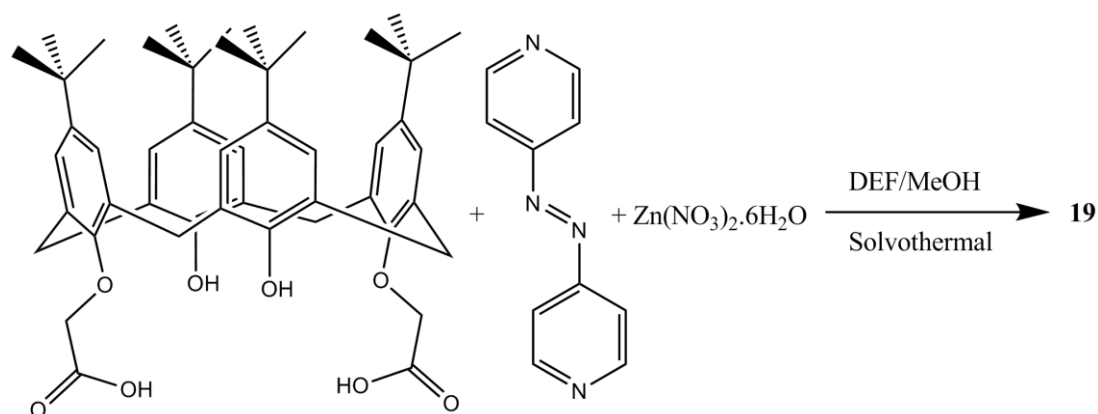


**Figure 124.** Diagram of **18** as viewed along the *c* axis showing the pinched bowl conformation adopted by the calix[4]arene molecule. Carbon atoms are represented by empty circles, with nitrogen, oxygen and zinc atoms coloured blue, red and green respectively. Hydrogen atoms, except those involved in H-bonding, which are represented by small green circles, are omitted.



**Scheme 20.** Synthetic route for the preparation of  $\text{Zn}(\text{OH}_2)_2(\text{L}^3)(4, 4'\text{-azopy})\cdot\text{DEF}\}_n$ , **19**.

Employment of the same reactions conditions and molar quantities as with **17** and **18**, but with the substitution of the neutral pillaring linker with 4,4'-azopy, following scheme 20, gave **19** as red prisms. Again, the crystals were of suitable quality for

single crystal X-ray diffraction, but required synchrotron radiation to collect a data set of adequate quality for structural elucidation. Analysis of this data reveals a similar extended 2D bilayer sheet structure of formula  $\{[\text{Zn}(\text{OH}_2)_2(\text{L}^3)(4,4\text{-azopy})].\text{DEF}\}_n$ , in which subtle differences in the coordination of the carboxylate groups compared to **17** gives rise to a different network topology. As with **17**,  $\text{Zn}_2\text{L}^3_2$  dimers are formed by the monodentate binding of carboxylate groups from two calix[4]arene molecules to single zinc atoms, however intramolecular hydrogen bonding between one of coordinated carboxylate oxygens and the ether oxygen of the same group with one of the phenolic OH groups forces the moiety to adopt a bent configuration. This has the effect of shortening one of the pendant carboxylate groups giving a dimeric unit in which calix[4]arene molecules are off-set. The structure also differs from **17** in the coordination geometry observed around each metal centre. Two 4,4'-azopy molecules coordinate to each metal centre *via* their pyridinyl nitrogens, however the presence of two coordinated water molecules per zinc gives octahedral geometry, figure 125.

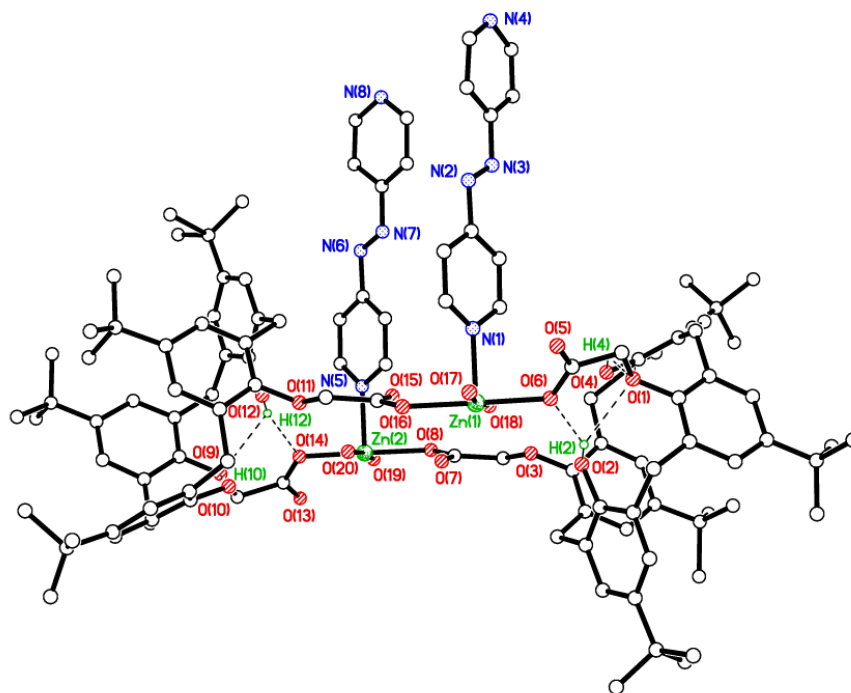


**Figure 125.** Diagram of the  $\text{Zn}(\text{OH}_2)_2(\text{L}^3)(4, 4'\text{-azopy})$  dimer comprising **19**, showing the coordination environment around the metal centres. Hydrogen atoms, except those involved in H-bonding interaction are omitted. Hydrogen bonds are represented by dotted lines.

Dimer units pack closely into layers observed in the  $a/c$  plane with no interactions between the closest neighbours. When viewed along the  $c$  axis, a pattern reminiscent of hexagonal close packing is observed, with the 4,4'-azopy ligands extending parallel to the  $b$  axis linking each dimer unit to four others to form 2D bilayer sheets located in the  $a/b$  plane, figure 126 and 127.

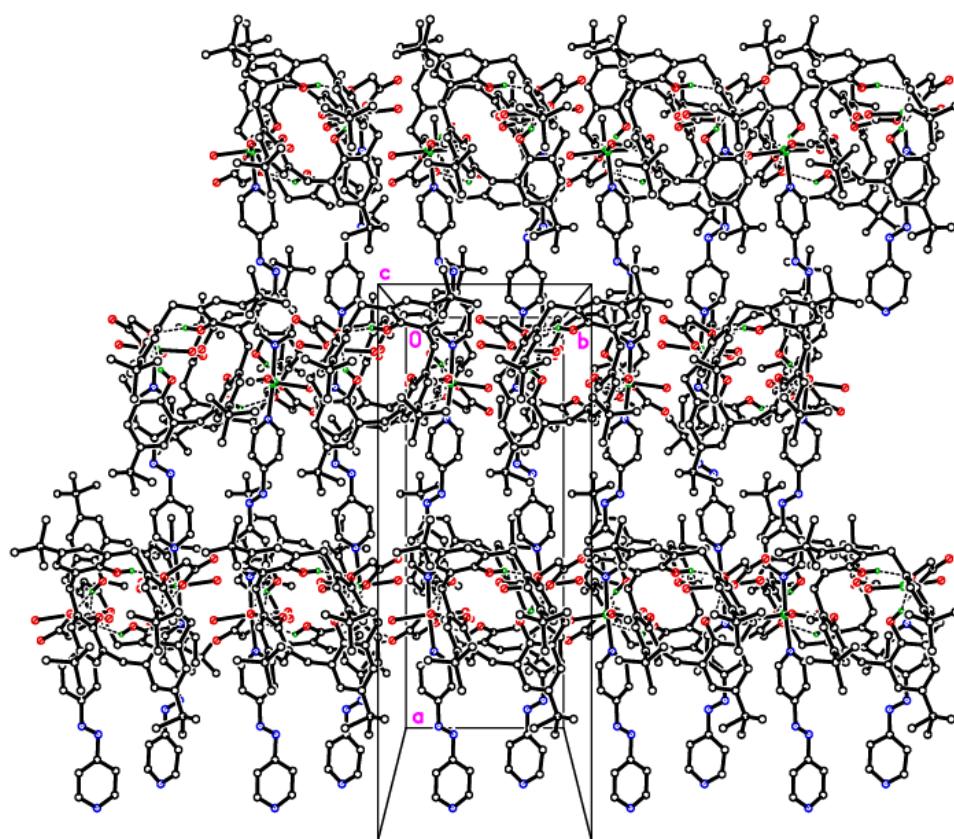


**Figure 126.** Diagram of **19** as viewed along the  $c$  axis, showing the hexagonal close packing type arrangement of dimer units, with linking 4,4'-azopy molecules forming the extended 2D structure. Carbon atoms are represented by empty circles, with nitrogen, oxygen and zinc atoms coloured blue, red and green respectively. Hydrogen atoms, except those involved in H-bonding, which are represented by small green circles, are omitted.

As with the **17** and **18**, the calix[4]arene adopts a pinched conformation, in this example mediated by the presence of hydrogen bonding between the phenolic hydroxy groups and the acid functions, which precludes the presence of guest solvent molecules in the bowl of the calix[4]arene. When viewed along the  $a$  axis, eight void spaces per unit cell are visible, located around the 4,4'-azopy molecules,

figure 127. Diffuse electron density observed in these void spaces was modelled using the PLATON squeeze procedure, giving approximately half a DEF molecule per void space, or four per unit cell.

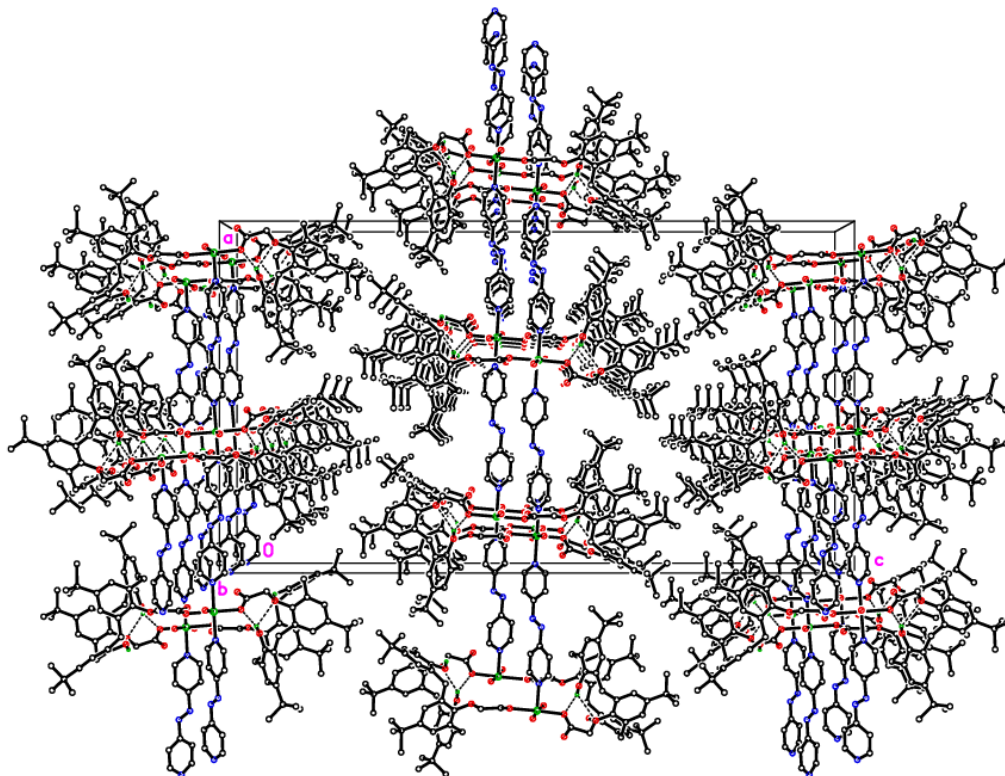


**Figure 127.** Diagram of **19** as viewed along the  $b$  axis. 2D bilayer sheets are visible in the  $a/b$  plane, with void spaces observed around the 4,4'-azopy molecules. Carbon atoms are represented by empty circles, with nitrogen, oxygen and zinc atoms coloured blue, red and green respectively. Hydrogen atoms, except those involved in H-bonding, which are represented by small green circles, are omitted.

### 5.2.1. Thermogravimetric analysis

Thermogravimetric analyses were conducted on structures **17**, **18** and **19** under an inert carrier flow of nitrogen in order to assess their porosities and solid state stabilities, the data can be viewed in the graph in figure 128. Unexpectedly, for structure **17** no weight loss was observed in the range 30 to 250 °C. This is in contradiction to the single crystal X-ray diffraction data, which offers evidence of 2.25 guest DEF molecules, and elemental analyses which suggest the presence of 2 DEF molecules per formula unit. It can be concluded that either no guest solvent

molecules were present in the sample analysed, due to their removal during sample preparation, or that the solvent was encapsulated by the framework and was not removable until after the thermal decomposition had begun. Due to the similarities between this profile and those of structures **18** and **19** at temperatures above 280 °C, at which all three structures begin to thermally decompose, it is reasonable to assume that rather than being tightly bound within the framework, the guest DEF molecules were removed during sample preparation, which involved washing the sample with diethyl ether (see experimental section).

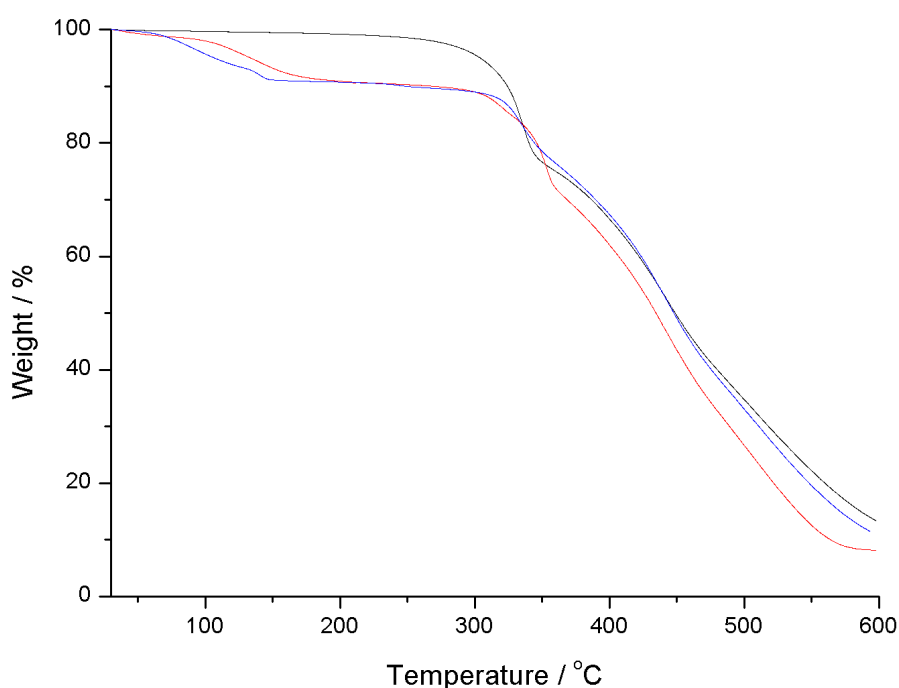


**Figure 128.** TGA data recorded for structures **17**(black),**18** (red) and **19**(blue).

Structures **18** and **19** exhibit very similar profiles, undergoing a weight loss of 9.7 and 11.1 %, respectively over the range 30-250°C. In the case of **18**, this weight loss is attributable to the loss of two DEF molecules per formula unit (calculated 10.0 %). While the single crystal X-ray diffraction data suggests the presence of only one of these guest molecules, disorder observed in the pyridinyl linker allows for a greater quantity of guest molecules to be accommodated, with elemental analyses conducted on **18** offering evidence of the presence of a second DEF molecule per formula unit. For structure **19**, the loss of one DEF molecule and the two coordinated water molecules per formula unit equates to a loss of 11.9 wt %, which is in good

agreement with the recorded TGA data. Thermal decomposition for all three structures commences at ~ 280 °C as indicated by rapid and continuous weight loss. Due to the similarities in metal coordination modes between the structures, similar decomposition profiles are expected, with minor variations between the curves attributable to relative thermal stabilities of 4,4'-bipy, DPE and 4,4'-azopy.

### 5.3. Conclusion

Three novel 2D structures have been synthesised using the solvothermal reaction of a lower-rim acid appended calix[4]arene with zinc nitrate and a variety of bipyridyl pillaring linkers. The structures have been characterised and their porosities investigated using TGA. Similar packing motifs are observed in all three examples, with the coordination of calix[4]arene molecules to metal centres in a lower-rim to lower-rim fashion giving dimeric units, which are further linked in to the extended structures through the coordination of the bipyridyl linker. Minor variations in carboxylate coordination mode are observed, with **17** and **19** exhibiting monodentate binding of carboxylate groups from two calix[4]arene molecules to two single metal centres and **18** exhibiting paddlewheel SBUs, with each of these units involving carboxylate groups from four neighbouring calix[4]arene molecules. The assertion that the dimensionality of lower-rim acid functionalised calix[4]arene coordination polymers may be increased by the inclusion of a neutral pillaring linker is therefore supported, however the use of a ditopic pillaring linker in reactions of this type affords only 2D structures. Further research using the calix[4]arene diacid ligand should therefore focus on the inclusion of tritopic neutral linkers in the synthesis of 3D structures.

## 5.4. References

---

- 1 L. R. MacGillivray, J. L. Atwood, *J. Am. Chem. Soc.*, 1997, **119**, 6931.
- 2 B. Q. Ma, Y. Zhang, P. Coppens, *CrystEngComm*, 2001, **20**, 1.
- 3 A. Nakamura, T. Sato, R. Kuroda, *CrystEngComm*, 2003, **56**, 318.

## **Chapter 6**

### **Experimental section**

## 6.1. General considerations

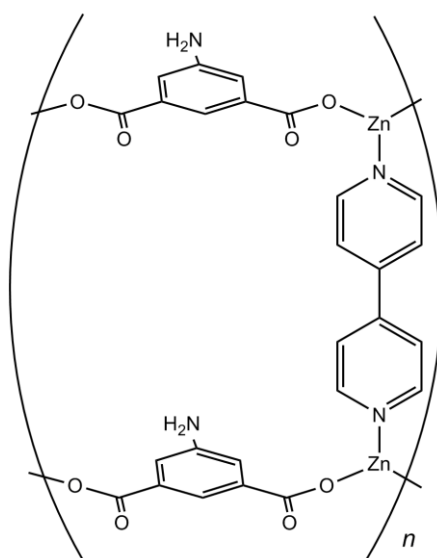
All reagents were purchased from Sigma-Aldrich and were used with no further purification. Solvents were purchased from Fisher Scientific. Tetrahydrofuran and ethanol were dried (where the use of dry solvents is specified) by heating to reflux over sodium and benzophenone and distilled and degassed prior to use. All samples were prepared for CO<sub>2</sub> adsorption studies *via* solvent exchange, by immersion in chloroform for 2 weeks, during which time the solvent was replaced four times. Samples were activated prior to testing by heating to 120 °C for 12 hrs under dynamic vacuum. Infra-red data (Nujol mulls, KBr windows) were collected using a Nicolet Avatar 360 FT IR spectrometer. Elemental analyses were performed by the National Elemental Analysis service at London Metropolitan University. Mass spectrometry data were recorded by the EPSRC National Mass Spectrometry Service Centre at Swansea University. TGAs were recorded on a TA instruments 2950 TGA HR V5.3 thermogravimetric analyser under an inert (N<sub>2</sub>) carrier flow from 30 °C to 600 °C with a scanning rate of 2 °C min<sup>-1</sup>. CO<sub>2</sub> isotherms were measured on a Micromeritics ASAP2020 Volumetric Adsorption Analyser and a HidenIsochema Intelligent Gravimetric Analyser. NMR spectra were performed at room temperature on a Varian VXR 400 S spectrometer at 400 MHz (<sup>1</sup>H) and 105.1 MHz (<sup>7</sup>Li) NMR, a Gemini 300 NMR spectrometer at 300 MHz (<sup>1</sup>H) or a Bruker Advance DPX-300 spectrometer at 300 MHz. The <sup>1</sup>H NMR spectra were calibrated against the residual protio impurity of the deuterated solvent. Single crystal X-Ray crystallography was conducted by M. R. J. Elsegood on a Bruker SMART 1000 CCD diffractometer using narrow slice 0.38 ω-scans for data collection, SAINT (integration and cell refinement), and SHELXTL<sup>1</sup> (solution, refinement and graphics) at 124 the Chemistry Department at Loughborough University. Alternatively X-ray crystallography was conducted by D. L. Hughes or A. –M. Fuller (structures **14**, **15** and **16**) on an Oxford Diffraction Xcalibur-3 CCD diffractometer equipped with a Mo-Kα radiation and graphite monochromator. Intensity data were measured by thin-slice ω- and φ-scans. Data were processed using the CrysAlis-CCD and –RED programs.<sup>2</sup> Structures were determined by the direct methods, on F2, in SHELXL. Powder X-ray diffraction data was collected by Bertrand Leze using a ThermoARL Xtra powder X-ray diffractometer equipped with a copper X-ray tube.

## 6.2. Synthesis of known compounds

The reduced Schiff base linker,  $LH_2$ , was synthesised using the method reported by Yang *et al.*<sup>3</sup> with recrystallisation from methanol/water giving the diacid, which was used without further purification. The calix[4]arene diester, 25,27-bis(methoxycarbonylethoxy)-26,28-dihydroxycalix[4]arene was prepared using the method reported by Shinkai and Iwamoto<sup>4</sup>. Saponification of the calix[4]arene diester using KOH in ethanol/water and recrystallisation from methanol/water gave the diacid  $L^2H_2$ . Analogous reactions using *p*-tertbutylcalix[4]arene gave the ligand 25,27-bis(methoxycarbonylethoxy)-26,28-dihydroxy-*p*-tertbutylcalix[4]arene,  $L^3H_2$ .

## 6.3. Pillared MOFs based on 5-aminoisophthalic acid

### 6.3.1. Synthesis of $\{[Zn(5-AIP)(4,4'-bipy)_0.5].2DMF\}_n$ (**1**).



5-aminoisophthalic acid (0.5 mmol, 0.09 g),  $Zn(NO_3)_2 \cdot 6H_2O$  (0.75 mmol, 0.22 g) and 4,4'-bipyridyl (0.375 mmol, 0.06 g) were dissolved in a DMF/methanol mixture (12ml, 1:1) in 23ml Teflon lined steel reaction vessel. The vessel was sealed and heated to 80°C for 48 h, and then cooled at rate of 2°C per hour to room temperature, yielding 0.194 g of colourless hexagonal prisms (yield 80 % based on Zn). Elem. anal. calcd. for  $C_{26}H_{18}N_4O_8Zn_2 \cdot 2H_2O$ : C 45.84, H 3.26, N 8.22; found: C 45.81, H 2.96, N 8.5 %; IR (KBr,  $cm^{-1}$ ) 3430(w), 3249(m), 3134(w), 1668(s), 1614(s), 1574(s), 1538(w), 1494(w), 1441(m), 1420(w), 1345(s), 1248(m), 1226(w), 1189(w), 1133(m), 1100(s), 1048(w), 1016(w), 962(s), 933(m), 893(w), 826(m),

794(s), 778(s), 731(s) 679(m), 658(w), 644(m).

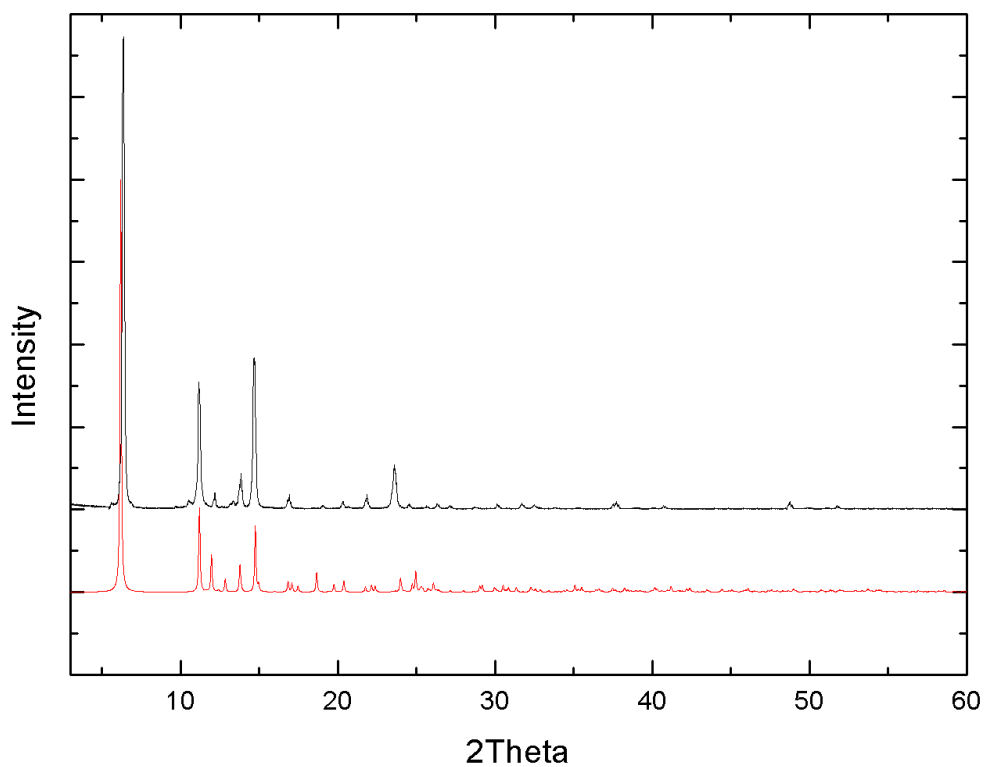
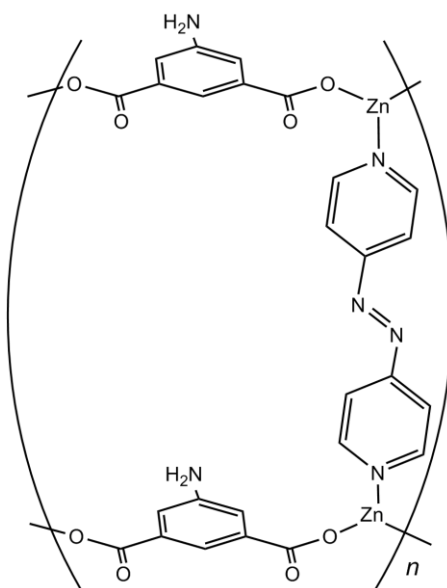


**Figure 130.** Powder X-ray diffraction data for **1**, showing the simulated (red) and collected (black) patterns.

6.3.2. *Synthesis of*  $[\text{Zn}(\text{5-AIP})(\text{4,4'}$ -azopy) $_{0.5}]\cdot 1.5\text{DMF}]_n$  (**2**).



5-aminoisophthalic acid (0.5 mmol, 0.09 g),  $\text{Zn}(\text{NO}_3)_2\cdot 6\text{H}_2\text{O}$  (0.75 mmol, 0.22 g)

and 4,4'-azopyridine (0.375 mmol, 0.07 g) were dissolved in a DMF/methanol mixture (12ml, 1:1) in 23ml Teflon lined steel reaction vessel. The vessel was sealed and heated to 80°C for 48 h, and then cooled at rate of 2°C per hour to room temperature. The reaction yielded 0.150 g of orange prisms (yield 60 % based on Zn). Elem. anal. calcd. for  $C_{26}H_{18}N_6O_8Zn_2$ : C 46.38, H 2.69, N 12.48; found: C 46.20, H 2.79, N 12.42 %; IR (KBr,  $cm^{-1}$ ) 3445(w), 3337(w), 2361(w), 1692(w), 1674(s), 1609(m), 1569(m), 1544(m), 1499(w), 1324(w), 1253(w), 1220(w), 1206(w), 1091(m), 1017(w), 1004(w), 980(w), 935(w), 892(w), 836(m), 807(w), 775(m), 726(m), 659(m), 554(m).

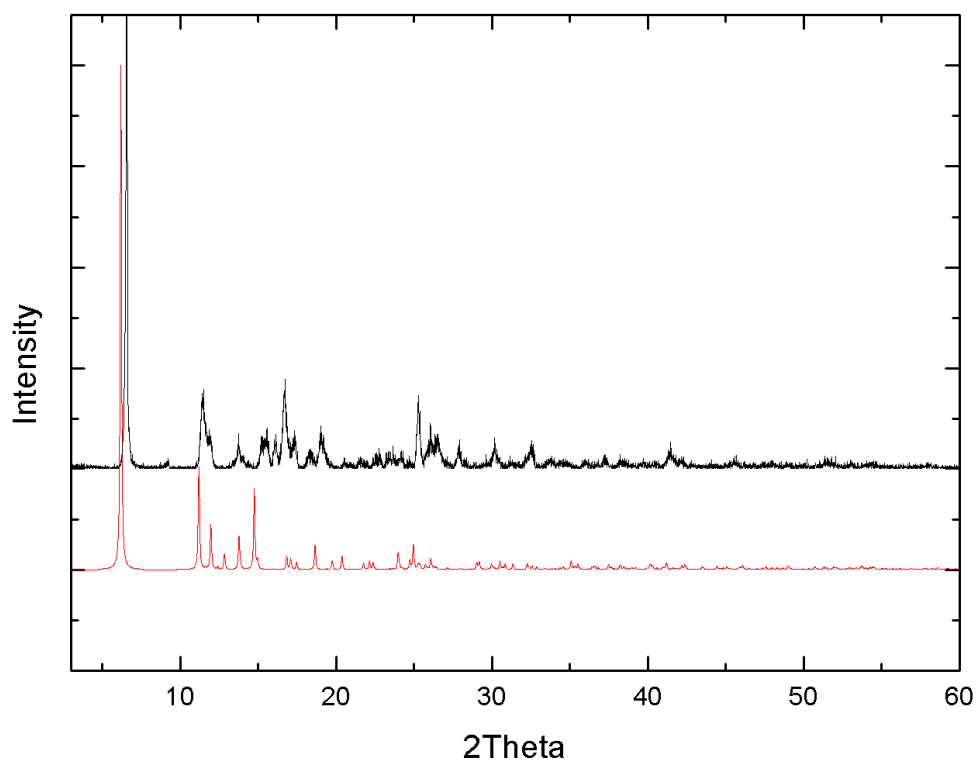
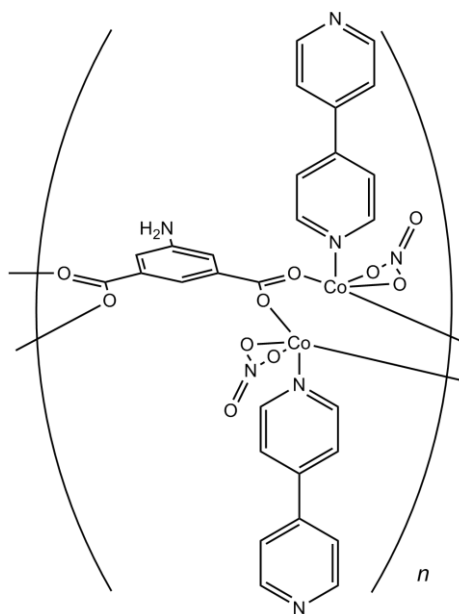


**Figure 131.** Powder X-ray diffraction data for **2**, showing the collected pattern (black) against the simulated pattern for the isostructural **1** (red).

6.3.3. Synthesis of  $\{[\text{Co}_2(\text{NO}_3)_2(5\text{-AIP})(4,4'\text{-bipy})_2]\cdot 2\text{EtOH}\}_n$  (**3**).



5-aminoisophthalic acid (0.5 mmol, 0.09 g),  $\text{Co}(\text{NO}_3)_3\cdot 6\text{H}_2\text{O}$  (0.5 mmol, 0.15 g) and 4,4'-bipyridyl (0.5 mmol, 0.08 g) were dissolved in a DMF/Ethanol mixture (12ml, 1:1) in 23ml Teflon lined steel reaction vessel. The vessel was sealed and heated to  $80^\circ\text{C}$  for 48 h, and then cooled at rate of  $2^\circ\text{C}$  per hour to room temperature. The reaction yielded 0.292 g of purple hexagonal prisms (yield 80 % based on Co). Elem. anal. calcd. for  $\text{C}_{28}\text{H}_{21}\text{Co}_2\text{N}_7\text{O}_{10}\cdot 4\text{C}_2\text{H}_6\text{O}$ : C 46.02, H 4.87, N 10.73; found C 45.67, H 4.48, N 10.35 %; IR (KBr,  $\text{cm}^{-1}$ ) 3446(w), 3341(w), 3228(w), 1677(s), 1603(m), 1571(m), 1547(m), 1411(w), 1325(w), 1220(w), 1094(w), 1005(w), 1046(w), 1005(w), 968(w), 937(w), 892(w), 816(m), 775(m), 727(m), 660(w), 633(w).

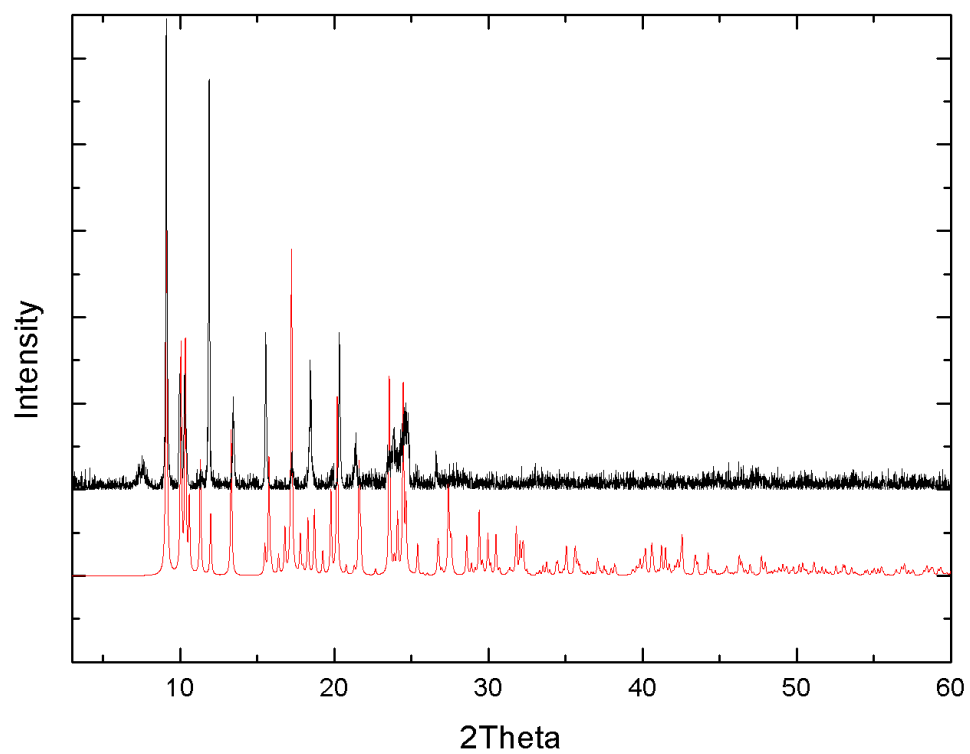
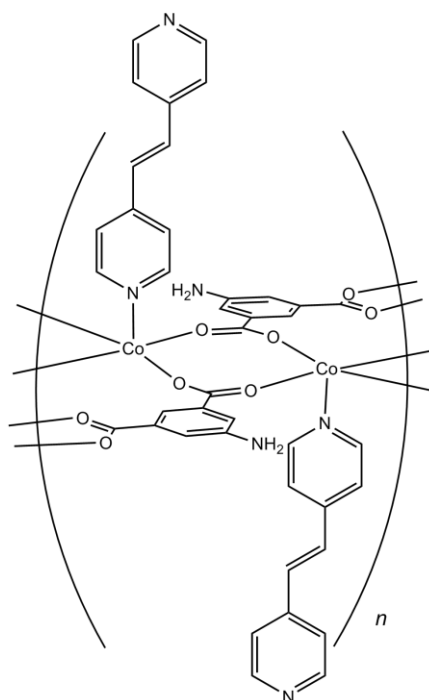


**Figure 132.** Powder X-ray diffraction data for **3**, showing the simulated (red) and collected (black) patterns

6.3.4. *Synthesis of*  $\{[\text{Co}(\text{5-AIP})(\text{DPE})].3\text{DMF}\}_n$  (**4**).



5-aminoisophthalic acid (0.5 mmol, 0.09 g),  $\text{Co}(\text{NO}_3)_3 \cdot 6\text{H}_2\text{O}$  (0.5 mmol, 0.15 g) and DPE (0.5 mmol, 0.09 g) were dissolved in DMF/Ethanol (12ml, 1:1) in 23ml Teflon lined steel reaction vessel. The vessel was sealed and heated to  $80^\circ\text{C}$  for 48 h, and then cooled at rate of  $2^\circ\text{C}$  per hour to room temperature, yielding 0.168 g purple prisms (80 % based on Co). Elem. anal. calcd. for  $\text{C}_{20}\text{H}_{15}\text{CoN}_3\text{O}_4$ : C 57.16, H 3.60, N 10.00; found C 57.25, H 3.77, N 9.87 %; IR (KBr,  $\text{cm}^{-1}$ ) 3436(w), 3248(w), 3133(w), 1675(s), 1616(s), 1573(s), 1506(w), 1441(m), 1340(s), 1248(m), 1226(w), 1211(w), 1132(m), 1096(s), 1028(m), 1002(w), 987(w), 961(m), 932(w), 893(w), 843(m), 794(m), 778(m), 730(s), 678(m), 659(m).

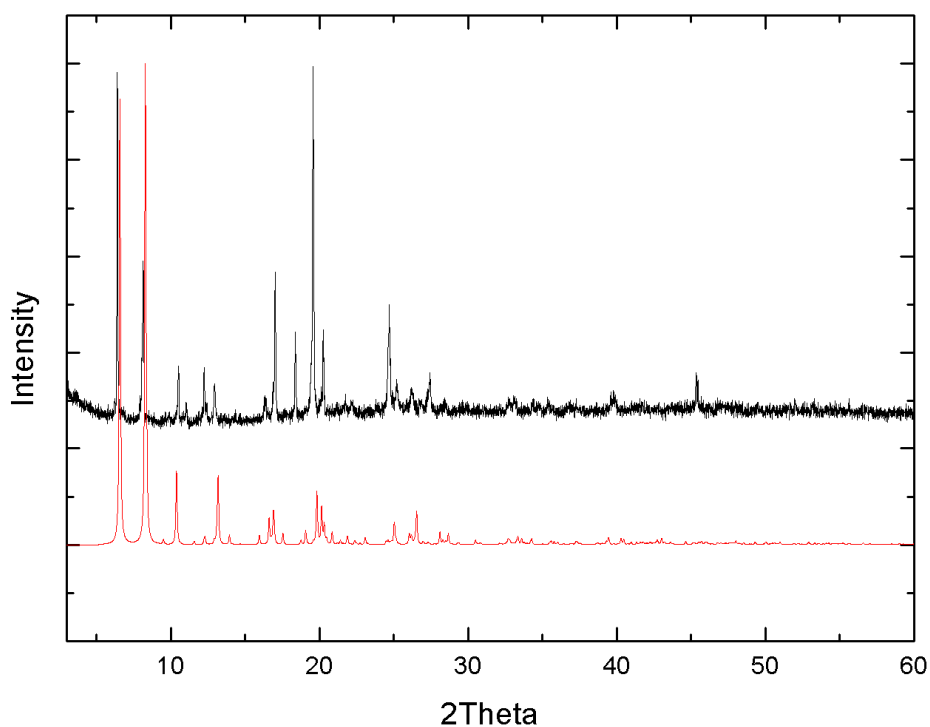
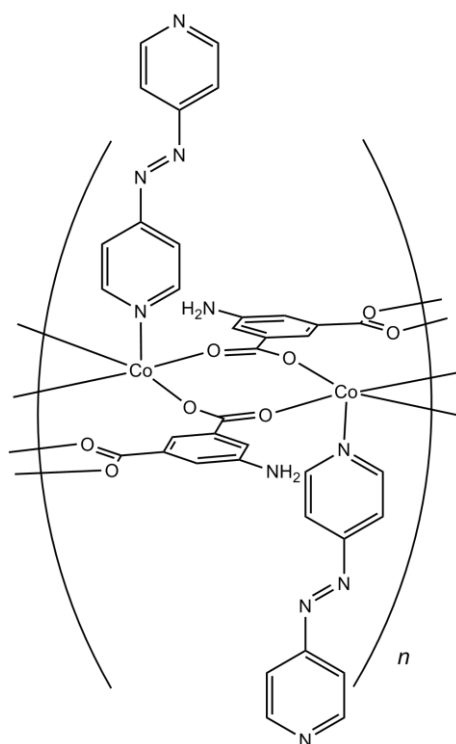


**Figure 133.** Powder X-ray diffraction data for **4**, showing the collected pattern (black) against the simulated pattern for the isostructural **7** (red).

6.3.5. Synthesis of  $\{[\text{Co}(5\text{-AIP})(4,4'\text{-azopy})].2\text{DMA}\}_n$  (**5**).



5-aminoisophthalic acid (0.5 mmol, 0.09 g),  $\text{Co}(\text{NO}_3)_3 \cdot 6\text{H}_2\text{O}$  (0.5 mmol, 0.15 g) and 4,4'-azopyridine (0.5 mmol, 0.09 g) were dissolved in DMF/Ethanol (12ml, 1:1) in 23ml Teflon lined steel reaction vessel. The vessel was sealed and heated to  $80^\circ\text{C}$  for 48 h, and then cooled at rate of  $2^\circ\text{C}$  per hour to room temperature. yielding 0.123 g dark red prisms (58 % based on Co). Elem. anal. calcd. for  $\text{C}_{18}\text{H}_{13}\text{CoN}_5\text{O}_4$  : C 51.20, H 3.10, N 16.59; found C 51.10, H 3.10, N 16.45 %; IR (KBr,  $\text{cm}^{-1}$ ) 3451(w), 3343(w), 3231(w), 1677(s), 1601(w), 1570(m), 1544(w), 1416(w), 1326(w), 1256(w), 1225(w), 1091(m), 1055(w), 1017(w), 964(w), 892(w), 848(w), 776(m), 726(m), 680(w), 660(w).

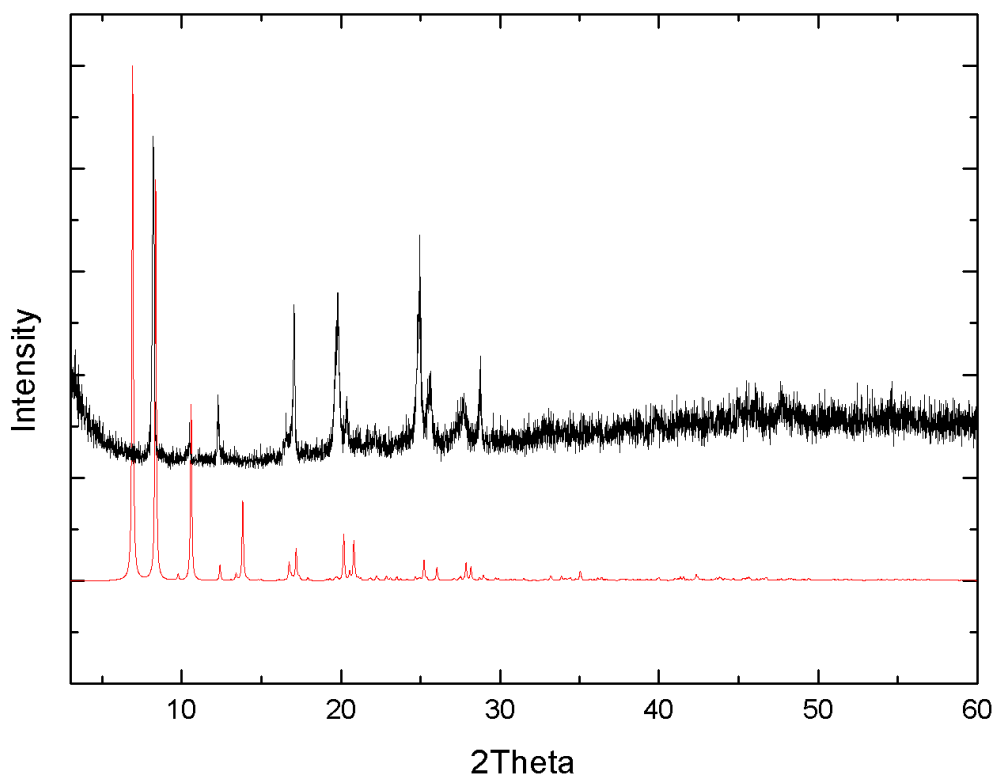
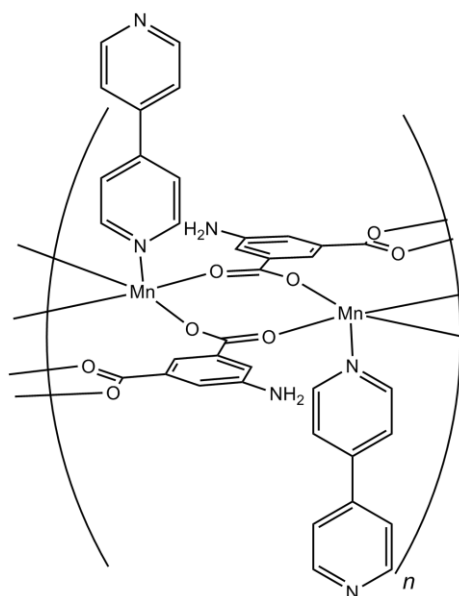


**Figure 134.** Powder X-ray diffraction data for **5**, showing the simulated (red) and collected (black) patterns.

6.3.6. *Synthesis of*  $\{[\text{Mn}(5\text{-AIP})(4,4'\text{-bipy})]\cdot 2\text{DMA}\}_n$  (**6**).



$\text{Mn}(\text{NO}_3)_3\cdot 4\text{H}_2\text{O}$  (0.5 mmol, 0.13 g), 5-aminoisophthalic acid (0.5 mmol, 0.09 g) and 4,4'-bipyridyl (0.5 mmol, 0.08 g) were dissolved in DMA/Methanol (12 ml, 1:1) and

sealed in a 23 ml Teflon lined steel reaction vessel. The vessel was sealed and heated to 80 °C for 48 hours, and then cooled at a rate of 2 °C per hour to room temperature, yielding 0.118 g yellow prisms (61 % based on Mn). Elem. anal. calcd. for  $C_{18}H_{13}MnN_3O_4$ : C 55.40, H 3.36, N 10.77; found C 55.26, H 3.45, N 10.89 %; IR (KBr,  $cm^{-1}$ ) 3452(w), 3344(m), 3225(w), 1673(s), 1602(m), 1550(s), 1414(m), 1326(w), 1254(w), 1221(m), 1092(m), 1042(w), 1005(w), 933(w), 894(w), 813(s), 779(s), 728(s), 657(w), 629(m).

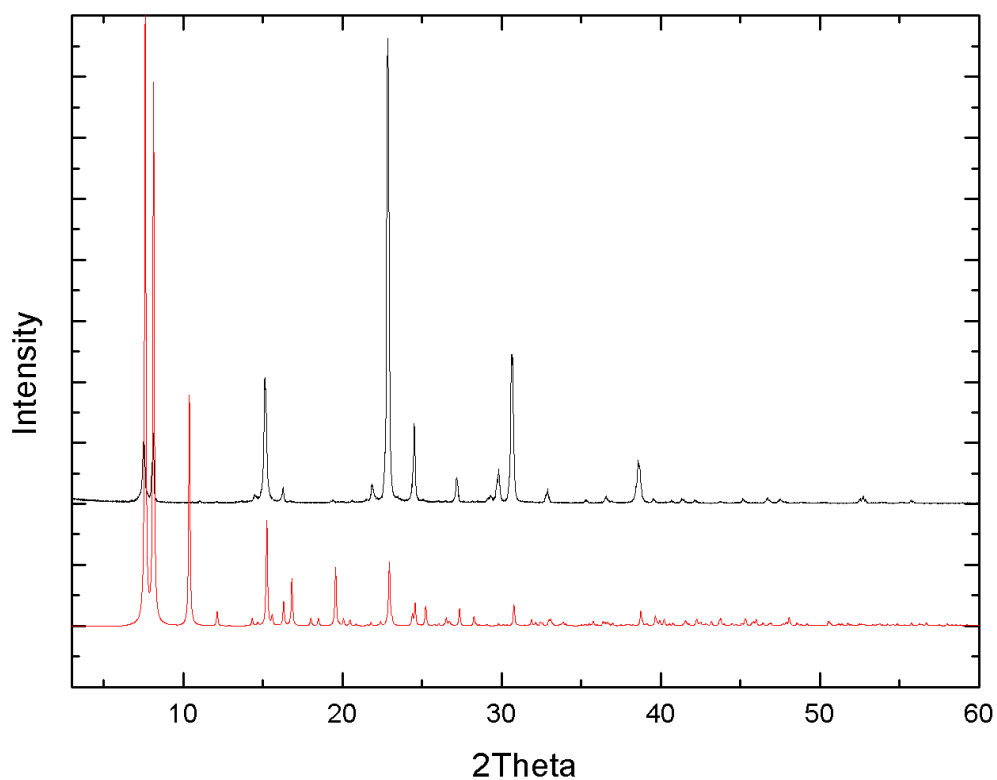
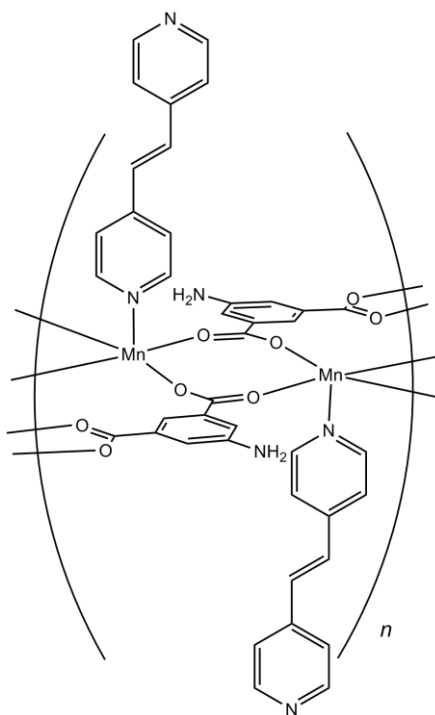


**Figure 135.** Powder X-ray diffraction data for **6**, showing the simulated (red) and collected (black) patterns

6.3.7. Synthesis of  $\{[\text{Mn}(5\text{-AIP})(\text{DPE})].1.5\text{DMF}\}_n$  (7).



$\text{Mn}(\text{NO}_3)_3 \cdot 4\text{H}_2\text{O}$  (0.5 mmol, 0.13 g), 5-aminoisophthalic acid (0.5 mmol, 0.09 g) and 1,2-bis(4-pyridyl)ethylene (0.5 mmol, 0.09 g) were dissolved in DMF/Methanol (12 ml, 1:1) and sealed in a 23 ml Teflon lined steel reaction vessel. The vessel was sealed and heated to 80 °C for 48 hours, and then cooled at a rate of 2 °C per hour to room temperature. The reaction yielded 0.171 g yellow prisms (82 % based on Mn). Elem. anal. calcd. for  $\text{C}_{20}\text{H}_{15}\text{MnN}_3\text{O}_4$  : C 57.70, H 3.63, N 10.09; found C 57.55, H 3.75, N 10.15 %; IR (KBr,  $\text{cm}^{-1}$ ) 3457(w), 3339(m), 3225(w), 1675(s), 1609(m), 1550(s), 1326(s), 1254(w), 1220(w), 1091(w), 1070(w), 1016(w), 969(w), 956(w), 894(w), 827(m), 807(w), 779(m), 728(s).

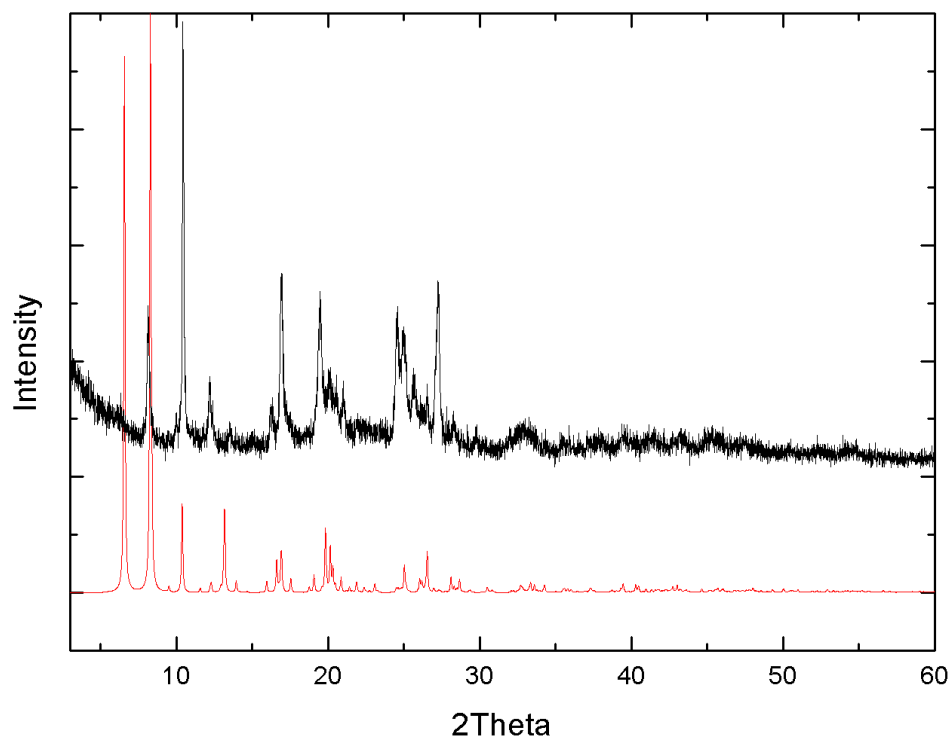
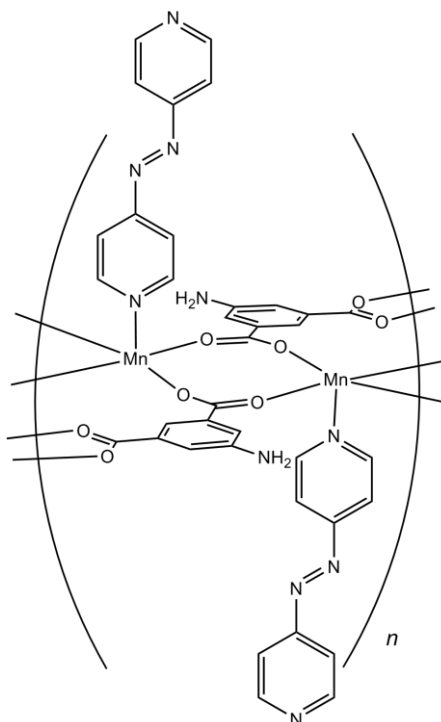


**Figure 136.** Powder X-ray diffraction data for **7**, showing the simulated (red) and collected (black) patterns.

6.3.8. *Synthesis of*  $\{[\text{Mn}(5\text{-AIP})(\text{Azopy})].\text{DMF}\}_n$  (**8**).



$\text{Mn}(\text{NO}_3)_3 \cdot 4\text{H}_2\text{O}$  (0.5 mmol, 0.13 g), 5-aminoisophthalic acid (0.5 mmol, 0.09 g) and

4,4'-azopyridine (0.5 mmol, 0.09 g) were dissolved in DMF/Methanol (12 ml, 1:1) and sealed in a 23 ml Teflon lined steel reaction vessel. The vessel was sealed and heated to 80 °C for 48 hours, and then cooled at a rate of 2 °C per hour to room temperature. The reaction yielded 0.128 g red prisms (61 % based on Mn). Elem. anal. calcd. for  $C_{18}H_{13}MnN_5O_4$  : C 51.69, H 3.13, N 16.74; found C 51.53, H 3.27, N 16.57 %; IR (KBr,  $cm^{-1}$ ) 3452(w), 3343(m), 3230(w), 1676(s), 1600(m), 1550(s), 1416(w), 1326(w), 1254(w), 1225(w), 1090(w), 1055(w), 1013(w), 1006(w), 933(w), 894(w), 864(m), 809(w), 779(m), 728(s).

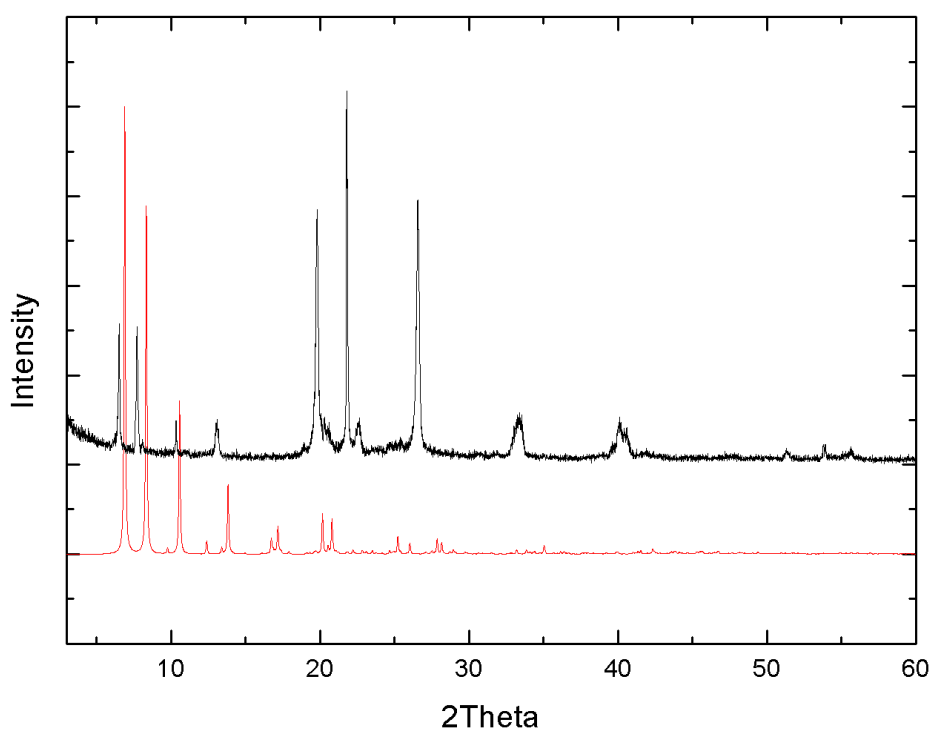
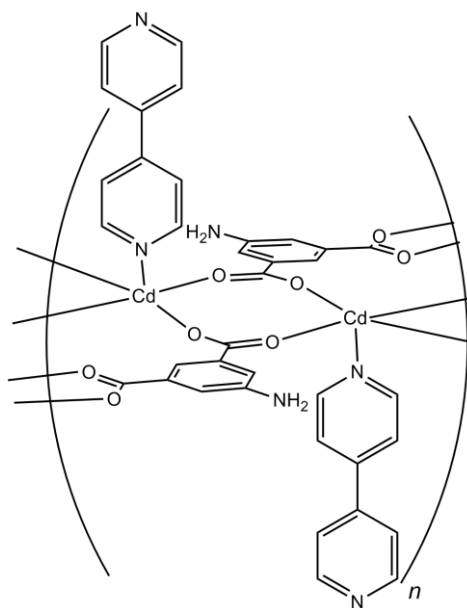


**Figure 137.** Powder X-ray diffraction data for **8**, showing the collected pattern (black) against the simulated pattern for the isostructural **5** (red).

6.3.9. Synthesis of  $\{[\text{Cd}(5\text{-AIP})(4,4'\text{-bipy})]\cdot 3\text{DMF}\}_n$  (**9**).



$\text{Cd}(\text{NO}_3)_2 \cdot 4\text{H}_2\text{O}$  (0.5 mmol, 0.15 g), 5-aminoisophthalic acid (0.5 mmol, 0.09 g) and 4,4'-bipyridyl (0.5 mmol, 0.08 g) were dissolved in DMF/Methanol (12 ml, 1:1) and sealed in a 23 ml Teflon lined steel reaction vessel. The vessel was heated to 85 °C for 72 hours, and then cooled at a rate of 2 °C per hour to room temperature, yielding 0.183 g colourless prisms (82 % based on Cd). Elem. anal. calcd. for  $\text{C}_{18}\text{H}_{13}\text{CdN}_3\text{O}_4 \cdot \text{C}_3\text{H}_7\text{NO}$ : C 48.43, H 3.87, N 10.76; found C 48.15, H 3.52, N 10.66 %; IR (KBr,  $\text{cm}^{-1}$ ) 3350(w), 3221(w), 1669(s), 1653(w), 1603(s), 1545(s), 1517(w), 1413(w), 1320(w), 1253(w), 1220(w), 1166(w), 1150(w), 1094(m), 1068(m), 1044(m), 1008(w), 965(w), 934(w), 898(w), 856(w), 814(w), 778(s), 732(s), 657(w), 631(w).

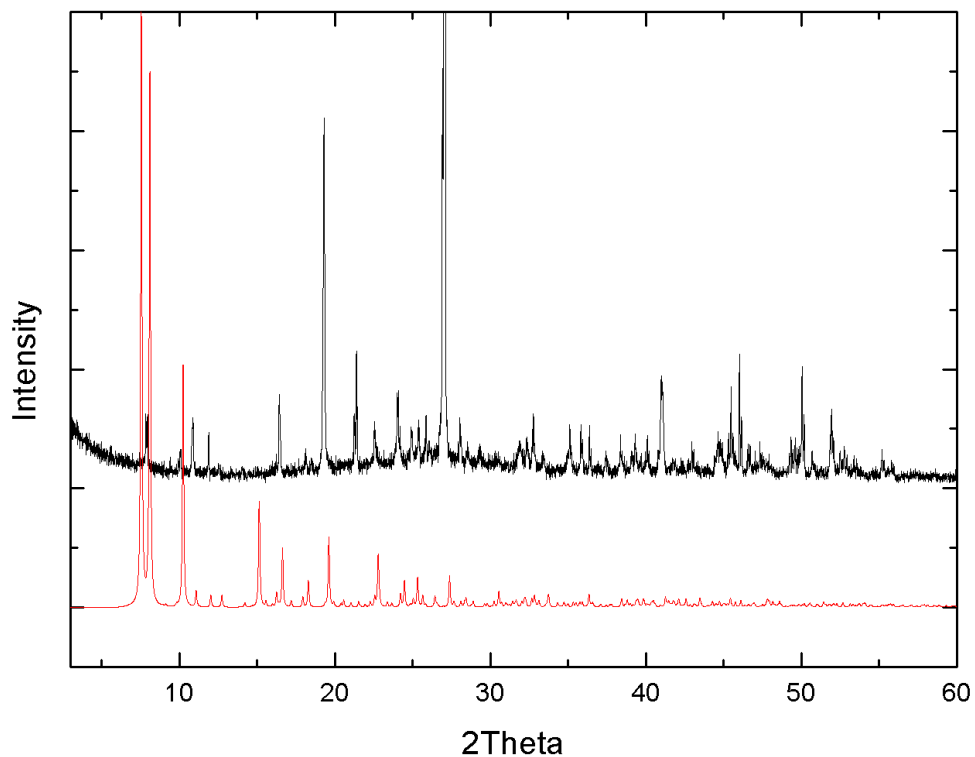
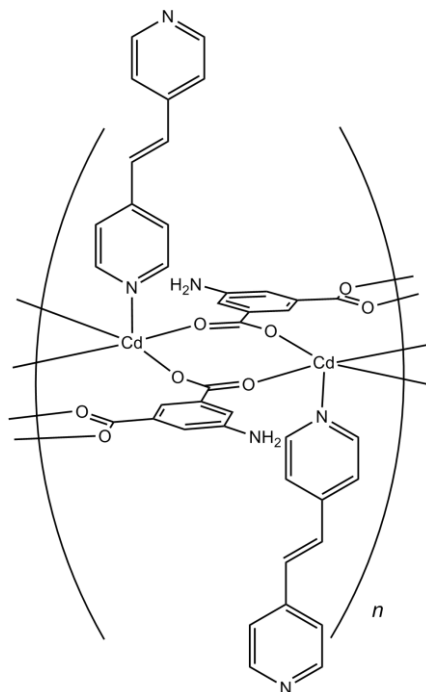


**Figure 138.** Powder X-ray diffraction data for **9**, showing the simulated (red) and collected (black) patterns.

6.3.10. *Synthesis of*  $\{[\text{Cd}(5\text{-AIP})(\text{DPE})].1.7\text{DMF}\}_n$  (**10**).



$\text{Cd}(\text{NO}_3)_2 \cdot 4\text{H}_2\text{O}$  (0.5 mmol, 0.15 g), 5-aminoisophthalic acid (0.5 mmol, 0.09 g) and

1,2-bis(4-pyridyl)ethylene (0.5 mmol, 0.09 g) were dissolved in DMF/Methanol (12 ml, 1:1) and sealed in a 23 ml Teflon lined steel reaction vessel. The vessel was heated to 85 °C for 72 hours, and then cooled at a rate of 2 °C per hour to room temperature. The reaction yielded 0.135 g pale yellow prisms (57 % based on Cd). Elem. anal. calcd. for C<sub>20</sub>H<sub>15</sub>CdN<sub>3</sub>O<sub>4</sub>: C 50.70, H 3.19, N 8.87, O 13.51; found C 50.65, H 3.10, N 8.78 %; IR (KBr, cm<sup>-1</sup>) 3351(s), 3221(w), 1665(s), 1698(s), 1544(s), 1502(w), 1495(w), 1427(s), 1325(w), 1252(w), 1221(w), 1207(w), 1169(w), 1150(w), 1096(m), 1070(w), 1017(m), 1004(w), 1017(m), 1004(w), 977(w), 935(w), 898(w), 864(w), 832(m), 808.4(w), 779(s), 731(s), 660(w).

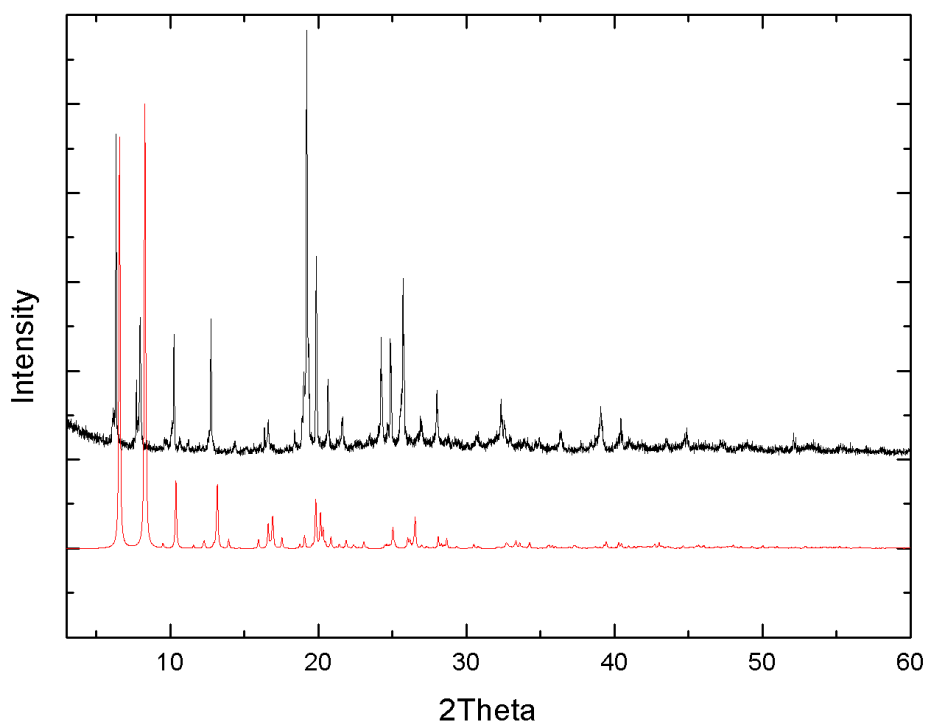
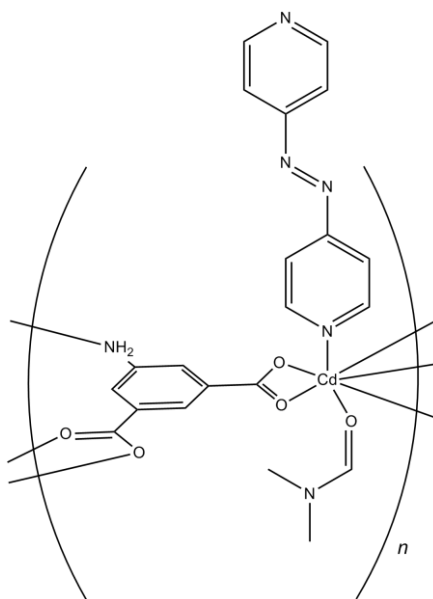


**Figure 139.** Powder X-ray diffraction data for **10**, showing the collected pattern (black) against the simulated pattern for the isostructural **7** (red).

6.3.11. Synthesis of  $\{[\text{Cd}(5\text{-AIP})(4,4'\text{-azopy})].\text{DMF}\}_n$  (**11**)



$\text{Cd}(\text{NO}_3)_2 \cdot 4\text{H}_2\text{O}$  (0.5 mmol, 0.15 g), 5-aminoisophthalic acid (0.5 mmol, 0.09 g) and 4,4'-azopyridine (0.5 mmol, 0.09 g) were dissolved in DMF/Methanol (12 ml, 1:1) and sealed in a 23 ml Teflon lined steel reaction vessel. The vessel was heated to 85 °C for 72 hours, and then cooled at a rate of 2 °C per hour to room temperature. The reaction yielded 0.149 g dark red prisms (54 % based on Cd). Elem. anal. calcd. for  $\text{C}_{18}\text{H}_{13}\text{CdN}_5\text{O}_4 \cdot \text{C}_3\text{H}_7\text{NO}$ : C 45.96, H 3.67, N 15.31; found C 45.80, H 3.69, N 15.04; IR (KBr,  $\text{cm}^{-1}$ ) 3259(w), 3184(w), 1653(s), 1648(s), 1609(m), 1559(m), 1545(m), 1517(w), 1507(w), 1499(w), 1424(w), 1318(m), 1263(w), 1224(w), 1195(w), 1172(w), 1127(w), 1087(m), 1052(w), 1027(w), 1016(m), 998(w), 970(m), 941(w), 912(w), 887(w), 848(w), 836(w), 801(m), 777(m), 723(s), 665(w);

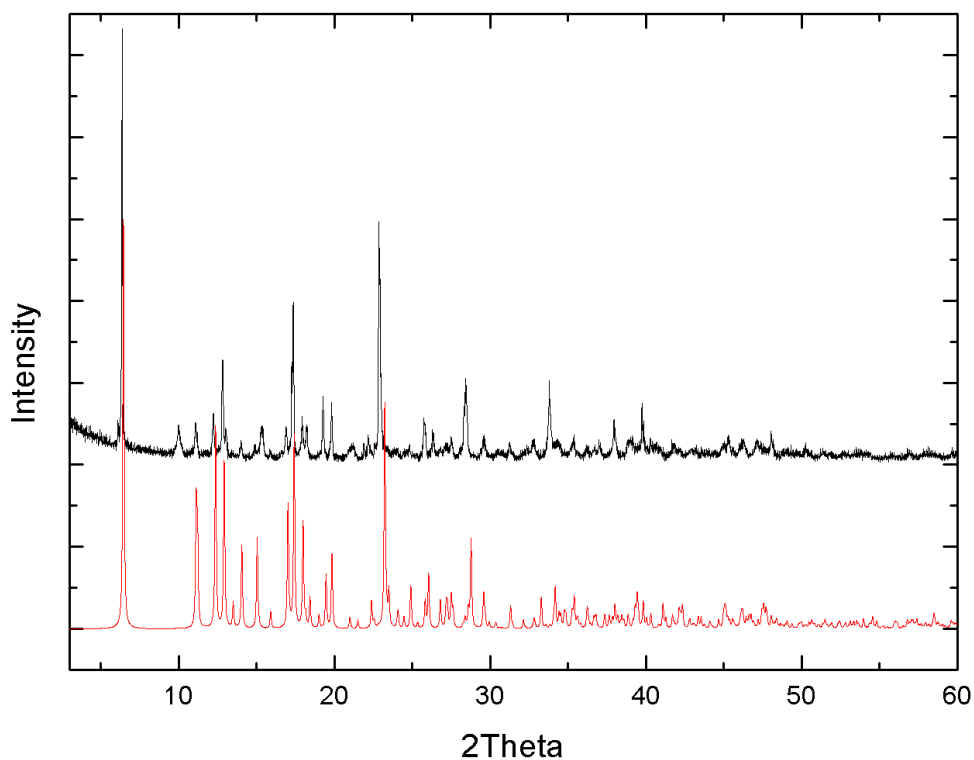
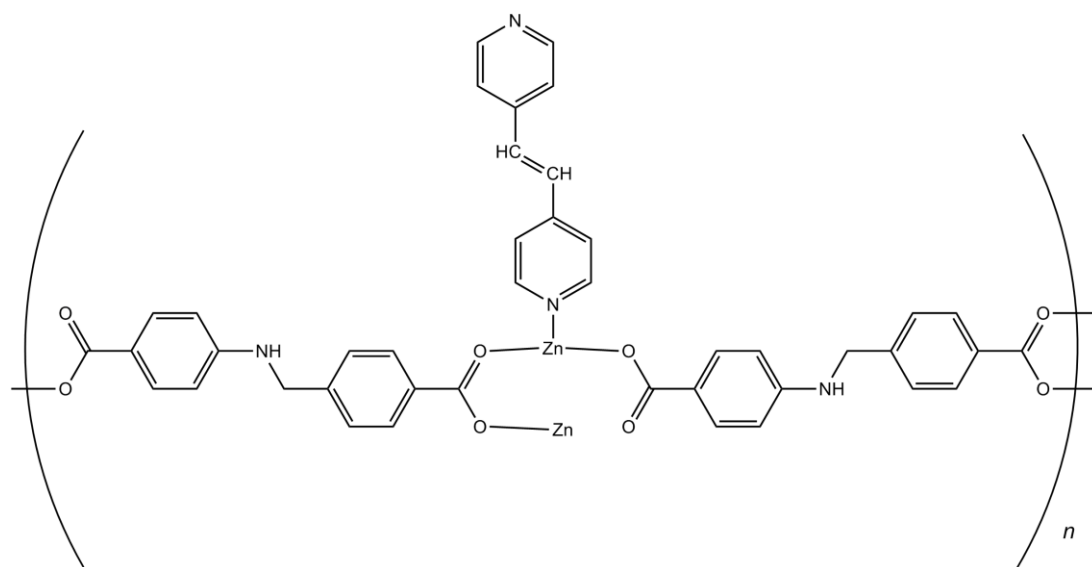


**Figure 140.** Powder X-ray diffraction data for **11**, showing the simulated (red) and collected (black) patterns.

#### 6.4. Pillared MOFs based on a reduced Schiff base dicarboxylic acid

##### 6.4.1. Synthesis of $\{[\text{Zn}_2(\text{L})_2(\text{DPE})] \cdot \text{H}_2\text{O}\}_n$ (**12**).



Ligand  $\text{LH}_2$  (0.2 mmol, 0.05 g),  $\text{Zn}(\text{OH})_2$  (0.2 mmol, 0.02 g) and DPE (0.1 mmol, 0.02 g) were added to 10 ml distilled water. The suspension was transferred to a 23

ml teflon lined steel reaction vessel which was subsequently sealed and heated to 110 °C for 72 hours. The vessel was then cooled at a rate of 2 °C hour<sup>-1</sup> to room temperature, yielding 0.09 g yellow prisms (51 % based on Zn). Elem. anal. calcd. for C<sub>42</sub>H<sub>32</sub>N<sub>4</sub>O<sub>8</sub>Zn<sub>2</sub>: C 59.24; H 3.79; N 6.58; found C 59.12, H 3.72, N 6.51; IR/cm<sup>-1</sup> (KBr): 3314(b), 2723(w), 2672(w), 2359(w), 2331(w), 1684 (w), 1612(s), 1549(m), 1521(m), 1506(w), 1432(w), 1415(w), 1335(m), 1282(m), 1225(w), 1205(w), 1181(m), 1139(w), 1113(w), 1099(w), 1085(w), 1063(w), 1063(m), 966(w), 955(w), 890(w), 845(m), 833(m), 787(m), 764(m), 721(w), 706(w), 668(w).

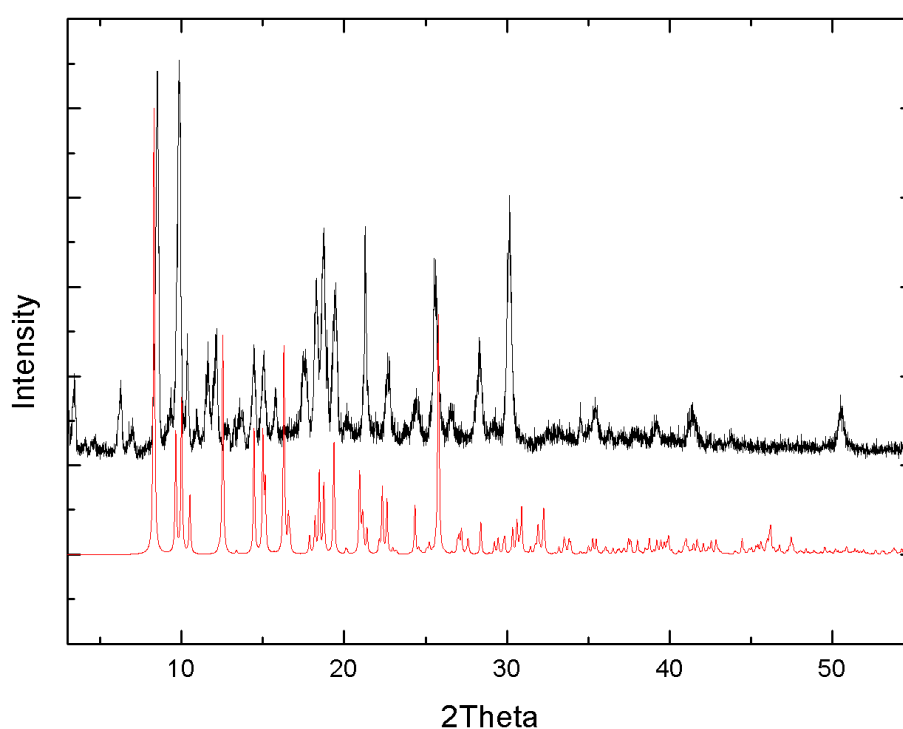
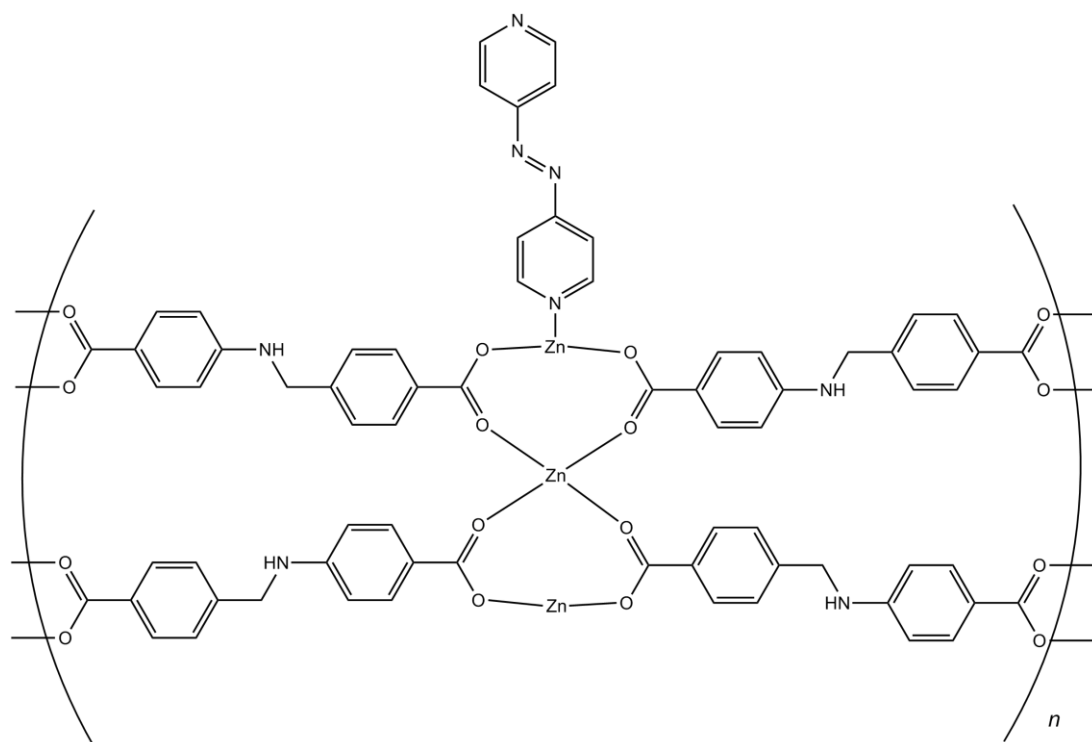


**Figure 141.** Powder X-ray diffraction data for **13**, showing the simulated (red) and collected (black) patterns.

6.4.2. Synthesis of  $\{[\text{Zn}_3(\text{L})_3(4,4'\text{-azopy})].7.5\text{H}_2\text{O}\}_n$  (**13**).



Ligand **LH**<sub>2</sub> (0.2 mmol, 0.05 g), Zn(OH)<sub>2</sub> (0.2 mmol, 0.02 g) and 4,4'-azopy (0.1 mmol, 0.02 g) were added to 10 ml distilled water. The suspension was transferred to a 23 ml teflon lined steel reaction vessel which was subsequently sealed and heated to 110 °C for 72 hours. The vessel was then cooled at a rate of 2 °C hour<sup>-1</sup> to room temperature, yielding 0.04 g red prisms (51 % based on Zn). Elem. anal. calcd. for C<sub>55</sub>H<sub>41</sub>N<sub>7</sub>O<sub>12</sub>Zn<sub>3</sub>.7H<sub>2</sub>O; C 50.26; H 4.22; N 7.46; found C 50.61; H 4.29; N 7.08 %: IR/cm<sup>-1</sup> (KBr):3348(w), 2717(w), 2667(w), 2359(w), 2336(w), 1700(w), 1653(w), 1606(s), 1559(w), 1539(w), 1519(w), 1506(w), 1488(w), 1331(m), 1281(m), 1222(w), 1180(m), 1142(w), 1111(w), 1080(w), 1046(w), 1029(w), 1018(w), 987(w), 847(m), 782(m), 761(m), 721(w),703(w).

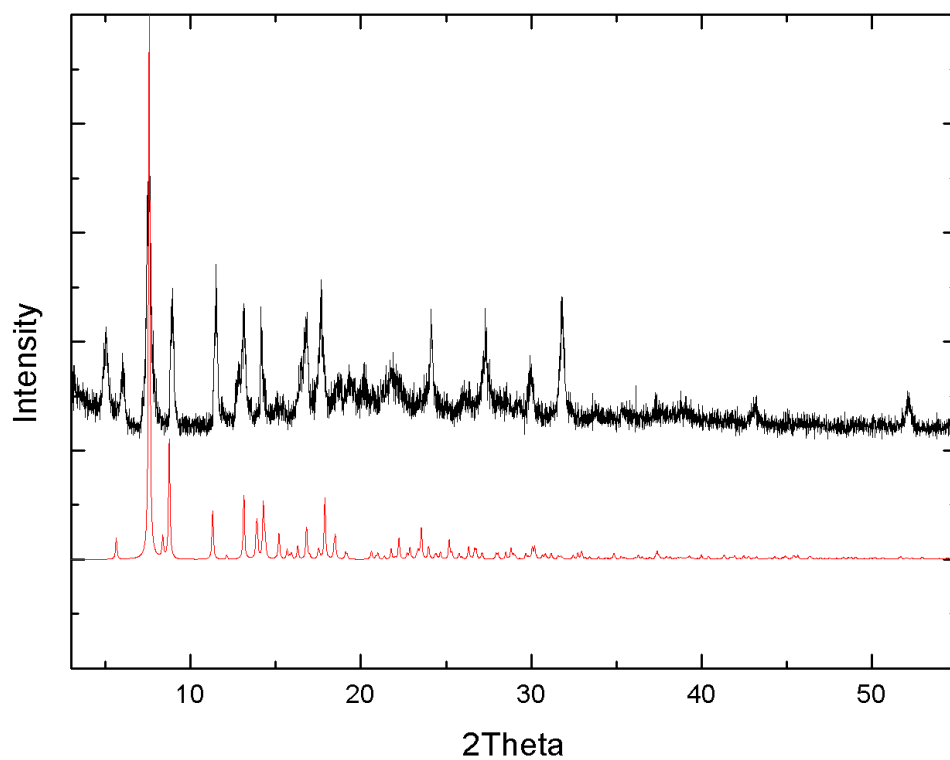
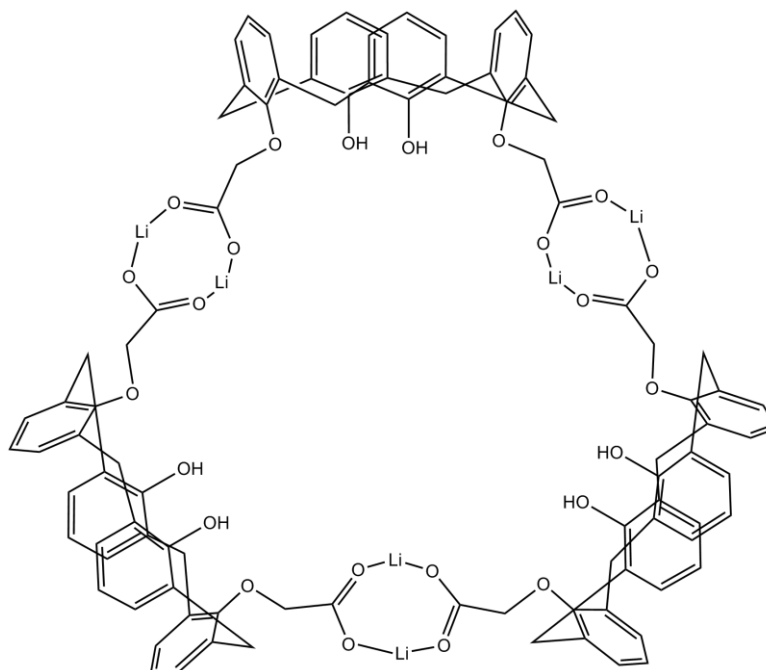


**Figure 142.** Powder X-ray diffraction data for **13**, showing the simulated (red) and collected (black) patterns.

## 6.5. 1D structures based on a lower-rim acid appended calix[4]arene

### 6.5.1. Synthesis of $\text{Li}_2(\text{L}^2)$ (**14**).



Ligand  $L^2H_2$  (0.61g, 0.81 mmol) and  $Li_2CO_3$  (0.06g, 0.77 mmol) were dissolved in refluxing ethanol (40 ml). After 2 hours the solution was cooled to room temperature and  $ZnCl_2$  (0.1g, 0.77 mmol) was added. The solution was stirred for 30 mins and then filtered, giving a light pink solution from which red crystals of suitable size for single crystal diffraction were grown by slow evaporation of the solvent (0.27 g, 63 % based on Li). Elem. anal. calcd. for  $C_{32}H_{26}Li_2O_8 \cdot 0.3H_2O$ : C, 68.83; H, 4.81; found: C, 69.12; H, 4.78; IR/ $cm^{-1}$  (KBr): 3340(b), 3184(b), 2962(s), 2930(s), 2863(s), 1784(s), 1751(s), 1734 (s), 1629 (s), 1579(s), 1537(s), 1267(s), 1261(s).  $^1H$  NMR ( $DMSO-d_6$ , 400 MHz, 273 K):  $\delta = 7.07$  (overlapping m, 4H, arylH), 7.01 (overlapping m, 4H, arylH), 6.69 (t, 2H,  $^3J_{HH}$  7.60 Hz, arylH), 6.47 (t, 2H,  $^3J_{HH}$  7.60 Hz, arylH), 4.26 (d, 4H,  $^2J_{HH}$  18 Hz, *endo-CH*<sub>2</sub>), 3.31 (d, 4H,  $^2J_{HH}$  18 Hz, *exo-CH*<sub>2</sub>):  $^7Li$  NMR ( $DMSO-d_6$ , 400 MHz, 273K)  $\delta = 17.08$ ;  $^{13}C$  NMR ( $DMSO-d_6$ , 75MHz, 273 K):  $\delta = 154.5$  ( $CH_2CO_2$ ), 134.51, 134.26, 129.26, 129.19, 128.88, 128.77, 128.62, 119.21 (all arylC), 79.42 ( $OCH_2$ ), 31.40 ( $ArCH_2Ar$ ).

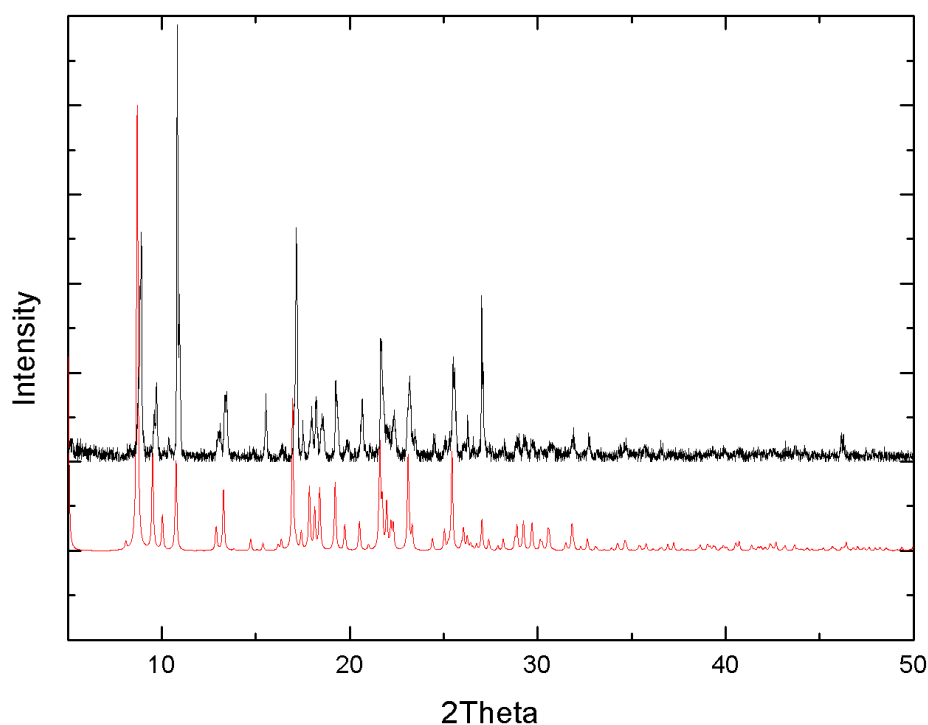
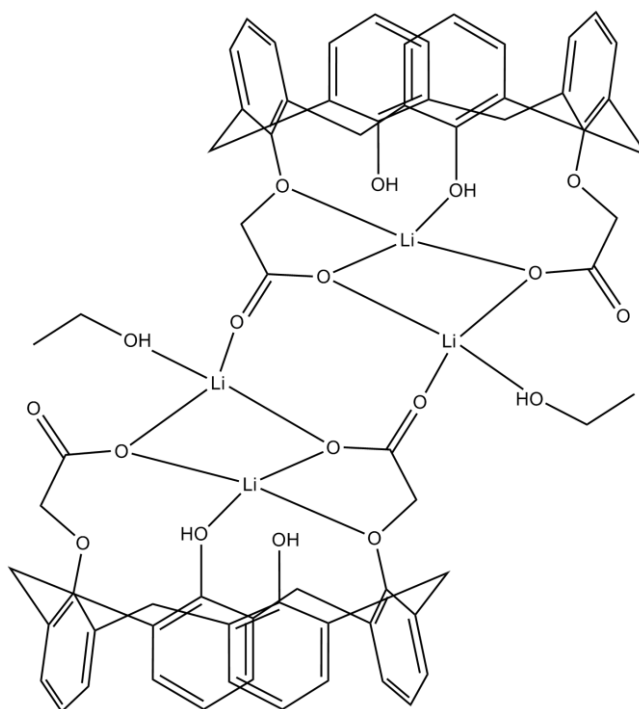


**Figure 143.** Powder X-ray diffraction data for **14**, showing the simulated (red) and collected (black) patterns.

### 6.5.2. Synthesis of $\text{Li}_2(\text{L}^2)(\text{C}_2\text{H}_6\text{O})_2$ (**15**).



To a solution of ligand  $\text{L}^2\text{H}_2$  (0.6 g, 1.1 mmol) in dry THF (30 ml), was added  ${}^t\text{BuLi}$  (1.2 ml, 1.6 M in pentane) at  $-78\text{ }^\circ\text{C}$ . The solution was stirred and allowed to warm to room temperature. Following evaporation of the THF, the grey/blue solid was extracted with dry ethanol (40 ml) giving a brightly coloured red solution from which crystals suitable for X-ray diffraction were grown over the course of 3 days (0.48 g, 72% based on  $\text{L}^2\text{H}_2$ ). Elem. anal. calcd. for  $\text{C}_{32}\text{H}_{26}\text{Li}_2\text{O}_8, 2\text{C}_2\text{H}_6\text{O} \cdot 0.2\text{H}_2\text{O}$ : C, 63.53; H, 6.22; found C, 63.30; H, 6.37. IR/ $\text{cm}^{-1}$  (KBr): 3349(b), 3313(b), 2958(s), 2922(s), 2854(s), 1679(s), 1632(s), 1261(s), 1205(s); MS (MALDI,  $m/z$ ) 1663.6  $[\text{C}_{33}\text{H}_{28}\text{O}_7\text{Li}_2]^+_{n=3}$ , 2215.7  $[\text{C}_{33}\text{H}_{28}\text{O}_7\text{Li}_2]^+_{n=4}$ , 2768.9  $[\text{C}_{33}\text{H}_{28}\text{O}_7\text{Li}_2]^+_{n=5}$ .  ${}^1\text{H}$  NMR ( $\text{DMSO-d}_6$ , 400 MHz, 273 K):  $\delta = 7.12$  (d, 4H,  ${}^2J_{\text{HH}} 7.40$  Hz, arylH), 7.05 (d, 4H,  ${}^2J_{\text{HH}} 7.56$  Hz, arylH), 6.77 (t, 2H,  ${}^3J_{\text{HH}} 7.56$  Hz, arylH), 6.58 (t, 2H,  ${}^3J_{\text{HH}} 7.57$  Hz, arylH), 4.39 (s, 4H,  $\text{OCH}_2$ ), 4.21 (d, 4H,  ${}^2J_{\text{HH}} 12.0$  Hz, *endo-CH*<sub>2</sub>), 3.42 (d, 4H,  ${}^2J_{\text{HH}} 12$  Hz, *exo-CH*<sub>2</sub>), 1.05 (t, 3H,  ${}^3J_{\text{HH}} 7.00$  Hz,  $\text{CH}_3\text{CH}_2\text{OH}$ ):  ${}^7\text{Li}$  NMR ( $\text{DMSO-d}_6$ , 400 MHz, 273K):  $\delta = 1.97$ ;  ${}^{13}\text{C}$  NMR ( $\text{DMSO-d}_6$ , 75MHz, 273 K):  $\delta = 170.07$  ( $\text{CH}_2\text{CO}_2$ ), 151.96, 151.75, 133.71, 128.88, 128.54, 127.80, 125.06, 119.35 (all aryl C), 75.68 ( $\text{OCH}_2$ ), 30.54 ( $\text{ArCH}_2\text{Ar}$ ).

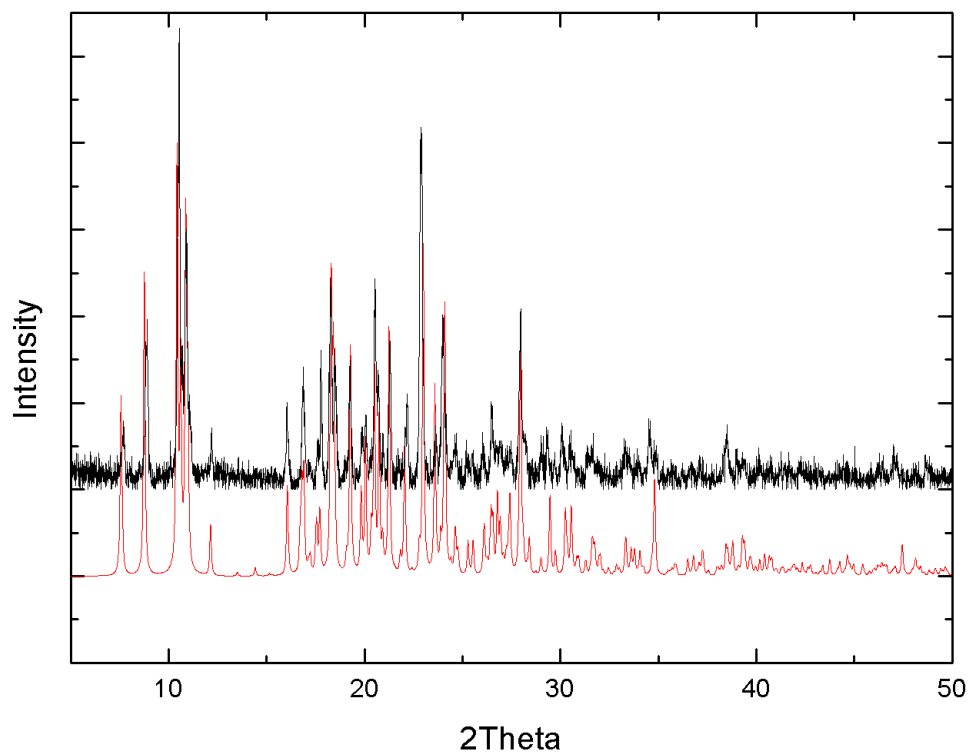
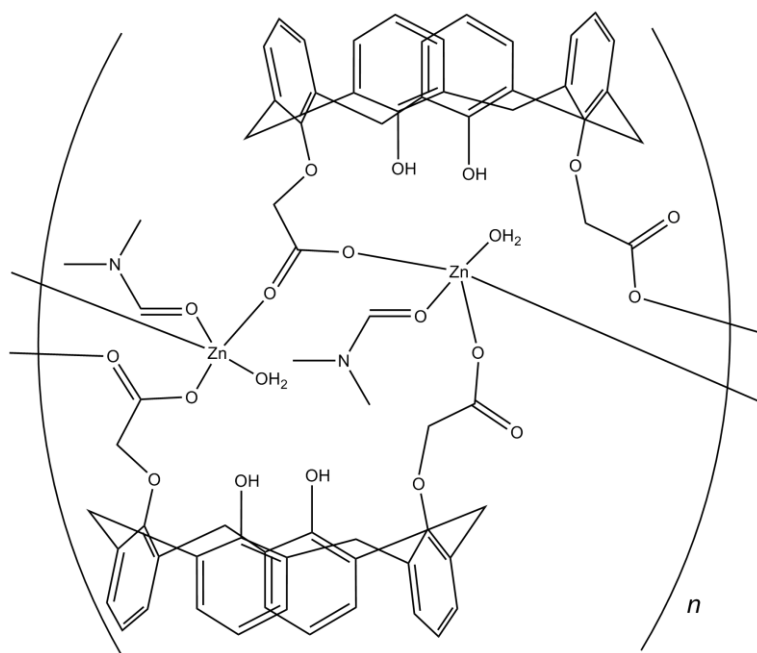


**Figure 144.** Powder X-ray diffraction data for **15**, showing the simulated (red) and collected (black) patterns.

6.5.3. *Synthesis of*  $[\text{Zn}(\text{L}^2)(\text{DMF})(\text{H}_2\text{O})]_n$  (**16**).



Ligand  $L^2H_2$  (0.16 g, 0.25 mmol) and  $Zn(OAc)_2$  (0.05 g, 0.25 mmol) were dissolved in a DMF/ethanol/water (12:3:1 ml) mixture in a glass vial. The vial was sealed, heated to 85 °C for 4 days and then cooled at a rate of 2 °C h<sup>-1</sup> to room temperature, yielding purple fine needles (0.08 g, 47 % based on Zn). Elem. anal. calcd. for  $C_{32}H_{28}NO_9Zn \cdot 1.5C_3H_7NO$ : C, 59.97; H, 5.24; N, 2.87; found: C, 60.23; H, 5.24; N, 2.88; IR/cm<sup>-1</sup> (KBr): 3368(b), 2726(s), 2670(s), 1654(s), 1628(s), 1589(s), 1410(s), 1304(s), 1254(s), 1221(s), 1195(s), 1156(s), 1091(s) 1068(s), 1041(s), 967(b), 930(s), 910(s), 821.7(s), 760(s), 744(s), 721(s), 690/9s/0, 665(s); <sup>1</sup>H NMR (DMSO d<sub>6</sub>, 400 MHz, 273 K):  $\delta$  = 8.02 (s, 1H, *CHO*), 7.05 (d, 8H, <sup>2</sup>J<sub>HH</sub> 7.36 Hz, *arylH*), 6.78 (t, 2H, <sup>3</sup>J<sub>HH</sub> 7.43 Hz, *arylH*), 6.53 (t, 2H, <sup>3</sup>J<sub>HH</sub> 7.30 Hz, *arylH*), 4.52 (overlapping m, 6H, *endo-CH*<sub>2</sub>, *OCH*<sub>2</sub>), 3.33 (overlapping m, 56H, *exo-CH*<sub>2</sub>, *H*<sub>2</sub>O,) 2.95 (s, 3H, *CH*<sub>3</sub>), 2.80 (s, 3H, *CH*<sub>3</sub>). Attempts to obtain <sup>13</sup>C NMR spectroscopic data on this complex were thwarted by poor solubility (even in hot dmsod<sub>6</sub>, the complex quickly drops out of solution).

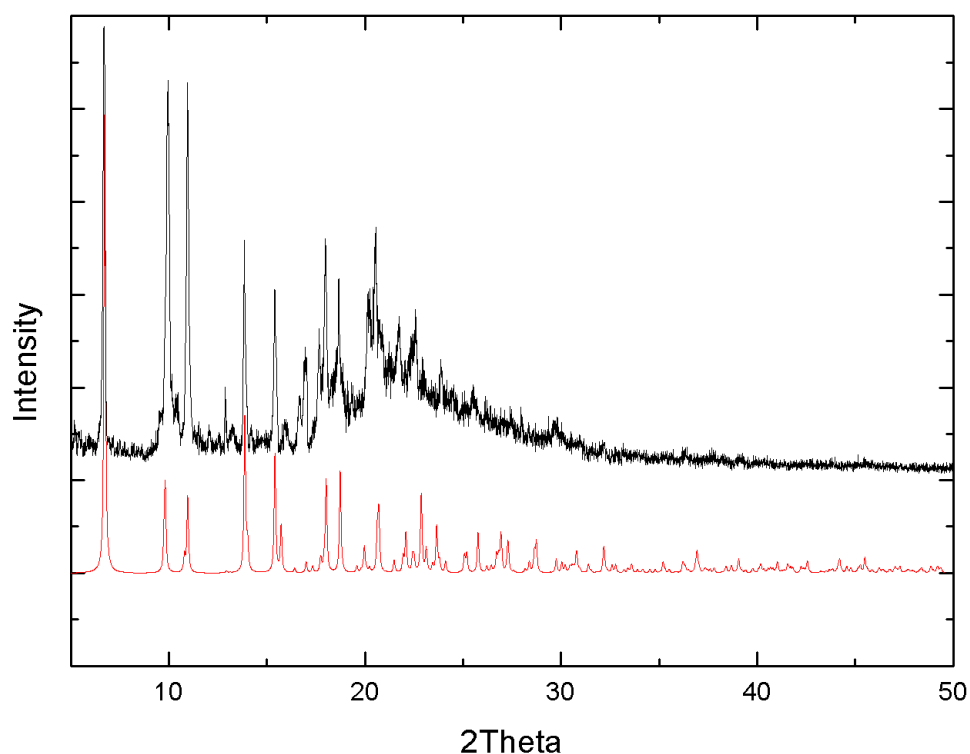
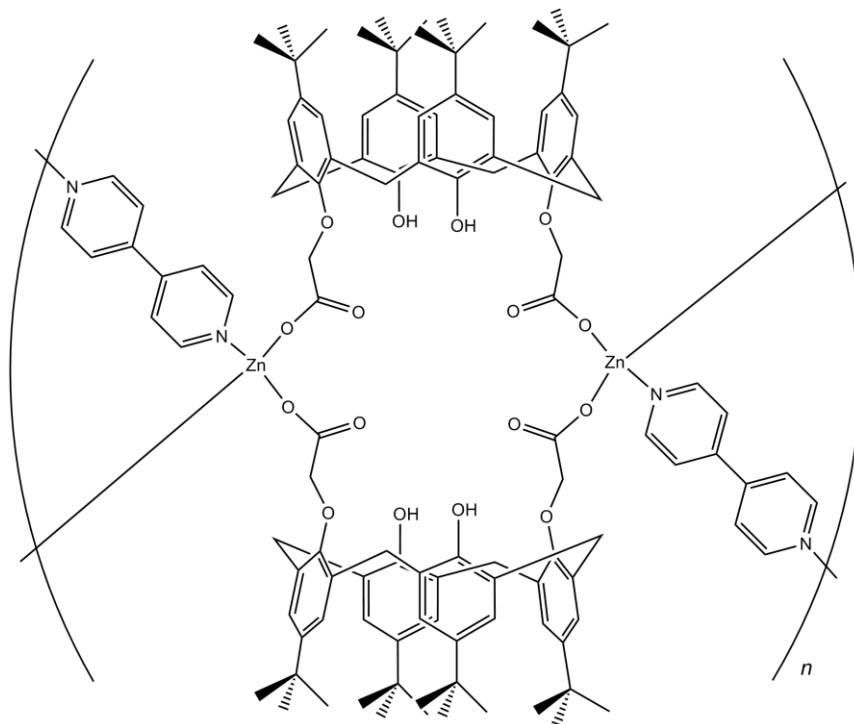


**Figure 145.** Powder X-ray diffraction data for **16**, showing the simulated (red) and collected (black) patterns.

## 6.6. Pillared metal-organic frameworks based on a lower-rim acid appended calix[4]arene

### 6.6.1. Synthesis of $\{[\text{Zn}(\text{L}^3)(4,4'\text{-bipy})].2.25\text{DEF}\}_n$ (**17**)



Ligand  $\text{L}^3\text{H}_2$  (0.5 mmol, 0.36 g),  $\text{Zn}(\text{NO}_3)_2 \cdot 6\text{H}_2\text{O}$  (0.5 mmol, 0.15 g) and 4,4'-bipy (0.5 mmol, 0.08 g) were dissolved in a DEF/MeOH mixture (20 ml, 1:1). The solution was sealed in a 23 ml teflon lined steel reaction vessel and heated to 75 °C for 96 hours. The reaction vessel was then cooled at a rate of 2 °C hour<sup>-1</sup> to room temperature yielding 0.365 g colourless prisms (74 % based on Zn). Elem. anal. calcd. for  $\text{C}_{58}\text{H}_{66}\text{N}_2\text{O}_8\text{Zn} \cdot 2\text{C}_5\text{H}_{11}\text{NO}$ : C 68.81, H 7.47, N 4.72; found C 68.42, H 7.81, N 4.78 %; IR/cm<sup>-1</sup> (KBr): 3330(b), 2726(w), 2.667(w), 1651(s), 1615(s), 1592(s), 1535(w), 1481(s), 1418(w), 1363(s), 1305(s), 1276 (w), 1264(w), 1234(w), 1201(s), 1127(m), 1109(w), 1071(w), 1049(m), 965(w), 948(w), 917(w), 871(m), 816(m), 785(w), 764(w), 722(m), 700(w), 645(w).

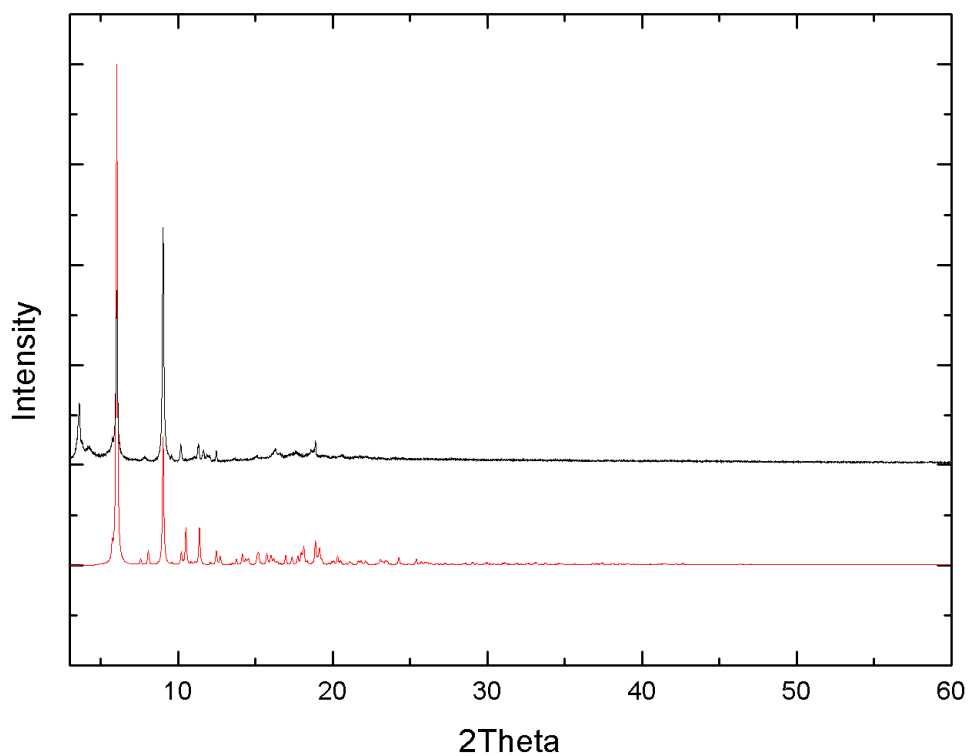
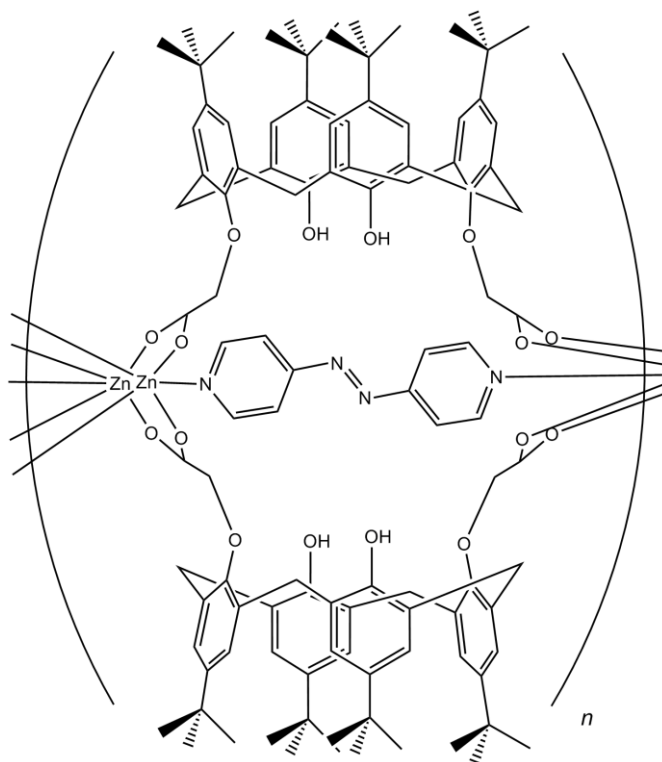


**Figure 146.** Powder X-ray diffraction data for **17**, showing the simulated (red) and collected (black) patterns.

6.6.2. Synthesis of  $\{[\text{Zn}_2(\text{L}^3)_2(\text{DPE})].\text{DEF}\}_n$  (**18**).



Ligand  $L^3H_2$  (0.5 mmol, 0.36 g),  $Zn(NO_3)_2 \cdot 6H_2O$  (0.5 mmol, 0.15 g) and DPE (0.5 mmol, 0.09 g) were dissolved in a DEF/MeOH mixture (20 ml, 1:1). The solution was sealed in a 23 ml teflon lined steel reaction vessel and heated to 75 °C for 96 hours. The reaction vessel was then cooled at a rate of 2 °C hour<sup>-1</sup> to room temperature yielding 0.336 g pale yellow prisms (73 % based on Zn) which were of suitable quality for single crystal X-ray diffraction. Elem. anal. calcd. for  $C_{108}H_{126}N_2O_{16}Zn_2 \cdot 2C_5H_{11}NO$ : C 69.43, H 7.31, N 2.74; found C 69.31, H 7.33, N 2.64; IR/cm<sup>-1</sup> (KBr): 3412(s), 2725(w), 2667(w), 1662(s), 1612(s), 1559(w), 1545(w), 1507(w), 1365(s), 1343(w), 1328(w), 1303(w), 1290(w), 1264(w), 1245(w), 1194(m), 1164(w), 1123(w), 1108(w), 1097(w), 1072(w), 1039(m), 980(w), 931(w), 915(w), 871(m), 819(w), 800(w), 778(w), 761(w), 722(m).

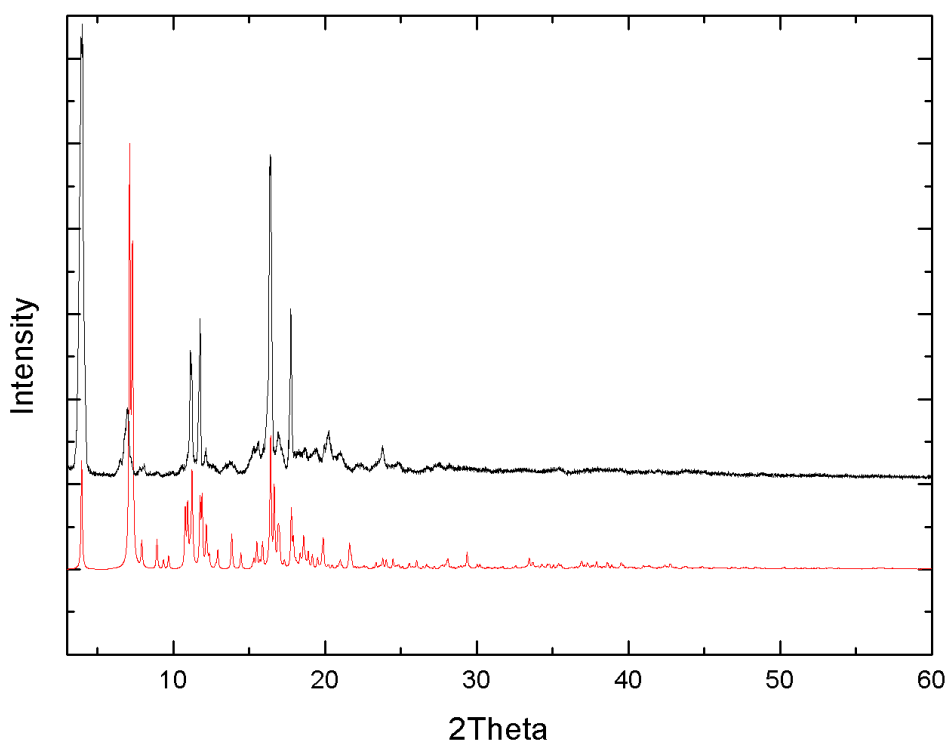
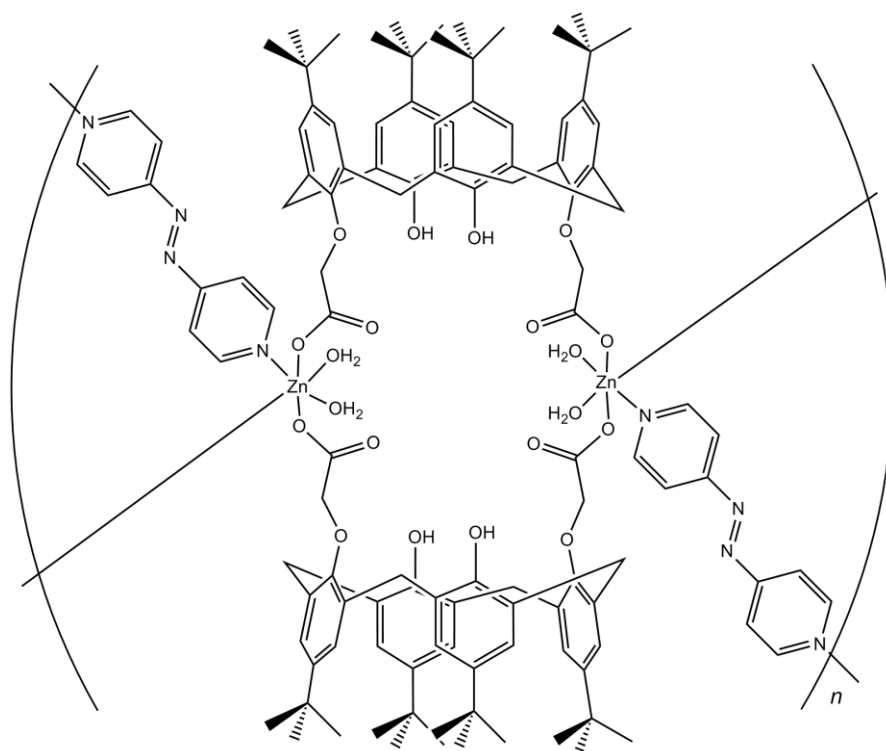


**Figure 147.** Powder X-ray diffraction data for **18**, showing the simulated (red) and collected (black) patterns.

### 6.6.3. Synthesis of $\{[\text{Zn}(\text{OH}_2)_2(\text{L}^2)(4,4'\text{-azopy})].\text{DEF}\}_n$ (**19**)



Ligand  $\text{L}^3\text{H}_2$  (0.5 mmol, 0.36 g),  $\text{Zn}(\text{NO}_3)_2 \cdot 6\text{H}_2\text{O}$  (0.5 mmol, 0.15 g) and 4,4'-azopy (0.5 mmol, 0.09 g) were dissolved in a DEF/MeOH mixture (20 ml, 1:1). The solution was sealed in a 23 ml teflon lined steel reaction vessel and heated to 75 °C for 96 hours. The reaction vessel was then cooled at a rate of 2 °C hour<sup>-1</sup> to room temperature yielding 0.328 g orange prisms (63 % based on Zn). Elem. anal. calcd. for  $\text{C}_{58}\text{H}_{70}\text{N}_4\text{O}_{10}\text{Zn} \cdot \text{C}_5\text{H}_{11}\text{NO}$ : C 65.81; H 7.10; N 6.09; found C 65.54; H 7.11; N 6.05 %; IR/cm<sup>-1</sup> (KBr): 3417(s), 2725(w), 2661(w), 1648(m), 1632(s), 1594(w), 1580(m), 1484(s), 1363(s), 1339(w), 1301(m), 1266(w), 1266(w), 12.6(m), 1195(m), 1169(w), 1125(m), 1098(w), 1055(m), 1028(w), 976(w), 941(w),m 917(w), 871(m), 845(w), 835(w), 818(w), 803(w), 767(w), 723(m), 694(w), 668(w), 632(w).

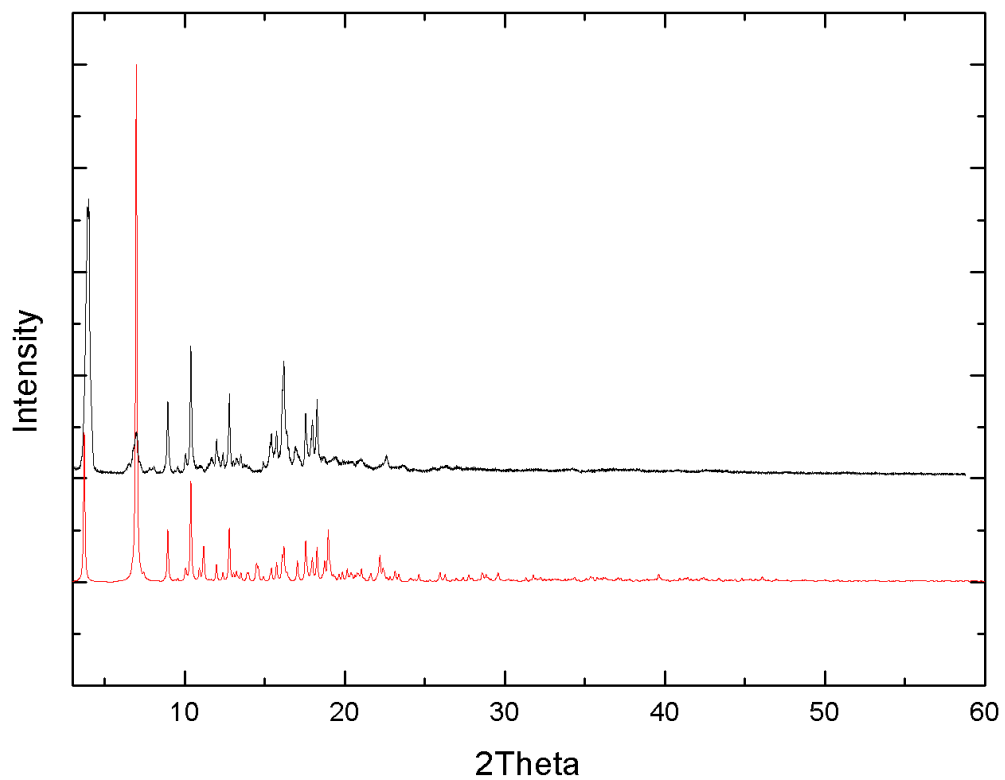


**Figure148.** Powder X-ray diffraction data for **19**, showing the simulated (red) and collected (black) patterns.

## 6.7. References

---

- 1 G. M. Sheldrick, SHELX-97 – *Programs for crystal structure determination (SHELXS) and refinement (SHELXL)*, University of Gottingen, Germany (1997).
- 2 *Programs CrysAlis-CCD and –RED*, Oxford Diffraction Ltd., Abington, UK (2005).
- 3 Y. Y. Liu, Z. H. Wang, J. Yang, B. Liu, Y. Y. Liu, J. F. Ma, *CrystEngComm*, 2011, **13**, 3811.
- 4 S. Shinkai, K. Iwamoto, *J. Org. Chem.* 1992, **57**, 7066.

## **Chapter 7**

## **Appendix**

**Table 2.** Crystallographic data for structures **1**, **3**, **5** and **6**

Structure	1	3	5	6
Formula	C <sub>13</sub> H <sub>9</sub> N <sub>2</sub> O <sub>4</sub> Zn·C <sub>3</sub> H <sub>7</sub> NO	C <sub>28</sub> H <sub>21</sub> Co <sub>2</sub> N <sub>7</sub> O <sub>10</sub> ·2(C <sub>2</sub> H <sub>6</sub> O)	C <sub>18</sub> H <sub>13</sub> CoN <sub>5</sub> O <sub>4</sub> ·2(C <sub>4</sub> H <sub>9</sub> NO)	C <sub>18</sub> H <sub>13</sub> MnN <sub>3</sub> O <sub>4</sub> ·2(C <sub>3</sub> H <sub>9</sub> NO)
Formula weight (g mol <sup>-1</sup> )	395.69	825.51	596.51	540.48
Temperature (K)	100	150	100	150
Radiation, λ (Å)	Mo Kα, 0.71073	Mo Kα, 0.71073	Mo Kα, 0.71073	Mo Kα, 0.71073
Crystal system	Monoclinic	Monoclinic	Monoclinic	Orthorhombic
Space group	<i>I</i> 2/a	<i>C</i> 2/c	<i>P</i> 2 <sub>1</sub> /c	<i>P</i> bam
<i>a</i> (Å)	16.112 (6)	20.5321 (19)	13.20 (2)	14.103 (2)
<i>b</i> (Å)	7.649 (3)	9.8581 (9)	16.71 (2)	17.021 (3)
<i>c</i> (Å)	29.100 (13)	18.1007 (17)	14.11 (2)	11.6095 (18)
α (°)				90
β (°)	101.562 (5)	109.2702 (13)	104.24 (3)	90
γ (°)				90
<i>V</i> (Å <sup>3</sup> )	3514 (2)	3458.4 (6)	3017 (7)	2786.8 (8)
<i>Z</i>	8	4	4	4
Calculated density (Mgm <sup>-3</sup> )	1.496	1.585	1.313	1.288
Adsorption coefficient (mm <sup>-1</sup> )	1.43	1.03	0.62	0.52
Transmission factors (max., min)	27.5, 2.6	2.3, 27.9	2.5, 31.2	2.3, 30.5
Crystal size (mm)	0.05 × 0.01 × 0.01	0.53 × 0.19 × 0.07	0.10 × 0.09 × 0.06	0.92 × 0.47 × 0.45
θ <sub>max</sub> (°)	27.5	28.2	27.5	30.6
Reflections measured	8779	16932	13115	26786
Unique reflections, R <sub>int</sub>	3988, 0.025	4235, 0.033	6401, 0.046	4439, 0.059
Reflections with <i>F</i> <sup>2</sup> > 2σ( <i>F</i> <sup>2</sup> )	3435	3213	4462	3677
Number of parameters	215	319	290	188
R <sub>1</sub> , wR <sub>2</sub> [ <i>F</i> <sup>2</sup> > 2σ( <i>F</i> <sup>2</sup> )]	0.042, 0.108	0.050, 0.159	0.106, 0.340	0.102, 0.267
<i>F</i> (000)	1624	1696	1244	1132
Least-squares matrix	Full	Full	Full	Full
GoF	1.10	1.05	1.09	1.08
Largest difference peak and hole (e Å <sup>-3</sup> )	0.43 and -0.47	0.89 and -0.79	1.03, -0.81	1.72, and -1.30

**Table 3.** Crystallographic data for structures **7**, **9**, **11** and **12**

Structure	7	9	11	12
Formula	C <sub>38</sub> H <sub>57</sub> MnN <sub>9</sub> O <sub>10</sub>	C <sub>18</sub> H <sub>13</sub> CdN <sub>4</sub> O <sub>4</sub> ·3(C <sub>3</sub> H <sub>7</sub> NO)	C <sub>16</sub> H <sub>16</sub> CdN <sub>4</sub> O <sub>5</sub>	C <sub>42</sub> H <sub>32</sub> N <sub>4</sub> O <sub>8</sub> Zn <sub>2</sub> ·0.98(H <sub>2</sub> O)
Formula weight (g mol <sup>-1</sup> )	854.87	667.00	456.73	870.12
Temperature (K)	150	150	150	100
Radiation, λ (Å)	Mo Kα, 0.71073	Mo Kα, 0.71073	Mo Kα, 0.71073	Mo Kα, 0.71073
Crystal system	Monoclinic	Orthorhombic	Triclinic	Triclinic
Space group	P2 <sub>1</sub> /c	P2 <sub>1</sub> 2 <sub>1</sub> 2	P <sup>-</sup> 1	P <sup>-</sup> 1
<i>a</i> (Å)	13.880(6)	14.0579 (14)	8.1035 (15)	8.7073 (7)
<i>b</i> (Å)	17.016(7)	17.2541 (17)	8.1227 (15)	10.1502 (10)
<i>c</i> (Å)	29.100 (13)	11.6948 (12)	13.739 (3)	11.8518 (10)
α (°)		90	89.277 (3)	65.406 (7)
β (°)	14.142(9)	90	84.236 (3)	76.580 (7)
γ (°)		90	77.887 (3)	78.160 (7)
<i>V</i> (Å <sup>3</sup> )	3229 (3)	2836.6 (5)	879.7 (3)	919.43 (15)
<i>Z</i>	4	4	2	1
Calculated density (Mgm <sup>-3</sup> )	1.758	1.562	1.724	1.571
Adsorption coefficient (mm <sup>-1</sup> )	0.495	0.83	1.28	1.37
Transmission factors (max., min)	0.797, 0.717	25.8, 2.4	27.1, 2.6	27.6, 3.0
Crystal size (mm)	0.72 × 0.52 × 0.48	0.52 × 0.08 × 0.04	0.22 × 0.19 × 0.07	0.11 × 0.05 × 0.02
θ <sub>max</sub> (°)	28.2	28.4	28.4	27.5
Reflections measured	22679	24400	17030	8520
Unique reflections, R <sub>int</sub>	7901, 0.117	7075, 0.066	4355, 0.053	4169, 0.041
Reflections with <i>F</i> <sup>2</sup> > 2σ( <i>F</i> <sup>2</sup> )	3715	5319	3728	3318
Number of parameters	300	273	244	376
R <sub>1</sub> , wR <sub>2</sub> [ <i>F</i> <sup>2</sup> > 2σ( <i>F</i> <sup>2</sup> )]	0.1711, 0.3899	0.067, 0.167	0.033, 0.075	0.050, 0.134
F(000)	1812	1386	456	446
Least squares matrix	Full	Full	Full	Full
GoF	1.13	1.01	1.06	1.07
Largest difference peak and hole (e Å <sup>-3</sup> )	5.16 and -1.42	4.48 and -0.77	1.07, -0.77	0.66, and -0.97

**Table 4.** Crystallographic data for structures **13**, **14**, **15** and **16**

Structure	13	14	15	16
Formula	C <sub>55</sub> H <sub>41</sub> N <sub>7</sub> O <sub>12</sub> Zn <sub>3</sub> ·7.5(H <sub>2</sub> O)	C <sub>32</sub> H <sub>26</sub> Li <sub>2</sub> O <sub>8</sub>	C <sub>34</sub> H <sub>32</sub> Li <sub>2</sub> O <sub>9</sub>	C <sub>35</sub> H <sub>35</sub> NO <sub>10</sub> Zn
Formula weight (g mol <sup>-1</sup> )	1323.17	552.40	598.48	695.01
Temperature (K)	100	140	140	140
Radiation, λ (Å)	Mo Kα, 0.71073	Mo Kα, 0.71073	Mo Kα, 0.71073	Mo Kα, 0.71073
Crystal system	Monoclinic	Trigonal	Triclinic	Orthorhombic
Space group	C2/c	R-3	P-1	P2 <sub>1</sub> 2 <sub>1</sub> 2 <sub>1</sub>
a (Å)	21.2518 (17)	35.2552(11)	10.3639(7)	9.9928(5)
b (Å)	23.3115 (18)	35.2552(11)	11.7721(5)	17.3371(11)
c (Å)	12.3700 (9)	11.7244(3)	11.8355(8)	17.7642(9)
α (°)		90	87.429(4)	90
β (°)	96.612 (7)	90	78.483(3)	90
γ (°)		120	83.793(4)	90
V (Å <sup>3</sup> )	6087.5 (8)	12620.2(6)	1406.22(15)	3077.6(3)
Z	4	18	2	4
Calculated density (Mgm <sup>-3</sup> )	1.444	1.308	1.413	1.500
Adsorption coefficient (mm <sup>-1</sup> )	1.25	0.093	0.101	0.862
Transmission factors (max., min)	27.5, 3.0	1.071, 0.845	22.5, 2.92	1.00, 0.917
Crystal size (mm)	0.08 × 0.05 × 0.03	0.37 x 0.26 x 0.23	0.09 x 0.04 x 0.01	0.17 x 0.03 x 0.02
θ <sub>max</sub> (°)	22.5	28.4	22.5	27.5
Reflections measured	9389	49096	16007	40585
Unique reflections, R <sub>int</sub>	3860, 0.053	3890, 0.065	3662, 0.081	5399, 0.199
Reflections with F <sup>2</sup> > 2σ(F <sup>2</sup> )	2201	2675	2285	3606
Number of parameters	349	428	418	427
R <sub>1</sub> , wR <sub>2</sub> [F <sup>2</sup> > 2σ(F <sup>2</sup> )]	0.108, 0.321	0.057, 0.159	0.079, 0.167	0.076, 0.113
F(000)	2724	5184	628	1448
Least squares matrix	Full	Full	Full	Full
GoF	1.07	0.990	1.066	1.019
Largest difference peak and hole (e Å <sup>-3</sup> )	0.86 and -2.11	0.35 and -0.33	0.28, -0.33	0.83, and -0.56

**Table 5.** Crystallographic data for structures **17**, **18**, and **19**

Structure	17	18	19
Formula	C <sub>58</sub> H <sub>66</sub> N <sub>2</sub> O <sub>8</sub> Zn·2.25(C <sub>5</sub> H <sub>11</sub> NO)	C <sub>108</sub> H <sub>126</sub> N <sub>2</sub> O <sub>16</sub> Zn <sub>2</sub> ·C <sub>5</sub> H <sub>11</sub> NO	C <sub>116</sub> H <sub>140</sub> N <sub>8</sub> O <sub>20</sub> Zn <sub>2</sub> ·C <sub>5</sub> H <sub>11</sub> NO
Formula weight (g mol <sup>-1</sup> )	1212.08	1939.99	2198.24
Temperature (K)	100	100	100
Radiation, λ (Å)	Synchrotron, 0.7749	Mo Kα, 0.71073	Synchrotron, 0.7749
Crystal system	Monoclinic	Triclinic	Orthorhombic
Space group	C2/c	P $\bar{1}$	Pna2 <sub>1</sub>
a (Å)	17.8321 (17)	10.539 (8)	26.249 (3)
b (Å)	46.606 (4)	12.738 (10)	10.0932 (13)
c (Å)	18.9497 (18)	23.029 (19)	47.440 (6)
α (°)		103.240 (16)	90
β (°)	114.056 (6)	95.592 (14)	90
γ (°)		91.319 (17)	90
V (Å <sup>3</sup> )	14381 (2)	2992 (4)	12569 (3)
Z	8	1	4
Calculated density (Mgm <sup>-3</sup> )	1.120	1.077	1.162
Adsorption coefficient (mm <sup>-1</sup> )	0.5	0.46	0.56
Transmission factors (max., min)	24.2, 2.4	27.3, 2.9	33.1, 2.7
Crystal size (mm)	0.25 × 0.05 × 0.01	0.12 × 0.10 × 0.05	0.28 × 0.09 × 0.02
θ <sub>max</sub> (°)	24.3	27.3	22.5
Reflections measured	44156	32328	104420
Unique reflections, R <sub>int</sub>	8869, 0.075	12975, 0.070	33131, 0.053
Reflections with I <sup>2</sup> > 2σ(I <sup>2</sup> )	6524	10016	27271
Number of parameters	736	747	1331
R <sub>1</sub> , wR <sub>2</sub> [I <sup>2</sup> > 2σ(I <sup>2</sup> )]	0.071, 0.213	0.125, 0.349	0.084, 0.224
F(000)	5184	1032	4672
Least squares matrix	Full	Full	Full
GoF	1.03	1.06	1.02
Largest difference peak and hole (e Å <sup>-3</sup> )	0.85 and -0.42	1.33 and -0.90	4.00, -0.82